Continental Topography and Gravity

by

© Randell Alexander Stephenson, M.Sc.

A thesis submitted
in partial fulfilment of the requirements
for the Degree of Doctor of Philosophy

Department of Geology
Dalhousie University
Halifax, Canada
10 September 1981

Table of Contents | Page

Page

List of Figures

Page

List of Tables

Abstract

The long term rheological behaviour of the continental lithosphere is investigated by means of isostatic response functions $\hat{Q}(k)$, gravity normalized by topography in the wavenumber k domain, and by the erosional decay of continental topography.

Q(k) has been modelled in the past assuming time-independent topographic loads and lithospheric rheology. New models are developed which describe the response of a thin [Maxwell] viscoelastic plate lithosphere to topography which erodes. The rate of erosion is assumed to be linearly proportional to the topography remaining at any given time. Model parameters are D, the plate's flexural rigidity; τ, its viscoelastic relaxation time constant; and σ, the erosion time constant of harmonic topography. Model predictions of time-dependent Q(k,t) and power spectra of continental topography are compared to calculations of each for several North American tectonic provinces.

The results show that a viscoelastic lithosphere with τ as small as 1-10 Ma can support the remnant topography of very old regions such as the Canadian Shield. In general, viscoelastic models provide better agreement than elastic models with the observed topography decay data. The results do not tightly constrain parameters D and τ but possible values are comparable with those based on other studies. σ appears to be wavenumber dependent, lying in the range 200-400 Ma for topographic wavelengths in the range 100-1000 km.

The observed response functions $\hat{Q}(k)$ suggest that stresses induced by erosion through time are almost completely relaxed at the present, a result which precludes pure elasticity as a viable lithosphere rheology. The effects of erosion on $\hat{Q}(k)$ can explain why previous analyses have returned values of D lower than those based on other kinds of data.

One feature of the Canadian Shield $\hat{Q}(k)$ not explicable in terms of the rheological models is its directional anisotropy. A model in which the lithosphere is loaded at its base by forces associated with small scale upper mantle convection as well as by surface topography is proposed as a possible explanation.

List of Symbols

b, B	erosion rate-topography transfer function
df	degrees of freedom
$d\hat{Q}$	standard error of an estimate $\hat{Q}$
D	flexural rigidity of a thin plate
e, E	[function] erosion
E	[constant] Young's modulus
$\dot{f}$	time-derivative of a function f
$F\{f(\vec{r})\}=F(\vec{k})$	Fourier transform of a space domain function $f(\vec{r})$
$F^{-1}\{F(\vec{k})\}=f(\vec{r})$	inverse Fourier transform of a wavenumber domain function $F(\vec{k})$
g, G	gravity
$h, H, \vec{H}$	topographic height above sea level
$\vec{i}, \vec{j}$	orthogonal unit vectors
$\vec{k}=k_{(x)}\vec{i}+k_{(y)}\vec{j}$	position vector in the wavenumber domain
$\ell, L, \bar{L}$	total height of surface topography
$L\{F(t)\}=\bar{F}(s)$	Laplace transform of a time function F(t)
$L^{-1}\{\bar{F}(s)\}=F(t)$	inverse Laplace transform of a function $\bar{F}(s)$
M	number of data in a finite digital space [or time] series
M_H	misfit of models and observed topography spectra
M_Q	misfit of models and observed isostatic response functions
n, N	geological noise in observed gravity
n_e, N_e	local noise in observed erosion rates
p, P	surface load on a thin plate

q, Q	isostatic response function
$\hat{Q}$	isostatic response function estimate
$\vec{r} = x\vec{i} + y\vec{j}$	position vector in the space domain
s	Laplace variable
S_F	power spectrum of a model function $f(\vec{r})$
$\tilde{S}_F$	raw estimated power spectrum of an observed function $f(\vec{r})$
$\hat{S}_F$	smoothed estimated power spectrum of an observed function $f(\vec{r})$
t	time
T	length of a finite digital space [or time] series
T_L	thickness of the mechanical lithosphere
$w, W, \overline{W}$	deformation of a thin plate
z	depth
Z	uplift rate-topography transfer function
$\hat{Z}$	uplift rate-topography transfer function estimate
γ^2	coherence squared spectrum
$\hat{\gamma}^2$	estimated coherence squared spectrum
Γ	gravitational constant
Δ	digitization interval of a finite digital space [or time] series
ε	erosion time constant parameter
η	Newtonian viscosity
λ	flexural parameter
ν	Poisson's ratio

ρ	density
σ	erosion time constant
τ	viscous relaxation time constant
ψ	flexural response function
ω	erosion time constant parameter

Acknowledgements

Chris Beaumont provided overall supervision and his willingness when asked to find time for me in his very busy schedule is gratefully acknowledged. Much of my financial support derived from research grants to Dr. Beaumont from the Earth Physics Branch, Department of Energy, Mines, and Resources, Ottawa.

Other persons with whom I had interesting and profitable conversations about my research and/or who critically read all or parts of various versions of the manuscript include: Drs. Charlotte Keen, Bedford Institute of Oceanography, and Peter Reynolds, who between them constituted the remainder of my supervisory committee; Bob Courtney and Garry Quinlan, student colleagues in the Oceanography Department; Dr. Marcia McNutt, United States Geological Survey; Drs. Alan Goodacre and Jack Sweeney, Earth Physics Branch; Ross Boutilier and Dr. John Peters, Oceanography Department; Dr. John Cordes, Physics Department; and Dr. Marcos Zentilli of the Geology Department.

Finally, I wish to acknowledge the thoroughly enjoyable and fulfilling experience I've had as a graduate student in the Geology Department at Dalhousie University and as a resident of Halifax and Nova Scotia.

Nothing is more important for teaching us to understand the concepts we have than constructing fictitious ones [Ludwig Wittgenstein 1948].

Chapter 1. Introduction

1.1 Lithosphere and Isostasy

The Earth's mechanical behaviour in response to small stresses at high strain rates is revealed by its seismic wave response. The strength of the Earth's crust and mantle in such a mode, that is, its ability to sustain short period shearing stresses, appears to be very great. On the other hand, the ability of the Earth to resist permanent deformation by shear stresses applied over much longer lengths of time is certainly much less. Similarly, the mechanics of the deformation induced by such stresses will likely be much different. The strain rates of interest in this thesis pertain to processes which occur over millions of years; such processes are sometimes referred to, in the temporal sense, as "geological" processes. For example, the strain rates representative of detectable geological phenomena such as lithosphere accretion at mid-oceanic ridges and consumption at trenches are characteristic of lengths of time in the range 1-1000 Ma.

Historically, studies of the "geological" state of stress and mechanical behaviour of the Earth have been based on the existence of gravity anomalies [e.g. Jeffreys 1976]. Gravity anomalies are indicators of lateral mass heterogeneities, and therefore non-hydrostatic stresses, in the Earth's interior. Long wavelength gravity anomalies may be related to geodynamic processes such as thermal convection in the mantle [e.g. McKenzie 1967], itself perhaps the mechanism of lithosphere plate movements [e.g. Davies and Runcorn, eds. 1980] and the ultimate source of the tectonic forces responsible for mountain-building. In turn, the crustal topography and internal density anomalies formed during mountain-building episodes are responsible for much of the higher frequency gravitational variation observed across continental regions. Having been established by tectonic forces, such gravity anomalies, and their implicit crustal mass heterogeneities, apparently persist in geologically very old regions such as the Precambrian Canadian Shield. This observation has sometimes been used to argue that the outermost portion of the Earth must possess a finite strength, at least within such a time frame, only above which can deviatoric stresses induce mechanical failure. This apparently rigid part of the Earth, consisting of the crust and perhaps some of the upper mantle, is conformable with the plate tectonic concept of a rigid lithosphere, with its continental loads, passively drifting across the Earth's surface above an effectively inviscid, convecting mantle. Such a mechanically-defined lithosphere may be different, particularly in terms of its apparent thickness, than "lithospheres" modelled on the basis of seismological or thermal observations.

The existence of the lithosphere's surface topography probably represents the Earth's greatest departure from a state of hydrostatic equilibrium. The way in which the attendant non-hydrostatic stresses are redistributed beneath the topography leads to the concept of isostasy. It is the mechanism by which excess topographic masses at the surface of the Earth are compensated by mass deficiencies within the Earth such that all stresses are presumed to be hydrostatic below some constant depth of compensation. Thus, the concept of isostasy has been traditionally kept separate from considerations of mantle convection and the possibly resulting dynamic uplift of surface topography. Rather, isostasy has been concerned with loads on the surface of the lithosphere acting downwards.

Topographic loading of a mechanically rigid lithosphere induces flexural deformation because of the lithosphere's ability to sustain horizontal shear stresses. The compensating mass is therefore distributed below and around the site of the excess surface topography resulting in a condition known as regional isostatic compensation. The theoretical foundation of the regional isostatic model was established by Vening Meinesz in 1931.

In contrast with regional isostasy are the classical models of local isostatic compensation of Pratt [1855] and Airy [1855]. They are referred to as local models because in both cases the mass deficiency which effects the isostatic compensation of the surface topography lies immediately below the topography itself. Each model is conceived in terms of vertical crustal columns of equal mass lying above the compensation depth. In order to achieve isostatic compensation in such a scheme, Pratt considered that the densities of adjacent columns varied while Airy maintained a single column density but allowed the depth of the base of each to change according to the height of the topography above. Such models do not require the specification of a deformational process, whether brittle or ductile in character, by which the isostatic compensation is achieved. They therefore do not lead to inferences about the mechanics of the Earth. The Pratt model, for example, requires that a change in the topographic height, perhaps due to erosion, is compensated by a density change occurring uniformly throughout a vertical column. The mechanism by which this would occur is problematic. Alternatively, the Airy model would require vertical movements of entire columns in response to small changes in topography thereby implying the inability of the lithosphere to sustain shear stresses of any magnitude. Thus, Airy isostasy can be considered to be a special case of the regional model in which the lithosphere has no flexural strength.

1.2 Isostatic Response Functions

In the absence of dynamic forces the Earth's topography generally approaches a state of isostatic equilibrium [Heiskanen and Vening Meinesz 1958]. Dorman and Lewis [1970] showed that the extrinsic character of the isostatic response could be determined directly from observational data rather than by making a priori assumptions about particular isostatic models such as those of Pratt and Airy. Dorman and Lewis assumed that the Earth is linear in its response to topographic loading and that the gravity observed at some field point could therefore be represented as a two-dimensional convolution of the surrounding topography with some unknown function which they referred to as the isostatic response function; the isostatic response function is here designated as $q(\vec{r})$ where $\vec{r}=x\vec{i}+y\vec{j}$ and $\vec{i}$ and $\vec{j}$ are unit orthogonal vectors. Thus,

$$g(\vec{r}_o) = \int_s\int q(\vec{r}_o-\vec{r})\ h(\vec{r})\ dxdy + n(\vec{r}_o) \quad , \qquad (1\text{-}1)$$

where s represents a two-dimensional surface, g and h represent gravity and topography respectively, and n, denoting "noise", refers to that portion of the gravity anomaly not caused by the isostatic compensation of h. Dorman and Lewis assumed that the noise component, due primarily to tectonically-emplaced crustal density heterogeneities, would be small compared to the isostatic component and, in particular, that it would not be correlated with the topography. Neidell [1963] had also considered the Earth's isostatic response as a convolution of topography and gravity. He had attempted to empirically determine spatial domain coefficients of the convolution filter but was hampered by lack of data and computational difficulties. Dorman and Lewis [1970], on the other hand, considered the frequency or wavenumber domain equivalent of Equation (1-1), found by taking its two-dimensional Fourier transform. Fourier transforming a spatial function $f(\vec{r})$ allows it to be represented in terms of its spectral components and is defined as

$$\mathcal{F}\{f(\vec{r})\} = F(\vec{k}) = \int_{-\infty}^{\infty}\int f(\vec{r})\ \exp[-2\pi i\vec{k}\cdot\vec{r}]\ dxdy \qquad (1\text{-}2i)$$

where $\cdot$ represents the scalar product and $\vec{k}=k_{(x)}\vec{i}+k_{(y)}\vec{j}$ is the wavenumber; the inverse Fourier transform is defined as

$$\mathcal{F}^{-1}\{F(\vec{k})\} = f(\vec{r}) = \int_{-\infty}^{\infty}\int F(\vec{k})\ \exp[2\pi i\vec{k}\cdot\vec{r}]\ dk_{(x)}dk_{(y)} \qquad (1\text{-}2ii).$$

Note that the wavelength of a periodic function of wavenumber $|\vec{k}|$ is defined here as $|\vec{k}|^{-1}$.

The transform of Equation (1-1) can be found using (1-2i) and taking into account the convolution theorem of Fourier transforms which states that a convolution in one domain transforms into a multiplication in the other. Equation (1-1) transformed is therefore

$$G(\vec{k}) = Q(\vec{k})\, H(\vec{k}) + N(\vec{k})$$

or

$$Q(\vec{k}) = \frac{G(\vec{k}) - N(\vec{k})}{H(\vec{k})} \tag{1-3}$$

In this form, the transform of the isostatic response function, $Q(\vec{k})$, represents the transfer function of a linear filter, consisting of a lithosphere of unspecified mechanical properties, subject to an input function $H(\vec{k})$ and having output $G(\vec{k})$. The term "isostatic response function" is now commonly reserved to apply only to $Q(\vec{k})$ rather than to its space-domain transform counterpart, $q(\vec{r})$, as it was originally introduced by Dorman and Lewis [1970].

Dorman and Lewis were interested in inverting observed response functions in order to reveal changes in the density structure of the crust related to topographic uplift. They did so [Lewis and Dorman 1970, Dorman and Lewis 1972], using United States gravity and topography data, in terms of a generalized local compensation model. Later, their data were reconsidered in terms of a regional isostatic compensation model by Banks et al. [1977] who developed a method of geophysical inversion based on linear programming techniques. Similar techniques and models were used by Banks and Swain [1978], McNutt and Parker [1978], Stephenson [1978], and McNutt [1980] to respectively interpret isostatic response functions from East Africa, Australia, the Canadian Shield, and the Phanerozoic orogens of the United States. The basic techniques originally developed by Dorman and Lewis have also been extensively applied to data from oceanic regions of various ages and tectonic character [McKenzie and Bowin 1976, Watts 1978, Cochran 1979, Detrick and Watts 1979, McNutt 1979, Sandwell and Poehls 1980, Louden 1981, Louden and Forsyth in press, Sinha et al. in press].

1.3 Aims and Outline

The fundamental questions to be addressed in the present study pertain to the rheology, in the geological time frame, of the mechanical lithosphere. There are four general classes of rheological models in terms of which the lithosphere can be considered. They are as follows.

(1) The lithosphere is elastic and will indefinitely sustain shearing stresses with no apparent time-dependent effects.

(2) The lithosphere is characterized by an elastic-plastic rheology. This type of rheoid possesses a finite yield strength which may be depth-dependent. The upper part of the lithosphere likely deforms cataclastically when the yield strength is surpassed whereas

the lower part likely deforms ductilely. The demarcation between the two failure regimes would be related to confining or lithostatic pressure [Turcotte et al. 1978, Beaumont 1979]. The purely elastic model (1) can be considered to be a special case of the elastic-plastic class of models which has a yield strength which is never exceeded during the geological processes under consideration.

(3) The mechanical lithosphere is characterized by linear viscoelastic [Maxwell] rheology. A Maxwell body deforms in response to an instantaneous stress change such that there is immediate elastic strain followed by viscous flow at a constant rate. There is no yield strength below which the viscous relaxation fails to occur. In this respect, the viscoelastic class of models is fundamentally different from the elastic-plastic class. The elastic model (1) can be considered to be one case of the viscoelastic class of models in which the time constant characterizing the viscous relaxation is too great to allow significant relaxation to take place within the upper bound of the geological time frame [~1000 Ma].

(4) The lithosphere is a non-linear rheoid which has depth [pressure] and temperature dependent properties.

The true intrinsic rheological structure of the mechanical lithosphere almost certainly falls into class (4) at least with respect to pressure and temperature dependence. Nevertheless, geophysical applications of models in classes (1), (2), and (3) have been numerous and successful [cf. Forsyth 1979] whereas those in class (4) are analytically difficult to apply. There is, however, no general agreement on which of the three former, more analytically tractable types of rheologies best represents the large scale deformational behaviour of the mechanical lithosphere.

The problem of the rheology of the lithosphere is addressed in this thesis by considering variations in the topography and gravity of continental geological provinces having vastly different tectonic ages. Consequently, the role of erosion of topography and its isostatic effects are of fundamental importance. Explicit analytical modelling is carried out in terms of the third, or viscoelastic, class of rheological models of which the purely elastic class is a subset. Particular emphasis is placed on whether or not the results support or refute the presence of viscous relaxation of elastic stresses and by implication the existence of a finite yield strength in the lithosphere during geologically observable lengths of time. One limitation of the present approach, in which continental isostatic evolution is considered, is that the results may apply only to the continental portion of the Earth's lithosphere. The presence of a sialic crust as a component of continental lithosphere indicates that it may be to some degree rheologically different than its oceanic counterpart.

The observational basis of the work is the transfer function technique developed by Dorman and Lewis [1970]. The isostatic response functions of six tectonically distinct regions of North America have been computed using the methodology presented in Chapter 2. These new data are interpreted and discussed first [Chapter 3] in terms of the commonly employed elastic isostatic response model developed by Banks et al. [1977]. A consequence of the elastic model is that the flexural stresses induced by a persistent topographic load can be sustained by the lithosphere throughout geological lengths of time. Erosion does not affect such a model because elastic strain is instantaneously recovered as the load is removed. Thus, the isostatic compensation existing at any given moment pertains only to the topography which is present at that moment.

The isostatic response function characteristic of a visco-elastic lithosphere, however, will vary depending on the age of the topographic load and will be strongly affected by the form of the erosion of the topography. In order to facilitate the development of models which can predict the isostatic effects of erosion, some quantitative model of large scale continental erosion is necessarily adopted. A mathematically suitable erosion model is postulated in Chapter 4 and is discussed in terms of the recent topographic evolution of South Island, New Zealand, a continental region undergoing rapid tectonic uplift and massive erosion.

In Chapter 5 general models of the deformational and isostatic response of a viscoelastic lithosphere loaded by eroding topography are presented. The models can be used not only to calculate the time dependent isostatic response function of the viscoelastic lithosphere but also the form of the decay of continental topography through geological time spans. The results are compared to the observed spectral topography of the sampled geological provinces and are discussed in the light of the predicted and observed isostatic response functions.

Chapter 6 is concerned with those parts of the gravity and topography measured at the Earth's surface which may be related to upward flexure of the lithosphere by forces derived from upper mantle convection. These effects are strictly speaking not isostatic in origin but information about them may reside in observed isostatic response functions. A method by which such information may be detected in response functions observed in regions of low topographic relief is outlined and is applied to the Canadian Shield.

The results of the preceding chapters and their geophysical implications are compiled and summarized in Chapter 7. The thesis is concluded with an examination of the most prominent individual gravity anomalies found in North America. A preliminary geodynamic model which may explain them is proposed and is briefly discussed in terms of a potential application of some of the techniques developed earlier.

Chapter 2. Data Sources and Reduction

2.1 Selection of Data

2.1.1 Introduction. The information which is sought in the present study pertains to isostatic processes and the rheology of continental lithosphere and is assumed to reside in observable geophysical and physical properties of continents, specifically gravity anomalies and topography. Because of the complex history of continental crust, both in terms of its origin and its post-tectonic modification, however, other irrelevant or intractable information, deemed to be "noise", is also present in these observations. The level of the noise, especially in the gravity observations, is enhanced by measurement error. Consequently, the analysis of the observations is a statistical exercise and, for meaningful results using noisy data, large data sets are required. In the present case, the two-dimensional spectral relationship of continental gravity and topography is analyzed. The wavelengths of interest are in the range 100-1000 km. Therefore, data sets need to be derived from continental regions of at least these dimensions. Study areas of suitable size must also have extensive gravity measurement coverage. Another constraint is imposed by the desire to confine data sets to tectonically homogeneous geological provinces so that the topography and isostatic response functions of continental lithosphere of different ages can be compared.

2.1.2 Study areas. Five large geographic regions of North America were selected for study [cf. Figure 2-1]: Cordilleran and Appalachian regions, and three structurally distinct provinces of the Precambrian Canadian Shield, the Grenville, Churchill, and Superior provinces. Each region is roughly uniform in terms of its geological make-up. A sixth study area covers much of the Canadian Shield, overlapping the three smaller Grenville, Churchill, and Superior regions [Figure 2-1]. Attributes of the six data sets deriving from these regions are listed in Table 2-1.

Gravity data, corrected for terrain effects where appropriate, for Canadian continental and adjacent marine areas were provided by the Gravity Data Centre, Earth Physics Branch, Ottawa [updated to September 1979] and for the conterminous United States by the National Geophysical and Solar-Terrestrial Data Center [NGSDC], National Oceanic and Atmospheric Administration, Boulder, Colorado [as of Autumn 1978]. Associated station elevations are provided for all individual Bouguer gravity data but, as a measure of regional topography, may be biased by preferential selection of gravity observation locations [i.e., hilltops for airborne surveys, roadways in valleys for landbased surveys]. The raw topographic data used in the spectral analysis, except for some marine areas where they are not available, therefore have been derived from a file of 5 minute by 5 minute average elevations for North America provided by NGSDC [1980]. Where these data are not available the elevations associated with the gravity observations have been used. In limited areas where no data were available linear interpolation or extrapolation of adjacent data has been performed to provide continuity.

Figure 2-1. Generalized tectonic map of North America [after King and Edmonston 1972] showing the main geological provinces and chosen study areas. The corner letters refer to the study areas as follows: [W] Cordilleran, [A] Appalachian, [T] Canadian Shield, [G] Grenville, [C] Churchill, and [S] Superior. Legend: (1) Phanerozoic orogens: Ap - Appalachian, Cd - Cordilleran; (2) Canadian Shield structural provinces: Ch - Churchill, Gr - Grenville, Nn - Nain, Sp - Superior, Sv - Slave; (3) cv - regions of Phanerozoic and Proterozoic sedimentary cover.

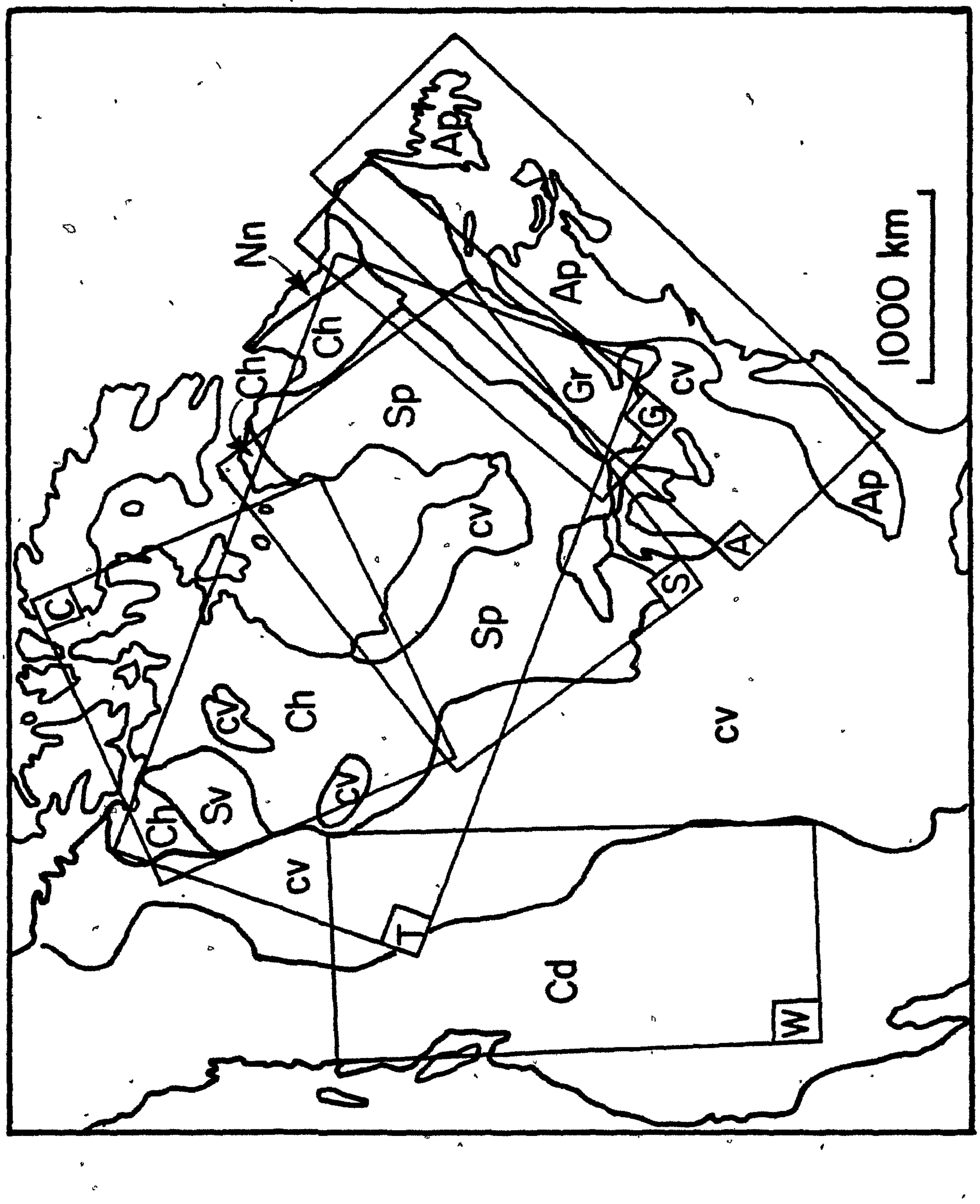
Ap
Ap
Nn
Ch
Ch
Sp
Ap
Gr
cv
G
cv
C
Ch
cv
Sp
A
Ap
S
cv
Ch
cv
Sv
Ch
cv
T
Cd
W
1000 km

Table 2-1. Attributes of the chosen study areas. The bracketed letters refer to their location as shown in Figure 2-1.

Geological province	Dimensions [km]	Area [$10^6 km^2$]	Number of gravity data	Mean elevation [m]	Mean GEM8 geoid [mGal]	Mean free-air anomaly [mGal]	Mean Bouguer anomaly [mGal]
[W]Cordilleran	1200 x 2400	2.88	108397	1350	5	-10	-152
[A]Appalachian	3000 x 1000	3	118000	175	-11	6	- 10
[T]Canadian Shield	3200 x 1600	5.12	91513	261	-24	0	- 28
[G]Grenville	2000 x 600	1.2	23294	355	-15	- 4	- 39
[C]Churchill	1600 x 1600	2.56	47495	167	-28	0	- 18
[S]Superior	2000 x 1500	3	84125	199	-24	1	- 21

2.2 Spectral Analysis

2.2.1 Mapping and digitization. Dorman and Lewis [1970] originally formulated isostatic response functions in terms of both spherical and planar coordinates. However, the depth of the isostatic compensation of topograhy is expected to be very small relative to the Earth's radius. Dorman and Lewis estimated that as a result the spherical harmonic expansion of gravity and topography up to degree and order 500 would be necessary to adequately resolve any spherically determined response function. Since it is unlikely that this could be done accurately, isostatic response functions have generally been formulated in terms of planar coordinates. Banks et al. [1977] point out that it is probable that the effect of the planar approximation for continent-sized regions is much less than the other errors already present in the data.

The gravity and topography data considered here, from the areas of North America shown in Figure 2-1, were mapped onto a plane using a Lambert conformal conic projection with standard parallels chosen appropriate to each study area. The distance distortion introduced by the transformation is very small, not greater than 1% for the largest of the study areas [cf. Richardus and Adler 1972, p. 95] and less for the others. It should also be noted, however, that directional relationships are not correctly represented by the Lambert conformal projection; parallel lines, for example, do not map spherical great circles.

The mapped data were averaged within equidimensional cells to produce a grid of discrete function values suitable for two-dimensional

Fourier transformation. Cell averages of the Goddard Earth Model 8 [Wagner et al. 1977] spherical harmonic representation of the Earth's gravity field to degree and order 16 were subtracted from the gridded data in order to detrend it of gravity anomalies having wavelengths of the order of the grid dimensions. The mean value of the GEM8 gravity field for each of the study areas are listed in Table 2-1. It can be assumed that such long wavelength gravity anomalies are derived from sources beneath the lithosphere and are not related to the compensation of surface topography.

Bouguer anomalies are used in the computation of the isostatic response functions because they have been corrected for terrain effects and because their usage is consistent with previous studies. Contour maps of the detrended Bouguer gravity field and the topography based on the digitized data of each of the six study areas are presented in Figures 2-2 through 2-7. It can be seen in these figures that there is in general a relationship between positive topographic relief and negative Bouguer anomalies, a result of the isostatic compensation of the topography.

2.2.2 Computation of raw spectral data. (i) Fourier transform. The discretized gravity and topography arrays [subsection 2.2.1] were transformed to the wavenumber domain using a Fast Fourier Transform [FFT] algorithm [Brenner 1968]. The FFT is used to efficiently compute the Fourier transform $F(\vec{k})$ [Equation (1-2i)] of a finite digital series assumed to be infinitely repeating itself. By Fourier's Integral Theorem [e.g. Rayner 1971] a repeating series can be exactly represented by a sum of cosine and sine waves, the amplitudes of which are the

Figure 2-2. (a) Topography and (b) Bouguer gravity field of the Cordilleran study area [W] based on digitized data [cf. subsection 2.2.1]. Gravity has been detrended of the GEM8 [16 x 16] field; regions of positive Bouguer anomalies are stippled. Contour intervals are (a) 400 m and (b) 50 mGal. Tectonic legend is the same as Figure 2-1; dimensions of the study area are 1200 km by 2400 km.

(a)

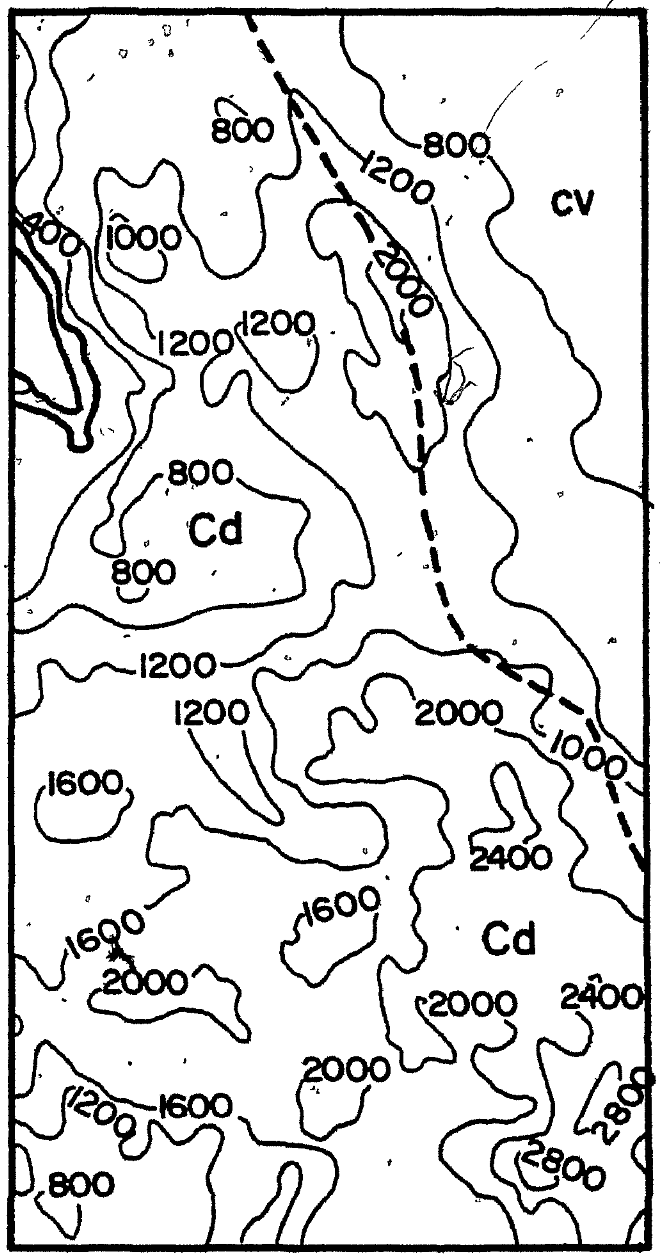
800
800
1200
CV
400
1000
2000
1200
1200
800
Cd
800
1200
1200
2000
1000
1600
2400
1600
1600
Cd
2000
2000
2400
2000
1200
1600
2800
800
2800

(b)

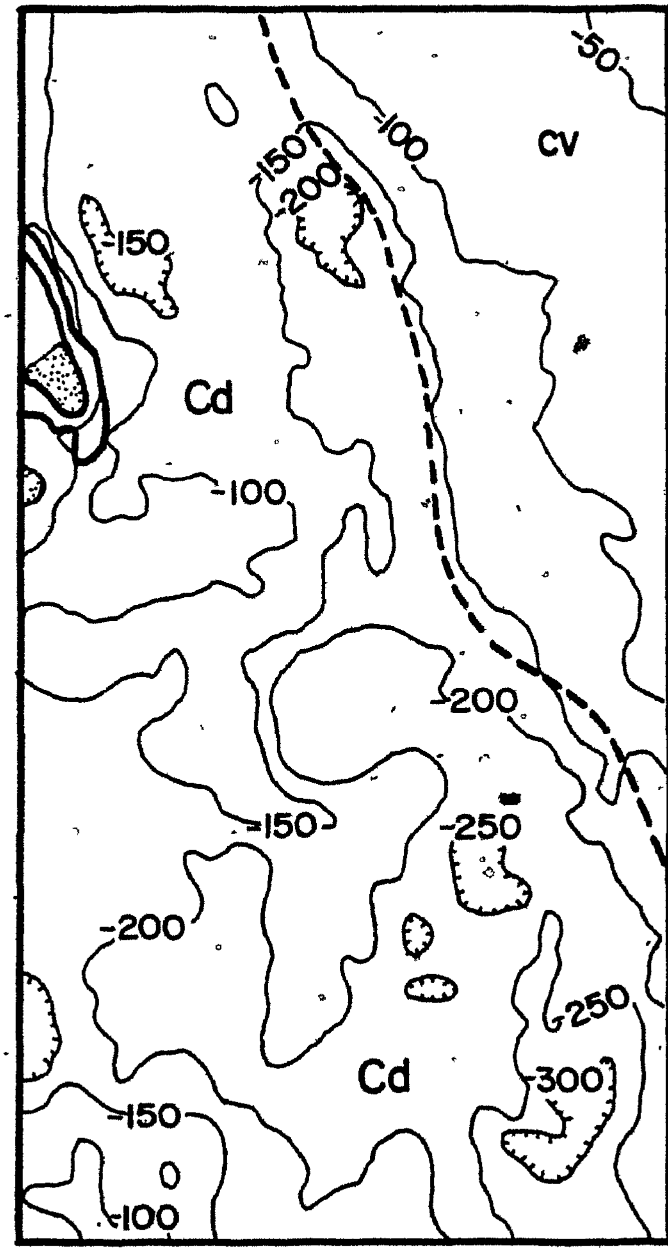

Figure 2-3. (a) Topography and (b) Bouguer gravity field of the Appalachian study area [A] based on digitized data [cf. subsection 2.2.1]. Gravity has been detrended of the GEM8 [16 x 16] field; regions of positive Bouguer anomalies are stippled. Contour intervals are (a) 200 m and (b) 20 mGal. Tectonic legend is the same as Figure 2-1; dimensions of the study area are 3000 km by 1000 km.

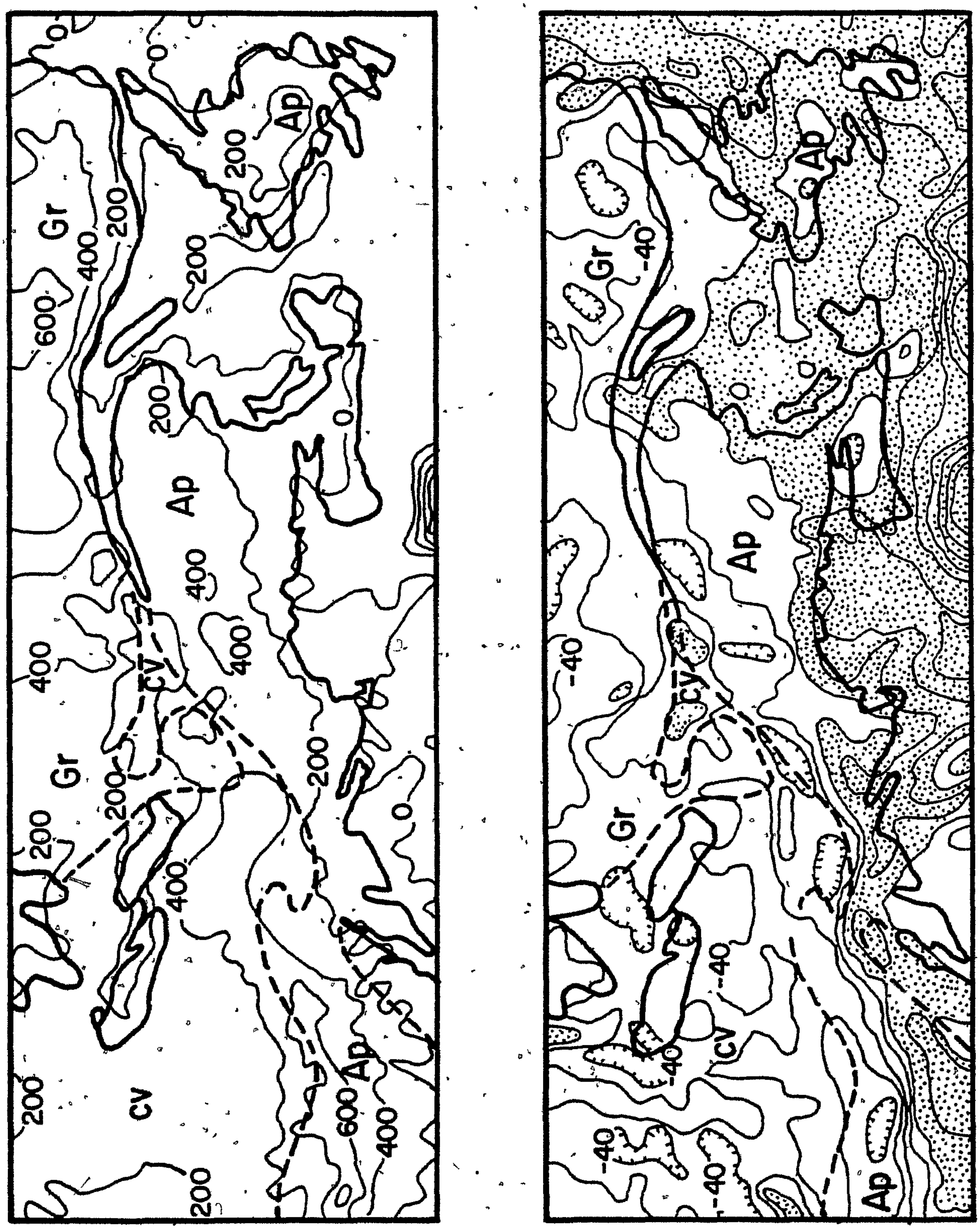

(a)

(b)

Figure 2-4. (a) Topography and (b) Bouguer gravity field of the Canadian Shield study area [T] based on digitized data [cf. subsection 2.2.1]. Gravity has been detrended of the GEM8 [16 x 16] field; regions of positive Bouguer anomalies are stippled. Contour intervals are (a) 200 m and (b) 20 mGal. Tectonic legend is the same as Figure 2-1; dimensions of the study area are 3200 km by 1600 km.

(a)

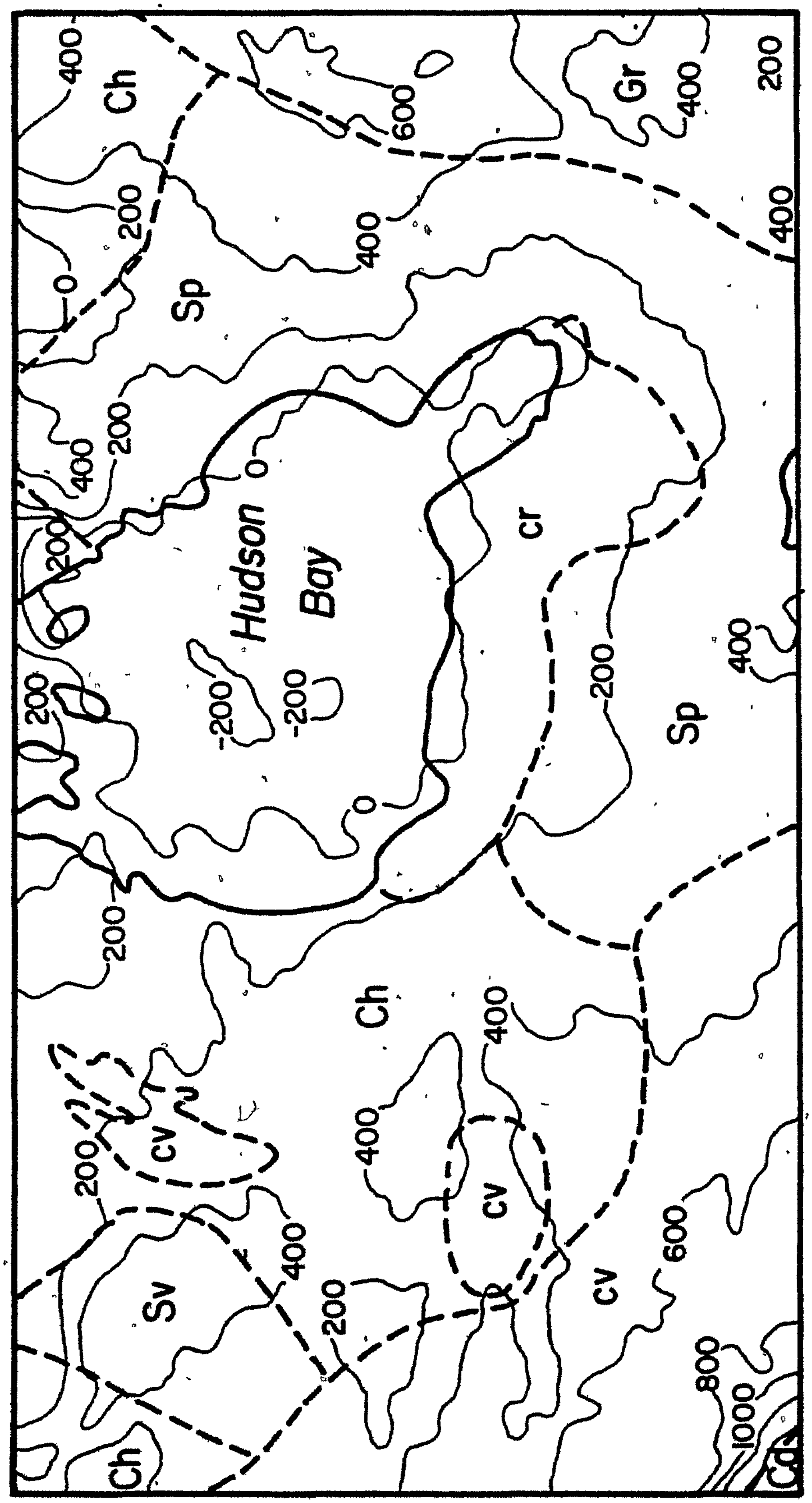

(b)

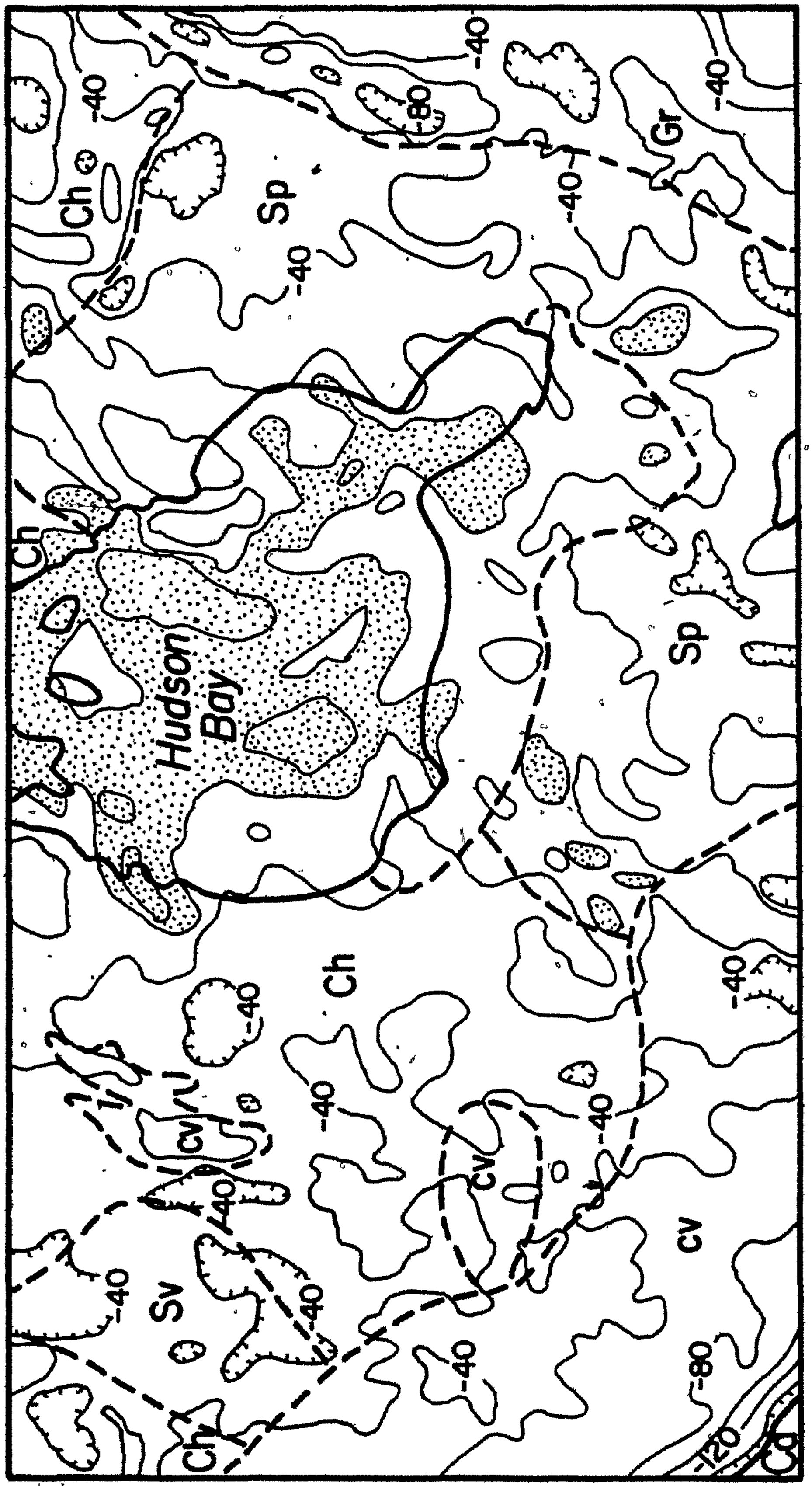

Figure 2-5. (a) Topography and (b) Bouguer gravity field of the Grenville province study area [G] based on digitized data [cf. subsection 2.2.1]. Gravity has been detrended of the GEM8 [16 x 16] field; regions of positive Bouguer anomalies are stippled. Contour intervals are (a) 200 m and 20 mGal. Tectonic legend is the same as Figure 2-1; dimensions of the study area are 2000 km by 600 km.

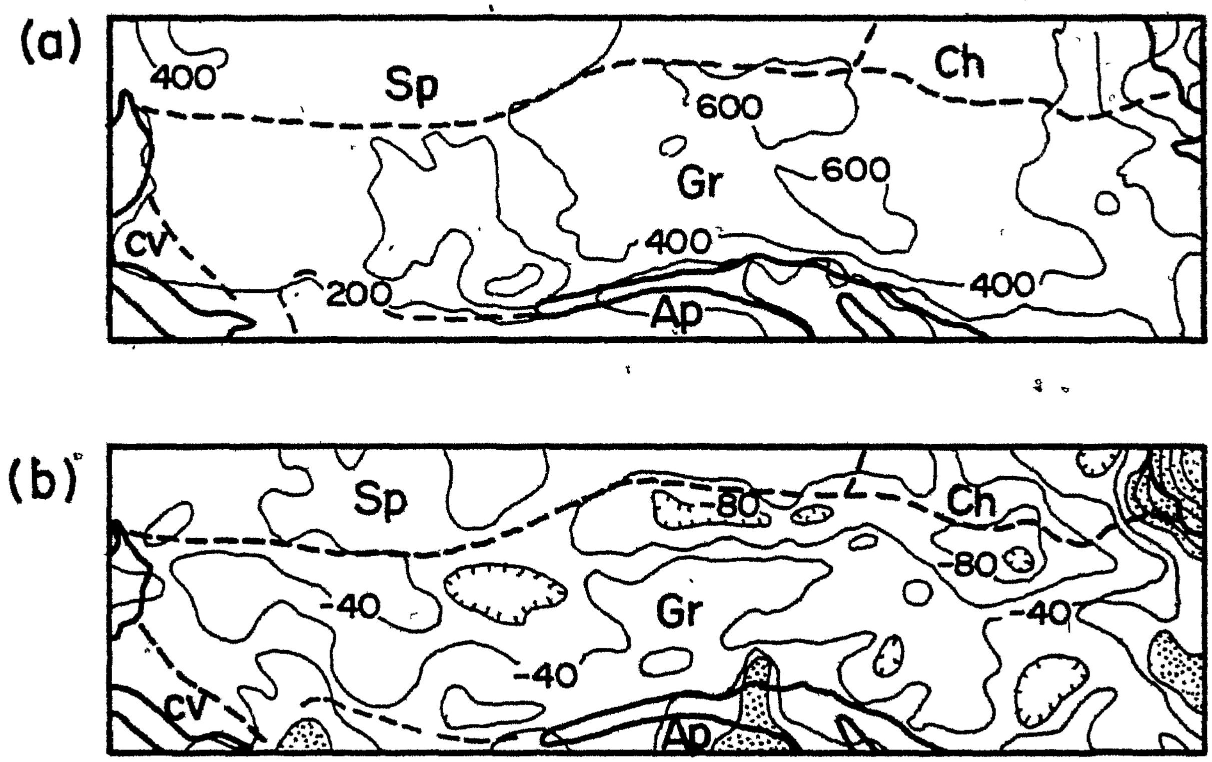
(a)
400
Sp
Ch
600
Gr
600
cv
400
200
400
Ap
(b)
Sp
-80
Ch
-80
-40
Gr
-40
-40
cv
Ap

Figure 2-6. (a) Topography and (b) Bouguer gravity field of the Churchill province study area [C] based on digitized data [cf. subsection 2.2.1]. Gravity has been detrended of the GEM8 [16 x 16] field; regions of positive Bouguer anomalies are stippled. Contour intervals are (a) 200 m and (b) 20 mGal. Tectonic legend is the same as Figure 2-1; dimensions of the study area are 1600 km by 1600 km.

(a)

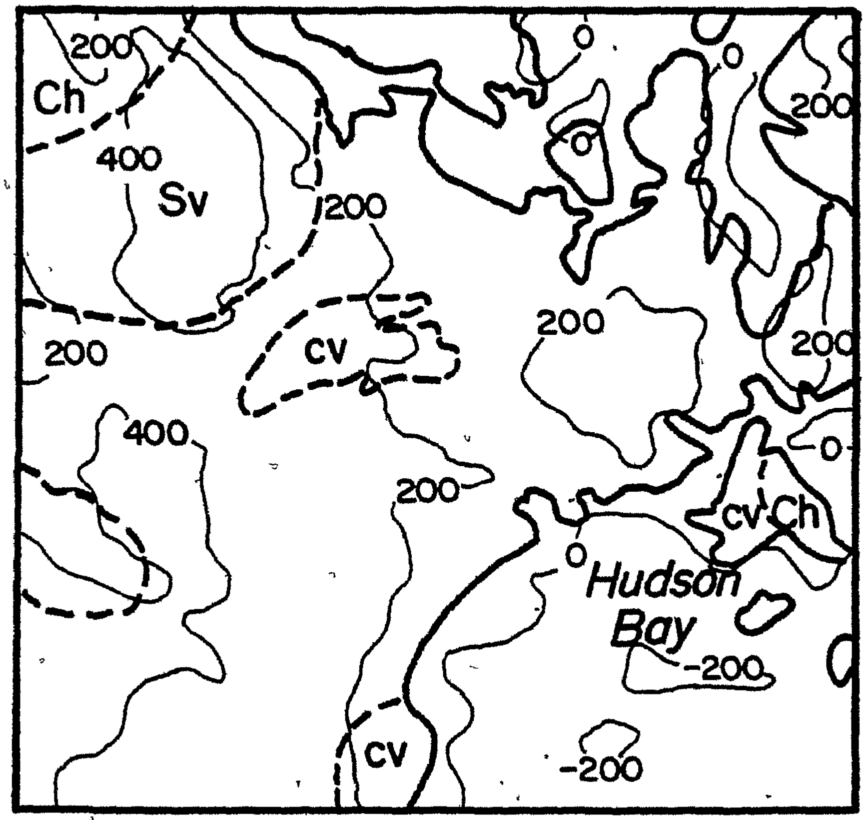
Ch
Sv
cv
cv
cv
Ch
Hudson
Bay
200
400
-200

(b)

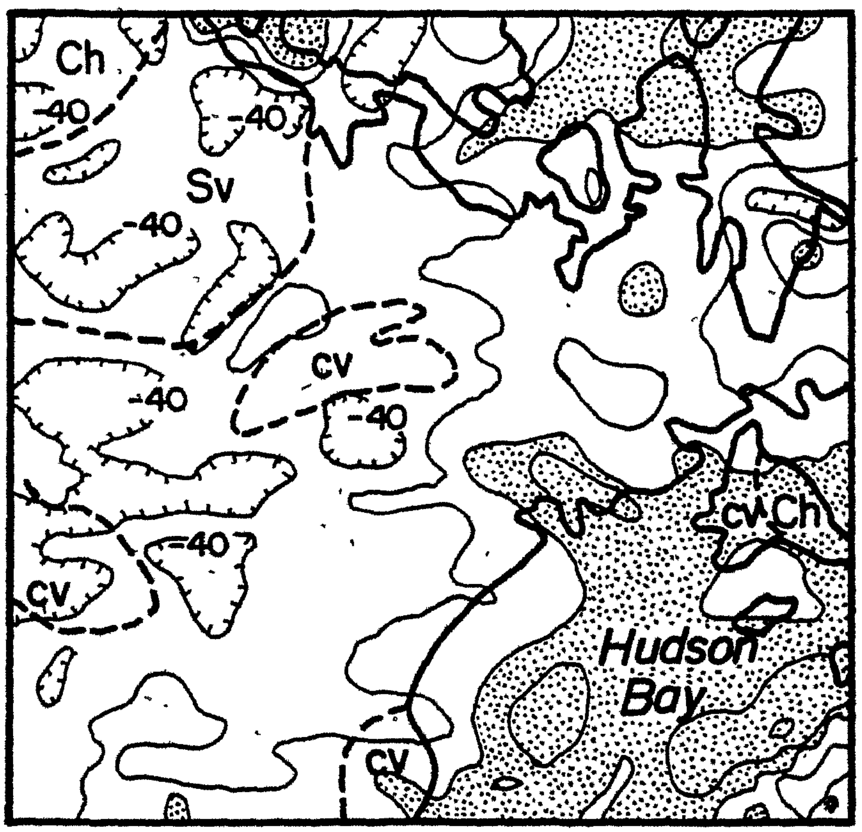
Ch
Sv
cv
cv
cv
Ch
Hudson
Bay
-40

Figure 2-7. (a) Topography and (b) Bouguer gravity field of the Superior province study area [S] based on digitized data [cf. subsection 2.2.1]. Gravity has been detrended of the GEM8 [16 x 16] field; regions of positive Bouguer anomalies are stippled. Contour intervals are (a) 200 m and (b) 20 mGal. Tectonic legend is the same as Figure 2-1; dimensions of the study area are 2000 km by 1500 km.

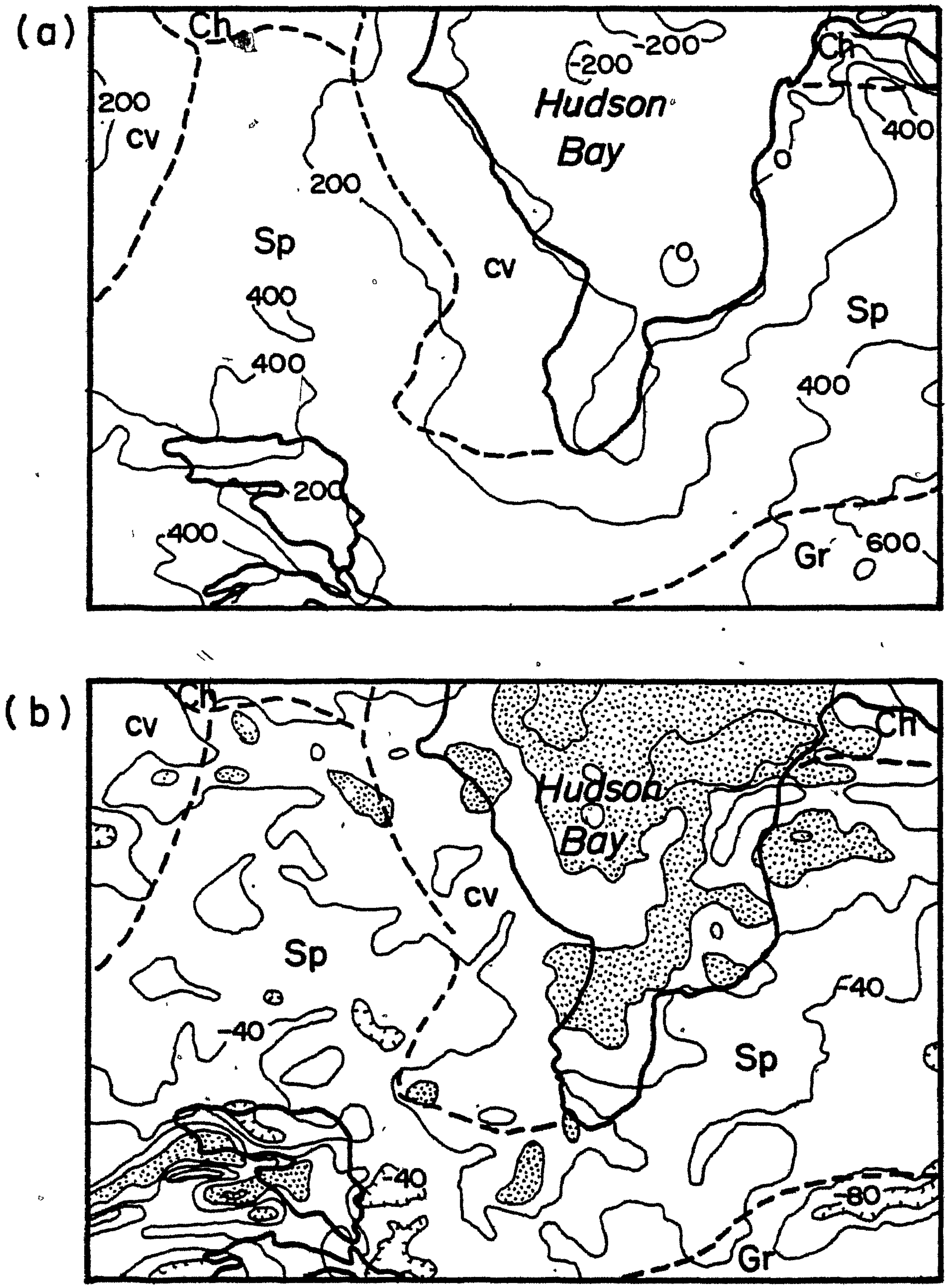
(a)
Ch
-200
-200
200
Hudson
Bay
Ch
cv
400
0
200
Sp
0
cv
400
Sp
400
400
200
400
600
Gr
0
(b)
Ch
cv
0
Hudson
Bay
Ch
cv
0
Sp
-40
-40
Sp
-40
-80
Gr

direct output of the FFT. To completely describe the spectral configuration of a repeating, discrete data series requires a finite number of pairs of cosine and sine terms in each dimension with frequencies [or wavenumbers]

$$k_n = \frac{n}{T}\,; \quad n = 0, \pm 1, \pm 2, \ldots . \pm M/2 \tag{2-1}$$

where T is the length of the series and M is the number of data [the digitization interval is therefore $T/M=\Delta$] in that dimension. The k_n are known as the harmonic frequencies. The discrete Fourier transform is found by normalizing the cosine and sine coefficient pairs by the calculated frequency bandwidth which is constant and is, from (2-1), equal to T^{-1}. The normalized coefficients respectively represent the real and imaginary parts of the complex Fourier transform, the moduli of which comprise the raw estimates of the amplitude spectrum $|F(\vec{k})|$ for finite discrete $k=k_n$ in each dimension. In turn, the raw phase spectrum is determined by the complex angles indicated by the relative magnitudes of the real and imaginary coefficients. Raw power and cross spectral estimates are given by [e.g. Rayner 1971]

$$\tilde{S}_F(\vec{k}) = \frac{1}{T} F(\vec{k}) F^*(\vec{k}) \tag{2-2}$$

and

$$\tilde{S}_{FF_o}(\vec{k}) = \frac{1}{T} F(\vec{k}) F_o^*(\vec{k}) \tag{2-3}$$

for finite discrete $k=k_n$ in each dimension, where $F(\vec{k})$ and $F_o(\vec{k})$ are the discrete Fourier transforms, as described above, for digital spatial data series $f(\vec{r})$ and $f_o(\vec{r})$, and * indicates complex conjugate. For two-dimensional $f(\vec{r})$ where $\vec{r}=x\vec{i}+y\vec{j}$, and $\vec{i}$ and $\vec{j}$ are orthogonal unit vectors, having Fourier transform $F(\vec{k})$ where $k=k_{(x)}\vec{i}+k_{(y)}\vec{j}$, the constituent harmonic sinusoids and therefore raw spectral estimates have wavenumbers of moduli $[k^2_{(x)n}+k^2_{(y)n}]^{1/2}$ directed at angles $\tan^{-1}[k_{(y)n}/k_{(x)n}]$ from the x coordinate axis. Harmonic wavenumbers in two dimensions with these attributes are referred to as $\vec{k}_n$.

(ii) Aliasing. The highest frequency or wavenumber for which an estimate of the discrete Fourier transform, and therefore an estimate of the power or cross spectrum, is available is known as the Nyquist frequency k_M and is, from Equation (2-1),

$$k_M = \frac{\pm 1}{2\Delta} \tag{2-4}$$

noting that $T=M\Delta$. If there exists in the signal appreciable variance of wavelength less than 2Δ it will not be adequately sampled and, as a result, any calculated spectrum will be contaminated by what is known as aliasing error [cf. Jenkins and Watts 1968]. In the present analysis of two-dimensional gravity and topography data, aliasing is not considered to be a significant problem. The cell averaging procedure by which the array values were found is effectively a smoothing operation which, given a random sampling of observations within each cell, filters the overall field of signals with frequency greater than k_M.

(iii) Finiteness of data. The Fourier transform calculated by the FFT refers to a data series consisting of a finite sequence of observations assumed to be infinitely repeated. A potential consequence of this artifact are discontinuities at the edges of the data. As a result, the calculated power and cross spectra may be contaminated by high frequency elements required to reproduce the discontinuities. A common way to deal with this phenomenon [e.g. Rayner 1971, Tukey 1967] is to taper the edges of the observed series in order to smooth the interpolation between opposite edges.

Lewis and Dorman [1970], in their spectral analysis of United States topography and gravity, tapered data in the north-south direction and reflected them about the western edge. The Fourier transform of a function which is real and symmetric about its origin is also real and symmetric. Thus, reflection of a data set prior to transformation has the effect of reducing the inherent phase and directional information. McNutt [1978], analyzing Australian data, added border ramps to the topography array, predicted using Lewis and Dorman's calculated isostatic response function the wavenumber domain gravity associated with the modified topography data, transformed back to the space domain, and used the predictions to border the original gravity array. This method does not necessarily remove edge discontinuities in the gravity data although tests on artificial data seem to indicate that it is reliable [McNutt 1980, pers. comm.]. However, the statistical properties of spectra produced in this fashion are not well known. In the present case, therefore, edge discontinuities simply have been smoothed using a Gaussian shaped taper function applied to 20-30% of the observations following Tukey [1967]. Prior to smoothing the averages of the data sets were removed in order to reduce as much as possible the amplitude of the taper function.

2.2.3 Spectral characteristics. The fundamental assumptions which govern spectral analysis are that the time series, or in the present case space series, under consideration is the result of a stationary, stochastic process such that the observed series is one normally distributed, randomly chosen realization of all possible sets of observations, and that the resulting calculated pairs of Fourier series coefficients are independent of one another. In such circumstances, it is a well known result [e.g. Jenkins and Watts 1968, Rayner 1971] that a calculated raw power spectral estimate $\tilde{S}_F(\vec{k}_n)$ has a probability distribution, with respect to its true value $\tilde{S}^T_F(\vec{k}_n)$, proportional to a χ^2 probability distribution function with degrees of freedom df_n:

$$\frac{df_n\ \tilde{S}_F(\vec{k}_n)}{\tilde{S}^T_F(\vec{k}_n)} = \chi^2_{df_n}. \tag{2-5}$$

The number of degrees of freedom df_n is 2, one for each of the attendant Fourier series coefficients from which $\tilde{S}_F(\vec{k}_n)$ has been calculated. A consequence of this property is that the standard deviation of an estimate $\tilde{S}_F(\vec{k}_n)$ is of the same order of magnitude as the estimate itself [e.g. Jenkins and Watts 1968, Rayner 1971]. Some form of spectral smoothing, or windowing, is therefore required to overcome this unacceptable attribute of calculated spectral estimates. One method commonly used to improve the statistical properties of estimated spectra, and which is particularly suitable when spectra are computed directly using the Fast Fourier Transform, is simply to average the raw spectral estimates $\tilde{S}_F(\vec{k})$ within wavenumber bands which are greater in width than the elementary discrete wavenumber interval T^{-1} [cf. Equation (2-1)]. The resulting estimates of the smoothed power spectrum, represented by $\hat{S}_F(\vec{k})$, are assumed to reside at the mean wavenumbers of each band over which the raw estimates were averaged. For a given band r having mean wavenumber $\vec{k}_r$, the smoothed spectral estimate $\hat{S}_F(\vec{k}_r)$ is referred to as an ensemble average on the grounds that the constituent raw spectral data comprise an ensemble of random estimates of the power of the data series at wavenumber $\vec{k}_r$.

Two-dimensional smoothed spectra $\hat{S}_F(\vec{k})$ where $\vec{k}=k_{(x)}\vec{i}+k_{(y)}\vec{j}$ are calculated not only on the basis of chosen wavenumber bands, to which the wavenumber moduli of the raw spectral data are referred, but also on the basis of chosen angular limits to which their directions are referred as illustrated in Figure 2-8. Note that for real observed data, gravity and topography in the present case, only two quadrants of the resulting array of raw spectral data contain independent information since there is no spectral distinction between directions which are 180° divergent. Thus, the number of degrees of freedom df_r associated with any smoothed estimate $\hat{S}_F(\vec{k}_r)$ derive from raw estimates in one direction only; there are two for each of these arising from the attendant sine and cosine Fourier series coefficients [cf. subsection 2.2.2(i)]. However, tapering of the original data series to suppress edge effects [cf. subsection 2.2.2(iii)] reduces df_r by a factor estimated to be equivalent to the fraction of the data not affected by tapering [Tukey 1967; Rayner 1971, pp. 86, 118]. Thus,

$$df_r \simeq 2m_r[1 - \frac{M'}{M}] \qquad (2\text{-}6)$$

Figure 2-8. The two-dimensional wavenumber domain. Circles indicate the locations of raw spectral estimates at harmonic wavenumbers; open circles are complex conjugates of their filled counterparts. Only two quadrants contain independent data. An ensemble of data, providing a smoothed spectral estimate at $\vec{k}_r$, is contained by the thick solid lines in the first quadrant. An ensemble of data, providing a smoothed isotropic transfer function estimate at $|\vec{k}_r|$, is contained by the thin solid lines in the first and second quadrants.

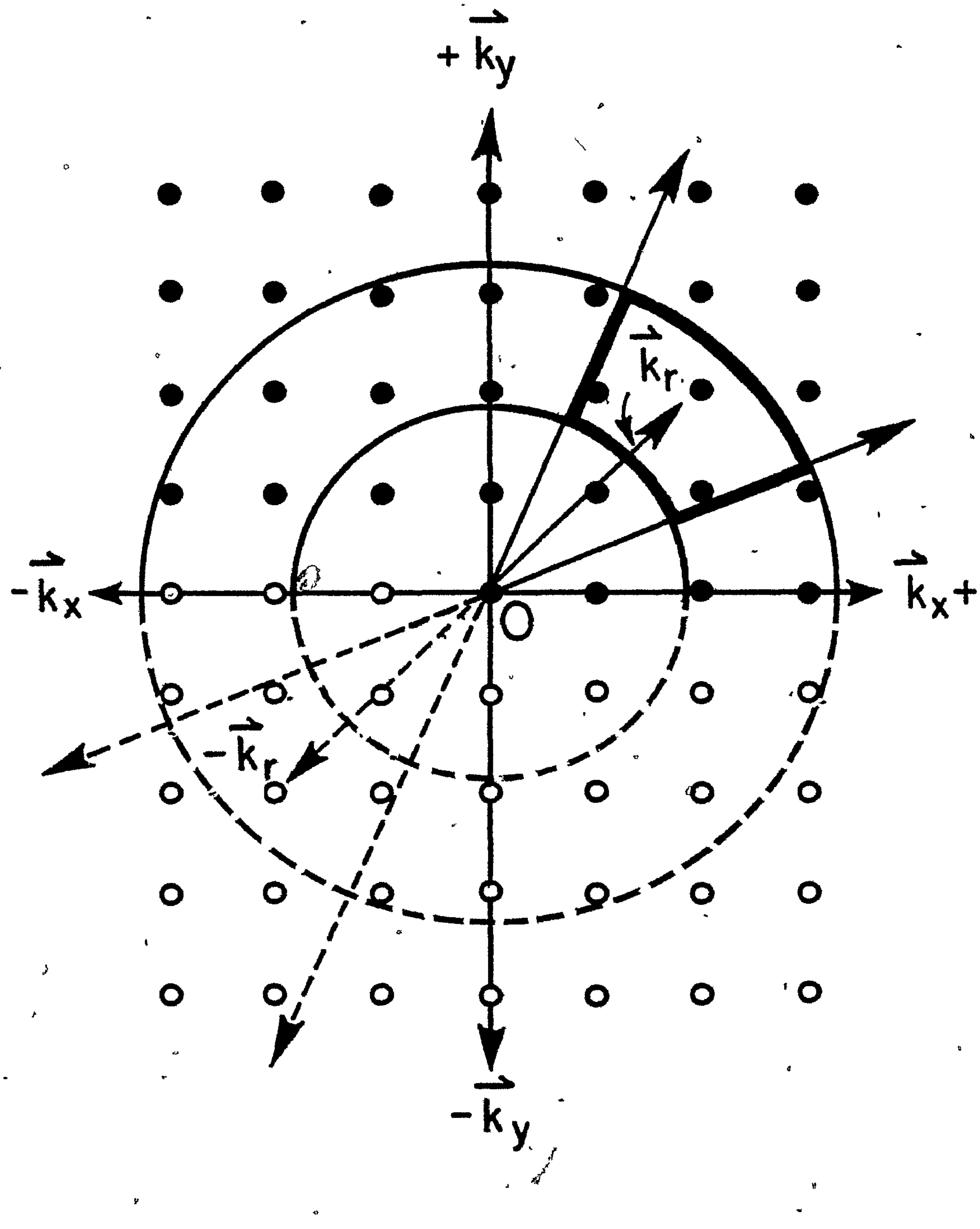

$+\vec{k}_y$
$\vec{k}_r$
$-\vec{k}_x$
$\vec{k}_x+$
O
$-\vec{k}_r$
$-\vec{k}_y$

where m_r is the number of raw estimates in ensemble r, M is the number of data in the original data series, and M' is the number of data in the original series modified by the tapering function. The 100[1−α]% confidence limits associated with a smoothed spectral estimate $\hat{S}_F(\vec{k}_r)$, using df_r as provided by (2-6), can be calculated from Equation (2-5) and result in

$$\Pr\left\{\chi^2_{df_r}(\alpha/2) \le \frac{df_r\,\hat{S}_F(\vec{k}_r)}{S_F^T(\vec{k}_r)} \le \chi^2_{df_r}(1-\alpha/2)\right\} = 1 - \alpha.$$

This expression is written more conveniently as

$$\Pr\left\{\frac{df_r\,\hat{S}_F(k_r)}{\chi^2_{df_r}(1-\alpha/2)} \le S_F^T(\vec{k}_r) \le \frac{df_r\,\hat{S}_F(\vec{k}_r)}{\chi^2_{df_r}(\alpha/2)}\right\} = 1 - \alpha \qquad (2\text{-}7).$$

2.2.4 Estimation of transfer functions. The isostatic response function $Q(\vec{k})$ was defined in Chapter 1 as the transfer function, or admittance, relating an input, the Fourier transform of continental topography $H(\vec{k})$, to an output, the Fourier transform of gravity anomalies $G(\vec{k})$ resulting solely from topography, less random noise $N(\vec{k})$:

$$Q(k) = \frac{G(\vec{k}) - N(\vec{k})}{H(\vec{k})} \qquad (1\text{-}3).$$

Because of the noise inherent in observed gravity anomalies, an observation of $Q(\vec{k})$ cannot simply be made by normalizing observed $G(\vec{k})$ by observed $H(\vec{k})$. In the present case the noise is assumed to derive from tectonically-emplaced lateral density variations in the Earth's upper crust. If these density variations occur randomly, that is, they are not correlated with the observed topography, then the best estimate of the isostatic response function, is provided by [Munk and Cartwright 1966, p. 543]

$$\hat{Q}(\vec{k}) = \hat{S}_{GH}(\vec{k})/\hat{S}_{H}(\vec{k}) \qquad (2\text{-}8)$$

where $\hat{S}_{GH}(\vec{k})$ is a smoothed estimate of the cross spectrum of the gravity and topography, based on raw spectral estimates formulated by Equation (2-3), and $\hat{S}_{H}(\vec{k})$ is a smoothed estimate of the power spectrum of the topography, based on raw estimates by (2-2). It is the smoothing, accomplished by ensemble averaging [subsection 2.2.3], which minimizes the random noise. The estimated isostatic response function $\hat{Q}$ may be assumed to be real and, in $\vec{k}$ space, directionally isostropic given the analogous assumption that the response of the lithosphere to a point load, in $\vec{r}$ space, is concentrically symmetric and centred at the location of the load. Because of the assumed isotropy of $\hat{Q}(\vec{k})$, the ensemble of raw spectral data which is averaged to find it comprises all of those data which fall within a given wavenumber band or annulus, symmetric about the $\vec{k}$ space origin [Figure 2-8]. Thus, $\hat{Q}$ is estimated as a function of wavenumber modulus $|\vec{k}|=k=[k^2_{(x)}+k^2_{(y)}]^{1/2}$ unlike two-dimensional power spectrum estimates which are referred also to the wavenumber direction [subsection 2.2.3, Figure 2-8]. Since $Q(k)$ is assumed to be real, the imaginary component of the estimated isostatic response, $\mathrm{Im}[\hat{Q}(k)]$, is expected to be small and may be considered to be an indication of noise in the observations.

The estimate of $\hat{Q}(k_r)$ from noisy data [Equation (2-8)] is based on least squares minimization of residuals in which it was assumed all of the variance associated with Q derived from variance associated with the observed gravity anomalies. In turn, the variance of the gravity observations was assumed to be entirely due to geological noise $N(\vec{k})$, where

$$N(\vec{k}) = G(\vec{k}) - Q(\vec{k})\, H(\vec{k})$$

from Equation (1-3). McNutt [1978, pp. 177-178] shows that the standard error $d\hat{Q}(k_r)$ characterizing a given $\hat{Q}(k_r)$ estimate under these circumstances can be determined by considering the residuals between the constituent raw gravity spectral estimates $\tilde{S}_G(k_n)$ and those predicted by the product $\hat{Q}(k_r)\ \tilde{S}_H(k_n)$ and is provided by

$$d\hat{Q}(k_r) = \frac{1}{df_r - 1} \left[\frac{\hat{S}_G(k_r)}{\hat{S}_H(k_r)} - \{\mathrm{Real}[\hat{Q}(k_r)]\}^2\right] \tag{2-9}$$

where $\hat{S}_G(k_r)$ is the smoothed ensemble estimate of the power spectrum of the gravity anomalies. McNutt's expression for $d\hat{Q}(k_r)$ is modified here to the extent that the number of degrees of freedom df_r associated with an estimate $\hat{Q}(k_r)$ should reflect the effects of tapering of the original data series according to Equation (2-6).

A statistical measure of the portion of observed gravity anomalies attributable to topography for any k_r is the coherence squared $\gamma^2(k_r)$, an estimate of which, in the presence of noise, is provided by [Munk and Cartwright 1966, p. 580]

$$\hat{\gamma}^2(k_r) = \frac{m_r[\hat{S}_{GH}(k_r)\hat{S}^*_{GH}(k_r)/\hat{S}_G(k_r)\hat{S}_H(k_r)] - 1}{m_r - 1} \tag{2-10}$$

where * indicates complex conjugate and m_r is the number of raw data in ensemble r centred at k_r.

2.3 Analysis of Synthetic Data

2.3.1 Introduction. One consideration in calculating a smoothed estimate of the power spectra of continental topography and gravity is that the true spectra are expected to be "red": that is, power at low frequencies is expected to be several orders of magnitude greater than power at the highest observable frequencies. For example, Lewis and Dorman [1970, Fig. 7] found that gravity and topography spectra of the United States varied by approximately 1 and 2 orders respectively in the wavelength range 2000-100 km. If, because of spectral redness, raw spectral estimates are rapidly varying in a non-linear fashion within a chosen wavenumber ensemble band r, the averaged ensemble estimate $\hat{S}_H(k_r)$ may be biased somewhat toward higher values.

Secondly, recall that the observed data sets have been multiplied by a Gaussian-shaped tapering function in order to suppress artificial high frequency spectral power related to discontinuities at the edges of the data [subsection 2.2.2]. This operation is equivalent to the convolution of the Fourier transforms of the untapered data and the tapering function. Thus, while the power spectrum of the tapering function would be expected to be strongly red, it is necessarily more so than the spectrum of the observations; otherwise, the convolution operation would serve to blur the high power at low frequencies into the high frequency raw estimates of the calculated spectrum. The artificial high frequency power related to edge discontinuities would therefore be enhanced rather than suppressed.

Thirdly, the convoluted effects of the tapering cannot be separated from the calculated transfer function. In particular, the application of the same tapering function to both topography and gravity data sets may result in artificial coherence between gravity and topography at wavelengths characteristic of the taper length. If this effect is significant then the statistically extracted transfer function between them may be prejudiced.

In order to investigate these potential problems of the data reduction method described in section 2.2 a synthetic two-dimensional gravity and topography data set was constructed. Topography on a 32 x 64 grid, with digitization interval of 50 km in each dimension, was synthesized in the space domain by summation of a finite series of cosine waves with amplitudes compatible with those of the expected topography spectra and with random phase. The frequencies of the constituent cosine waves randomly distributed about the harmonic frequencies so that the FFT would be affected by edge discontinuities. The synthetic gravity field was similarly constructed, the amplitudes of its component waves being determined by the product of those of the topography and an isotropic, real transfer function, chosen to be similar to expected $Q(k)$ for continental lithosphere.

2.3.2 Results and discussion. Figure 2-9 shows the true power spectrum of the synthesized topography compared to ensemble estimates $\hat{S}_H(k_r)$ [calculated at constant wavenumber intervals of 0.001 km^{-1}] with associated 95% confidence limits. Filled squares and open circles indicate calculated $\hat{S}_H(k_r)$ with and without tapering of the original synthetic data. Also shown is the computed power spectrum of the tapering function used to produce $\hat{S}_H(k)$. The known transfer function between topography and gravity is compared to its estimate $\hat{Q}(k)$, with and without tapering, in Figure 2-10. The tapering function used in calculating the illustrated results, the power spectrum of which is shown in Figure 2-9, was applied to three rows or columns on each edge of the original 32 x 64 data grids [26% of the data]. Tapers of other lengths were also examined, though the results are not reproduced here, and those which affected 20-40% of the data, a range consistent with that suggested by Tukey [1967], were found to be satisfactory, their effects not being significantly different from one another.

It can be seen in Figure 2-9 that tapering suppresses high frequency contamination by edge discontinuities very effectively with minimal spectral blurring. Blurring, rather than averaging bias, is probably responsible for the systematic slight underestimation of $\hat{S}_H(k)$ but this effect is very minor; moreover, the topography and, especially, gravity spectra of the study areas are likely to be less red than the synthetic spectrum chosen here [cf. section 5.3] so that, regardless of its source, this effect will likely be reduced using the real data. The spectrum of the tapering function is noted to be significantly redder than the synthetic spectrum.

Figure 2-9. Comparison of a known synthetic topography power spectrum $S_H(k)$ with two sets of estimates $\hat{S}_H(k)$ [showing 95% confidence intervals] found using tapered and untapered data [left-hand scale] and with the estimated power spectrum of the tapering function $\hat{S}_F(k)$ [right-hand scale].

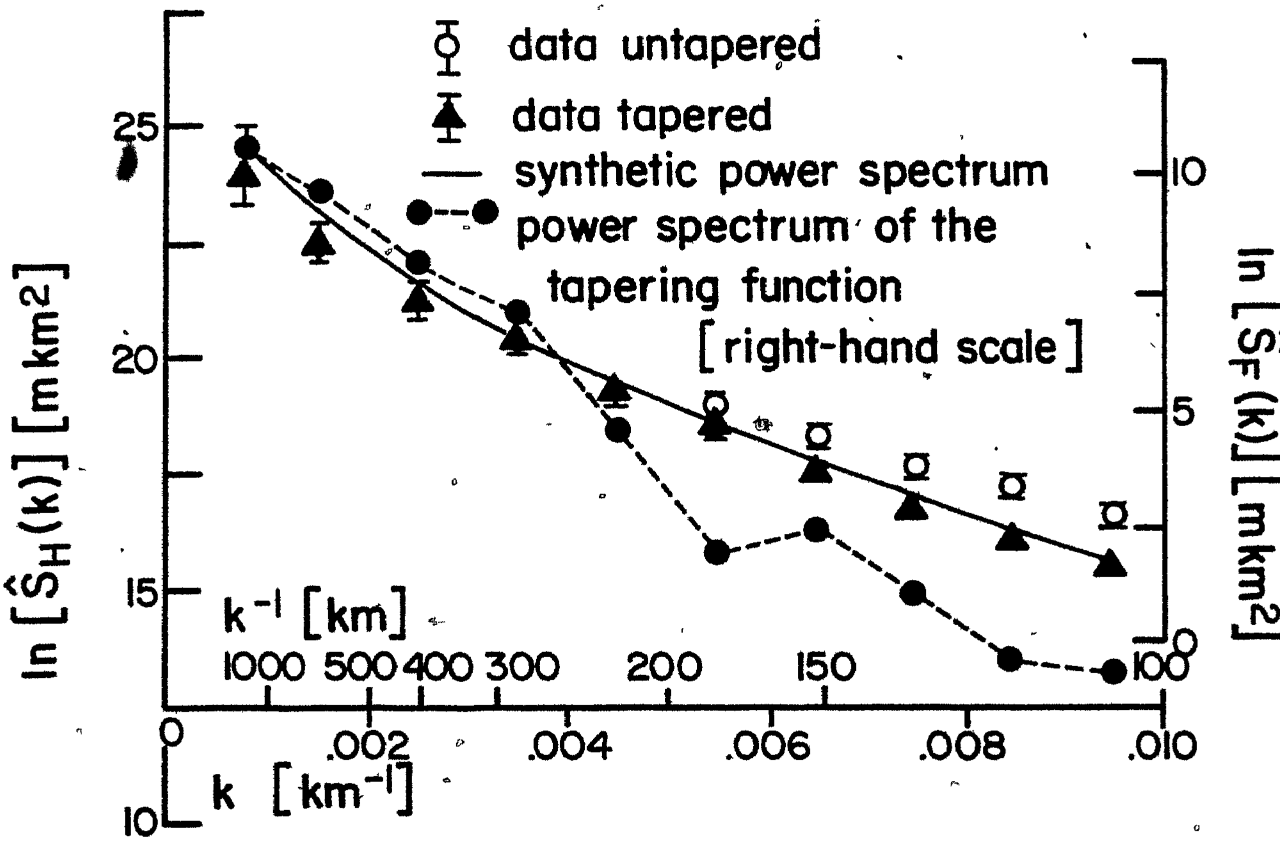
data untapered
data tapered
synthetic power spectrum
power spectrum of the tapering function [right-hand scale]
25
20
15
10
ln [$\hat{S}_H(k)$] [m km^2]
10
5
0
ln [$\hat{S}_F(k)$] [m km^2]
k^{-1} [km]
1000 500 400 300 200 150 100
0 .002 .004 .006 .008 .010
k [km^{-1}]

Similar results prevail in the case of the transfer function estimation [Figure 2-10]. Tapering appears to provide reliable results; there is no apparent introduction of spurious coherence related to the wavelength of the taper based on results using tapers of different lengths. The slight overestimation of $\hat{Q}(k)$ for intermediate k is probably due to averaging bias; if so, the effect is exaggerated because the synthetic transfer function considered here falls off more rapidly than those expected using real data [cf. section 3.3]. Moreover, the observed offset is negligible compared to the expected effects of superimposed geological and measurement noise.

The crucial assumption regarding geological noise is that it is random in the sense of being uncorrelated with topography. No such noise was included in the synthetic data analysis because it is known theoretically that it will have no effect on the extraction of the correct transfer function as long as there are sufficient data [Munk and Cartwright 1966]. The synthetic data analysis was directed specifically at determining the effects of "noise" derived from the finite nature of the data and the need for tapering. For this reason no ad hoc synthetic analysis of correlated geological noise was performed.

2.4 Summary

In this chapter the raw gravity and topography data to be used in subsequent analyses have been presented. The source regions of the data are much more tectonically homogeneous than those used in previous studies of continental isostatic response functions [Dorman and Lewis

Figure 2-10. Comparison of a known synthetic transfer function $Q(k)$ with its estimates $\hat{Q}(k)$ found using tapered and untapered data; error bars correspond in length to two standard errors.

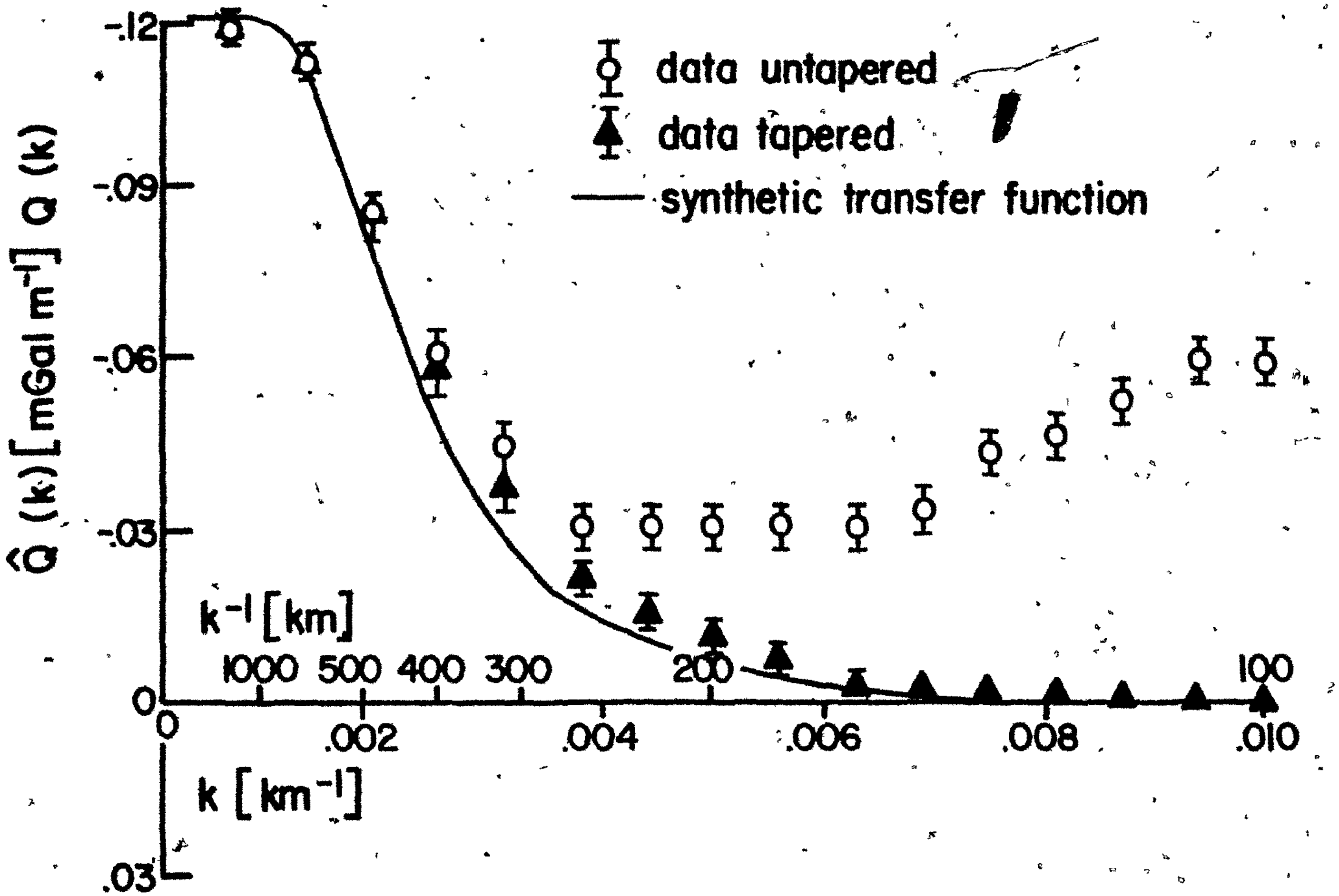
data untapered
data tapered
synthetic transfer function
$\hat{Q}$ (k) [mGal m^{-1}] Q (k)
-.12
-.09
-.06
-.03
0
.03
k^{-1} [km]
1000 500 400 300 200 100
0 .002 .004 .006 .008 .010
k [km^{-1}]

1970, McNutt and Parker 1978, McNutt 1980]. Moreover, the data themselves are probably more reliable, particularly in respect to using original digitized topography data rather than those measured at gravity stations.

The standard spectral analysis techniques with which the isostatic response functions and topography power spectra of the study regions are to be computed from the raw data have been briefly reviewed. There has been no uniformity among previous continental response function studies regarding the treatment of discontinuities at the edges of finite data sets. In the present case it was decided to simply taper the edges of the data following Tukey [1967]. The tapering method was applied to a synthetic data set in order to test its reliability and was found to produce no discernible artifacts.

Chapter 3. Time-invariant Isostatic Response of Continents

3.1 Introduction

3.1.1 Thin elastic plate lithosphere. Given that adequate topography and gravity data exist to calculate the isostatic response functions of segments of the continental lithosphere, they can be compared to theoretical functions based on simple models in order to better understand the rheological and structural properties of the lithosphere. In this chapter, the observed isostatic response functions of various geological provinces of North America are considered in terms of the elastic class of rheological models of the lithosphere introduced in Chapter 1. Specifically the mechanical lithosphere is modelled as a thin elastic plate, one which has a small thickness compared to the wavelength of its deformation. The deformation w at a point $\vec{r}=x\vec{i}+y\vec{j}$, where $\vec{i}$ and $\vec{j}$ are orthogonal unit vectors, produced by a load $p(\vec{r})$ [dimensionally a force per unit area] on a thin elastic plate overlying a fluid substratum is given by the solution of [Nadai 1963]

$$D\nabla^4 w(\vec{r}) = p(\vec{r}) \qquad (3\text{-}1i)$$

where D is the plate's flexural rigidity, a function of its thickness T_L and the elastic moduli of its constituent material, Young's modulus E and Poisson's ratio ν:

$$D = \frac{ET_L^3}{12(1-\nu^2)} \qquad (3\text{-}1ii).$$

If the plate is assumed to be incompressible then ν=.5 and $D=ET_L^3/9$. The thin plate at any point $\vec{r}$ is assumed to have a uniform vertical deformation; that is, $w(\vec{r})$ is not a function of the vertical coordinate z and therefore

$$\nabla^4 w(\vec{r}) = (\nabla^2)^2 w(\vec{r}) = \left[\frac{\partial^2}{\partial x^2} + \frac{\partial^2}{\partial y^2}\right]^2 w(\vec{r}).$$

The thin plate model of the lithosphere is illustrated in Figure 3-1. Note that the total load $p(\vec{r})$ consists of (1) forces acting on the surface of the plate because of overlying material of density ρ_o and height $\ell(\vec{r})$ and (2) buoyancy forces acting on the base of the plate caused by the displacement of the fluid substratum of density ρ_m by the plate deflection $w(\vec{r})$. Thus,

$$p(\vec{r}) = -\rho_o g\ \ell(\vec{r}) - \rho_m g\ w(\vec{r}) \tag{3-2}$$

where g is the gravitational acceleration and z is positive downwards. Therefore, for a positive, downward-directed load $p(\vec{r})$ and resulting deflection $w(\vec{r})$, $\ell(\vec{r})$ is a negative quantity.

Applications of thin plate theory to geophysical problems of crustal or lithospheric deformation have been numerous with early contributions by Gunn [1943a,b; 1944] who considered, in particular, the loading response of the lithosphere and gravity effect of the Hawaiian Islands. More recent use of thin plate theory in geophysical modelling began with Walcott's [1970a] study of crustal deformation associated with a number of individual continental and oceanic loads. These included North American Pleistocene lakes and the Hawaiian Islands.

Figure 3-1. Elastic plate model of a layered lithosphere of thickness T_L loaded by a topographic block [diagonally lined] of height ℓ centred at $\vec{r}$ isostatically compensated by lithospheric flexure. Buoyancy forces, proportional to the plate deflection w, load the base of the plate. Gravity anomalies are generated in the cross-hatched regions, produced by the deflection of the Mohorovicic discontinuity. The density contrast at the Moho is $\Delta\rho=\rho_m-\rho_o$. There is no density contrast at the base of the lithosphere. Measurable topography h remains above sea level [z=0].

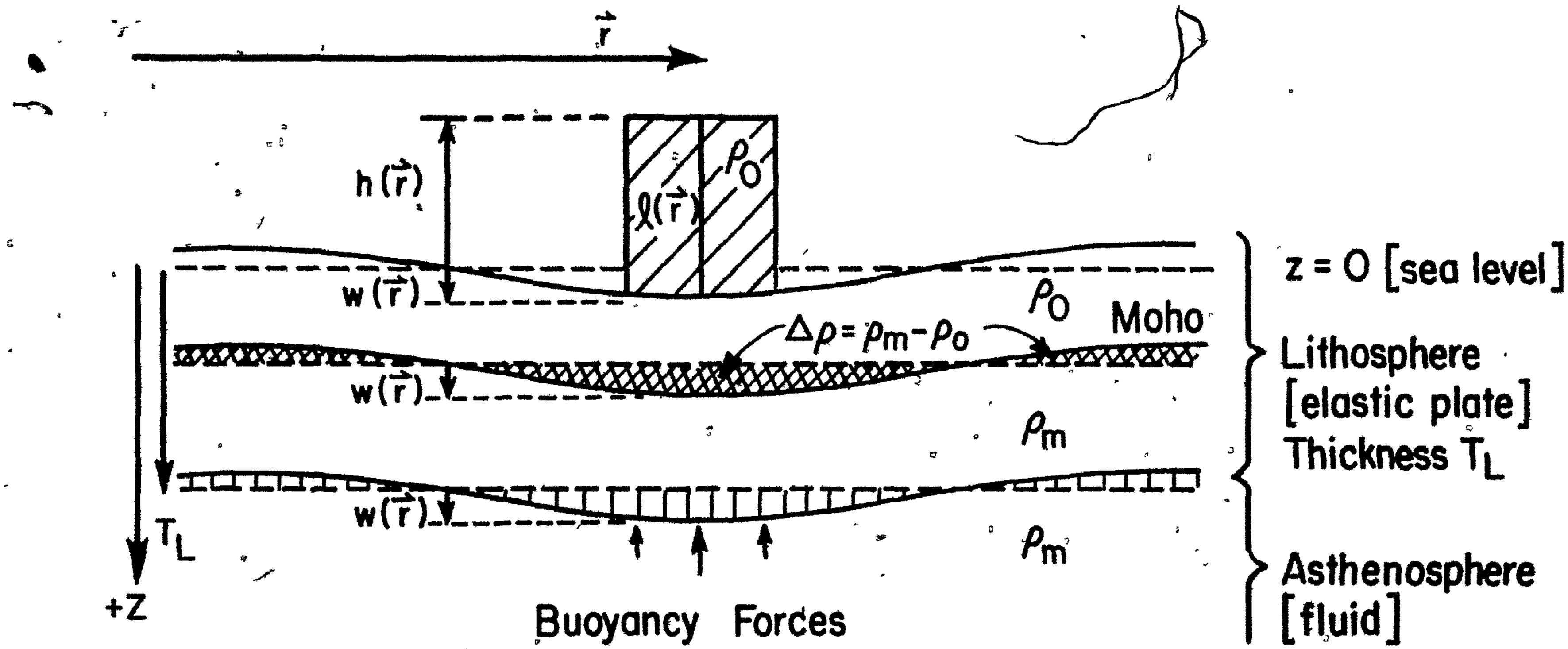

$\vec{r}$
$h(\vec{r})$
$\ell(\vec{r})$
ρ_0
$w(\vec{r})$
ρ_0
Moho
$\Delta\rho = \rho_m - \rho_0$
$w(\vec{r})$
ρ_m
$w(\vec{r})$
T_L
+Z
ρ_m
Buoyancy Forces
z = 0 [sea level]
Lithosphere
[elastic plate]
Thickness T_L
Asthenosphere
[fluid]

Elastic plate models of the lithosphere have also been applied to the analysis of other oceanic islands [Watts and Cochran 1974, Watts et al. 1975], sedimentary basins [Walcott 1972, Cochran 1973, Haxby et al. 1976], and the outer topographic rises associated with Pacific Ocean subduction zones [Walcott 1970a, Hanks 1971, Watts and Talwani 1974, Parsons and Molnar 1976, Caldwall et al. 1976]. A model of the isostatic response function characteristic of a thin elastic plate was first derived by Walcott [1976]. A more rigorous formulation was provided by Banks et al. [1977] who used it to invert the United States isostatic response data of Lewis and Dorman [1970].

In the present context of elastic plate theory, local isostatic compensation [of the Airy type] can be accommodated by the ideal case in which the elastic plate has zero thickness or no flexural strength. In physical terms this may correspond to isostatic adjustment by vertical faulting of rigid lithosphere. The response to changes in the topographic load, for example as a result of erosion, would be essentially instantaneous and therefore time-invariant. On the other hand, local compensation of topography may also be achieved by means of some form of ductile deformation in which case it represents a final isostatic condition prior to which the characteristic isostatic response function of the lithosphere would have varied depending on the age of the load and the style of the deformation. In such a case, the effects of erosion of topography must be explicitly considered. A model of this kind in which elastic stresses are relaxed by linear viscous flow is considered in Chapter 5.

3.1.2 Elastic plate isostatic response analysis. Estimates of the flexural rigidity of continental lithosphere based on thin elastic plate models of isostatic response functions [Banks et al. 1977, Banks and Swain 1978, McNutt and Parker 1978, McNutt 1980] are up to four orders of magnitude less than those based on models of the isostatic compensation of individual continental features [e.g. Walcott 1970a, Haxby et al. 1976]. Major criticisms of the response function method of isostatic analysis [Forsyth 1979, Cochran 1980] have in part been based on these anomalous results. It should be noted, however, that flexural studies of individual continental loads are few, owing to lack of suitable data, and are themselves ambiguous in their results, perhaps due to sensitivity to local changes in crustal structure [e.g. Walcott 1970a]. The response function technique was designed to overcome these problems [Dorman and Lewis 1970] but has encountered other, major, problems of its own. The main problems related to continental lithospheric studies using isostatic response functions fall into three categories which are discussed below.

(i) Geological heterogeneity. The regions for which isostatic response functions have been computed, primarily the United States [Lewis and Dorman 1970] and Australia [McNutt 1978], are geologically complex but were chosen because of the need to sample large regions in order to minimize the geological noise related to non-isostatic upper crustal lateral density variations [cf. section 2.1]. Allied to this general problem of noisy data are methodological problems. First, isostatic response computations are somewhat sensitive to data reduction techniques [for example, tapering of data as opposed to reflecting data to suppress edge effects] so that the direct comparison of response functions calculated using different methods, a common practice in the literature, should be avoided. The sensitivity of the results to changes in methodology is probably enhanced by the degree of noisiness of the raw data. Secondly, the degree of noisiness of the data is such that coherence between topography and gravity [cf. subsection 2.2.4] is often so low, for much of the sampled spectral range, that the validity of any computed transfer function between them may be questionable.

(ii) The complex tectonic origin of continental topography and its subsequent evolution. Both Forsyth [1979] and Cochran [1980] have pointed out that the model of topography being loaded onto a flexurally competent lithosphere is probably an unrealistic one; in general, continental crust and presumably its topography are generated in thermally weakened zones of orogenesis. Both authors suggest that low values of flexural rigidity based on analyses of continental isostatic response functions reflect the strength of the lithosphere during the tectonically active stage when topography was formed. In such a model, consideration of the effects of topographic erosion occurring after the time at which the lithosphere achieved some greater flexural strength is inescapable. The deeply eroded nature of cratonic regions suggests that the amount of subsequent erosion has exceeded the original topography.

(iii) Isostatic compensation of topography by means other than elastic flexure. For example, faulting of the upper crust may provide partial isostatic compensation to some high amplitude topographic features. Any compensation mechanism such as this giving rise to gravity anomalies will result in artificially low flexural rigidities determined by means of a plate model. Similar effects might be expected if the thin elastic plate is an inadequate model of the lithosphere.

First, use of thin plate theory may not be appropriate for the analysis of the loads under consideration. That is, the smallest wavelengths of the observed isostatic response function may be too small in comparison with the thickness of the plate. Calculations by McKenzie and Bowin [1976] and Courtney [1981, pers. comm.] indicate this to be the case when the plate thickness exceeds approximately half the wavelength of the imposed load. Isostatic response functions calculated from United States [Lewis and Dorman 1970] and Australian [McNutt 1978] data take into account topographic loads of less than 60 km and 40 km wavelength respectively. On the other hand, estimates of the flexural rigidity of continental lithosphere based on studies of individual loads indicate plate thicknesses, using Equation (3-1ii), in the range 35-60 km [as summarized by Cochran 1980]. Short wavelength estimates form only a small portion of the United States and Australian response data and any problem resulting from the invalidity of the thin plate assumption may also be small; nevertheless, it remains that the effects of any incorrect application of a thin plate model would be to force the model toward artificially low flexural strength. This follows from calculations by McKenzie and Bowin [1976, Fig. 14] and Walcott [1976, Fig. 1; citing Foucher (1974, pers. comm.)] which show that "thick" plate deformational response to surface loading would be greater in amplitude than that predicted by thin plate theory.

Secondly, the assumption of purely elastic behaviour may be in error. For example, some studies of the flexural characteristics of the continental lithosphere during the formation of foreland sedimentary basins [Beaumont 1981] indicate that stratigraphic relations within such basins are most simply modelled by a viscoelastic lithosphere, one which can relax elastic stresses by linear viscous flow. As mentioned in subsection 3.1.1 the state of local Airy isostatic compensation of surface loads may be a consequence of such a process. Other more complicated mechanisms of stress relaxation also fall into category (iii). In any case, the isostatic response of such a lithosphere, observed at any given time, will be a function of its loading history, a matter in which erosion of topography is important as well as lithosphere rheology. Whether the interpretation of the isostatic response of such a lithosphere in terms of a thin elastic plate would always return artificially low flexural rigidities is difficult to predict. On the other hand the isostatic response function of such a lithosphere might be expected to vary in some consistent fashion with the age of the topographic load.

The three categories of problems involved in the interpretation of continental isostatic response functions in terms of elastic thin plate theory, listed above, can be summarized as those resulting from (i) inadequate data and methodology, (ii) an incorrectly assumed or untenable loading history, and (iii) an incorrect model of lithospheric response to loading. In this chapter, the analysis of continental isostatic response functions based on elastic thin plate theory is performed with problems deriving from category (i) minimized as much as possible. Response functions have been computed for geological regions which are as tectonically homogeneous as possible; each has been found using the same methodology; the methodology was successfully tested by analyzing synthetic data [section 2.3]; and the minimum topographic wavelength considered for each is greater than 100 km [cf. section 2.2] so that the thin plate modelling approximation is suitable. Thus, the results of the present analysis can be interpreted in terms of the problems discussed in categories (ii) and (iii) only. The model of continental isostatic response which is being tested is one in which the lithosphere behaves elastically with elastic properties which do not change with age and in which the load, as measured by the isostatic response function, is truly that due to topography existing at the present. For such a model, the isostatic response functions of different tectonic regions should be the same unless variations exist between regions in the depths to major density discontinuities in the lithosphere such as the Mohorovicic discontinuity. The choice of depths to major density discontinuities is constrained by other geophysical data such as those provided by seismic refraction studies. If, within the uncertainties of such constraints, this model of continental isostatic response cannot be rejected, then, in turn, the flexural rigidity of the continental lithosphere so determined cannot be rejected even if it is significantly different from those found using other kinds of data.

If, on the other hand, such a model can be rejected on the basis of variations in the observed isostatic response functions of different geological provinces, then the properties and/or loading history of the lithosphere must be assumed to be such that the lithosphere's characteristic isostatic response function varies depending on its tectonic age. Any model in this class of models will be difficult to interpret in terms of a thin elastic plate lithosphere, the isostatic response of which is forced only by modern topography, because it will depend on the load history, as discussed in problem categories (ii) and (iii) listed above. In the absence of a quantitative model in which the effects of erosion are explicitly considered, it is speculative to suggest that observed isostatic response functions indicating increasing flexural rigidity of continental lithosphere as the age of the topography increases supports a model of cooling and thickening lithosphere [Stephenson 1978] or that indications of the reverse phenomenon imply viscous relaxation of continental lithosphere [McNutt and Parker 1978]. Models which include topographic erosion and which can account for time-dependence of isostatic response functions are developed and applied to observations in Chapter 5.

3.2 The Isostatic Response of a Thin Elastic Plate

3.2.1 Deformation of a thin elastic plate by a harmonic load.

The plate load $p(\vec{r})$ in Equation (3-1i) is expressed in terms of its harmonic components by its two-dimensional Fourier transform $F\{p(\vec{r})\} = P(\vec{k})$, where the wavenumber $\vec{k}=k_{(x)}\vec{i}+k_{(y)}\vec{j}$, given by Equation (1-2i). The deformation of the plate in response to $P(\vec{k})$ is therefore found by Fourier transforming Equation (3-1i):

$$D[2\pi k]^4 \, W(\vec{k}) = P(\vec{k}) \tag{3-3}$$

if D is not a function of position and noting that [Sneddon 1951, p. 27]

$$F\left\{\frac{d^n f(r)}{dx^n}\right\} = [i2\pi k]^n \, F(\vec{k})$$

where $F\{f(\vec{r})\} = F(\vec{k})$, assuming that the first [n-1] derivatives of $f(\vec{r})$ vanish as $|\vec{r}| \to \infty$.

The Fourier transform of Equation (3-2), in which $p(\vec{r})$ was decomposed into surface and buoyancy forces, is

$$P(\vec{k}) = -\rho_o \, gL(\vec{k}) - \rho_m \, gW(\vec{k}) \qquad (3\text{-}4).$$

Equations (3-3) and (3-4) combined result in

$$W(\vec{k}) = -\frac{\rho_o}{\rho_m} \, \psi(k) \, L(\vec{k}) \qquad (3\text{-}5i)$$

where

$$\psi(k) = \left[1 + \frac{[2\pi k]^4 D}{\rho_m g}\right]^{-1} \qquad (3\text{-}5ii)$$

and $\psi(k)$ is called the flexural response function [after Walcott 1976].

3.2.2 Theoretical isostatic response functions. In the thin plate model of the lithosphere gravity anomalies $g(\vec{r})$ are assumed to be generated entirely by the density perturbation resulting from plate deflection $w(\vec{r})$ in response to surface loading $\ell(\vec{r})$ [Figure 3-1]. The isostatic response function is defined as the Fourier transform of the gravity normalized by the Fourier transform of the measurable topography [Equation (1-3)]. Figure 3-1 illustrates that the measurable topography

$h(\vec{r})$ consists of only that portion of the surface load $\ell(\vec{r})$ remaining above the undeformed plate surface; i.e.,

$$\ell(\vec{r}) = h(\vec{r}) - w(\vec{r}) ,$$

the Fourier transform of which is

$$L(\vec{k}) = H(\vec{k}) - W(\vec{k}) \qquad (3\text{-}6).$$

In consideration to (3-6), Equations (3-5) become

$$W(\vec{k}) = -\frac{\rho_o}{\Delta\rho} \psi'(k) H(\vec{k}) \qquad (3\text{-}7i)$$

where

$$\psi'(k) = \left[1 + \frac{[2\pi k]^4 D}{\Delta\rho g}\right]^{-1} \qquad (3\text{-}7ii)$$

and $\Delta\rho = \rho_m - \rho_o$.

The Fourier transform of the gravity anomaly produced by the density perturbation $\rho'(\vec{r},z)$ is [Parker 1973]

$$G(\vec{k}) = 2\pi\Gamma \int_b^\infty P'(\vec{k},z) \exp[-2\pi kz]\, dz \qquad (3\text{-}8)$$

where $F\{\rho'(\vec{r},z)\} = P'(\vec{k},z)$ and Γ is the gravitational constant. Banks et al. [1977] show that a vertical displacement $w(\vec{r})$ in a medium of density $\rho(\vec{r},z)$ produces the perturbation

$$\rho'(\vec{r},z) = w(\vec{r}) \frac{\partial\rho}{\partial z} \qquad (3\text{-}9)$$

if the normal density distribution of the plate is assumed to be a function of z only and if the medium is assumed to be incompressible. The Fourier transform of (3-9),

$$P'(\vec{k},z) = W(\vec{k}) \frac{\partial\rho}{\partial z} ,$$

substituted into Equation (3-8) gives

$$G(\vec{k}) = 2\pi\Gamma\ W(\vec{k}) \int_0^\infty \frac{\partial\rho}{\partial z} \exp\,[-2\pi kz]\ dz \qquad (3\text{-}10)$$

which, used in conjunction with Equations (3-7), gives an expression for the theoretical isostatic response of a thin elastic plate,

$$Q_e(k) = -2\pi\Gamma \frac{\rho_o}{\Delta\rho}\, \psi'(k) \int_0^{T_L} \frac{\partial\rho}{\partial z} \exp\,[-2\pi kz]\ dz \qquad (3\text{-}11).$$

Since the isostatic compensation of the topography, and resulting gravity anomalies, are associated completely with the deformation of the plate, the integration of the density gradient in Equation (3-11) is finite, proceeding only to the normal depth of the base of the plate, T_L, the plate thickness.

Note that in the case k=0, $\psi'(k)$ and exp $[-2\pi kz]$ become unity and Equation (3-11) reduces to

$$Q_e(k=0) = -2\pi\Gamma\ \rho_o$$

since

$$\int_0^{T_L} \frac{\partial\rho}{\partial z} dz = \rho(z)\Big]_0^{T_L} = \rho_m - \rho_o = \Delta\rho .$$

3.2.3 Local isostatic response. (i) Thin plate case. Figure 3-2 schematically illustrates a topographic block of height ℓ and density ρ_o loaded onto a layered crust at a point $\vec{r}$ compensated locally by the Airy isostatic compensation mechanism. The block "floats" on the crust passively deforming it to produce a compensating root lying immediately below. The relationship between the height of the block ℓ and the size of the root w can be determined by equating the excess mass, lying above z=0 with the mass of the zones of deficient compensating density below:

$$[\ell(\vec{r}) + w(\vec{r})]\ \rho_o = -w(\vec{r})[\rho_1-\rho_o] - w(\vec{r})\ [\rho_m-\rho_1] \tag{3-12i}$$

or simply

$$w(\vec{r}) = -\frac{\rho_o}{\rho_m}\ \ell(\vec{r}) \tag{3-12ii}$$

for Airy compensation. Making the substitution ℓ=h−w and Fourier transforming gives

$$W(\vec{k}) = -\frac{\rho_o}{\Delta\rho} H(\vec{k}) \tag{3-13}$$

where $\Delta\rho=\rho_m-\rho_o$. Equation (3-13) is analogous to the thin plate equation (3-7i) and shows that Airy compensation is the special case of thin plate compensation with $\psi'(k)=1$, a consequence either of a plate with zero flexural rigidity or a load with a wavenumber approaching zero. The isostatic response function produced by Airy compensation is therefore simply Equation (3-11) with $\psi'(k)=1$:

Figure 3-2. A topographic block [diagonally lined] of height ℓ centred at $\vec{r}$ is locally compensated by a layered lithosphere. Gravity anomalies are generated in the cross-hatched regions with density contrasts $\Delta\rho_1$ and $\Delta\rho_2$. The measurable topography h remains above sea level [z=0]. The base of the lithosphere is not shown.

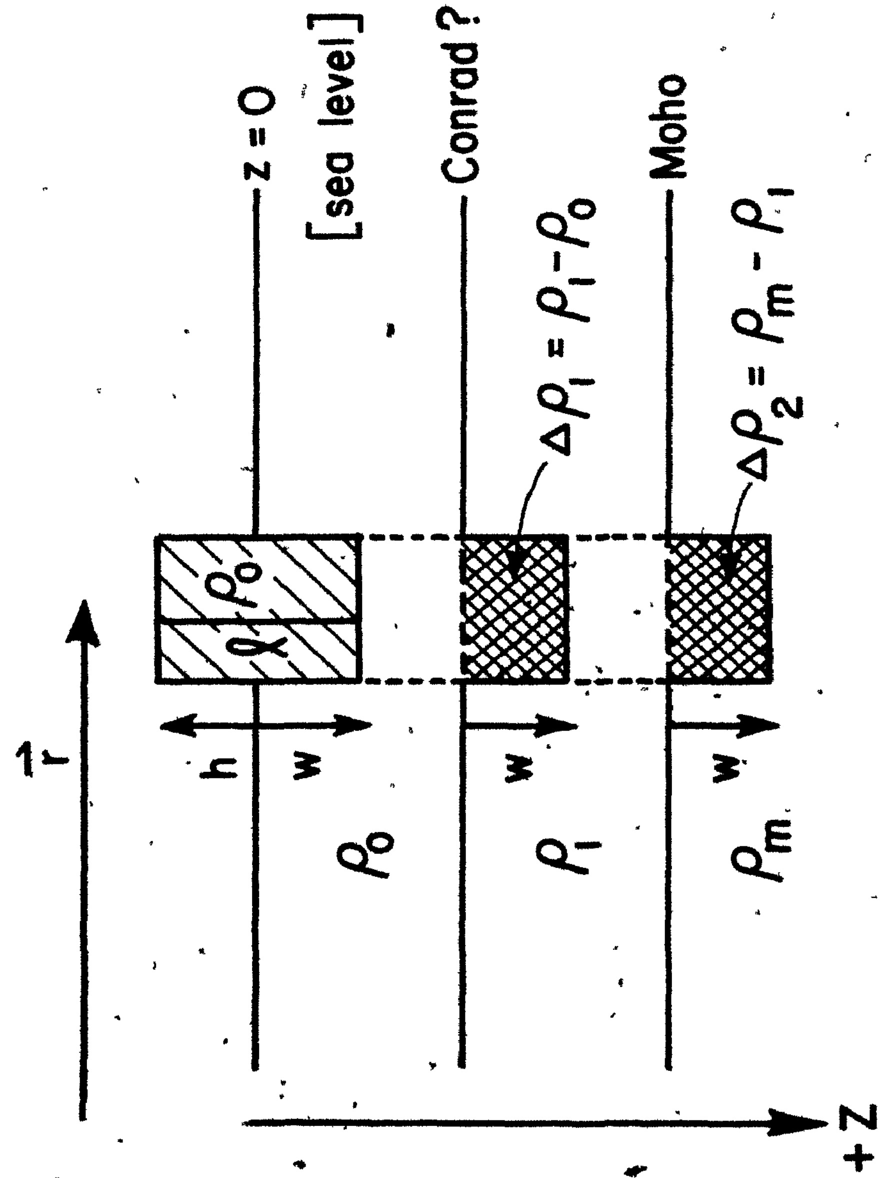
z = O
[sea level]
Conrad ?
Moho
$\Delta\rho_1 = \rho_1 - \rho_0$
$\Delta\rho_2 = \rho_m - \rho_1$
ρ_0
ρ_1
ρ_m
ℓ
h
w
w
w
r
+Z

$$Q_\ell(k) = -2\pi\Gamma \frac{\rho_o}{\Delta\rho} \int_o^{T_L} \frac{\partial\rho}{\partial z} \exp\,[-2\pi kz]\; dz \tag{3-14}$$

[or, if preferred, Equation (3-13) inserted into (3-10)].

(ii) General case. Dorman and Lewis [1970] formulated a general local compensation model in terms of a linear relation between a compensating density structure $\rho_c(\vec{r},z)$ lying immediately below topography $h(\vec{r})$,

$$\rho_c(\vec{r},z) = \underline{\rho}(z)\; h(\vec{r}) \tag{3-15}$$

where $\underline{\rho}(z)$ is the compensating density associated with a unit topographic load. For complete compensation of topography of density ρ_o occurring above a depth T_L

$$\int_o^{T_L} \rho_c(\vec{r},z)\; dz = -\rho_o\; h(\vec{r}) \tag{3-16}$$

which, in the case of the Airy model, is exactly equivalent to the column mass equality statement of Equation (3-12i) [where $h=\ell+w$]. The theoretical isostatic response of the general model given by (3-15) is just the Fourier transform of the gravity anomaly produced by the vertical line source described by the normalized compensating density $\underline{\rho}(z)$ [Dorman and Lewis 1970, McNutt 1978]:

$$Q_\ell(k) = 2\pi\Gamma \int_o^{T_L} \underline{\rho}(z)\; \exp\,[-2\pi kz]\; dz \tag{3-17}.$$

Alternatively, Equation (3-17) can be derived by direct substitution of the Fourier transform of (3-15) into Parker's [1973] harmonic gravity equation (3-8) noting that $\rho_c(\vec{r},z)$ is equivalent to the density perturbation $\rho'(\vec{r},z)$. It is obvious from the comparison of Equations (3-14) and (3-17) that the generalized compensation density per unit topography $\underline{\rho}(z)$ equals the Airy compensating density gradient $[-\rho_o/\Delta\rho][\partial\rho/\partial z]$.

3.3 North American Isostatic Response Functions

3.3.1 Observations. Figures 3-3(a,b) show observed isostatic response functions $\hat{Q}(k)$ for the six study areas outlined in subsection 2.1.2 [illustrated in Figure 2-1]. For each, ensemble estimates $\hat{Q}(k_r)$ were calculated at constant wavenumber intervals based on the dimensions of the study area. Fewer ensembles are possible as the dimensions of the study area decrease. Note, for example, only three $\hat{Q}(k_r)$ are provided for the small [600 km x 2000 km] Grenville province study area. These three estimates are, moreover, associated with large standard errors, also a consequence of the small number of raw data. As k_r increases, topographic power decreases resulting in a reduction in the signal to noise ratio [cf. Equation (1-3)]. This effect is offset by the parallel increase in the number of raw data available per ensemble with increasing k_r [cf. Figure 2-8]. Consequently, standard errors $d\hat{Q}(k)$ associated with $\hat{Q}(k)$ remain approximately constant throughout the spectral range. Note that the smallest errors are those associated with the isostatic response functions of the Cordilleran region where the topographic signal is greatest. The errors associated with response

Figure 3-3. Comparison of isostatic response functions $\hat{\tilde{Q}}(k)$ from (a) the Cordilleran, Appalachian, and Canadian Shield study areas and (b) the Grenville, Churchill, and Superior province study areas; error bars correspond in length to two standard errors.

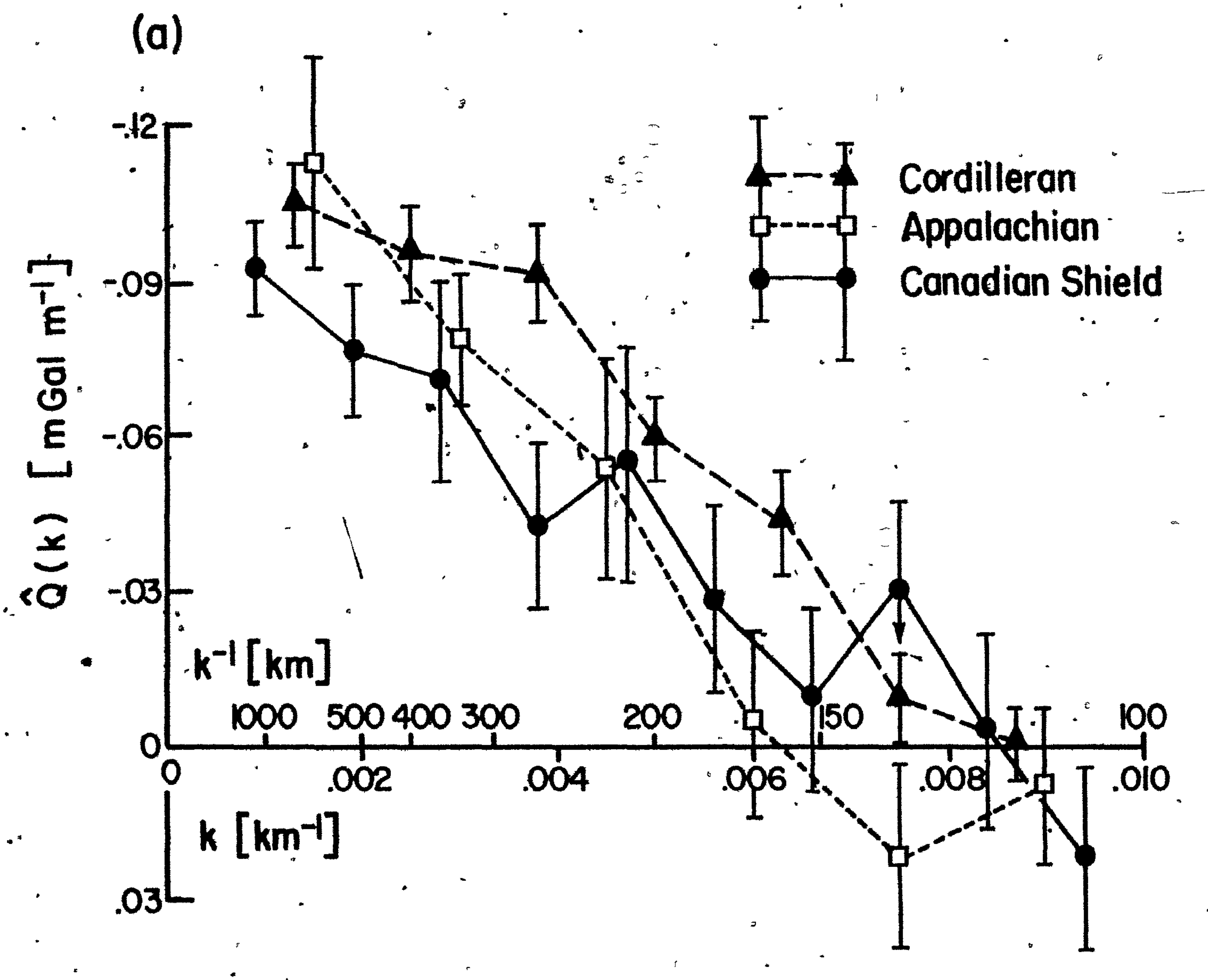
(a)
Cordilleran
Appalachian
Canadian Shield
Q̂(k) [mGal m⁻¹]
-.12
-.09
-.06
-.03
0
.03
k⁻¹ [km]
1000
500
400
300
200
150
100
0
.002
.004
.006
.008
.010
k [km⁻¹]

(b)

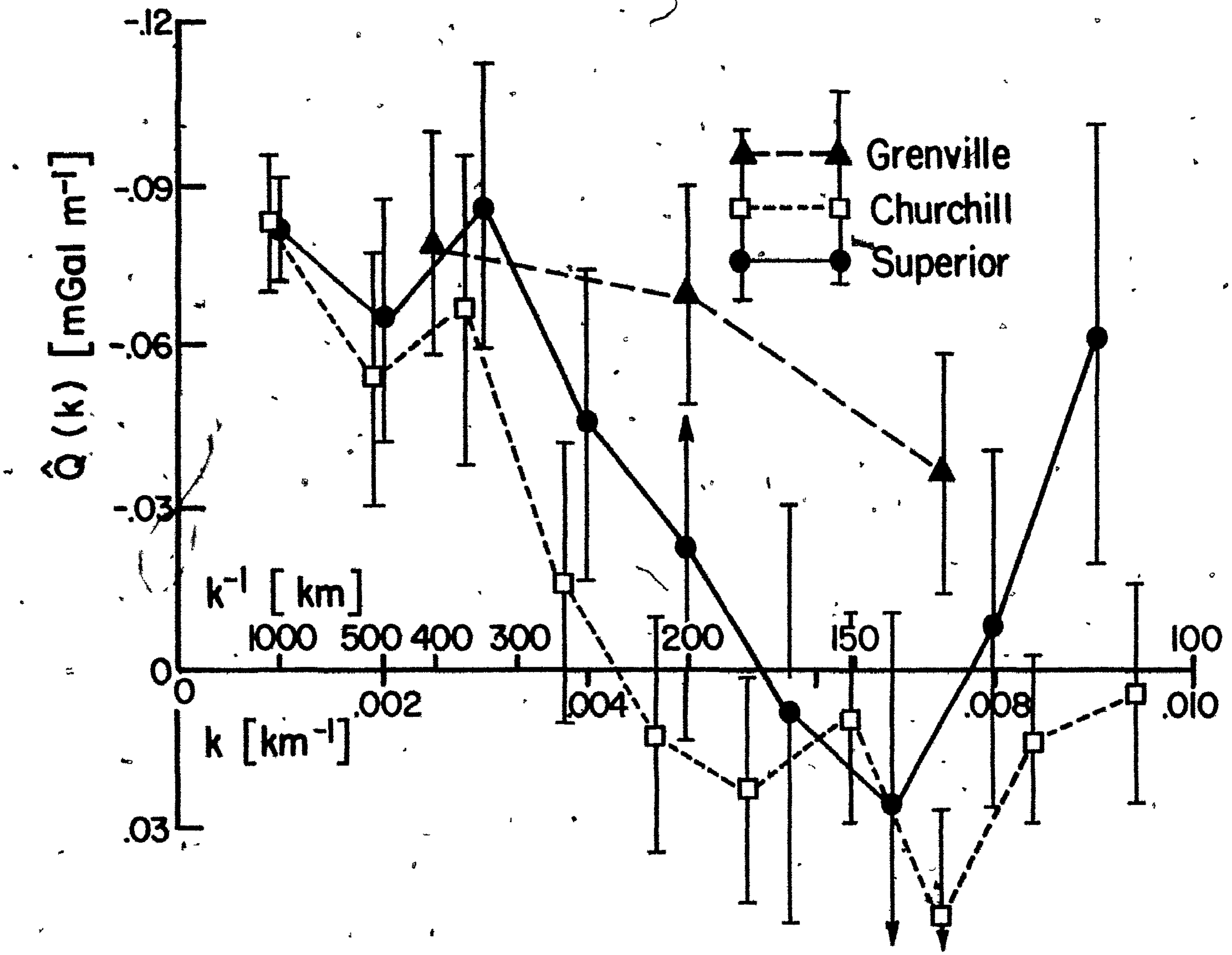

Grenville
Churchill
Superior
$\hat{Q}(k)$ [mGal m^{-1}]
-.12
-.09
-.06
-.03
0
.03
k^{-1} [km]
1000 500 400 300 200 150 100
0
.002
.004
.008
.010
k [km^{-1}]

Table 3-1. Results: ensemble wavenumber [k_r], wavelength [k_r^{-1}], number of ensemble raw spectral data [m_r], isostatic response estimate [$\hat{Q}(k_r)$], standard error of $\hat{Q}(k_r)$[$d\hat{Q}(k_r)$], unbiased coherence squared estimate [$\hat{\gamma}^2(k_r)$].

k_r[km^{-1}]	k_r^{-1}[km]	m_r	$\hat{Q}(k_r)$[mGal m^{-1}]	$d\hat{Q}(k_r)$	$\hat{\gamma}^2(k_r)$
(a) Cordilleran region.					
0	-	1	-0.113	-	-
0.0013	800	10	-0.105	0.008	0.93
0.0025	400	28	-0.097	0.009	0.85
0.0037	267	36	-0.092	0.009	0.78
0.0050	200	59	-0.060	0.008	0.57
0.0063	160	62	-0.044	0.010	0.21
0.0075	133	91	-0.010	0.009	0.02
0.0087	114	90	-0.001	0.007	0
(b) Appalachian region.					
0	-	1	-0.055	-	-
0.0015	667	14	-0.113	0.020	0.64
0.0030	333	38	-0.079	0.013	0.42
0.0045	222	58	-0.054	0.021	0.07
0.0060	167	80	-0.005	0.018	0
0.0075	133	98	0.021	0.018	0.01
0.0090	111	124	0.007	0.015	0
(c) Canadian Shield.					
0	-	1	-0.108	-	-
0.0009	1067	10	-0.093	0.009	0.90
0.0019	533	28	-0.077	0.013	0.46
0.0028	356	42	-0.071	0.020	0.16
0.0037	267	60	-0.043	0.016	0.09
0.0047	213	62	-0.055	0.023	0.05
0.0056	178	91	-0.029	0.018	0.01
0.0066	152	90	-0.010	0.018	0
0.0075	133	111	-0.031	0.017	0.01
0.0084	119	124	-0.004	0.019	0
0.0093	107	141	0.021	0.018	0

Table 3-1, continued.

$k_r[km^{-1}]$	$k_r^{-1}[km]$	m_r	$\hat{Q}(k_r)[mGal\ m^{-1}]$	$d\hat{Q}(k_r)$	$\hat{\gamma}^2(k_r)$
(d) Grenville province.					
0	–	1	−0.106	–	–
0.0025	400	15	−0.079	0.021	0.55
0.0050	200	44	−0.070	0.021	0.17
0.0075	133	60	−0.037	0.022	0.04
(e) Churchill province.					
0	–	1	−0.107	–	–
0.0009	1067	10	−0.083	0.013	0.79
0.0019	533	12	−0.054	0.025	0.18
0.0028	356	26	−0.067	0.029	0.10
0.0037	267	26	−0.016	0.026	0
0.0047	213	40	0.012	0.022	0
0.0056	178	42	0.022	0.021	0.02
0.0066	152	58	0.009	0.019	0
0.0075	133	48	0.046	0.020	0.06
0.0084	119	74	0.013	0.015	0.01
0.0093	107	64	0.004	0.020	0
(f) Superior province.					
0	–	1	−0.106	–	–
0.0010	1000	11	−0.082	0.010	0.82
0.0020	500	20	−0.065	0.023	0.19
0.0030	333	30	−0.086	0.027	0.19
0.0040	250	40	−0.046	0.029	0.02
0.0050	200	44	−0.023	0.035	0
0.0060	167	57	0.008	0.039	0
0.0070	143	66	0.025	0.036	0
0.0080	125	75	−0.008	0.033	0
0.0090	111	86	−0.061	0.041	0.01

functions of the Canadian Shield, where the topographic signal is smallest, are, on the other hand, very large. The Canadian Shield study area isostatic response function [Figure 3-3(a)], which is, in most part, based on gravity and topography data also used to calculate the individual response functions of the Grenville, Churchill, and Superior structural provinces [cf. Figure 2-1], would be expected to have features similar to those of the three smaller study areas. This is the case for estimates at small wavenumbers, $k<0.004\ \mathrm{km}^{-1}$; for larger k the Churchill and Superior observations are exceptionally noisy, and within the bounds of the indicated standard errors are generally not different from zero. The observed isostatic response of the larger Canadian Shield study area, in contrast, falls off to zero less rapidly and lies between the Churchill/Superior data and those of the Grenville province. The data illustrated in Figures 3-3(a,b) are enumerated in Tables 3-1(a-f); small values of the unbiased coherence squared $\hat{\gamma}^2(k)$ testify to the high noise levels of the Bouguer gravity data. Also listed in Tables 3-1(a-f) are k=0 estimates of the observed isostatic response based on the average Bouguer anomaly [geoid removed; cf. subsection 2.2.1] and topographic height of each region.

The general character of all of the calculated $\hat{Q}(k)$ are similar. (1) As $k\to 0$, $\hat{Q}(k)\to -.11$ mGal which equals $-2\pi\Gamma\rho_0$, the value predicted by the theoretical isostatic response of a thin elastic plate [Equation (3-11)]. Γ is the gravitational constant and $\rho_0 = 2700\ \mathrm{kg\ m}^{-3}$, the density of the topography. Large negative values of $\hat{Q}(k)$ for small k are a consequence of the gravity effect of low density crustal "roots" providing complete or nearly complete isostatic compensation of topography at these wavelengths. The contrasting gravitational attraction of the topography itself has been removed by means of the Bouguer gravity reduction. The actual k=0 estimates of $\hat{Q}$ listed in Table 3-1 are not considered in the interpretation of the response functions, in contrast with Banks et al. [1977], on the grounds that they can provide no information about the density and rheological structure of the lithosphere. (2) As k increases, $\hat{Q}(k) \to 0$, which also corresponds to the theoretical result [Equation (3-11)]. This happens if there is little or no isostatic compensation of topography of short wavelengths either because the flexural strength of the lithosphere is too great or because the gravity effects of any existing compensating density structures, measured at the Earth's surface, have been attenuated because of their depths.

3.3.2 General characteristics of the elastic plate model of isostatic response. The theoretical isostatic response of a thin elastic plate $Q_e(k)$, described by Equation (3-11), is a function of the integration to the base of the lithosphere T_L of the vertical density gradient $\partial\rho/\partial z$ of the lithosphere. If $\partial\rho/\partial z$ comprises a series of discrete density jumps rather than a continuous function, then (3-11) can be rewritten as

$$Q_e(k) = -2\pi\Gamma \frac{\rho_o}{\Delta\rho} \psi'(k) \sum_{i=1}^{N_L} \rho_i \exp\,[-2\pi k z_i] \tag{3-18}$$

where N_L is the number of vertical density discontinuities in the lithosphere and $\Delta\rho=\rho_m-\rho_o$, the difference between the lithosphere substratum and topographic densities. Note that, to maintain internal consistency, it is necessary that

$$\sum_{i=1}^{N_L} \rho_i = \Delta\rho \tag{3-19}$$

A simple and common assumption is that $N_L=1$ such that surface topography is isostatically compensated by the deformation of a single density interface presumed to be the Mohorovicic discontinuity, found at the base of the crust. Its existence is based on deep structural seismic refraction studies [e.g. Goodacre 1972]. Thus, Equation (3-18) reduces to the form

$$Q_e(k) = -2\pi\Gamma\ \rho_0\ \psi'(k)\ \exp\ [-2\pi k z_m] \tag{3-20}$$

where z_m is the depth of the compensation density structure. Clearly, the inclusion of the effects of other major density interfaces, such as the mid-crustal Conrad or Riel discontinuity which is believed to exist within the crust of the Canadian Shield and west-central Canada [e.g. Thomas et al. 1978, Green et al. 1979], can be easily accommodated.

The shape of the theoretical isostatic response function of a thin elastic plate, as it varies with k, depends strongly on the choice of z_m as well as on the chosen flexural rigidity D of the plate and these dependencies are illustrated in Figure 3-4. Recall that $\psi'(k)$ [in Equation (3-20)], which varies in the range 0 to 1, increases as D decreases [cf. Equation 3-4ii)] and is unity when D=0 such that topography is in a state of local isostatic compensation [subsection 3.2.3]. In such a case, as shown in Figure 3-4, the response function behaves as a simple exponentially decaying curve, the decay rate of

Figure 3-4. Theoretical isostatic response functions $Q_e(k)$ of the thin elastic plate model; model parameters as shown.

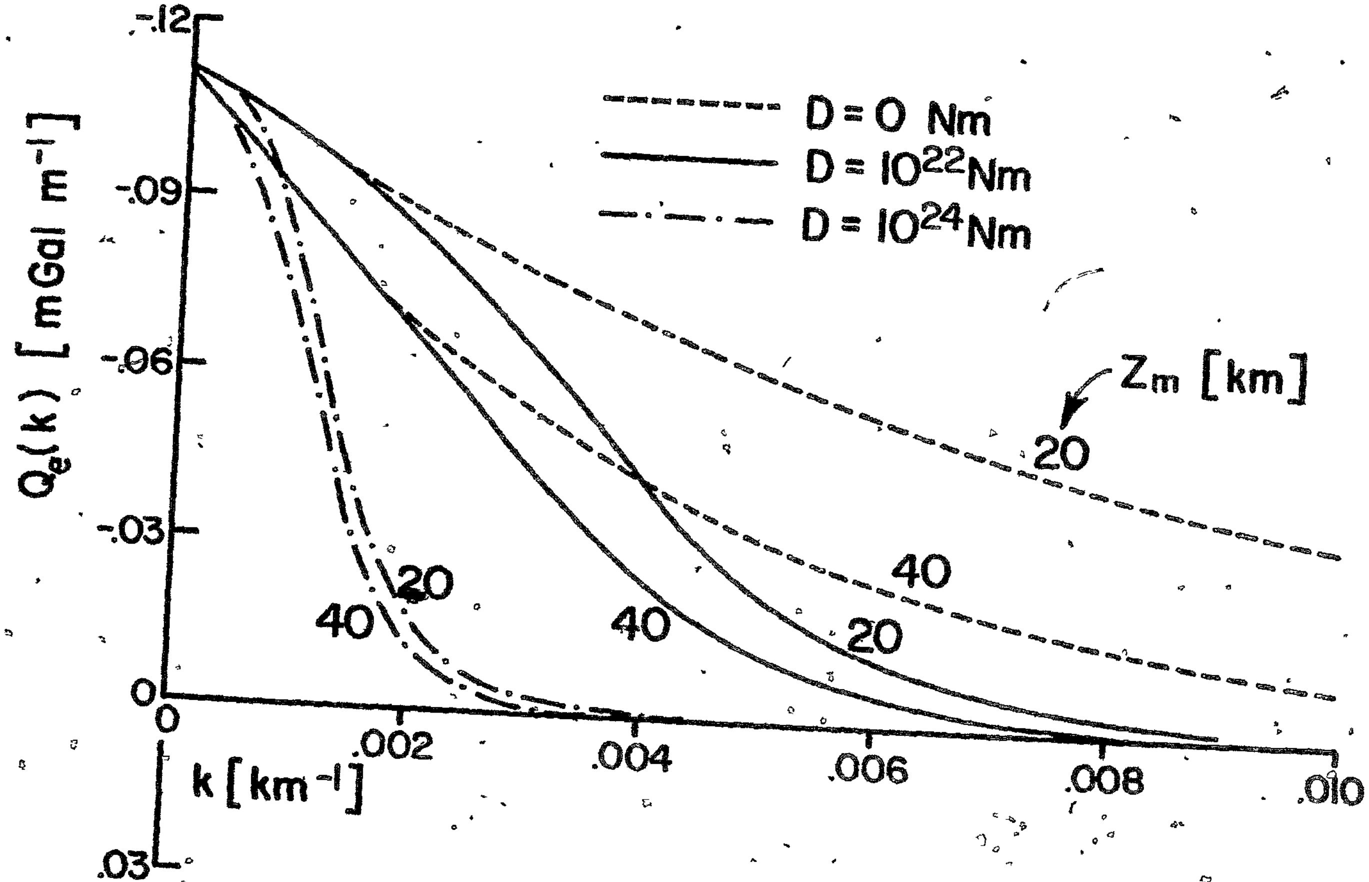

-.12
-.09
-.06
-.03
0
.03
0
.002
.004
.006
.008
.010
Qe(k) [mGal m-1]
k [km-1]
D = 0 Nm
D = 10^22 Nm
D = 10^24 Nm
Zm [km]
20
40
20
40
40
20
20
40

which is determined by the compensation depth z_m. As D increases, so that isostatic compensation is regional rather than local, $Q_e(k)$ falls off at smaller k in a fashion which is characteristically non-exponential.

The ambiguity inherent to the interpretation of observed isostatic response functions because of the co-dependence of the theoretical curves on compensation depth and flexural rigidity has been discussed by Cochran [1980] and McNutt [1980]. For example, Cochran argues that United States [Lewis and Dorman 1970] and Australian [McNutt and Parker 1978] isostatic response data can be interpreted to show that D for each region is similar with as much justification as McNutt and Parker's [1978] interpretation that Australian D was significantly lower. Cochran, in his analysis, emphasized adjustments of z_m within reasonably expected bounds of crustal thickness. McNutt [1980], on the other hand, argues that consideration of the nature of the curvature of observed $\hat{Q}(k)$ in the middle wavelength fall-off region is most important in determining flexural rigidity.

3.3.3 Results. Visual inspection of the observed isostatic response functions [Figures 3-3(a,b)] suggests that there may be systematic changes in their character as the age of the geological province from which they are derived varies. With respect to the Cordilleran, Appalachian, and Churchill province response functions, the older the geology, the more rapidly $\hat{Q}(k)$ falls off to zero values. Greater errors $d\hat{Q}(k)$ and smaller coherences $\hat{\gamma}^2(k)$ accompany the enhanced fall-off of $\hat{Q}(k)$ as age increases. The coherence between gravity and topography, at all but the smallest wavenumbers, in all regions except the Cordilleran region, is very small [cf. Table 3-1] although no smaller than that reported for Australia [McNutt 1978, p. 106] or presumably that of the United States [unreported]. The possibilities that the fall-off of observed isostatic response functions, the character of which is crucial to their interpretation, is controlled by the geological noise in the gravity data relative to the power of the topographic signal, and that the true isostatic response function in such a case is not resolvable, cannot be dismissed.

This caution notwithstanding, observed $\hat{Q}(k)$ have been compared to model predictions in terms of the one-norm misfit between them. The one-norm misfit is a measure of misfit which takes into account the error associated with the observations, and is defined as

$$M_Q = \sum_{r=1}^{N_k} \left| \frac{Q_e(k_r) - \hat{Q}(k_r)}{d\hat{Q}(k_r)} \right| \tag{3-21}$$

where N_k is the number of observed ensemble estimates in $\hat{Q}(k)$. M_Q is plotted as a function of flexural rigidity D and various compensation depths z_m, for each of the six study areas, in Figures 3-5(a-f); theoretical $Q_e(k)$ are calculated using Equation (3-20) in which it has been assumed that ρ_o and ρ_m are 2700 and 3300 kg m^{-3} respectively. These densities are in the ranges of those customarily assigned to upper crustal and mantle material; moreover, Banks et al. [1977] have shown that the results of comparisons of isostatic response data to those derived from the elastic plate model are not sensitive to the choice of ρ_o and ρ_m provided the choices are within geophysically reasonable bounds. Misfits M_Q were evaluated for each study area for D=0 as well as for values of D in the range 10^{18}–10^{28} Nm incrementing by powers

Figure 3-5. One-norm misfits M_Q between isostatic response observations and models [Equation (3-21)] having the indicated parameter values for the (a) Cordilleran, (b) Appalachian, (c) Canadian Shield, (d) Grenville, (e) Churchill, and (f) Superior study areas.

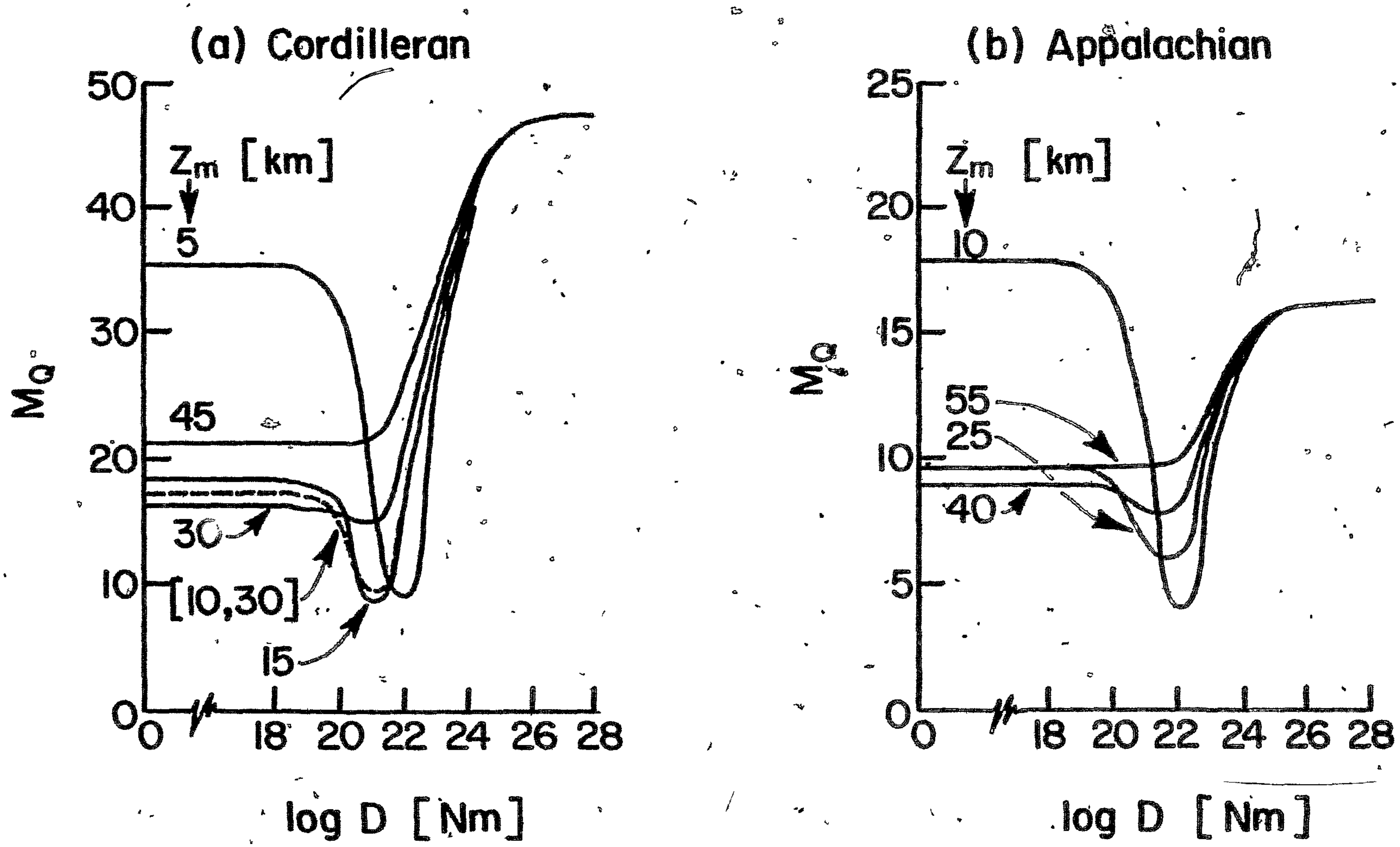
(a) Cordilleran
M_a
Z_m [km]
5
45
30
[10,30]
15
log D [Nm]
(b) Appalachian
M_a
Z_m [km]
10
55
25
40
log D [Nm]

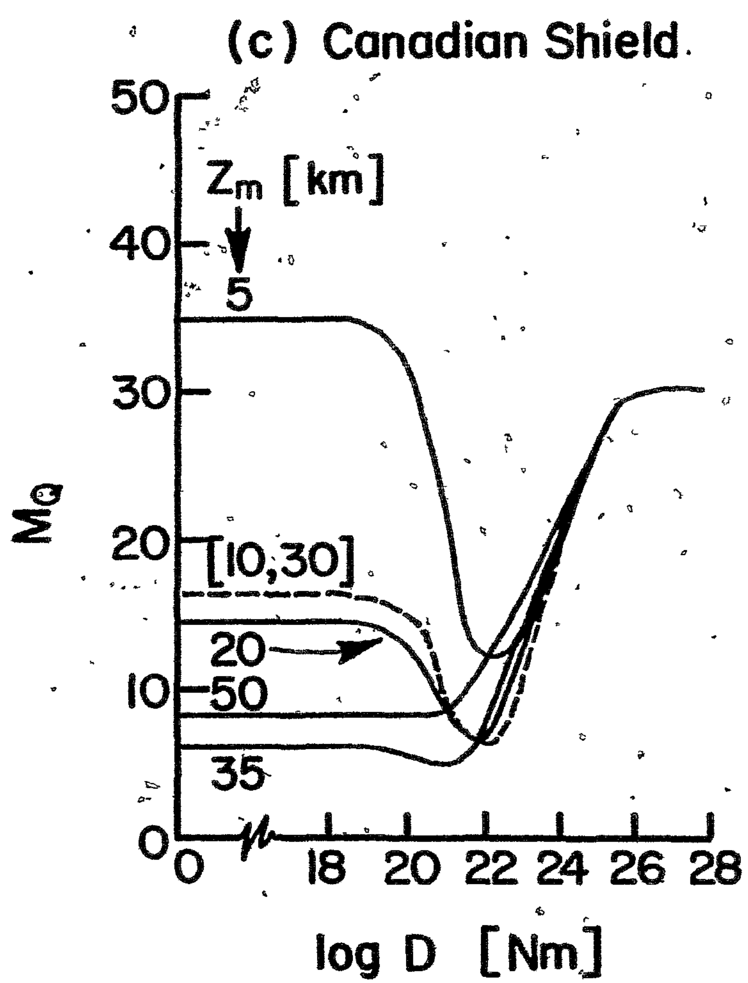
(c) Canadian Shield.
50
40
30
20
10
0
Z_m [km]
5
[10,30]
20
50
35
M_Q
0
18
20
22
24
26
28
log D [Nm]
(d) Grenville
10
8
6
4
2
0
Z_m [km]
40
10
[5,30]
25
M_Q
0
18
20
22
24
26
28
log D [Nm]

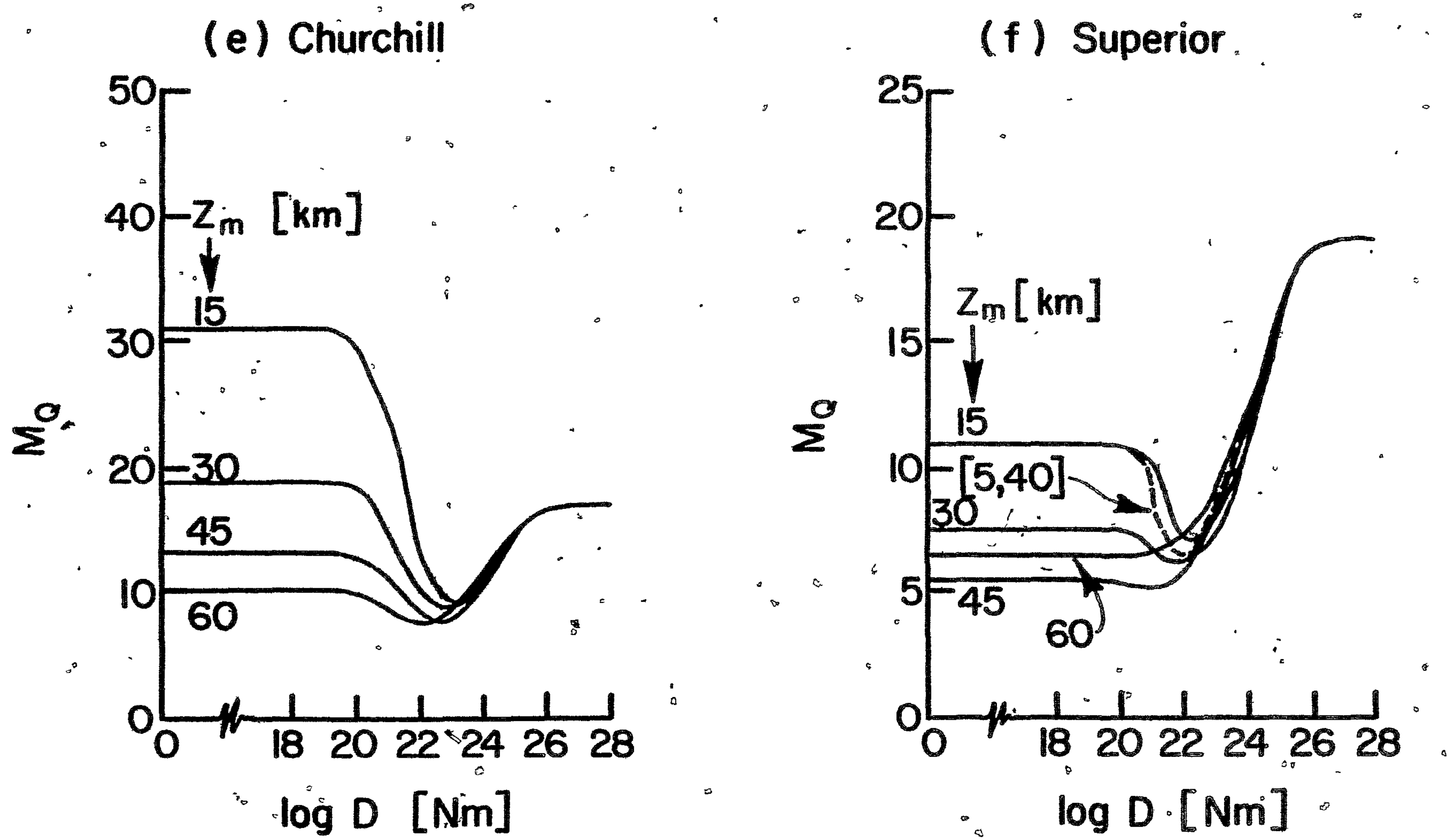
(e) Churchill
(f) Superior
M_Q
Z_m [km]
15
30
45
60
[5,40]
log D [Nm]
0
18
20
22
24
26
28
10
20
30
40
50
5
15
25

of 10. The compensation depth z_m was varied in the range 5–60 km incrementing by 5 km. Results for several sample values of z_m, within this range, including the value of z_m which provided the overall minimum M_Q, are incorporated into Figures 3-5(a-f). The theoretical isostatic response functions $Q_e(k)$ of the thin elastic plate model, calculated for the minimum misfit $[D, z_m]$ pairs, as illustrated in Figures 3-5(a-f) for each study area, are plotted in Figures 3-6(a-f) where they can be compared to the observed $\hat{Q}(k)$.

Examination of Figures 3-5(a-f) reveals that, for all data sets, as z_m becomes deeper the maximum flexural rigidity at which the smallest M_Q occurs decreases by about one order of magnitude. Concurrently, as compensation depth increases, the misfit results become progressively less sensitive to choice of D. The reason for this feature of the results can be seen in Figure 3-4, in which theoretical isostatic response functions are plotted: there is relatively greater displacement of the theoretical z_m=20 km curve than the z_m=40 km curve as D increases from 0 to 10^{24} Nm for each. Thus, as z_m increases there is less ability to distinguish among D.

The misfit results of Figures 3-5(a-f), taken as a whole, indicate that the reproduction of isostatic response observations by the thin elastic plate model is controlled more by the choice of the plate's flexural rigidity D than by its compensation depth z_m. Considering, for example, the Churchill province results [Figure 3-5(e)], a lithospheric flexural rigidity in this region of 10^{22}–10^{23} Nm is indicated regardless of the choice of z_m while, conversely, there is little reason to choose among z_m. Other sets of results, such as those

Figure 3-6. Comparison of observed isostatic response functions $\hat{Q}(k)$ with response functions $Q_e(k)$ of the elastic plate model for the (a) Cordilleran, (b) Appalachian, (c) Canadian Shield, (d) Grenville, (e) Churchill, and (f) Superior study areas; model parameters as shown; choice of parameters explained in the text.

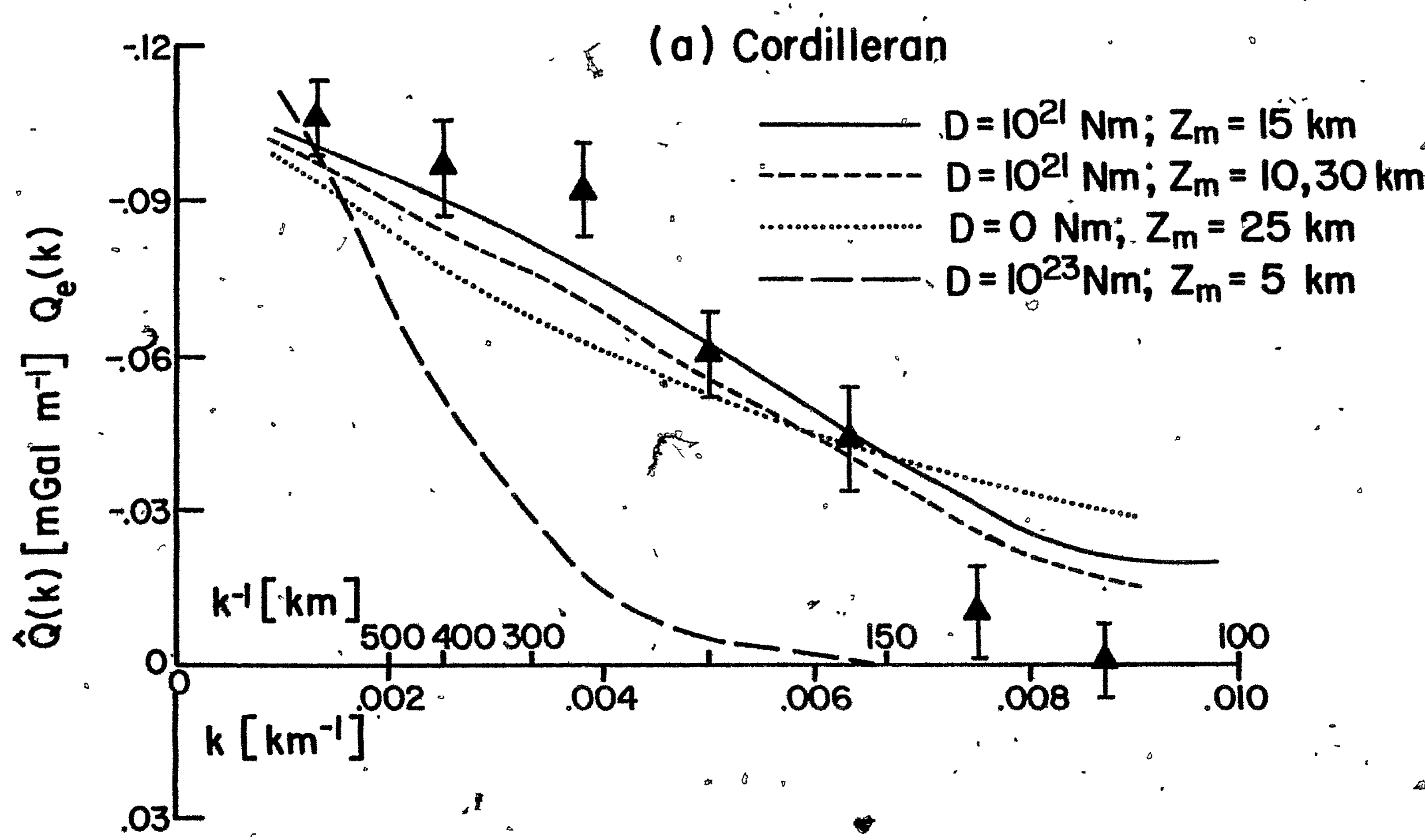
(a) Cordilleran
D = 10^21 Nm; Z_m = 15 km
D = 10^21 Nm; Z_m = 10,30 km
D = 0 Nm; Z_m = 25 km
D = 10^23 Nm; Z_m = 5 km
Q̂(k) [mGal m^-1] Q_e(k)
-.12
-.09
-.06
-.03
0
.03
k^-1 [km]
500 400 300
150
100
k [km^-1]
.002
.004
.006
.008
.010

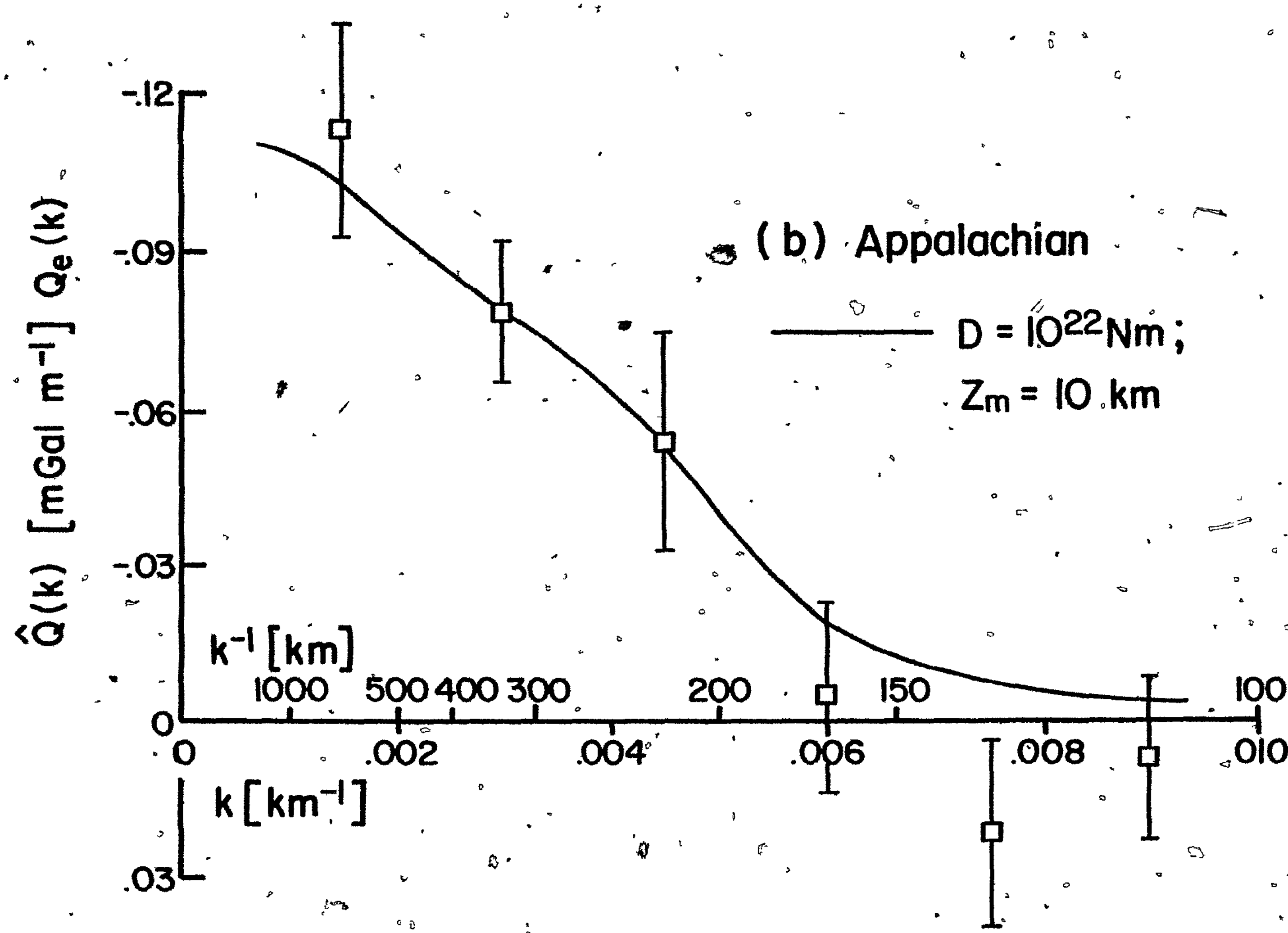

(b) Appalachian
D = 10^22 Nm;
Zm = 10 km
Q̂(k) [mGal m^-1] Qe(k)
-.12
-.09
-.06
-.03
0
.03
k^-1 [km]
1000 500 400 300 200 150 100
0 .002 .004 .006 .008 .010
k [km^-1]

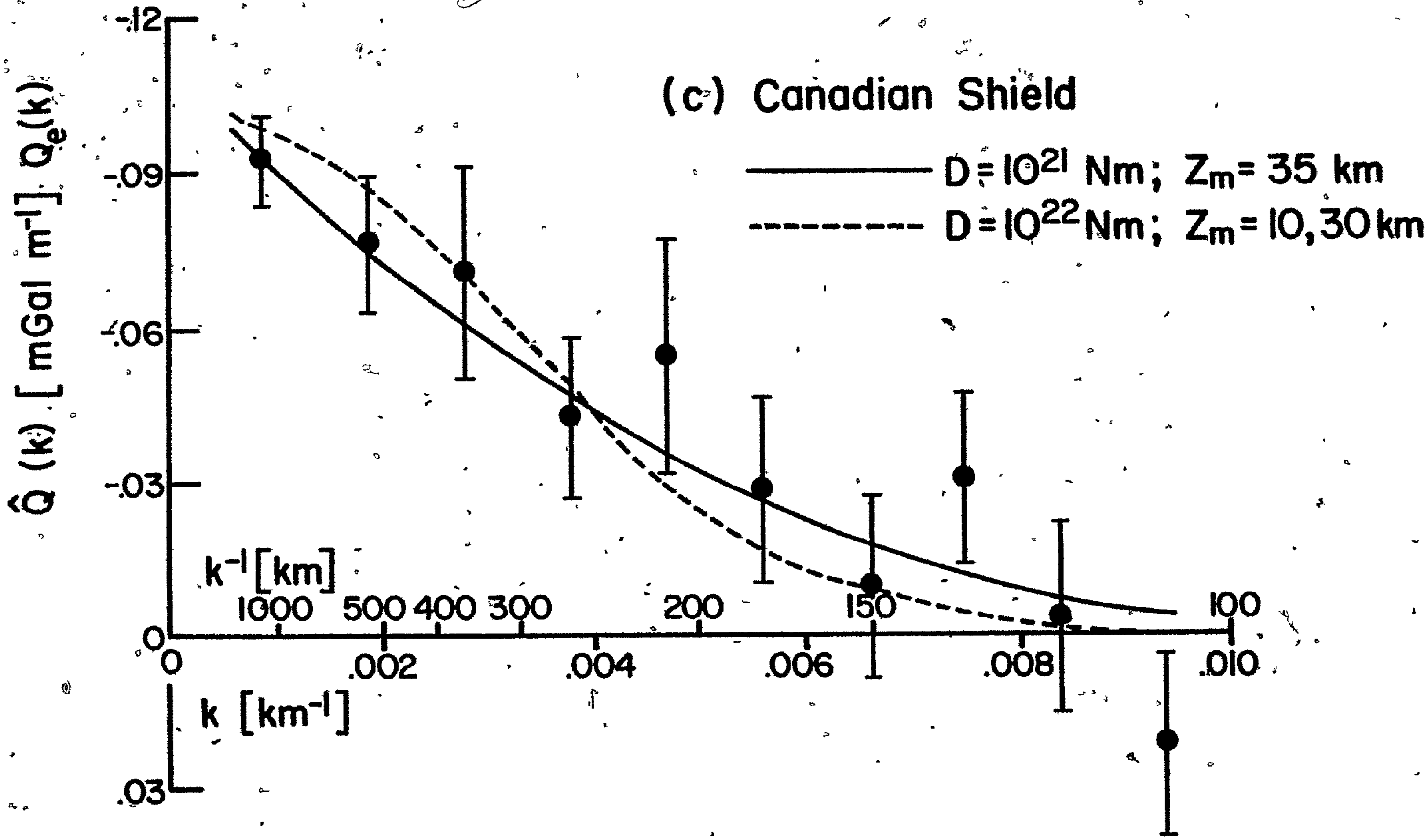
(c) Canadian Shield
D = 10^21 Nm; Zm = 35 km
D = 10^22 Nm; Zm = 10, 30 km
Q̂ (k), [mGal m^-1], Qe(k)
-.12
-.09
-.06
-.03
0
.03
k^-1 [km]
1000
500
400
300
200
150
100
0
.002
.004
.006
.008
.010
k [km^-1]

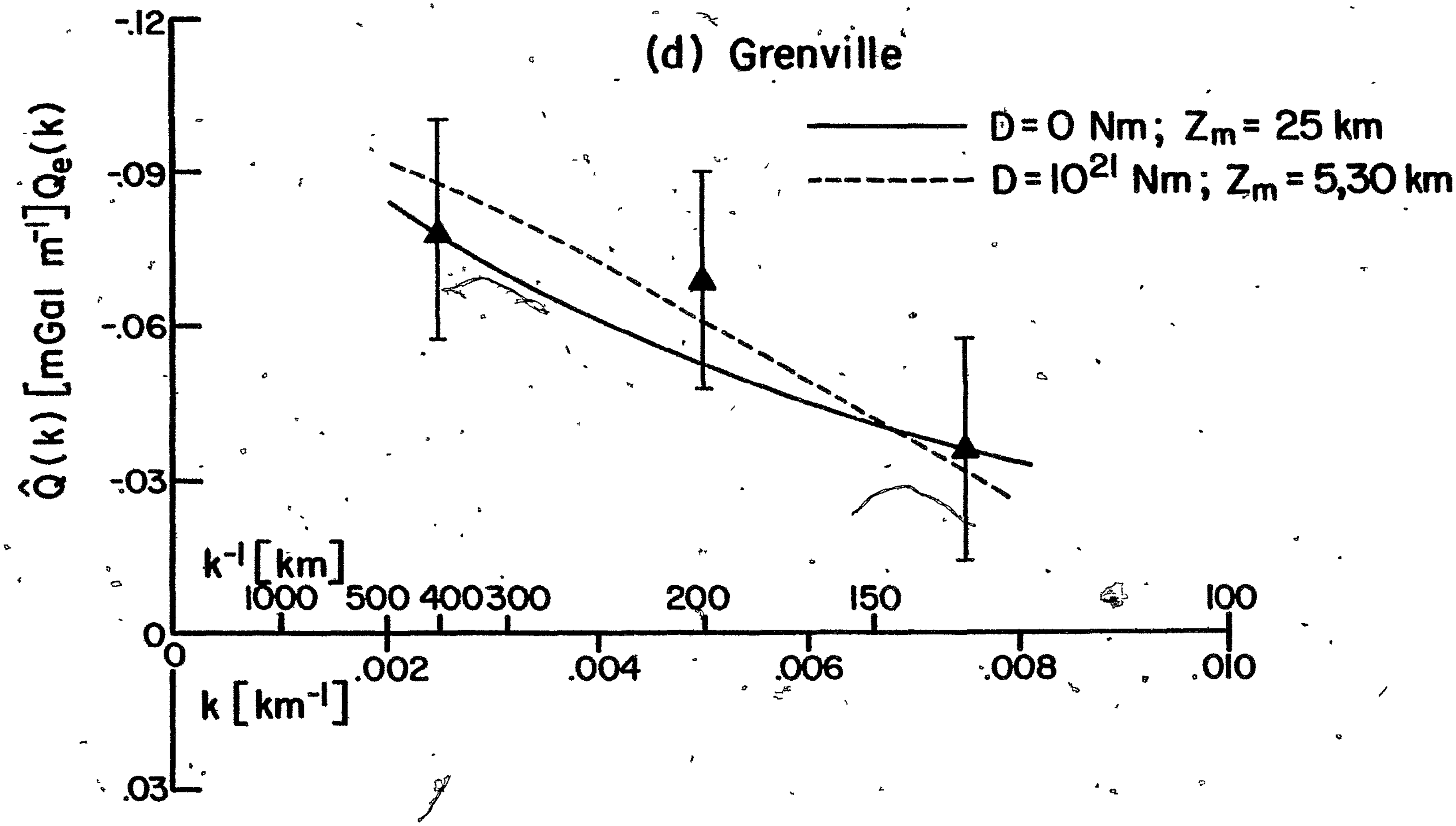
(d) Grenville
D = 0 Nm; Z_m = 25 km
D = 10^{21} Nm; Z_m = 5,30 km
$\hat{Q}(k)$ [mGal m^{-1}] $Q_e(k)$
-.12
-.09
-.06
-.03
0
.03
k^{-1} [km]
1000 500 400 300 200 150 100
k [km^{-1}]
0 .002 .004 .006 .008 .010

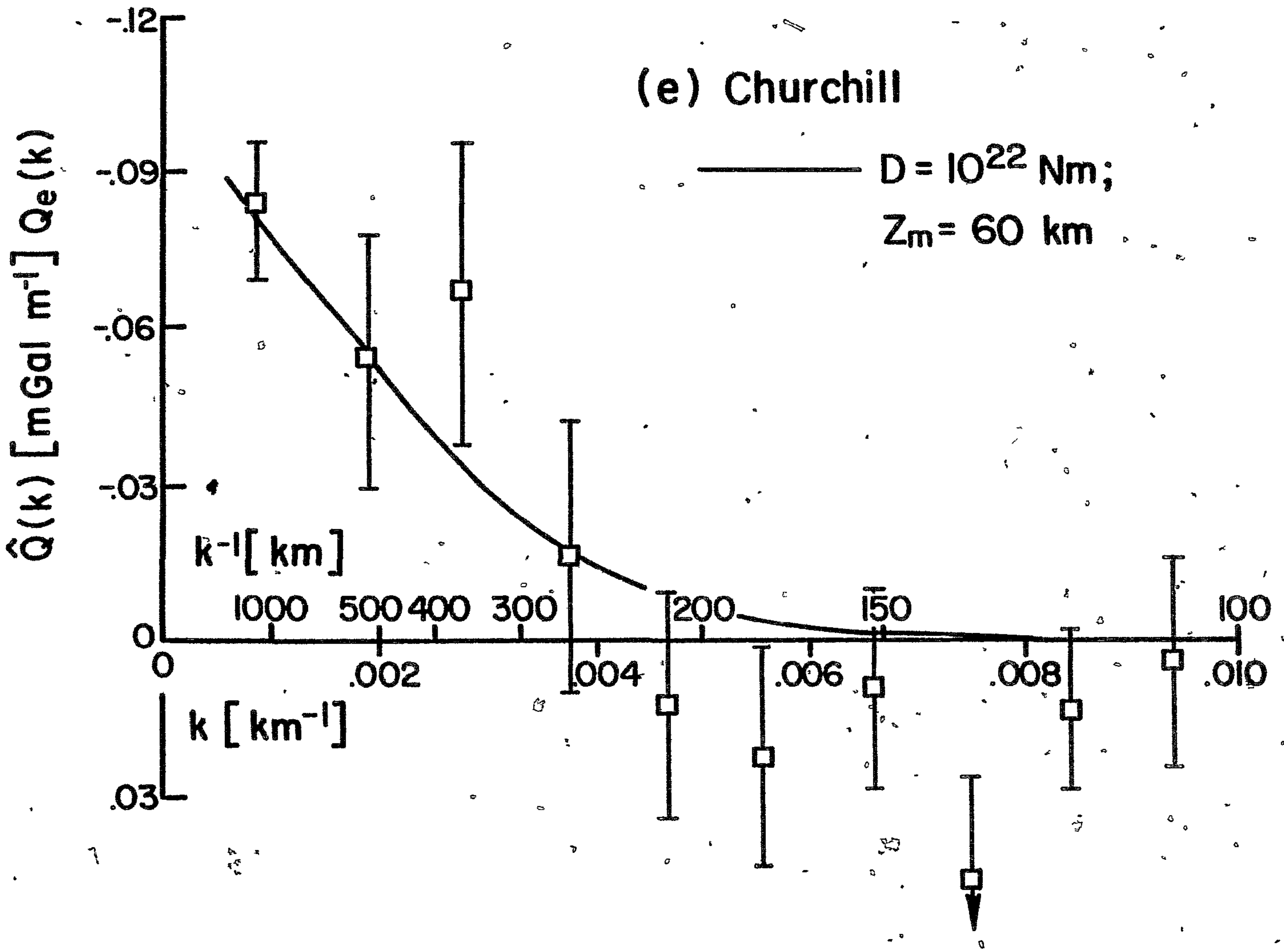
(e) Churchill
D = 10^{22} Nm;
Z_m = 60 km
$\hat{Q}(k)$ [mGal m^{-1}] $Q_e(k)$
-.12
-.09
-.06
-.03
0
.03
k^{-1} [km]
1000
500
400
300
200
150
100
0
.002
.004
.006
.008
.010
k [km^{-1}]

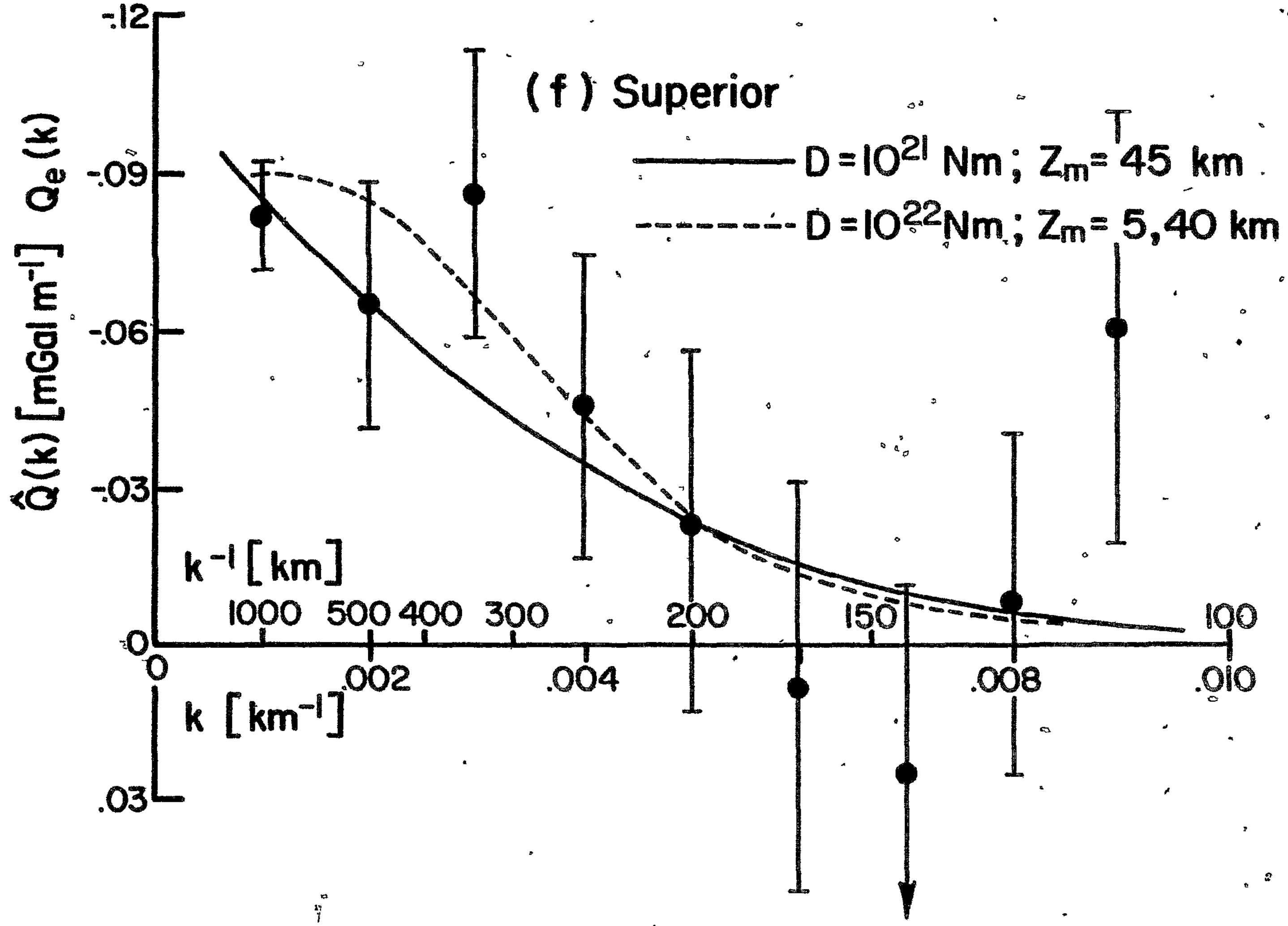
(f) Superior
D = 10^{21} Nm ; Z_m = 45 km
D = 10^{22} Nm ; Z_m = 5,40 km
$\hat{Q}(k)$ [mGal m^{-1}] $Q_e(k)$
-.12
-.09
-.06
-.03
0
.03
k^{-1} [km]
1000 500 400 300 200 150 100
0
.002
.004
.008
.010
k [km^{-1}]

of the Cordilleran region, show increased sensitivity to choice of z_m but never so much as to require changes in D greater than one order of magnitude.

This feature of the results suggests that comparisons of the observations to theoretical functions based on models in which more complex density structures are assumed to exist will not yield significantly different best-fitting choices of D. This proved to be the case for the observations considered in the light of models in which a mid-crustal Conrad density discontinuity was incorporated. No such model could produce a misfit as small as those already available from the single layer models and in all cases best fits were obtained for D falling within the range of values indicated by the single layer models. On the other hand, the acceptance or rejection of a two-layered model as opposed to one with a single compensation depth can be crucial in determining whether the isostatic response within a given region is achieved by means of regional, or flexural, compensation as opposed to local compensation. Such a result is intuitive for regions for which the single layer misfit data [Figures 3-5(a-f)] indicate a distinct regional response for shallow z_m but one which is not significantly better than that provided by local compensation at compensation depths approaching normal crustal thickness [~30-50 km]. All of the data sets under consideration have this characteristic with the exception of those of the Churchill and, to a slightly lesser extent, the Appalachian study areas. The misfits, as they vary with D, for arbitrarily chosen sample two layer models for each of the other four study areas are indicated by the dashed lines in the appropriate diagrams of Figure 3-5; the best-fitting theoretical isostatic response functions of these two layer models are plotted using dashed lines where appropriate in Figures 3-6. It should be noted that additional model complexities such as the two layer modification are not justified in the case of the Grenville data from which only three response estimates were available.

3.4 Discussion

3.4.1 Acceptability of results. The acceptability of the thin elastic plate model of isostatic response, in which the plate is loaded only by modern topography, can be judged on the basis of the existence of systematic, rather than random, deviations between the observations and their best-fitting modelled isostatic response functions. Allowing for errors associated with each of the observations, no strongly evidenced systematic lack of fit, with the exception of the Cordilleran results, is apparent from visual inspection of Figures 3-6(a-f).

In the case of the Cordilleran data, non-random effects do occur: at low wavenumbers the observations are consistently under-estimated by the theoretical response of the best-fitting model while at the highest wavenumbers the reverse occurs. Moreover, no elastic plate model, regardless of its chosen parameters or compensation depth(s) overcomes this systematic lack of fit. To illustrate this fact, also plotted in Figure 3-6(a), using dotted and dashed-dotted lines respectively, are the theoretical isostatic response functions of elastic plates which are much weaker [D=0 Nm, so that topographic isostatic compensation is local] and much stronger [$D=10^{23}$ Nm] than those indicated by the best-fitting one and two layer models [$D=10^{21}$ Nm]. Each model is single layered and the chosen compensation depths, 25 km and 5 km respectively, are those which produced the minimum misfits. That no satisfactory fit to the Cordilleran observations can be obtained by modification of the model parameters D and z_m suggests that a thin elastic plate may be an inadequate model of the lithosphere in this region or that the loading of the lithosphere, the effects of which are being measured by the isostatic response function, is more complex here than that resulting from the contemporary topography only. With respect to the latter hypothesis, it is noted that much of the United States portion of the Cordilleran study area is characterized by anomalously high heat flow [Sclater et al. 1980] implying the possible existence of thermal loading at the base of the lithosphere. Therefore, the failure of the present model to reproduce the character of the Cordilleran results is not taken as sufficient reason to reject the model.

3.4.2 Tectonic age variations and observed isostatic response functions. As noted in subsection 3.3.3, there are substantial differences between the observed isostatic response functions of the various geological provinces sampled. The model being tested in the present chapter is one in which observed isostatic response functions $\hat{Q}(k)$ are assumed to be the result of a thin elastic plate, of time-invariant properties, being loaded by modern topography. There are two unknown model parameters: compensation depth z_m and the flexural rigidity of the plate D. Since, under the terms of the model, D should not vary between geological provinces, the proposed test of the model was that differences between the observed response functions should best be explained by variations in z_m and that the indicated z_m should be geophysically reasonable. The implications of the results of two layer models are discussed first after which one layer models are considered.

(i) Two layer models. The ambiguity inherent to the interpretation of isostatic response functions in terms of the elastic plate model was anticipated in subsection 3.3.2 in which the general characteristics of the model predictions were analyzed and in subsection 3.3.3 in which two layer crustal models, which provided misfits with the observations not substantially greater than those provided by the best-fitting one layer models, were presented. Nevertheless, as noted in subsection 3.3.3, other than allowing all of the observed data to be reproduced by models with reasonable compensation depths and flexural rigidities clearly favouring regional rather than local isostatic compensation of topography [cf. Figures 3-5(a,c,d,f)], the consideration of two layer models did not greatly change the one layer results in terms of the minimum range of values of D required to model the response functions of all study areas.

The choice of compensation depths in two layer models, within the domain of geophysically reasonable choices, is necessarily arbitrary. Seismic refraction results [e.g. Goodacre 1972] provide estimates which pertain only to local areas of each geological province and cannot justifiably be used to adopt particular crustal density configurations; moreover, they are themselves only models of the true density structure of the crust. The results of Backus-Gilbert inversion of isostatic response functions do not resolve major density interfaces, assuming they exist, and are not realistic because they predict significant density inversions below the crust [Banks et al. 1977, McNutt 1978]. Inversion of response functions using a linear programming method in which the density gradient is constrained to be positive cannot mathematically provide solutions more complex than those with a single "Mohorovicic" density discontinuity [Banks et al. 1977, Banks and Swain 1978, McNutt 1978]. In this sense, it is nothing more than a very efficient method of finding best-fitting one layer "forward" models such as those presented in subsection 3.3.3.

It follows from the non-uniqueness inherent to the interpretation of gravity anomalies, of which isostatic response functions are derivative, that, for each of the data sets, any number of well-fitting models based on progressively more complex lithospheric density configurations could be found. The maximum choices of flexural rigidities allowed by such models can be judged on the basis of the misfit data presented in Figures 3-5(a-f) and they vary from about 5×10^{21} Nm for the Grenville province to perhaps 5×10^{24} Nm for the Churchill. The minimum, with the possible exception of the Churchill province, is 0 Nm.

(ii) One layer models. It is likely that the number of available observations does not justify the supposition of complex density models. It is therefore probably best to consider the data simply in terms of the best-fitting one layer models, the indicated parameters of which, for each of the study areas, are summarized in Figure 3-7. Any pairs of parameters $[D, z_m]$ which produced misfits within 10% of the minimum misfit are included among those providing the best-fitting models.

Figure 3-7. Summary of parameters, flexural rigidity D and compensation depth z_m, for the best-fitting elastic plate models.

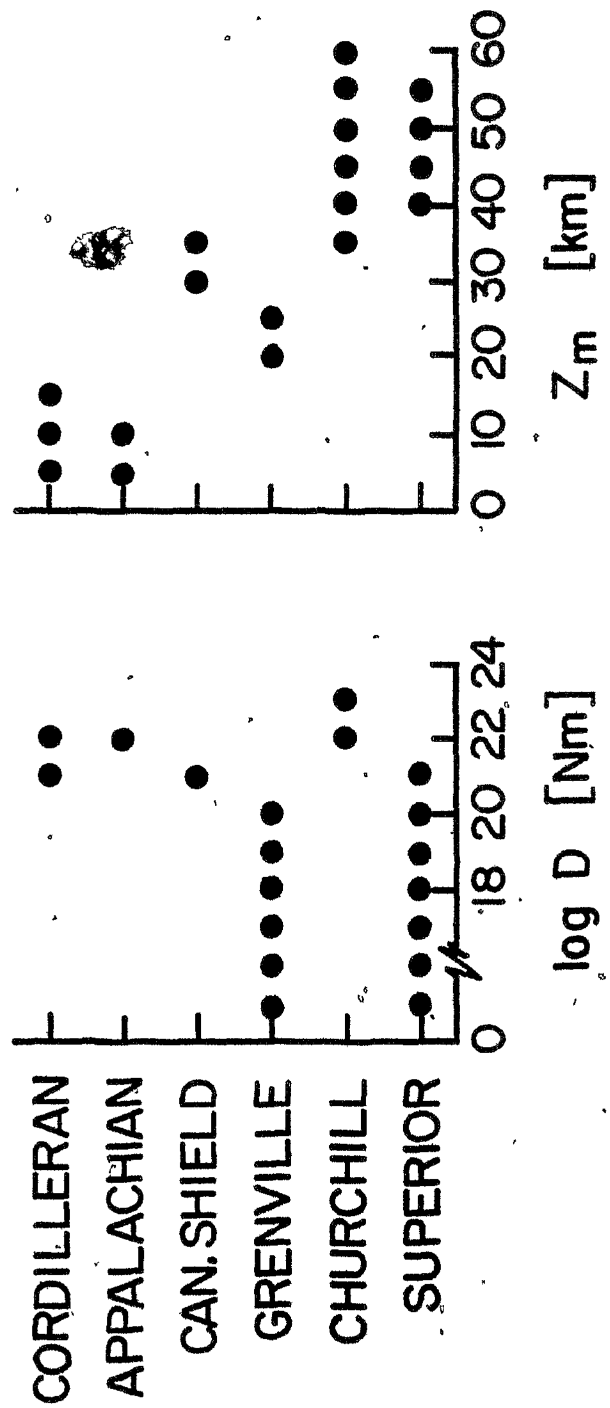

CORDILLERAN
APPALACHIAN
CAN. SHIELD
GRENVILLE
CHURCHILL
SUPERIOR
0
18
20
22
24
log D [Nm]
0
10
20
30
40
50
60
Z_m [km]

Figure 3-7 is constructed according to increasing relative tectonic ages of the study areas from top to bottom; note, however, that the Canadian Shield results are a hybrid of those of the Grenville, Churchill, and Superior regions and that the Grenville results are based on only three $\hat{Q}(k)$ estimates. It can be seen in Figure 3-7 that there is no systematic pattern of variation of the flexural rigidity D among the sampled geological provinces. If D is assumed to be constant its value presumably falls within the range 10^{20}-10^{22} Nm. However, flexural isostatic compensation of topography is strongly indicated for the Cordilleran, Appalachian, and Churchill regions whereas local compensation is acceptable within the Grenville and Superior provinces. On this basis, it is arguable that the flexural rigidity of the lithosphere measured in terms of the present model does vary depending on the lithosphere's tectonic age but that the dependence is not systematic. On the other hand, Figure 3-7 shows that there is a distinct tendency of z_m, as determined by the best-fitting single layer elastic models, to increase as the age of the lithosphere increases. This may be fortuitous; the measured isostatic response of the Cordilleran region may be contaminated by thermal effects as noted in subsection 3.4.1 whereas the shallow compensation depth returned for the Appalachian region, since much of its southern portion is characterized by shallow, compressional tectonics, may be indicative of a density contrast existing between mainly sedimentary supracrustal rocks and the denser orogenic basement complex. Otherwise, the systematic increase in z_m with age may itself be evidence of geodynamic processes such as (1) the downward migration of phase change boundaries as cooling of the lithosphere occurs and/or (2) the sinking of geochemical/petrological boundaries as elastic flexural stresses within the lithosphere are relaxed by some time-dependent deformation mechanism or simply (3) the effects of erosion stripping away upper crustal density discontinuities. Processes (1) and (2) would apparently deny the elastic plate model under consideration.

3.5 Summary

It has been shown that the interpretation of isostatic response functions, even in terms of the simplest model available, is very difficult despite using a tested methodology and probably the best data available, subdivided into as geologically homogeneous units as practical. This is mainly a consequence of the non-uniqueness of gravity anomalies. A forward modelling approach was used but the results are no less general than the linear programming inversion technique applied by Banks et al. [1977], Banks and Swain [1978], McNutt and Parker [1978], and McNutt [1980].

The elastic plate model under consideration is characterized by two parameters: the flexural rigidity D and the density gradient of the lithosphere, simply represented by one or two major discontinuities. Theoretical considerations as well as misfit analyses of individual observed response functions indicate that the results are slightly more sensitive to the choice of D, as argued by McNutt [1980], rather than to the assumed density structure. In terms of best-fitting models the qualitative differences between the observed isostatic response functions are accommodated mainly by changes in the density structure [Figure 3-7].

These two observations could be construed to indicate that the flexural rigidity of the lithosphere in all of the study areas is the same within the range 10^{20}–10^{22} Nm. Whether the difference in parameter sensitivities is great enough to be significant in the interpretation of the overall results is equivocal [cf. Cochran 1980]. Rather, the fact that the modelled flexural rigidities vary at least over two orders of magnitude is considered to be good reason to reject the time-invariant elastic plate model. The rejection of this model is supported by the Cordilleran results which do not acceptably conform to model predictions and by the systematic dependence of the modelled compensation depths on tectonic age [Figure 3-7].

Of the general classes of rheological models of the lithosphere introduced in Chapter 1, the time-invariant elastic plate model is the only one which has an isostatic function which reacts passively to massive erosion of topography such as that observed in old continental regions. If the elastic model is rejected as being unsuitable then more complex models are required and explicit consideration of the effects of erosion is inescapable. An analytically tractable erosion model is discussed next.

Chapter 4. A Linear Model of Continental Erosion

4.1 Introduction

Continental topography obviously erodes. If the lithosphere behaves as an elastic plate, the case discussed in Chapter 3, and is loaded by eroding topography, then its isostatic response [Equation (3-11)] is not a function of time; the reaction to erosion is instantaneous. At any observation time it is the remaining topography alone which is being flexurally compensated. Should the elastic properties of the plate change through time then transient effects may occur but these would not be the result of the age of the load and its erosion but, rather, presumably of the age and changing properties of the plate.

If the rheology of the lithosphere falls into one of the other three general classes of rheological models introduced in Chapter 1 [elastic-plastic, viscoelastic, and non-linear depth dependent], then it is necessary in considering the isostatic response of continents to incorporate the influence of the progressive decrease in the topographic load resulting from erosion.

Erosion can be thought of as a feedback mechanism. There are two competing isostatic effects to consider. (1) It is known from geological [e.g. Ambrose 1964] and geomorphological observations [e.g. Adams 1980] that regions of high topographic relief erode more rapidly than regions of low relief. But it is recognized, from the existence of pediplains [e.g. Pugh 1955] and from tectonic basin analysis [e.g. Fralick 1981], that eroded regions are isostatically rejuvenated. That is, as topography is worn away and the rate of erosion diminishes, the action of isostasy is one of uplift and enhanced erosion. (2) If the rheology of the lithosphere allows the stresses resulting from topographic loads to be relaxed in some time-dependent manner, then topographic height will decrease through time independently of erosion as a result of "sinking" into the relaxing lithosphere. The action of this aspect of isostasy is one of reduced erosion rate.

The notion of erosion acting as a kind of feedback suggests that its isostatic effects may be quantitatively modelled in terms of a linear filter network in which the feedback component processes measured topography into an eroded remnant. The foreward component of the network would describe the deformational response of the lithosphere to the initial topography less the fedback erosion. The development of such a model in which the isostatic behaviour of a viscoelastic lithosphere is considered will be pursued in Chapter 5. In this chapter [section 4.2], a simple quantitative linear relationship between erosion rate and topography is hypothesized. Since it is convenient to consider the isostatic response of lithosphere in the wavenumber domain the erosion model is also developed in the wavenumber domain. The parameters of the erosion model are discussed in section 4.3 in the light of the topography of South Island, New Zealand, a continental region undergoing rapid tectonic uplift and massive erosion.

4.2 The Erosion Model

4.2.1 <u>Erosion of spectral topography</u>. It is assumed that topography in the spectral domain erodes at a rate which is proportional to its height. Thus,

$$\dot{E}(\vec{k},t) = B(k)\, H(\vec{k},t) + N_e(\vec{k},t) \tag{4-1i}$$

where $\dot{E}(\vec{k},t)$ is the erosion rate of topography $H(\vec{k},t)$ at time t and the "noise" term $N_e(\vec{k},t)$ accounts for the effects on $\dot{E}(\vec{k},t)$ related to local changes in lithology, vegetation, and climate. The proportionality factor $B(k)$ can be more conveniently written as

$$B(k) = -[\sigma(k)]^{-1} \tag{4-1ii}$$

where $\sigma(k)$ has dimensions of time. The negative sign in (4-1ii) arises from the fact that the loading effects of erosion are opposite to those of topography. It has been assumed that $\sigma(k)$ is not a function of time and that it is independent of wavenumber direction. Furthermore, if erosion is a linear process in which each harmonic of topography can be considered independently, it is expected that the rate of erosion will be proportional to the maximum gradient of that harmonic and therefore to its wavenumber. Thus,

$$\sigma(k) = \omega k^{-\varepsilon} \; ; \; \sigma(k) > 0 \tag{4-2}$$

where ω and ε are constant and neither is negative. As $k \to 0$, the case of no harmonic topographic gradient, $\sigma \to \infty$, implying that no erosion occurs.

$\sigma(k)$ is referred to as the erosion time constant [for a given wavenumber], terminology which is derived from the solution of the simple differential equation embodied by Equations (4-1) in the case where there is no isostatic adjustment to erosion. That is,

$$H(\vec{k},t) = H_o(\vec{k}) + E(\vec{k},t) \tag{4-3}$$

where $H_o(\vec{k})$ represents the initial topography, prior to erosion, and the sign convention of (4-3) is consistent with that of Equation (4-1ii). The solution to (4-1i) can be found, for example, using the Laplace transform

$$L\{F(t)\} = \overline{F}(s) = \int_0^\infty F(t) \exp[-st]dt \tag{4-4i}$$

and its inverse

$$L^{-1}\{\overline{F}(s)\} = F(t) = \frac{1}{2\pi i} \oint_C \overline{F}(s) \exp[st]dt \tag{4-4ii}$$

where C is the Bromwich contour in the complex plane. Equations (4-1), ignoring the effects of $N_e(k)$, and (4-3) Laplace transform as

$$s\overline{E}(\vec{k},s) - E(\vec{k},0) = \frac{-1}{\sigma(k)} \overline{H}(\vec{k},s) \tag{4-5}$$

and

$$\overline{H}(\vec{k},s) = \frac{1}{s} H_o(\vec{k}) + \overline{E}(\vec{k},s) \qquad (4\text{-}6).$$

Given that $\mathring{E}(\vec{k},t)$ is the rate of erosion of topography of wavenumber $\vec{k}$ at time t, the function $E(\vec{k},t)$, the Laplace transform of which is $\overline{E}(\vec{k},s)$, represents the amount of erosion at $\vec{k}$ which has occurred since the system began at, say, t=0. $E(\vec{k},0)$ is therefore zero and combining (4-5) and (4-6) to eliminate $\overline{E}(\vec{k},s)$ gives

$$\overline{H}(\vec{k},s) = [s + 1/\sigma(k)]^{-1} H_o(\vec{k}) \qquad (4\text{-}7).$$

The inverse Laplace transform of (4-7) provides a solution for $H(\vec{k},t)$,

$$H(\vec{k},t) = H_o(\vec{k}) \exp [-t/\sigma(k)] \qquad (4\text{-}8),$$

and it is seen that the erosion results in the simple exponential decay of $H_o(\vec{k})$ with erosion time constant $\sigma(k)$.

4:2.2 <u>The erosion model in space and the effects of sea level changes</u>. The ability to deal explicitly with the effects of sea level changes [e.g. Turcotte and Burke 1978] on erosion rates in terms of the hypothesized model is sacrificed to the convenience of working in the Fourier domain. Consider Equation (4-1i); its space domain equivalent is

$$\dot{e}(\vec{r}_o,t) = \int_S\int b(\vec{r}_o-r)\cdot h(\vec{r},t)\, dxdy + n_e(\vec{r}_o,t) \qquad (4\text{-}9)$$

where s is the surface which contributes to the erosion. Equation (4-9) shows that the variation of erosion rate $\dot{e}(\vec{r},t)$, over a geographic region at time t, is assumed to be linearly determined by the distribution of the regional topography at that time $h(\vec{r},t)$ measured relative to some constant datum surface. The noise term, as in the wavenumber domain, accommodates that part of the erosion rate not caused by b and related to factors such as local climate and lithological variations. Equation (4-9) is analogous to Equation (1-1) in which the gravity anomaly at any point was written as the two-dimensional convolution of q, the inverse Fourier transform of the isostatic response function Q, and the topography. If (4-9) is recast such that it is the height of topography $h(\vec{r},t)$ above sea level $h_s(\vec{r},t)$ which is convolved with b instead of simply the height of the topography above a constant datum surface, then the sea level corrected erosion rate is given by

$$\begin{aligned}\dot{e}(\vec{r}_o,t) &= \iint b(\vec{r}_o-\vec{r})\,[h(\vec{r},t) - h_s(\vec{r},t)]dxdy \\ &= \iint b(\vec{r}_o-\vec{r})\,h(\vec{r},t)\,dxdy \\ &\quad - \iint b(\vec{r}_o-\vec{r})\,h_s(\vec{r},t)\,dxdy \qquad (4\text{-}10).\end{aligned}$$

The Fourier transform of Equation (4-10) is

$$\dot{E}(\vec{k},t) = B(k)H(\vec{k},t) - B(k)H_s(\vec{k},t)$$

where, since sea level may be assumed to be constant as a function of position $\vec{r}$, $H_s(\vec{k},t)$ is non-zero only when $\vec{k}=0$. However, it has already been assumed that $B(0)=0$ [Equation (4-2)] since there is no topographic gradient when $k=0$. Under such circumstances Equation (4-11) reduces to (4-1i). Thus, it is seen that erosion rates, determined by the convolution equation (4-1i), are relative to one another just as gravity anomalies, determined by the analogous convolution equation (1-1), are, of course, relative measurements. This characteristic of the erosion model is acceptable if the topography under consideration has remained above sea level, and therefore has continuously eroded, throughout its history.

Whether or not this criterion can be met and, if not, whether it has serious consequences, will necessarily have to be assessed when the model is compared to observations. It remains that the linear model can be judged only on the success or failure of its application.

4.3 Indirectly Testing the Erosion Model

4.3.1 Introduction. The proposed erosion model [Equations (4-1)] expresses erosion rate, in the wavenumber $\vec{k}$ domain, as the product of a transfer function, $B(k) = -[\sigma(k)]^{-1}$, and the spectral topography. It is desired to test this model and, before applying it to isostatic models, to try to determine numerically the time constant spectrum $\sigma(k)$.

Estimates of regional erosion rates, historically made on the basis of estuarine and deltaic sedimentation rates [e.g. Gordon 1979, Menard 1961], dissolved and suspended stream loads [e.g. Owens and Watson 1979], or paleobarometry and radio-isotope dates [e.g. Dallmeyer

1975, Doherty and Lyons 1980], cannot by themselves be directly applied to the problem at hand. England and Richardson [1980] considered average denudation rates of young orogenic belts based on paleobarometric observations in conjunction with crustal thicknesses beneath present-day mountain ranges and suggested that the erosion of orogens takes place with a time constant in the range 50-200 Ma. The relationship between this estimate of an erosion time constant and $\sigma(k)$, however, is not obvious. First, it implicitly includes the amplification of erosion which may occur as a result of isostatic readjustment; secondly, England and Richardson's time constant of erosion refers to topography consisting of many spectral components.

Ideally, to numerically determine $\sigma(k)$, prior to developing a complete model incorporating the isostatic response of erosion, it is necessary to find a large region, in a manner analogous to the calculation of isostatic response functions, for which topography and erosion rate data are available and from these data to calculate the transfer function $B(k) = -[\sigma(k)]^{-1}$. To the author's knowledge, however, there are no such large regions where erosion rate has been observed as a geographic function and therefore an alternative approach is required.

Knowledge of the uplift rate of South Island, New Zealand, as a function of position suggests an indirect method of testing the erosion relation postulated in section 4.2. Wellman [1979] has determined the variation in uplift rate across South Island on the basis of geomorphological observations such as the character of mountain summits and the tilt of stranded shorelines of glacial lakes. His uplift rate map is reproduced in Figure 4-1. The rapid uplift of South Island is

Figure 4-1. Uplift rate map of South Island, New Zealand, showing major geological faults [from Wellman 1979]; uplift rates in mm yr^{-1}.


N
200 km

tectonic in origin [e.g. Wellman 1979, C.J.D. Adams 1979], related to vertical displacement along the Alpine Fault, a major structural feature which forms part of the boundary between the Indian and Pacific plates. In conjunction with this tectonic uplift, South Island is undergoing rapid erosion which may be in approximate balance with the uplift [J. Adams 1980].

The proposed indirect test of the hypothesized erosion relation [Equations (4-1)] assumes that the character of the currently observed topography of South Island is produced by the interaction between the tectonic uplift and the erosion [J. Adams 1980]. The form of the erosion is assumed to be that of the model described by Equations (4-1) and discussed in section 4.2. In this section, a model of the linear transfer function between uplift rate and topography based on the above premises is developed and compared to South Island observations.

4.3.2 A model of tectonic uplift and topography. In a region undergoing rapid tectonic uplift and massive erosion the observed topography $h(\vec{r},t)$ at some time t is assumed here to be the result of the total uplift $w(\vec{r},t)$ to date modified by the erosion $e(\vec{r},t)$:

$$h(\vec{r},t) = h_o(\vec{r}) + w(\vec{r},t) + e(\vec{r},t) \tag{4-12}$$

where $h_o(\vec{r})$ represents the topography which pre-existed the ongoing phase of uplift. Equation (4-12) obviously describes a general model of topography for any region regardless of the mechanism of uplift. If tectonic activity has ceased then $w(\vec{r},t)$ may be purely a result of isostatic readjustment. In the present case it is assumed that any isostatic component in $w(\vec{r},t)$ is very small compared to the tectonic component.

The total uplift which has occurred by some t can be written

$$w(\vec{r},t) = ct\, \dot{w}_t(\vec{r}) \tag{4-13}$$

where $\dot{w}_t(\vec{r})$ is the uplift rate at the observation time t and c is a constant; c=1 if the uplift rate has not varied during its history. If the present uplift rate is greater than the past average then c<1 and vice versa. Note that c is assumed not to be a function of $\vec{r}$, an acceptable assumption provided the entire episode of uplift has been the result of a single tectonic regime. Equations (4-12) and (4-13) are combined and Fourier transformed to yield

$$H(\vec{k},t) = H_o(\vec{k}) + ct\, \dot{W}_t(\vec{k}) + E(\vec{k},t) \tag{4-14}.$$

Unless the uplift has been purely isostatic $H(\vec{k},t)$ and $H_o(\vec{k})$ are not necessarily in phase spatially. The Laplace transform, defined by Equation (4-4i), of (4-14) is

$$\overline{H}(\vec{k},s) = \frac{1}{s} H_o(\vec{k}) + \frac{c}{s^2} \dot{W}_t(\vec{k}) + \overline{E}(\vec{k},s)$$

which, combined with the Laplace transform of the hypothesized erosion model relating topography to erosion rate [section 4.2],

$$s\overline{E}(\vec{k},s) - E(\vec{k},0) = \frac{-1}{\sigma(k)} \overline{H}(\vec{k},s) \tag{4-5},$$

gives

$$\overline{H}(\vec{k},s) = \frac{1}{s+1/\sigma(k)} H_o(\vec{k}) + \frac{c}{s[s+1/\sigma(k)]} \dot{W}_t(\vec{k}) \tag{4-15}$$

where it has been assumed that $E(\vec{k},0)=0$. The inverse Laplace transform of (4-15), with the terms rearranged, is

$$\dot{W}_t(\vec{k}) = Z(k,t)\, H(\vec{k},t) - \exp\,[-t/\sigma(k)]\, Z(k,t)\, H_o(\vec{k}) \tag{4-16i}$$

where

$$Z(k,t) = [c\sigma(k)\,\{1 - \exp\,[-t/\sigma(k)]\}]^{-1} \tag{4-16ii}.$$

Because $\sigma(k)$ was assumed to be independent of the direction of the wave-number k [subsection 4.2.1], so also is $Z(k,t)$. If, by time t, uplift has exceeded erosion, that is,

$$ct\, \dot{W}_t(\vec{k}) + E(\vec{k},t) < 0$$

[recalling that in the present frame of reference uplift is negative], then topography has grown in amplitude and, from (4-14), $|H(\vec{k},t)|>|H_o(\vec{k})|$. Thus, the second term of the right-hand side of Equation (4-16i) is absolutely smaller than the first; it is further reduced by the effects of the exponential term. If geological evidence shows that it is likely that $|H_o(\vec{k})|<<|H(k,t)|$, as in the case of South Island [C.J.D. Adams 1979, Hurley et al. 1962], then the second term may be small enough such that it can be considered as noise. Thus, $Z(k,t)$ would define the theoretical transfer function, or admittance, under the given conditions, between *topography* and *uplift rate*.

The general shape of $Z(k,t)$ is illustrated in Figure 4-2. Replacing $\sigma(k)$ in Equation (4-16ii) by $\omega k^{-\varepsilon}$ [Equation (4-2); section 4.2] gives

$$Z(k,t) = [c\omega k^{-\varepsilon} \{1 - \exp [-tk^{\varepsilon}/\omega]\}]^{-1} \quad (4\text{-}17),$$

the asymptotic behaviour of which, as tk^{ε}/ω becomes large, is of the form [cf. Figure 4-2]

$$Z(k,t) = k^{\varepsilon}/c\omega \quad (4\text{-}18);$$

its k=0 intercept, $Z(0,t) = [ct]^{-1}$, is found from the Taylor series expansion of (4-17):

$$Z(k,t) = [ct - \frac{ct^2k^{\varepsilon}}{2!\omega} + \frac{ct^3k^{2\varepsilon}}{3!\omega^2} - \ldots.]^{-1}$$

Figure 4-2 shows that parameter c has a scaling effect only; t acts as a scaling factor as well as determining, in conjunction with parameters ε and ω, the rate at which $Z(k,t)$ becomes asymptotic.

It is hoped to constrain these parameters of $Z(k,t)$ and, in doing so, test the fundamental erosion relation postulated in section 4.2 by computing the observed transfer function between uplift rate and topography for South Island, New Zealand, using Wellman's [1979] uplift rate map and the methodology described in subsection 2.2.4.

Figure 4-2. The general form of the theoretical uplift rate-topography transfer function $Z(k,t)$; ε and ω are the parameters of the postulated erosion relation [section 4.2]; scaling factor c depends on whether the observed uplift rate was greater or smaller prior to observation time t. $Z(k,t)$ assumes its asymptotic form at wavenumbers greater than approximately $[4.5\omega t^{-1}]^{1/\varepsilon}$.

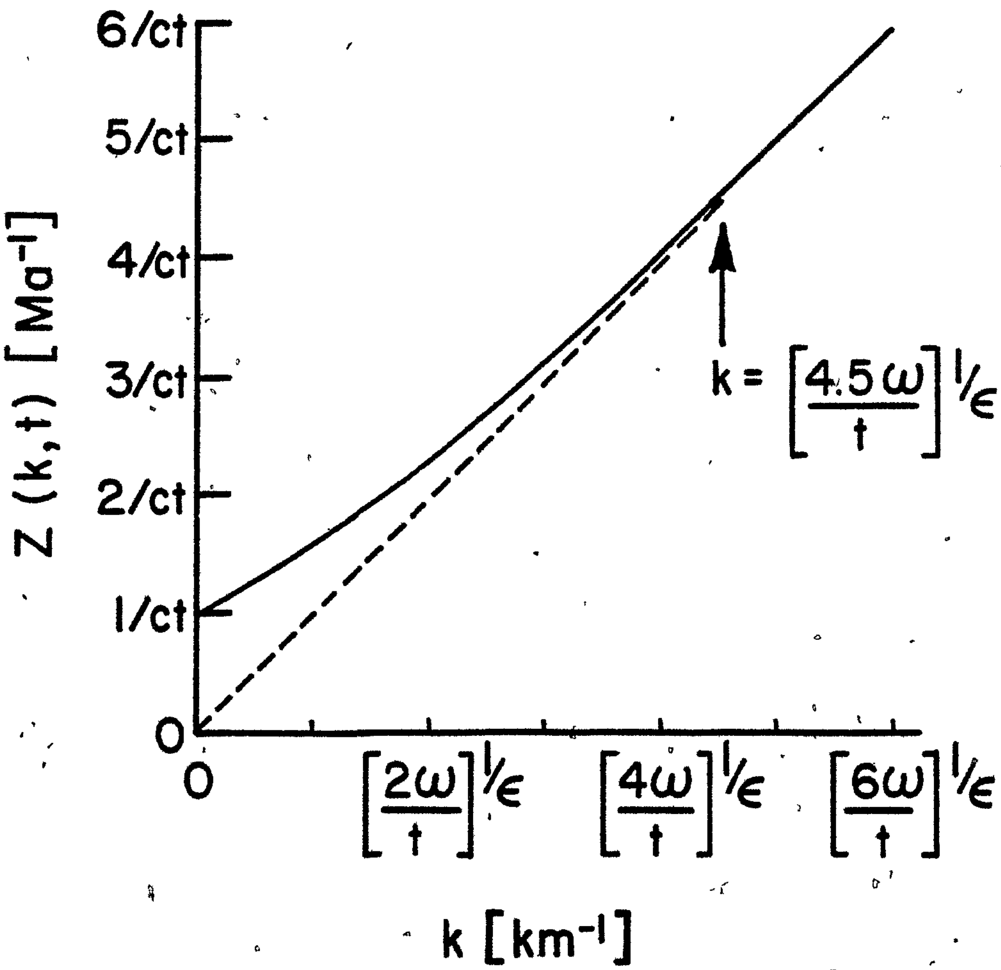
6/ct
5/ct
4/ct
3/ct
2/ct
1/ct
0
Z (k,t) [Ma^{-1}]
k = $\left[\frac{4.5\omega}{t}\right]^{1/\epsilon}$
0
$\left[\frac{2\omega}{t}\right]^{1/\epsilon}$
$\left[\frac{4\omega}{t}\right]^{1/\epsilon}$
$\left[\frac{6\omega}{t}\right]^{1/\epsilon}$
k [km^{-1}]

4.3.3 Calculation of the uplift rate-topography transfer function for South Island, New Zealand. A theoretical transfer function Z(k,t) between tectonic uplift rate and topography was formulated in subsection 4.3.2. An estimate of Z(k,t) is found here using the uplift rate data reported by Wellman [1979]. Wellman's map [Figure 4-1] was digitized by visual averaging within 20 km square cells over a region of total dimensions 720 km by 180 km [Figures 4-3(a,b)]. Topography was derived from 1:500,000 scale topographic maps, contour interval 1000 feet [New Zealand 1976, Sheets 3 and 4], visually digitized at longitudinal and latitudinal intervals each of 10 minutes. These estimated 10 minute by 10 minute topographic means were then averaged into the 324 [36 by 9] cells of the cartesian grid for which uplift rates had been determined. The contoured cell averages for each data set are shown in Figures 4-3(a,b).

The admittance between these two two-dimensional discrete functions was then estimated in the manner described in section 2.2 with one modification: because of the short data length in one dimension [9 points only] and the consequent large percentage of the grid which would be affected by tapering of the edges [subsection 2.2.2], the 36 by 9 grid was interpolated by means of a bicubic spline [Swain 1976] into one with dimensions 80 by 20 and digitization interval 8 km. Thus, a taper applied to the three outermost columns and rows of the data, for example, would affect far less of the total array. The reduction in the digitization interval results in additional high frequency spectral estimates [the Nyquist frequency, Equation (2-4), becomes greater] which are not supported by the actual observations and which

Figure 4-3. Contour maps of the 20 km by 20 km digitized (a) uplift rate data [Wellman 1979; cf. Figure 4-1] and (b) topography [New Zealand 1976] of the South Island, New Zealand study area; units are (a) mm yr^{-1} and (b) 100 m. Dimensions of the study area are 180 km by 720 km.

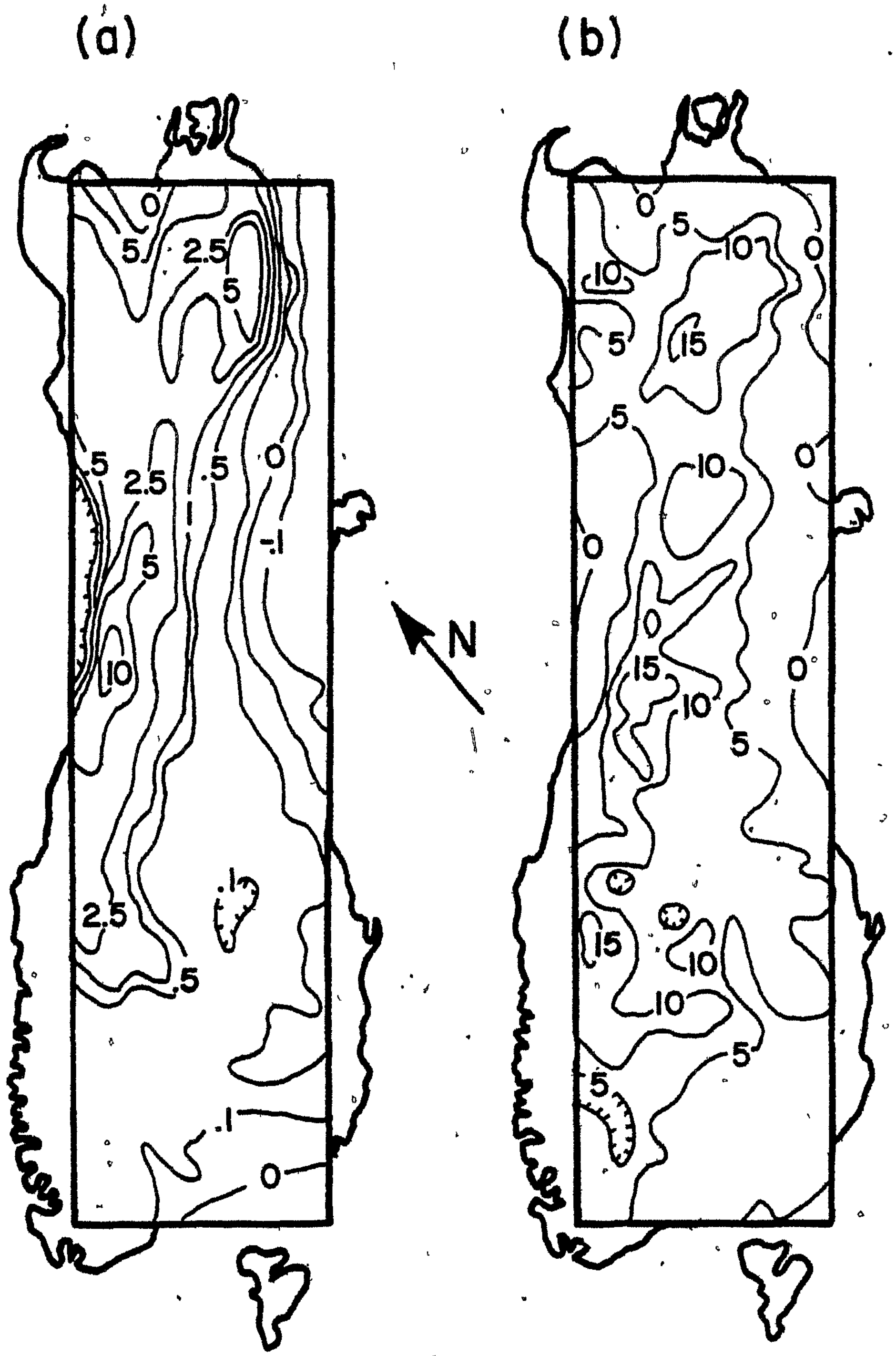
(a)
(b)
N
0
5
2.5
5
.5
2.5
.5
0
1
5
-.1
10
.1
2.5
.5
.1
0
0
5
10
0
10
5
15
5
10
0
0
0
15
10
5
0
15
10
10
5
5

are probably affected by aliasing [subsection 2.2.2]. For this reason, the additional part of the calculated transfer function is not considered in the subsequent analysis. Estimates at smaller wavenumbers are unlikely to have been affected by the grid interpolation.

4.3.4 <u>Results and discussion</u>. The results of the transfer function calculations are presented in Table 4-1; the admittance estimates $\hat{Z}(k,t)$ are plotted with their associated standard errors in Figure 4-4. The ratio of the means of the topography and uplift rate data sets is plotted as a k=0 estimate of the admittance. The mean unbiased coherence squared $\hat{\gamma}^2(k)$ of the three admittance estimates in the range $k \leq 0.0104$ km^{-1} [wavelength $\geq$ 96 km] is 0.50 and their minimum is 0.40. No admittance estimate at any higher wavenumber has $\hat{\gamma}^2 > 0.31$ and most are much less.

It is not surprising that the calculated transfer function between the uplift rate and topography of South Island is as incoherent as it is. One reason is that the noise component in the data is probably very large relative to the amount of data which is available. For example, Wellman [1979, p. 13] considers the uplift rate data "nowhere ... to be less than 25% in error." The smoothing of discontinuities along geological faults during the digitization of the uplift rates [cf. Figures 4-1, 4-2(a)] contributes more error.

More serious problems may arise out of the theoretical basis of the uplift rate-topography transfer function. First, the methodology used to estimate Z(k,t) [subsection 2.2.4] relies on the assumption that the noise associated with the output is not correlated with the input.

Figure 4-4. Observed uplift rate-topography transfer function $\hat{Z}(k,t)$ of South Island, New Zealand; filled circles represent estimates with $\hat{\gamma}^2 > 0.30$; error bars correspond in length to two standard errors.

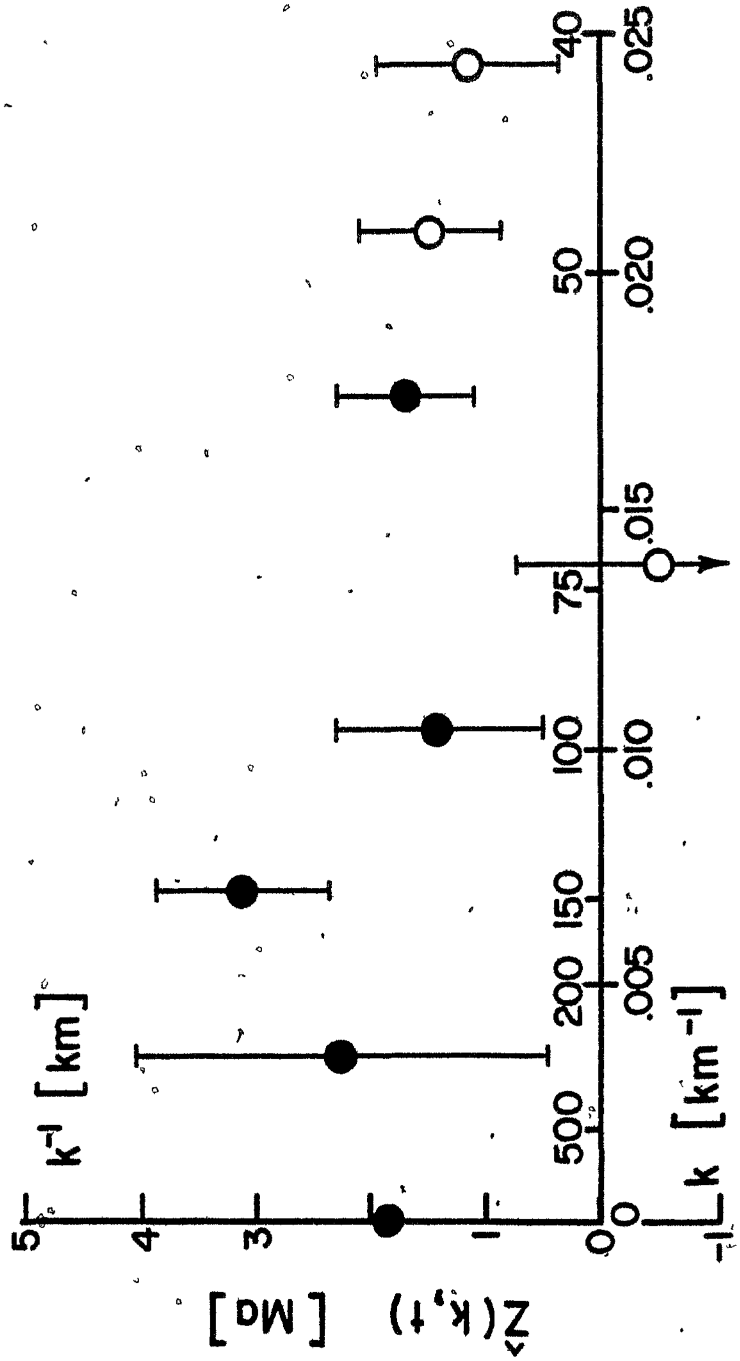
$\hat{Z}(k,t)$ [Ma]
k^{-1} [km]
k [km^{-1}]
500
200
150
100
75
50
40
0
.005
.010
.015
.020
.025
5
4
3
2
1
0
-1

Table 4-1. Results: ensemble wavenumber [k_r], wavelength [k_r^{-1}], number of ensemble raw spectral data [m_r], uplift rate-topography transfer function estimate [$\hat{Z}(k_r,t)$], standard error [$d\hat{Z}(k_r,t)$], unbiased coherence squared estimate [$\hat{\gamma}^2(k_r,t)$].

k_r [km^{-1}]	k_r^{-1} [km]	m_r	$\hat{Z}(k_r,t)$ [Ma]	$d\hat{Z}(k_r,t)$	$\hat{\gamma}^2(k_r,t)$
0	-	1	1.819	-	-
0.0035	288	3	2.273	1.800	0.60
0.0069	144	12	3.126	0.737	0.40
0.0104	96	14	1.406	0.924	0.49
0.0139	72	19	-0.505	1.068	0.01
0.0172	58	26	1.695	0.619	0.31
0.0208	48	24	1.490	0.649	0.09
0.0244	41	42	1.160	0.796	0.05

In the present case, the output and input are uplift rate and topography respectively. The assumption that topography and noise are uncorrelated may not be valid if a significant component of the currently existing topography of South Island derives from that predating the present phase of uplift [cf. initial topography $H_o(\vec{k})$ in Equation (4-16i)]. The observational basis of Z(k,t) requires that $H_o(\vec{k})$ be negligibly small.

Secondly, the postulated erosion relation [Equations (4-1); section 4.2], on which the uplift rate-topography transfer function Z(k,t) is founded, may not be valid. The erosion relation does not take into account lithological and climatic variations, the effects of which become increasingly important as wavenumber becomes larger. On South Island there is an observable relationship between erosion rate and rainfall distribution [Wellman 1979, J. Adams 1980] and, in turn, rainfall distribution is probably strongly affected by topography. Thus, "noise" due to rainfall would be highly correlated.

The uplift model was originally designed in order to provide a test of the suitability of the postulated erosion relation. The primary application of the erosion relation is toward the modelling of isostatic response functions and continental topography at wavenumbers less than 0.01 km^{-1}. In this respect, it is perhaps significant that the coherence of observed $\hat{Z}(k,t)$ is as great as it is [$\hat{\gamma}^2 > 0.31$] for $k \leq 0.01$ km^{-1}. Although the coherence is not large by statistical standards, it does indicate that the models can at least not be rejected when $k \leq 0.01$ km^{-1}.

There is no suggestion that $\hat{Z}(k,t)$ increases with k in this wavenumber range but this feature of the results is not inconsistent with theoretical $Z(k,t)$ [Figure 4-2] which may be slowly varying depending on t and the model parameters ε and ω. The k=0 intercept of $\hat{Z}(k,t)$ appears to be in the range 1-3 Ma and, if the models are correct, should equal the theoretical intercept $[ct]^{-1}$ [Equation (4-19)]. Variable t, the length of time during which uplift has occurred to produce the observed topography, is reasonably well known. The topographic character of South Island is dominated by the Southern Alps mountain range which began to be uplifted approximately 4 Ma ago [e.g. Wellman 1979, C.J.D. Adams 1979], an event which can be related to southern Pacific plate motions [Walcott 1979, Wellman 1979]. The observed intercept implies that the uplift rate of South Island is greater at the present than during the previous four million years if it is assumed that $t \approx 4$ Ma. Geological and tectonic considerations tend to support this consequence of the model: Walcott [1979, p. 5] states that the relative motion between the Pacific and Indian plates, the compressional component of which is primarily responsible for the uplift of South Island, is "faster today than at any time in the Tertiary." Moreover, radio-isotope studies have shown that the total late Cenozoic uplift has been about 5 km [C.J.D. Adams 1979]; present uplift rates, which reach a maximum of about 20 mm a^{-1} [cf. Figure 4-1], would account for a total uplift of up to 80 km if extrapolated over the given four million years.

4.3.5 Constraints on parameters. It is unlikely that the observations can provide any resolution of the model parameters ε and ω. The general shape of the theoretical transfer function $Z(k,t)$ shown in Figure 4-2 indicates that it would be relatively easier to determine model parameters by regression of data if the data are observed at wavenumbers in the asymptotic segment of $Z(k,t)$ than if they are not. In the asymptotic range $Z(k,t)$ has the relatively simple form

$$Z(k,t) = k^{\varepsilon}/c\omega \qquad (4\text{-}18)$$

with the scaling factor already determined by the $k=0$ intercept. At smaller wavenumbers the form of $Z(k,t)$ is too complex [Equation (4-17)] to provide a profitable regression model for noisy and sparse data.

The maximum wavenumber at which a reasonably coherent estimate of $Z(k,t)$ is observed from the South Island data is approximately 0.01 km^{-1} [cf. Table 4-1]. Reliable observations of $Z(k,t)$ at higher wavenumbers are unlikely because of the breakdown of the fundamental erosion relation [Equations (4-1)]. Therefore, in order to provide a profitable regression model for the observed data, it is necessary that $\hat{Z}(k,t)$ acquires its asymptotic form at a wavenumber less than or equal to 0.01 km^{-1}. Figure 4-2 shows that its ability to do so depends on the values of parameters ε and ω and on the age of the uplift t; the wavenumber at which asymptotic behaviour begins is approximately

$$k_o = \left[\frac{4.5\omega}{t}\right]^{1/\varepsilon} \qquad (4\text{-}20).$$

For South Island, t is assumed to be 4 Ma. Figure 4-5 illustrates the resulting lack of constraint of the South Island observations on ε and ω. The solid line represents the $k=0.01$ km^{-1} contour of Equation (4-20) in ε-ω space; ε and ω must have values on the shaded side of the contour

Figure 4-5. ε-ω parameter space showing the 0.01 km^{-1} contour of the minimum asymptotic wavenumber $k=[4.5\omega t^{-1}]^{1/\varepsilon}$ assuming t=4 Ma [solid line] and the 10 Ma contour of the erosion time constant $\sigma=\omega k^{-\varepsilon}$ for harmonic topography having wavenumber $k=0.01\ km^{-1}$ [dashed line]. Parameters ε and ω are expected to lie within the upper right-hand shaded region but can only be determined by the uplift-topography analysis if they lie in the lower left-hand shaded region [cf. text].

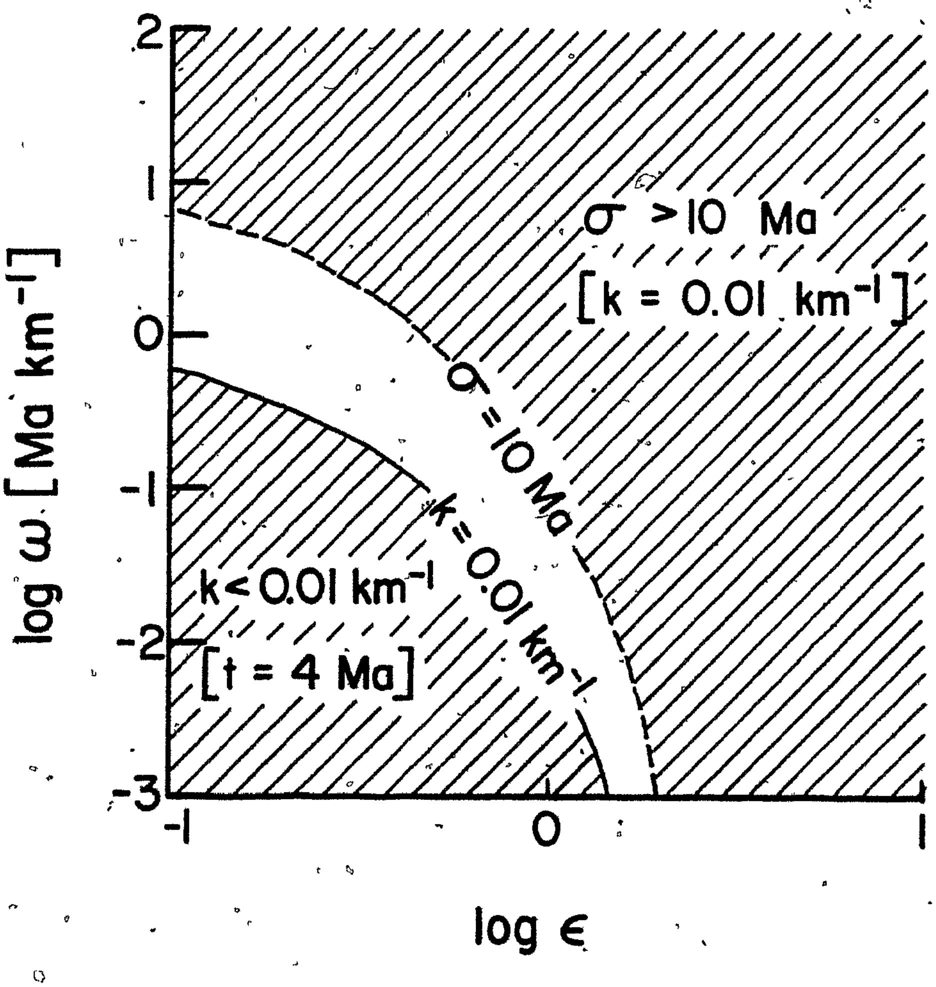

σ >10 Ma
[k = 0.01 km⁻¹]
σ = 10 Ma
k = 0.01 km⁻¹
k<0.01 km⁻¹
[t = 4 Ma]
log ω [Ma km⁻¹]
log ϵ
2
1
0
-1
-2
-3
-1
0
1

if $\hat{Z}(k,t)$ is to have asymptotic behaviour in the range of reliably observable wavenumbers.

However, it is unlikely that ε and ω have values in the indicated region. It was postulated in section 4.2 that harmonic topography erodes with an erosion time constant $\sigma(k)$ such that

$$\sigma(k) = \omega k^{-\varepsilon} \; ; \; \sigma(k)>0 \qquad (4\text{-}2).$$

It is anticipated, on the basis of the continental "average" erosion time constant of 50-200 Ma suggested on geological grounds by England and Richardson [1980], that σ for topography of wavenumber 0.01 km^{-1} is at least of the order of 10 Ma. The dashed line in Figure 4-5 represents the σ=10 Ma contour of Equation (4-2) in ε-ω space for k=0.01 km^{-1} topography. If 10 Ma is assumed to be a minimum bound on σ at this wavenumber then ε and ω must have values within the shaded upper right-hand region. These values are well-removed from those in the lower left-hand shaded region which are theoretically resolvable by the South Island tectonic uplift analysis as explained above. Thus, the uplift rate-topography model developed in this section cannot be used to determine the parameters ε and ω of the postulated erosion relation as it was hoped.

4.4 Summary

In order to investigate the isostatic response of continental regions using time-dependent models of the lithosphere, a quantitative model of topographic erosion is required. In this chapter, a model in which harmonic topography erodes at a rate which is proportional to its amplitude was postulated. It was assumed that erosion is a linear process in which each harmonic of topography could be considered independently and would be characterized by an erosion time constant dependent upon the harmonic wavenumber. The model does not take into account the effects on erosion of local changes in lithology, climate, and vegetation. These effects are expected to be unimportant when considering lengths of time of the order of hundreds of millions of years and topography of wavelengths greater than 100 km.

The postulated erosion model was indirectly tested by considering the topography and tectonic uplift of South Island, New Zealand. The theoretical linear transfer function relating topography and tectonic uplift was formulated on the premise that the observed form of the topography is produced solely by the interaction of the uplift and erosion. The form of the erosion was assumed to be that of the postulated harmonic erosion model. The observed transfer function between topography and uplift rate on South Island is characterized by a reasonable level of coherence at wavenumbers less than 0.01 km^{-1} only. In this range the calculated transfer function has a form compatible with that predicted by the uplift-topography model and implies, in terms of the model, that the present day uplift of South Island is greater than in the past, a result which is consistent with geological observations. For these reasons, it is concluded that the postulated harmonic erosion relation, fundamental to the uplift-topography analysis, cannot be rejected at wavenumbers less than or equal to 0.01 km^{-1}. It was shown, however, that the South Island analysis could not be expected to constrain the parameters of the erosion relation. The erosion relation is therefore applied to the development of general models of continental isostatic response without imposing a priori parameter constraints. The formulation and application of these models is pursued in Chapter 5.

Chapter 5. Eroding Topography and Isostatic Response of Continents

5.1 Introduction

In this chapter the isostatic response of the continental lithosphere is modelled in terms of a thin plate characterized by linear viscoelastic [Maxwell] rheology. A Maxwell viscoelastic body deforms such that there is instantaneous elastic strain followed by viscous flow at a constant rate. There is no yield strength below which viscous relaxation fails to occur.

The time derivative of the deformation, $\dot{w}(\vec{r},t)$, produced by a load $p(\vec{r},t)$ on a thin Maxwell viscoelastic plate overlying an incompressible fluid substratum is given by the solution of [Nadai 1963]

$$D\nabla^4 \dot{w}(\vec{r},t) = \dot{p}(\vec{r},t) + \frac{1}{\tau} p(\vec{r},t) \tag{5-1i}$$

where $\dot{p}(\vec{r},t)$ is the time derivative of $p(\vec{r},t)$, D is the plate's elastic flexural rigidity, defined in Chapter 3 [Equation (3-1i)], and τ is the viscous relaxation time constant of the plate. If the plate is assumed to be incompressible, then

$$\tau = 3\eta/E \tag{5-1ii}$$

where η and E are the Newtonian viscosity and Young's modulus respectively. In the limit as $\eta\to\infty$ [and therefore $\tau\to\infty$], Equation (5-1i) is clearly equivalent to the elastic thin plate equation (3-1i).

The isostatic response function $Q(k,t)$ characteristic of a viscoelastic lithosphere, because the lithosphere relaxes stresses at a rate determined by τ, is time-dependent. Noting this fact, McNutt and Parker [1978] explained the differences in the observed isostatic response functions of the United States and Australia in terms of the age of the predominant topography of each region. They concluded that the rheology of the continental lithosphere was viscoelastic and estimated its time constant of relaxation τ to be 45 Ma. McNutt and Parker did not, however, address the problem of the erosion of the topography. The effects of erosion are potentially very important because the time-dependent deformational response of a loaded viscoelastic lithosphere will vary according to the history of the load. Moreover, erosion of topography results in isostatic uplift, an effect opposite to that of the pre-existing and contemporary topography which would be to "sink" into the relaxing lithosphere.

Here, erosion is incorporated into general viscoelastic isostatic models formulated in terms of linear filter networks. The form of the erosion is assumed to be that hypothesized and discussed in Chapter 4. The use of linear systems theory results in mathematical simplicity but limits the choice of rheological and erosional models to those which are linear. Whether more complex models are required to satisfactorily reproduce the observed isostatic behaviour of the lithosphere can be determined by the success or failure of the linear approach. One important question which can be investigated by the viscoelastic analysis is whether the continental lithosphere necessarily possesses a finite yield strength as required by elastic-plastic models.

5.2 Isostatic Response of Eroding Loads

5.2.1 Deformation of a thin viscoelastic plate by a harmonic load. The Fourier transform [Equation (1-2i)] of the thin viscoelastic plate equation (5-1i),

$$D[2\pi k]^4 \dot{W}(\vec{k},t) = \dot{P}(\vec{k},t) + \frac{1}{\tau} P(\vec{k},t) \qquad (5\text{-}2),$$

expresses deformation in terms of harmonic loading $P(\vec{k},t)$ and, as in the elastic plate analysis, the load is assumed to consist of (1) surface forces resulting from overlying material of density ρ_o and thickness distribution $L(\vec{k},t)$, where L includes that portion of the overlying material occupying depressions in the plate due to its loading response, and (2) buoyancy forces acting on the base of the plate caused by the displacement of the fluid substratum, density ρ_m, by the plate deflection. Thus,

$$\dot{W}(\vec{k},t) + \frac{\psi(k)}{\tau} W(\vec{k},t) = -\frac{\rho_o}{\rho_m} \psi(k) \left[\dot{L}(\vec{k},t) + \frac{1}{\tau} L(\vec{k},t)\right] \qquad (5\text{-}3)$$

where $\psi(k)$, the flexural response function, is defined as before:

$$\psi(k) = \left[1 + \frac{[2\pi k]^4 D}{\rho_m g}\right] \qquad (3\text{-}5ii).$$

The deformational response of a thin viscoelastic plate to a harmonic load defined by Equation (5-3) describes a linear system in which an input function $L(\vec{k},t)$ produces an output signal $W(\vec{k},t)$. The transfer function of the system can be found by taking the Laplace transform [Equation (4-4i)] of (5-3):

$$s\overline{W}(\vec{k},s) - W(\vec{k},0^+) + \frac{\psi(k)}{\tau}\overline{W}(\vec{k},s)$$
$$= -\frac{\rho_o}{\rho_m}\psi(k)\left[s\overline{L}(\vec{k},s) - L(\vec{k},0^+) + \frac{1}{\tau}\overline{L}(\vec{k},s)\right] \tag{5-4}$$

for a plate loaded when $t>0$ and $L(\vec{k},0^+) = \lim_{t\to 0} L(\vec{k},t)$, similarly for $W(\vec{k},0^+)$, and $\psi(k)$ and τ are assumed to be independent of time. The response of the viscoelastic plate at $t=0^+$ may be considered to be purely elastic, there having been insufficient time for viscous flow, and, therefore, from Equation (3-5i),

$$W(\vec{k},0^+) = -\frac{\rho_o}{\rho_m}\psi(k)\,L(\vec{k},0^+) \quad ;$$

thus, Equation (5-4) simplifies to

$$\overline{W}(\vec{k},s) = T_I(k,s)\;\overline{L}(\vec{k},s) \tag{5-5i}$$

where

$$T_I(k,s) = -\frac{\rho_o}{\rho_m}\psi(k)\cdot\left[\frac{s + 1/\tau}{s + \psi(k)/\tau}\right] . \tag{5-5ii}$$

and $T_I(k,s)$ is the transfer function describing the deformational effect on a thin viscoelastic plate of a surface harmonic load.

5.2.2 <u>Erosion and the effective plate load</u>. The effective surface load on the viscoelastic plate at any time t, $L(\vec{k},t)$, may be thought of as equal to some assumed applied loading function $L_o(\vec{k},t)$ modified by erosion such that

$$L(\vec{k},t) = L_o(\vec{k},t) + E(\vec{k},t) \tag{5-6}$$

where $E(\vec{k},t)$ represents, as in section 4.2, the amount of erosion by time t of harmonic topography of wavenumber $\vec{k}$. In turn, $L(\vec{k},t)$, in a manner analogous to Equation (3-6) of the elastic analysis, consists of (1) a portion remaining above the undeformed plate surface, measurable as topography $H(\vec{k},t)$ at the time of observation and (2) a portion which occupies the plate deflection $W(\vec{k},t)$ at that time:

$$L(\vec{k},t) = H(\vec{k},t) - W(\vec{k},t) \tag{5-7}$$;

therefore, from Equations (5-6, 7),

$$L_o(\vec{k},t) = H(\vec{k},t) - W(\vec{k},t) - E(\vec{k},t) \tag{5-8i}$$.

If the plate is assumed to be suddenly loaded at t=0, subsequent to which the topography is modified only by erosion, then $L_o(\vec{k},t)$ has the form of a Heaviside step function:

$$L_o(\vec{k},t) = \begin{cases} 0 \; ; \; t<0 \\ L_o(\vec{k}) \; ; \; t\geq 0 \end{cases} \tag{5-8ii}$$

Thus, when $t\geq 0$, (5-8i) is analogous to the Fourier transform of Equation (4-12), used during the analysis of the New Zealand uplift data, except that the deformation $W(\vec{k},t)$ in the present case is due to isostatic adjustments rather than to a superimposed regime of tectonic forces.

Equation (5-8i) is schematically illustrated in Figure 5-1; it shows that eroded material does not continue to load the plate in some rearranged fashion but rather is removed from the system and deposited elsewhere, presumably at the continental margin [cf. Menard 1961].

5.2.3 <u>Solution for a load which does not erode.</u> If there is no erosion of topography then $E(\vec{k},t)=0$ and the effective plate load $L(\vec{k},t)=L_o(\vec{k},t)$ by Equation (5-6). But $L_o(\vec{k},t)$ has the form of a Heaviside step function [Equation (5-8ii)] and therefore the Laplace transform of the effective load is [cf. Equation (4-4i)]

$$\overline{L}(\vec{k},s) = \overline{L}_o(\vec{k},s) = \frac{1}{s} L_o(\vec{k}) \tag{5-9}$$

Equation (5-9) substituted into (5-5i) gives

$$\overline{W}(\vec{k},s) = \frac{1}{s} T_I(k,s) \, L_o(\vec{k}) \tag{5-10}$$

Figure 5-1. Schematic drawing of the erosion E of harmonic topography H occurring between t_o and t_1 showing the resulting rebound of the flexural deformation W of the lithosphere [Model 1; subsection 5.2.4]; the lithosphere is stippled. The effective surface load at any time consists of H-W [Equation (5-7)]; the sum H-W-E is constant in time [Equations (5-8)].

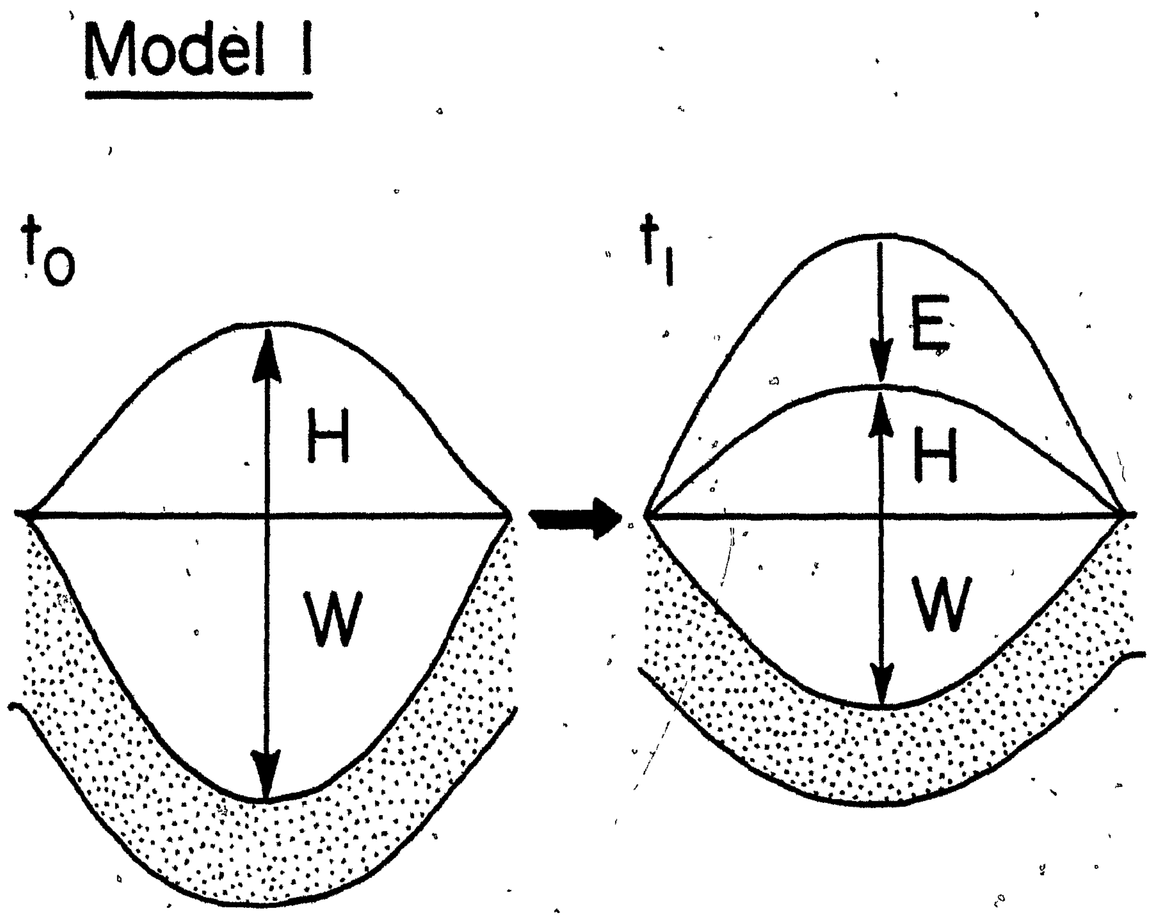
Model I
t0
t1
H
W
E
H
W

the inverse Laplace transform of which is directly obtainable [e.g. Roberts and Kaufman 1966, p. 181] and provides the solution of the deformation of a thin viscoelastic plate as a function of time which is produced by a constant harmonic load:

$$W(\vec{k},t) = -\frac{\rho_o}{\rho_m}\left[1 + [\psi(k) - 1]\cdot\exp[-t\psi(k)/\tau]\right] L_o(\vec{k}) \qquad (5\text{-}11).$$

Note that when $t \to 0$ or $\tau \to \infty$, Equation (5-11) must reduce to a form equivalent to the elastic plate solution, Equation (3-5i). The measurable topography as a function of time can be found by simply noting that $H(\vec{k},t)=L_o(\vec{k},t)+W(\vec{k},t)$ when $E(\vec{k},t)=0$ [Equations (5-8)].

Beaumont [1978] derived a more general result for the response of a viscoelastic plate under a constant load in terms of space-time Heaviside-Green functions. McNutt and Parker [1978] derived an expression for $W(\vec{k},t)$ of a viscoelastic plate but required the measurable topography rather than the total effective load to be held constant in time thus necessitating the assumption that after the formation of topography by a mountain-building episode its elevation was "maintained by subsequent minor rejuvenating pulses" [p. 774]. Their expression for $W(\vec{k},t)$ varies only slightly from Equation (5-11): it is of the same form but $[\rho_m-\rho_o]$ replaces ρ_m wherever the latter is found [including once in each $\psi(k)$ term] in (5-11). However, the notion that the effective load increases through time is an unrealistic one.

5.2.4 Solution for a load which erodes: Model 1. The effect of erosion on the isostatic deformation of a thin viscoelastic plate can be solved in terms of the transfer function of a linear system with erosional feedback. Consider the network illustrated in Figure 5-2 which has input $\overline{L}_o(\vec{k},s)$ and output $\overline{H}(\vec{k},s)$ such that

$$\overline{H}(\vec{k},s) = N_1(k,s)\ \overline{L}_o(\vec{k},s) \qquad \text{(5-12i)}.$$

The closed loop network transfer function $N_1(k,s)$ for a network of this configuration is [Doetsch 1974, p. 85]

$$N_1(k,s) = \frac{A_1(k,s)}{1 - A_1(k,s)\ B_1(k,s)} \qquad \text{(5-12ii)}.$$

According to Figure 5-2

$$\overline{H}(\vec{k},s) = A_1(k,s)\ [\overline{L}_o(\vec{k},s) + \overline{E}(\vec{k},s)] \qquad \text{(5-13)}$$

and

$$\overline{E}(\vec{k},s) = B_1(k,s)\ \overline{H}(\vec{k},s) \qquad \text{(5-14)}.$$

The Laplace transform of Equation (5-7) is

$$\overline{L}(\vec{k},s) = \overline{H}(\vec{k},s) - \overline{W}(\vec{k},s) \qquad \text{(5-15)}$$

which is used in conjunction with (5-5i) to write the transfer function between the measured topography $\overline{H}(\vec{k},s)$ and the effective load $\overline{L}(\vec{k},s)$:

Figure 5-2. Linear filter network with feedback describing Model 1. Filter A_1 determines the deformational response of the lithosphere [and therefore the height of topography $\overline{H}$ remaining above sea level] to the initial surface load $\overline{L}_o$ less erosion $\overline{E}$; filter B_1 determines the erosion of $\overline{H}$.

Model I

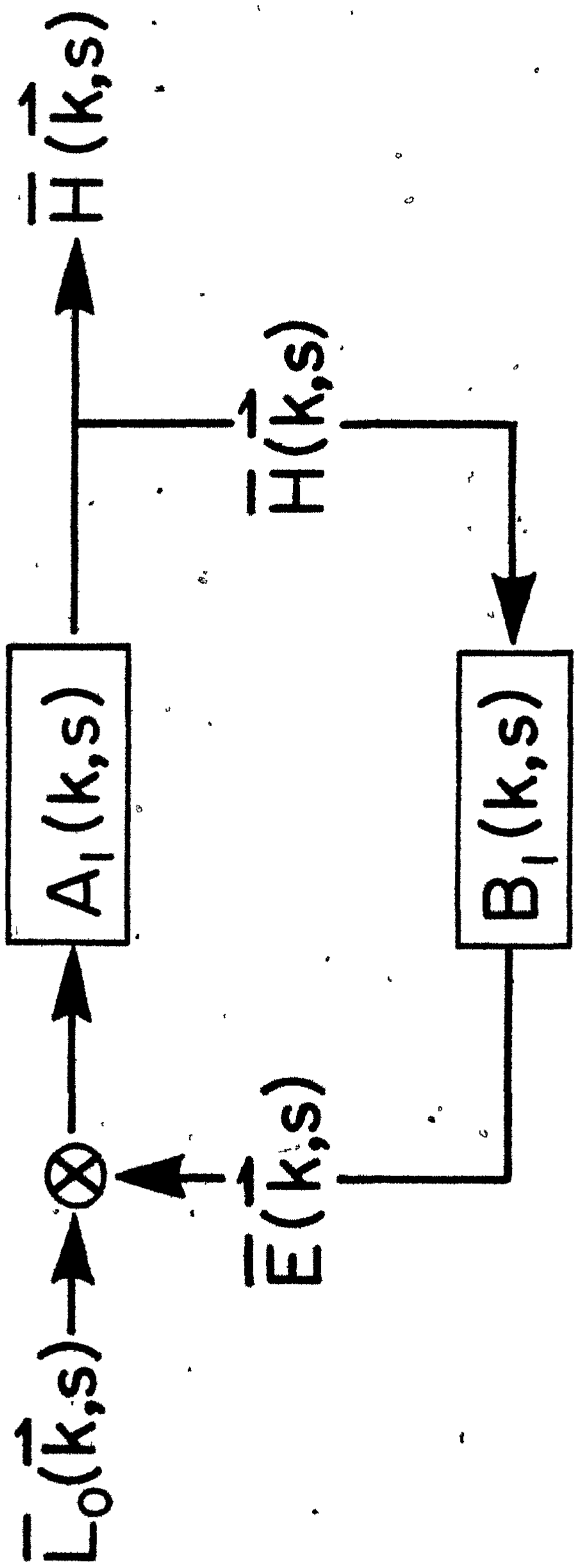

$$\overline{H}(\vec{k},s) = [1 + T_I(k,s)]\ \overline{L}(\vec{k},s) \qquad (5\text{-}16)$$

but $\overline{L}(\vec{k},s)=\overline{L}_o(\vec{k},s)+\overline{E}(\vec{k},s)$ from the Laplace transform of (5-6) and therefore, comparing Equations (5-13) and (5-16),

$$A_1(k,s) = 1 + T_I(k,s) \quad .$$

The relationship between erosion rate and topography was hypothesized to be of the form

$$\dot{E}(\vec{k},t) = -[\sigma(k)]^{-1}\ H(\vec{k},t) \qquad (4\text{-}1i,ii)$$

the Laplace transform of which gives, noting that no erosion has taken place by t=0,

$$\overline{E}(\vec{k},s) = T_E(k,s)\ \overline{H}(\vec{k},s) \qquad (5\text{-}17i)$$

where

$$T_E(k,s) = -[s\sigma(k)]^{-1} \qquad (5\text{-}17ii);$$

$T_E(k,s)$ is the transfer function describing the erosional effect of topography. Thus, comparing Equations (5-14) and (5-17i),

$$B_1(k,s) = T_E(k,s) \quad .$$

The network transfer function $N_1(k,s)$ is therefore known and Equation (5-12i) can be rewritten

$$\overline{H}(\vec{k},s) = \frac{1 + T_I(k,s)}{1 - T_I(k,s)\ T_E(k,s) - T_E(k,s)}\ \overline{L}_o(\vec{k},s) \qquad (5\text{-}18).$$

Making substitutions for $T_I(k,s)$, $T_E(k,s)$, and $L_o(\vec{k},s)$ [Equations (5-5ii), (5-17ii), and (5-9) respectively], (5-18) becomes

$$\overline{H}(\vec{k},s) = [1 - \psi(k)\rho_o/\rho_m] \left[\frac{s + \gamma_H}{s^2 + \alpha s + \beta}\right] L_o(\vec{k}) \qquad (5\text{-}19i)$$

where

$$\alpha = \frac{1 - \psi(k)\rho_o/\rho_m}{\sigma(k)} + \frac{\psi(k)}{\tau} \qquad (5\text{-}19ii),$$

$$\beta = \frac{[1 - \rho_o/\rho_m]\ \psi(k)}{\sigma(k)\tau} \qquad (5\text{-}19iii),$$

and

$$\gamma_H = \frac{[1 - \rho_o/\rho_m]\ \psi(k)}{\tau[1 - \psi(k)\ \rho_o/\rho_m]} \qquad (5\text{-}19iv).$$

Solving Equations (5-5i,ii), (5-9), and (5-17i,ii) in terms of the plate deflection $\overline{W}(\vec{k},s)$ gives

$$\overline{W}(\vec{k},s) = -\psi(k)\ \rho_o/\rho_m \left[\frac{s + \gamma_W}{s^2 + \alpha s + \beta}\right] L_o(\vec{k}) \qquad (5\text{-}20i)$$

where

$$\gamma_W = 1/\tau \tag{5-20ii}$$

and α and β are defined as before [Equations (5-19ii,iii)]. It can be immediately confirmed that if no erosion occurs, that is, $\sigma(k)\to\infty$, then $s^2+\alpha s+\beta \to s[s+\psi(k)/\tau]$ so that (5-20i) reduces to a form equivalent to (5-10).

For an elastic plate $\tau\to\infty$ and Equations (5-19i) and (5-20i) become

$$\overline{H}_e(\vec{k},s) = [1 - \psi(k)\rho_o/\rho_m]\ [s + \alpha_e]^{-1}\ L_o(\vec{k}) \tag{5-21i}$$

and

$$\overline{W}_e(\vec{k},s) = -\psi(k)\rho_o/\rho_m\ [s + \alpha_e]^{-1}\ L_o(\vec{k}) \tag{5-22}$$

where

$$\alpha_e = \frac{1 - \psi(k)\rho_o/\rho_m}{\sigma(k)} . \tag{5-21ii}$$

The inverse Laplace transforms of these expressions are [Roberts and Kaufman 1966, p. 189]

$$H_e(\vec{k},t) = [1 - \psi(k)\rho_o/\rho_m]\ \exp[-\alpha_e t]\ L_o(\vec{k}) \tag{5-23}$$

and

$$W_e(\vec{k},t) = -\psi(k)\rho_o/\rho_m \exp[-\alpha_e t]\, L_o(\vec{k}) \qquad (5\text{-}24).$$

Because $\psi(k)\leq 1$ [cf. Equation (3-5ii)] and $\rho_m > \rho_o$, α_e is always positive and therefore as $t\to\infty$ both $H_e(\vec{k},t)$ and $W_e(\vec{k},t)\to 0$ because of erosion. Note that there is no time dependence in the ratio $W_e(\vec{k},t)/H_e(\vec{k},t)$ because the exponential terms cancel one another and therefore the isostatic response [cf. Equations (3-10,11)] of an elastic plate with an eroding topographic load will be constant in time as expected.

Complete expressions for the eroding topography and resulting deformation of the viscoelastic plate are given by the inverse Laplace transforms of Equations (5-19i) and (5-20i) [e.g. Roberts and Kaufman 1966, p. 200] and are

$$H(\vec{k},t) = X_1(k,t)\, L_o(\vec{k}) \qquad (5\text{-}25i)$$

and

$$W(\vec{k},t) = Y_1(k,t)\, L_o(\vec{k}) \qquad (5\text{-}26i)$$

where [(5-25ii)]

$$X_1(k,t) = \begin{cases} \left[\dfrac{1-\psi(k)\rho_o/\rho_m}{r_2 - r_1}\right]\Big[[\gamma_H - r_1]\exp[-tr_1] - \\ \qquad [\gamma_H - r_2]\exp[-tr_2]\Big]; \quad \alpha^2 \neq 4\beta \\ [1-\psi(k)\rho_o/\rho_m]\Big[1 + [\gamma_H - \alpha/2]t\Big]\exp[-t\alpha/2]; \quad \alpha^2 = 4\beta \end{cases}$$

and [(5-26ii)]

$$Y_1(k,t) = \begin{cases} \left[\dfrac{-\psi(k)\rho_o/\rho_m}{r_2 - r_1}\right] \Big[[\gamma_W - r_1] \exp[-tr_1] - \\ \qquad [\gamma_W - r_2] \exp[-tr_2]\Big] \; ; \; \alpha^2 \neq 4\beta \\ [-\psi(k)\rho_o/\rho_m] \Big[1 + [\gamma_W - \alpha/2]t\Big] \exp[-t\alpha/2]; \; \alpha^2 = 4\beta \end{cases}$$

where $-r_1$ and $-r_2$ are the roots of $s^2+\alpha s+\beta=0$ and α and β are given in expressions (5-19ii,iii). $X_1(k,t)$ and $Y_1(k,t)$ are real for real or complex roots $-r_1$ and $-r_2$; the latter case, i.e., $\alpha^2-4\beta<0$, can be confirmed by inspection of (5-25ii) or (5-26ii) noting that r_1 and r_2, if complex, would be conjugate. That $X_1(k,t)$ and $Y_1(k,t)$ are real is, of course, simply a consequence of the assumption that $H(\vec{k},t)$, $W(\vec{k},t)$, and $E(\vec{k},t)$ and therefore $L_o(\vec{k})$ are spatially in phase. The form of the deformation of a uniform viscoelastic plate in response to eroding harmonic topography embodied by Equations (5-25,26) is referred to as Model 1.

5.2.5 Solution for a load resulting from erosion: Model 2. In Model 1 it was assumed that topography is suddenly applied to the lithosphere at t=0. It is implicit in such a model that even while tectonic processes are building the topography the underlying lithosphere has a large degree of flexural strength. This may not be realistic if orogeny is accompanied by thermal weakening of the lithosphere and if the orogenic processes occur over a period of time which is likely short compared to the cooling time of continental lithosphere [e.g. Sclater et al. 1980]. It may be that during this time, as topography is created and modified, the lithosphere is unable to sustain flexural stresses resulting from vertical loading of wavelengths as great as those of interest here. Thus, as the tectonic regime responsible for the orogenic episode dissipates, the topographic load existing at the end of the orogeny may be locally compensated by low density crustal roots. Concurrently and subsequently, the lithosphere cools and, ultimately, will attain flexural competence at the wavelengths of interest. The crustal roots compensating the topography may in this way become "frozen" into the cooled and thickened continental lithosphere as they apparently do in oceanic lithosphere. In oceans, surficial topography created at or near ridge crests where the lithosphere is very thin appears always to be locally compensated by crustal thickening regardless of its age. On the other hand, new topographic loads applied to old, cooled and thickened, oceanic lithosphere result in a flexural isostatic response [Watts 1978, Cochran 1979, Detrick and Watts 1979]. Heat flow [Pollack and Chapman 1977, Sclater et al. 1980] and seismological data [Kono and Amano 1978] suggest that continental lithosphere thickens with age in a fashion similar to oceanic lithosphere. Ocean crust topography does not significantly erode. On continents, however, if a load with "frozen in" local compensation is partially eroded after the time at which the lithosphere acquires flexural competence, the resulting negative load will be compensated flexurally. There is some support for this kind of model found in the comparison of isostatic response functions calculated for the Eastern and Western United States [McNutt 1980]. Topography in the western region, which is tectonically much younger, appears to be more locally compensated than in the older eastern region where there is some suggestion that crustal roots are overcompensating the "available" topography.

This alternative model of the evolution of the isostatic character of continental lithosphere resulting from erosion, referred to as Model 2, can be quantified by making only minor revisions to the system of equations developed for Model 1 in subsection 5.2.4. Assume that at a time $t_c>0$ the lithosphere suddenly becomes competent and that at t_c it supports a locally compensated surface load $L_\ell(\vec{k})$; t_c is presumed to occur a sufficiently long time after orogenesis such that most of the associated thermal anomaly has been dissipated. $L_\ell(\vec{k})$ can be partitioned, in the usual manner, into (1) measurable topography $H_\ell(\vec{k})$ and (2) the locally compensating "root" $W_\ell(\vec{k})$. It is known from Equation (3-14) that $W_\ell(\vec{k}) \doteq -\rho_o/\Delta\rho \; H_\ell(\vec{k})$ where $\Delta\rho$ is the density contrast at the base of the root [cf. subsection 3.2.3]. Any erosion occurring prior to $t=t_c$ is inconsequential because it is assumed to have been compensated locally. In terms of the subsequent dynamic evolution of the lithosphere, $H_\ell(\vec{k})$ may be thought of as being suddenly applied to a thin viscoelastic plate at t_c. $H_\ell(\vec{k})$ is not a load resulting in flexural stresses, however, because of the low density compensating root assumed to accompany it. The plate at this time is taken to be in an undeformed state. Subsequent erosion $E(\vec{k},t)$, $t>t_c$, producing eroded topography $H(\vec{k},t)$, is assumed to result in flexural rebound $W(\vec{k},t)$. A mass wasting condition, analogous to Equations (5-8) of Model 1, may be adopted such that

$$H_\ell(\vec{k},t) = H(\vec{k},t) - W(\vec{k},t) - E(\vec{k},t) = \begin{cases} 0; & t<t_c \\ H_\ell(k); & t\geq t_c \end{cases} \qquad (5\text{-}27);$$

it is schematically illustrated in Figure 5-3.

Model 2, in a manner similar to Model 1, can be formalized in terms of the linear system shown in Figure 5-4. The function $H_\ell(\vec{k},t)$ drives the system inasmuch as it is its erosion which results in isostatic plate deformation which in turn modifies the topography being eroded. Figure 5-4 shows that

$$\overline{H}(\vec{k},s) = N_2(k,s)\ \overline{H}_\ell(\vec{k},s) \qquad (5\text{-}28i)$$

where the closed loop network transfer function is

$$N_2(k,s) = \frac{A_2(k,s)}{1 - A_2(k,s)\ B(k,s)} \qquad (5\text{-}28ii).$$

The input $\overline{H}_\ell(\vec{k},s)$ is given by the Laplace transform of (5-27):

$$\overline{H}_\ell(\vec{k},s) = \overline{H}(\vec{k},s) - \overline{W}(\vec{k},s) - \overline{E}(\vec{k},s) = \frac{\exp[-t_c s]}{s} H_\ell(\vec{k}) \qquad (5\text{-}29).$$

The relationship between erosion and topography assumed for Model 1 is unchanged [Equations (5-17)]. However, the effective plate load is now assumed to be the erosion so that Equation (5-5i) becomes

$$\overline{W}(\vec{k},s) = T_I(k,s)\ \overline{E}(\vec{k},s) \qquad (5\text{-}30).$$

Figure 5-3. Schematic drawing of the erosion E of locally compensated harmonic topography H between t_c and t_1 according to Model 2; the original, locally compensating lithosphere is stippled. The effective surface load at any time consists of E and results in lithospheric deformation $\tilde{W}$ [Equation (5-30)]; the sum H-W-E is constant in time [Equation (5-27)].

Model 2

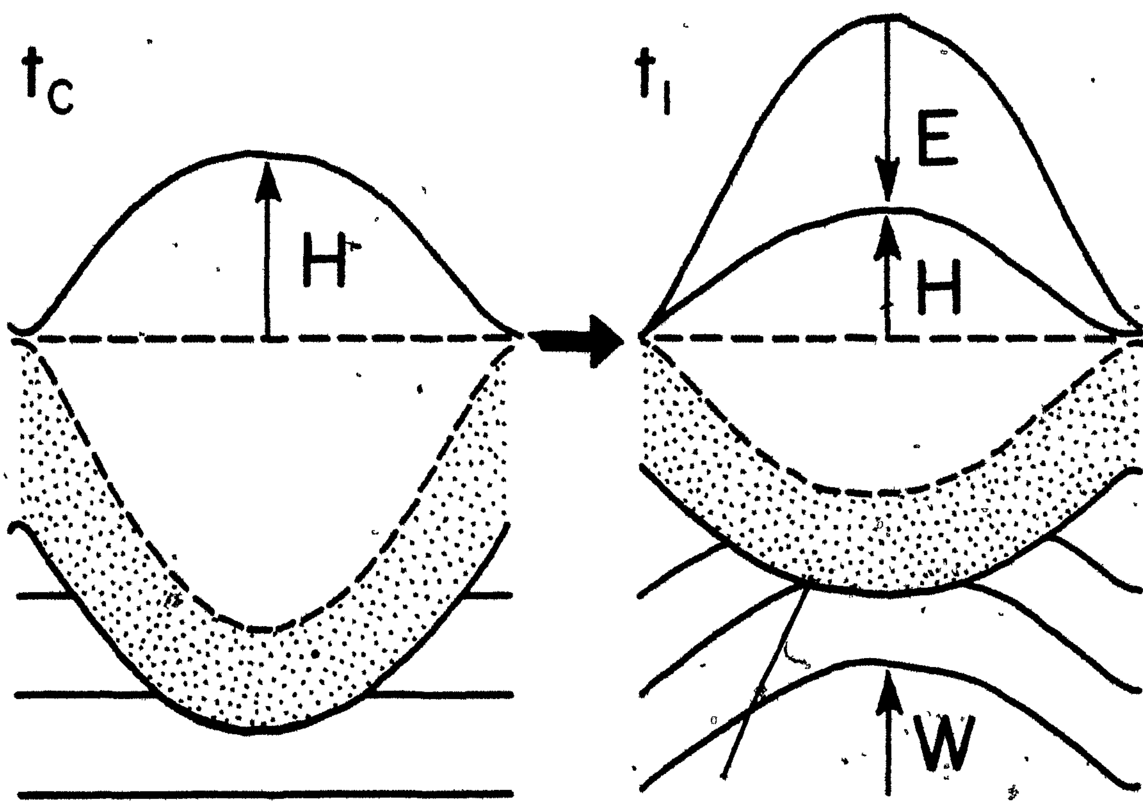

Figure 5-4. Linear filter network with feedback describing Model 2. Filter characteristics are explained in the text [subsection 5.2.5].

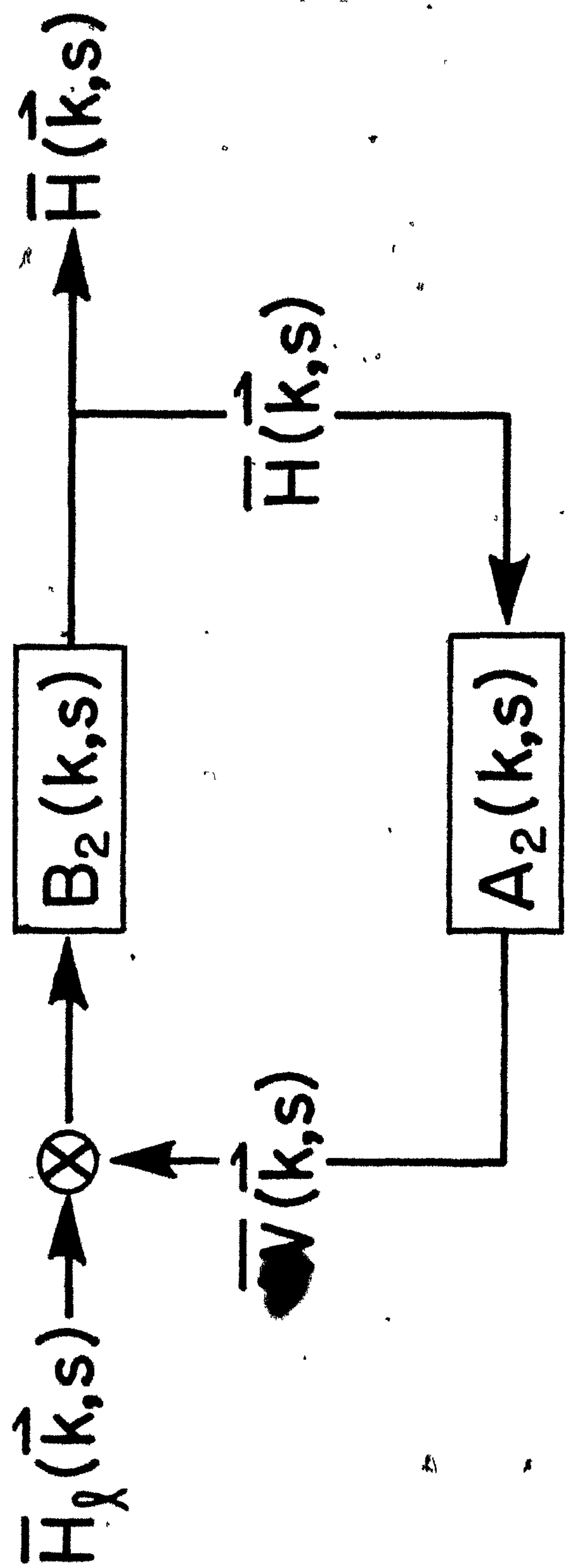

Model 2

According to Figure 5-4

$$\overline{H}(\vec{k},s) = B_2(k,s)\ [\overline{H}_\ell(\vec{k},s) + \overline{W}(\vec{k},s)] \tag{5-31}$$

and

$$\overline{W}(\vec{k},s) = A_2(k,s)\ \overline{H}(\vec{k},s) \tag{5-32}$$

Equation (5-17i) can be manipulated to give

$$\overline{H}(\vec{k},s) = [1 - T_E(k,s)]^{-1}\ [\overline{H}(\vec{k},s) - \overline{E}(\vec{k},s)] \tag{5-33}$$

but from (5-29) it is known that $\overline{H}(\vec{k},s)-\overline{E}(\vec{k},s)=\overline{H}_\ell(\vec{k},s)+\overline{W}(\vec{k},s)$ and, therefore, comparing Equations (5-31) and (5-33),

$$B_2(k,s) = [1 - T_E(k,s)]^{-1} .$$

Combining Equations (5-17i) and (5-30) gives

$$\overline{W}(\vec{k},s) = T_I(k,s)\ T_E(k,s)\ \overline{H}(\vec{k},s) \tag{5-34}$$

and it is seen immediately from (5-32) and (5-34) that

$$A_2(k,s) = T_I(k,s)\ T_E(k,s) .$$

The Model 2 network transfer function $N_2(k,s)$ is therefore known and Equation (5-28i) can be rewritten

$$\overline{H}(\vec{k},s) = [1 - T_I(k,s)\ \dot{T}_E(k,s) - T_E(k,s)]^{-1}\ \overline{H}_\ell(\vec{k},s) \qquad (5\text{-}35).$$

Making the appropriate substitutions results in

$$H(\vec{k},s) = \exp[-t_c s]\left[\frac{s + \psi(k)/\tau}{s^2 + \alpha s + \beta}\right] H_\ell(\vec{k}) \qquad (5\text{-}36)$$

where α and β are the same as for Model 1 [Equations (5-19ii,iii)]. Solving for $\overline{W}(\vec{k},s)$ gives

$$W(\vec{k},s) = \psi(k)\rho_o/\rho_m \exp[-t_c s]\ [\sigma(k)]^{-1}\left[\frac{s + 1/\tau}{s[s^2 + \alpha s + \beta]}\right] H_\ell(\vec{k}) \quad (5\text{-}37).$$

If there is no erosion after t_c, that is, $\sigma(k)\to\infty$; $\overline{W}(\vec{k},s)\to 0$ and, therefore, $W(\vec{k},t)\to 0$ as is expected. Similarly, as $\sigma(k)\to\infty$, $\overline{H}(\vec{k},s)$ $\to\exp[-t_c s]/s$ and therefore $H(\vec{k},t)\to H_\ell(\vec{k},t)$ as defined by (5-27).

For an elastic plate, that is, $\tau\to\infty$, Equations (5-36) and (5-37) become

$$\overline{H}_e(\vec{k},s) = \exp[-t_c s]\ [s + \alpha_e]^{-1}\ H_\ell(\vec{k}) \qquad (5\text{-}38)$$

and

$$\overline{W}'_e(\vec{k},s) = \psi(k)\rho_o/\rho_m \exp[-t_c s]\ [\sigma(k)]^{-1}\left[s[s + \alpha_e]\right]^{-1} H_\ell(\vec{k}) \qquad (5\text{-}39)$$

where α_e is defined as before [Equation (5-21ii)]. The inverse Laplace transforms of Equations (5-38) and (5-39) can be found from tables

[Roberts and Kaufman 1966, pp. 181, 189] and the convolution theorem of Laplace transforms,

$$L^{-1}\{\overline{F}(s)\ \overline{G}(s)\} = \int_o^t F(u)\ G(t-u)\ du$$

[where $L^{-1}\{\overline{F}(s)\} = F(t)$ and $L^{-1}\{\overline{G}(s)\} = G(t)$]. They are

$$H_e(\vec{k},t) = \exp[-\alpha_e\ (t-t_c)]\ H_\ell(\vec{k}) \qquad (5\text{-}40)$$

and

$$W_e(\vec{k},t) = \frac{\psi(k)\rho_o/\rho_m}{1-\psi(k)\rho_o/\rho_m}\left[1-\exp[-\alpha_e\ (t-t_c)]\right] H_\ell(\vec{k}) \qquad (5\text{-}41).$$

Note, as would be expected because of progressive erosion, that as $t\to\infty$, $H_e(\vec{k},t)\to 0$ but that a remnant crustal root will persist:

$$\lim_{t\to\infty} W_e(\vec{k},t) = \frac{\psi(k)\rho_o/\rho_m}{1-\psi(k)\rho_o/\rho_m}\ H_\ell(\vec{k}) \qquad (5\text{-}42).$$

Complete expressions for $H(\vec{k},t)$ and $W(\vec{k},t)$ predicted by Model 2 [Roberts and Kaufman 1966, pp. 183, 199] are

$$H(\vec{k},t) = X_2(k,t)\ H_\ell(\vec{k}) \qquad (5\text{-}43i)$$

and

$$W(\vec{k},t) = Y_2(k,t)\ H_\ell(\vec{k}) \qquad (5\text{-}44i)$$

where [(5-43ii)]

$$X_2(k,t) = \begin{cases} [\psi(k)/\tau - r_1] \exp[-(t-t_c)r_1] - [\psi(k)/\tau - r_2] \cdot \\ \quad \cdot \exp[-(t-t_c)r_2]; \ \alpha^2 \neq 4\beta \\ \exp[-(t-t_c)\alpha/2] \ [1 - t\alpha/2 + t\psi(k)/\tau]; \ \alpha^2 = 4\beta \end{cases}$$

and [(5-44ii)]

$$Y_2(k,t) = \begin{cases} \dfrac{\rho_o}{\Delta\rho} \left[1-\beta \left[\dfrac{[1/r_1-\tau]\exp[-(t-t_c)r_1]-[1/r_2-\tau]\exp[-(t-t_c)r_2]}{r_2 - r_1} \right] \right]; \\ \qquad \alpha^2 \neq 4\beta \\ \dfrac{\rho_o}{\Delta\rho} \left[1 - \exp[-(t-t_c)\alpha/2][1 + t\alpha/2 - t\beta\tau] \right] \ ; \ \alpha^2 = 4\beta \end{cases}$$

where $\Delta\rho = \rho_m - \rho_o$; $-r_1$ and $-r_2$ are the quadratic roots of $s^2+\alpha s+\beta=0$ as for Model 1.

5.2.6 Theoretical isostatic response functions. (i) Model 1. The theoretical plate deformation $W(\vec{k},t)$ and measurable topography $H(\vec{k},t)$ for Model 1 are provided by Equations (5-25) and (5-26). The theoretical gravity anomaly $G(\vec{k},t)$ arising from the resultant density perturbation can be calculated from $W(\vec{k},t)$ using Equation (3-10); $G(\vec{k},t)$ normalized by $H(\vec{k},t)$ provides the theoretical isostatic response $Q(k,t)$, a function of time. Although both $W(\vec{k},t)$ and $H(\vec{k},t)$ depend on $L_o(\vec{k})$ no knowledge of the latter is required since isostatic response varies with the ratio of the deformation to the topography.

(ii) Model 2. The density perturbation contributing to $G(\vec{k},t)$ in the case of Model 2 is assumed to be directly attributable to the initial locally compensating deformation $W_\ell(\vec{k})$ less the rebound deformation $W(\vec{k},t)$ resulting from erosion [Equations (5-44)]. The net deformation and consequent $G(\vec{k},t)$ depend on $H_\ell(\vec{k})$ since $W_\ell(\vec{k}) = -\rho_o/\Delta\rho$ $H_\ell(\vec{k})$. No knowledge is required of $H_\ell(\vec{k})$ to calculate $Q(k,t)$ since $H(\vec{k},t)$ is also dependent on $H_\ell(\vec{k})$ [Equations (5-43)]. Note the implication of Equation (5-41) that an elastic plate in Model 2 predicts an infinitely large $Q(k,t)$ as $t\to\infty$.

5.3 North American Topography and Model Predictions

5.3.1 Introduction. Two models, based on thin plate theory and an hypothesized linear erosion model, have been described which predict the change through time of the amplitude of isostatically compensated eroding topography $H(\vec{k},t)$ and its associated isostatic plate deformation $W(\vec{k},t)$. Assumptions related to the nature of the density structure of the lithosphere and the generation of gravity anomalies by $W(\vec{k},t)$ [cf. subsection 3.2.2] allows the calculation of the predicted time-dependent isostatic response function $Q(k,t)$ of each of the models. Because of these requisite additional assumptions and the inherent noisiness of observed gravity anomalies, the models are first tested by direct comparison of predicted and observed topography power spectra.

5.3.2 <u>Topography power spectra</u>. The two-dimensional topography power spectra estimates of the Cordilleran, Appalachian, Grenville, Churchill, and Superior ~~data~~ sets [section 2.1] have been computed using the methodology described in section 2.2 for constant wavenumber bandwidth of 0.001 km^{-1} and a directional arc length of 45^o, with estimates centred on the x and y axes and the 45^o diagonals. The four directionally independent spectra calculated thus, for each of the five listed study areas are presented in Figures 5-5(a-e). For each wavenumber at which spectral estimates exist the upper 95% confidence bound of the largest and the lower 95% confidence bound on the smallest of the four directional estimates are plotted [cf. Equation (2-7)]. The number of raw spectral data in each directional ensemble quadrant is approximately constant with the result that the 95% confidence interval for each is also approximately constant. It can be seen from Figures 5-5 that nowhere among the five sets of computed spectra is a single spectral estimate for a given direction with 95% confidence significantly different from all three of the other spectral estimates at the same wavenumber but in different directions.

In each geological region more spectral power may be expected to reside in the direction perpendicular to the structural grain [for example, east-west, parallel to the x-axis, in the case of the Cordilleran region] than in the direction parallel to strike. This is somewhat the case in the Appalachian region [Figure 5-5(b)], and to a lesser degree in the Grenville structural province [Figure 5-5(c)], but otherwise does not strongly prevail. The topographic power of the Cordilleran region is quite isotropic and is actually strongest in the

Figure 5-5. The observed topography power spectra $\hat{S}_H$ of the (a) Cordilleran, (b) Appalachian, (c) Grenville, (d) Churchill, and (e) Superior province study areas as functions of $\vec{k}$. Spoke orientations, e.g. ⊘, refer to $\vec{k}$ directions relative to the orientation of the boundaries of the respective study areas [cf. Figure 2-1]. The upper and lower 95% confidence limits refer to the largest and the smallest of the four directional spectral estimates for each observed k_r.

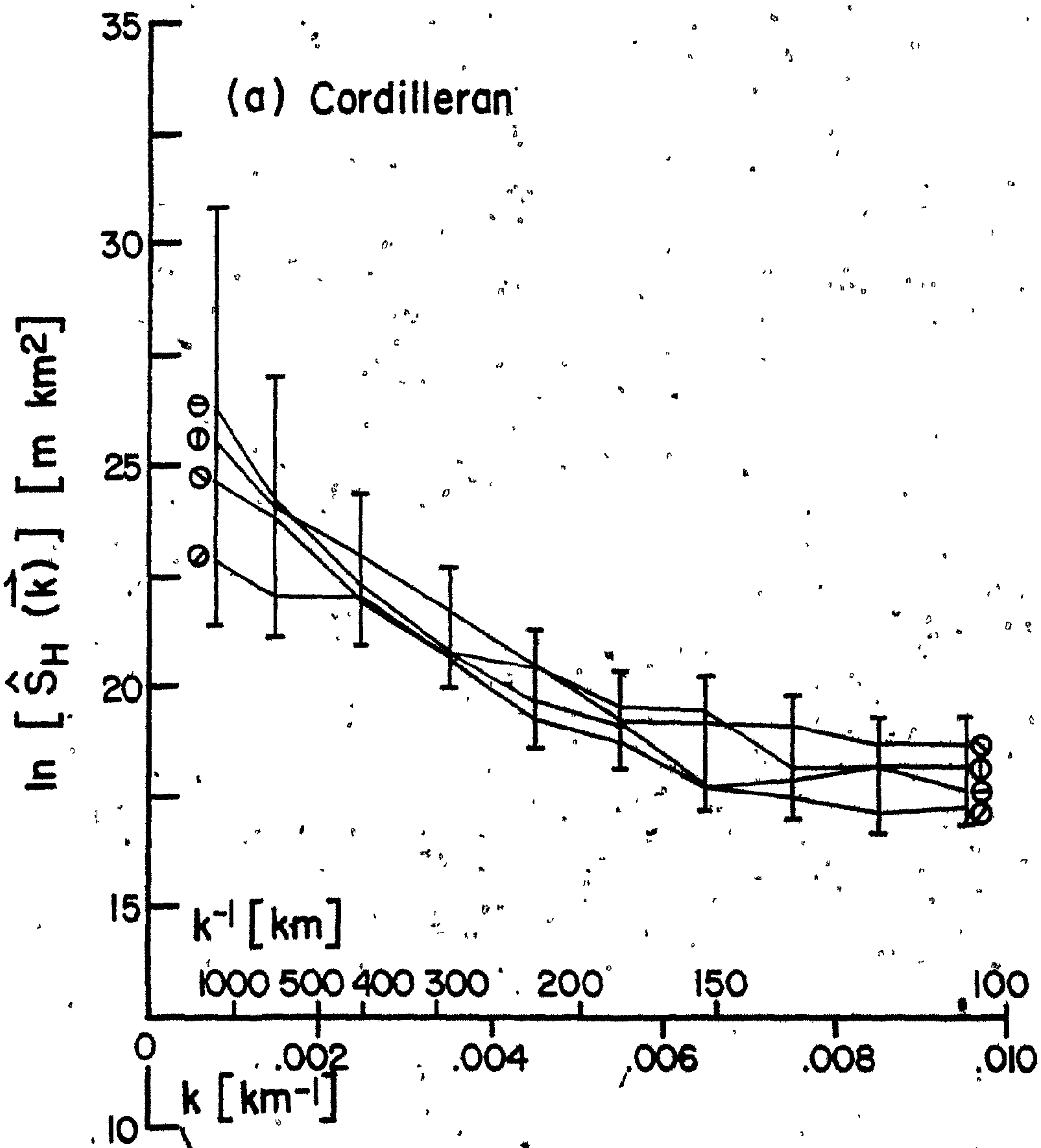
(a) Cordilleran
35
30
25
20
15
10
ln [$\hat{S}_H$ (k)] [m km^2]
k^{-1} [km]
1000 500 400 300 200 150 100
0 .002 .004 .006 .008 .010
k [km^{-1}]

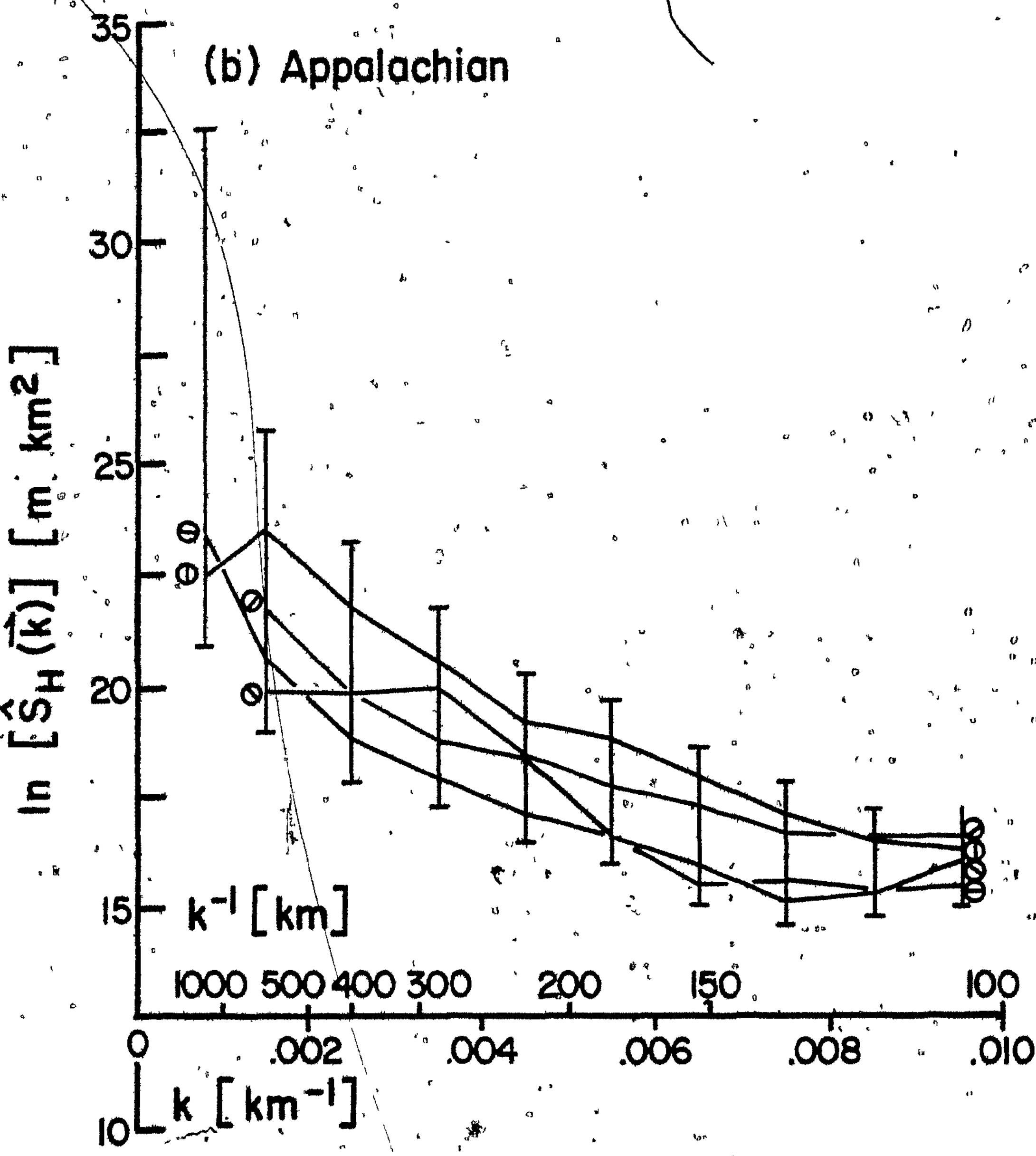
(b) Appalachian
35
30
25
20
15
10
ln [$\hat{S}_H(\vec{k})$] [m. km^2]
k^{-1} [km]
1000 500 400 300 200 150 100
0 .002 .004 .006 .008 .010
k [km^{-1}]

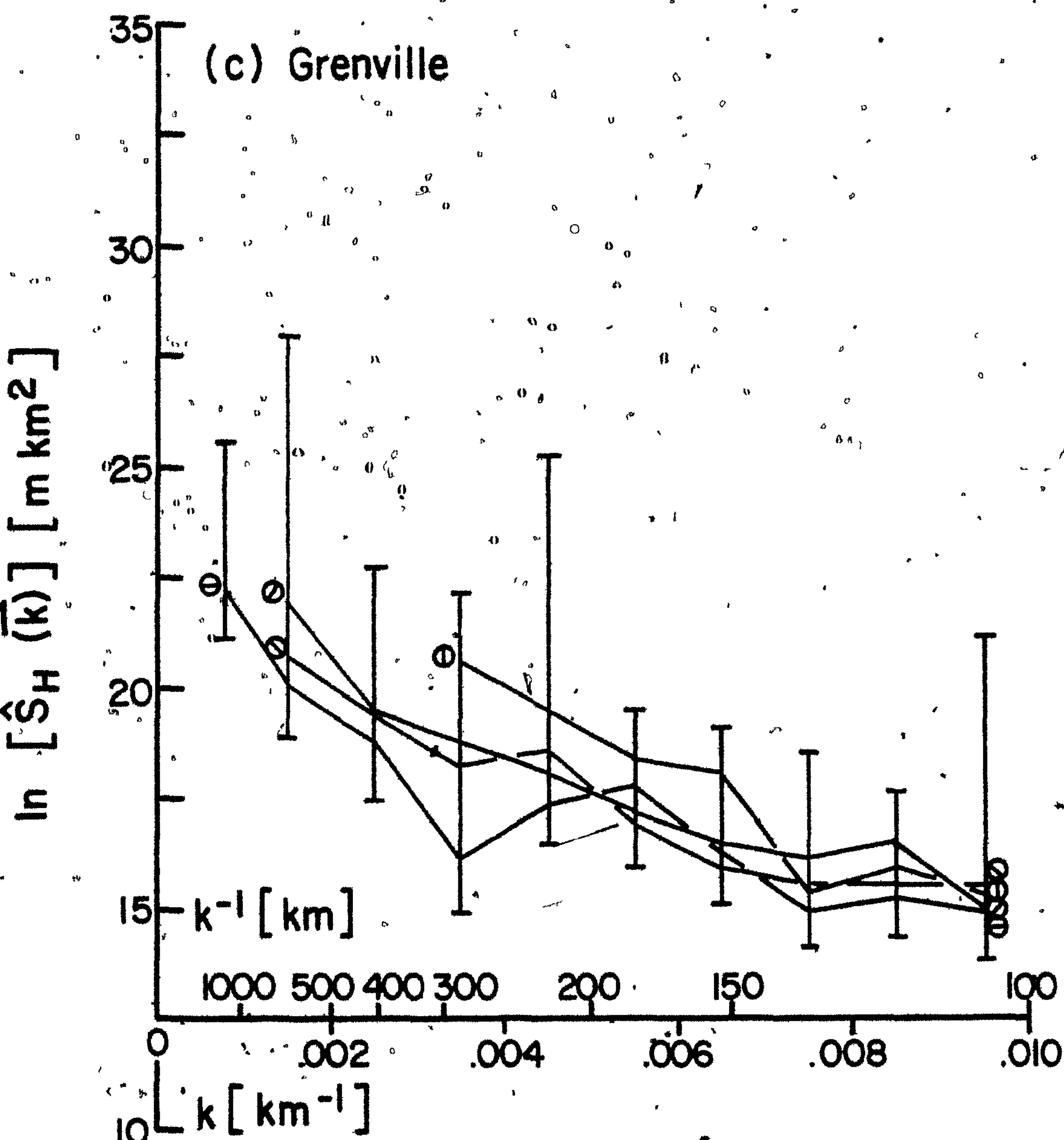
(c) Grenville
ln $[\hat{S}_H(\vec{k})]$ [m km^2]
35
30
25
20
15
10
k^{-1} [km]
1000 500 400 300 200 150 100
0 .002 .004 .006 .008 .010
k [km^{-1}]

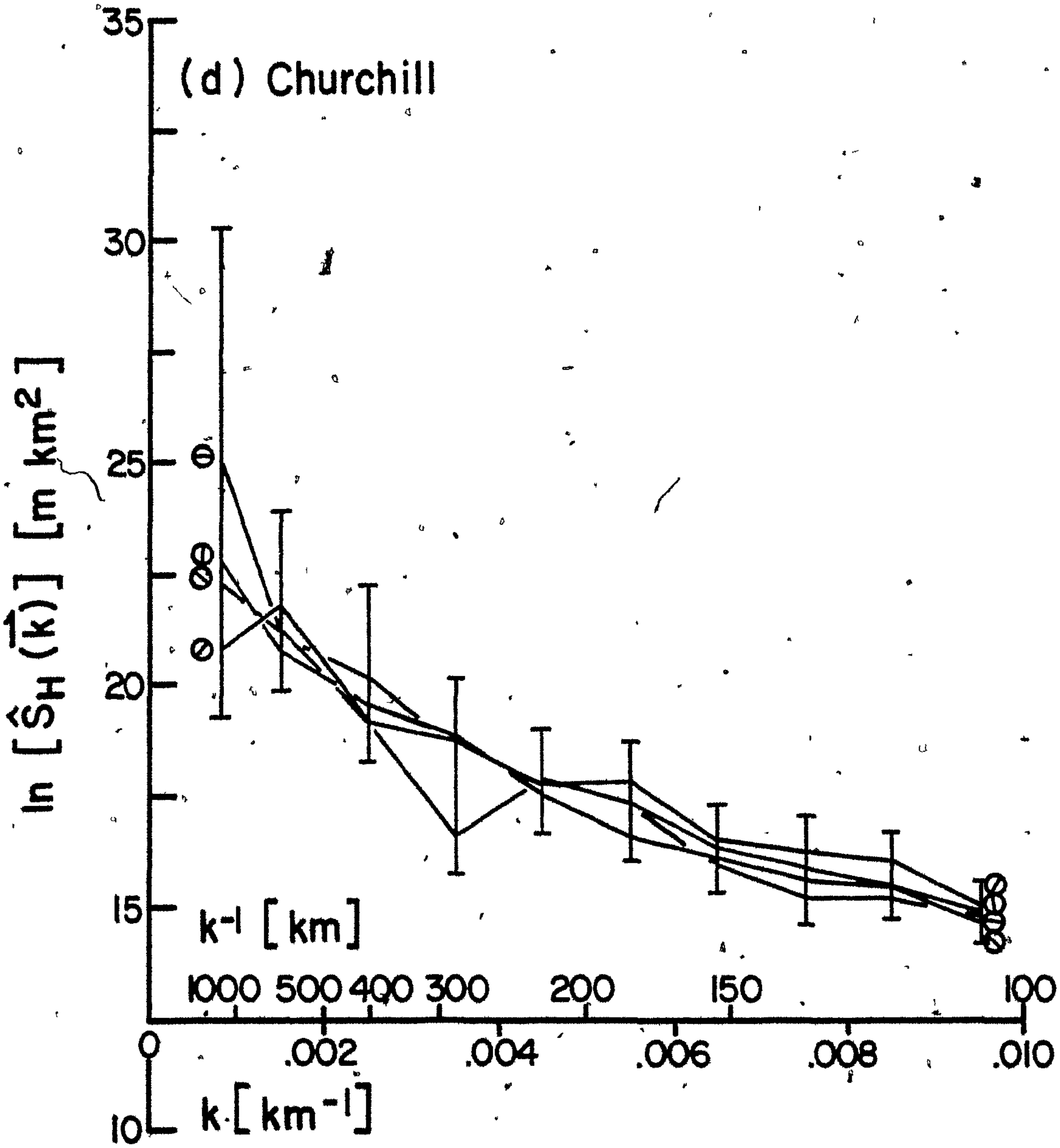

(d) Churchill
35
30
25
20
15
10
$\ln [\hat{S}_H(\vec{k})]$ [m km^2]
k^{-1} [km]
1000 500 400 300 200 150 100
0 .002 .004 .006 .008 .010
k [km^{-1}]

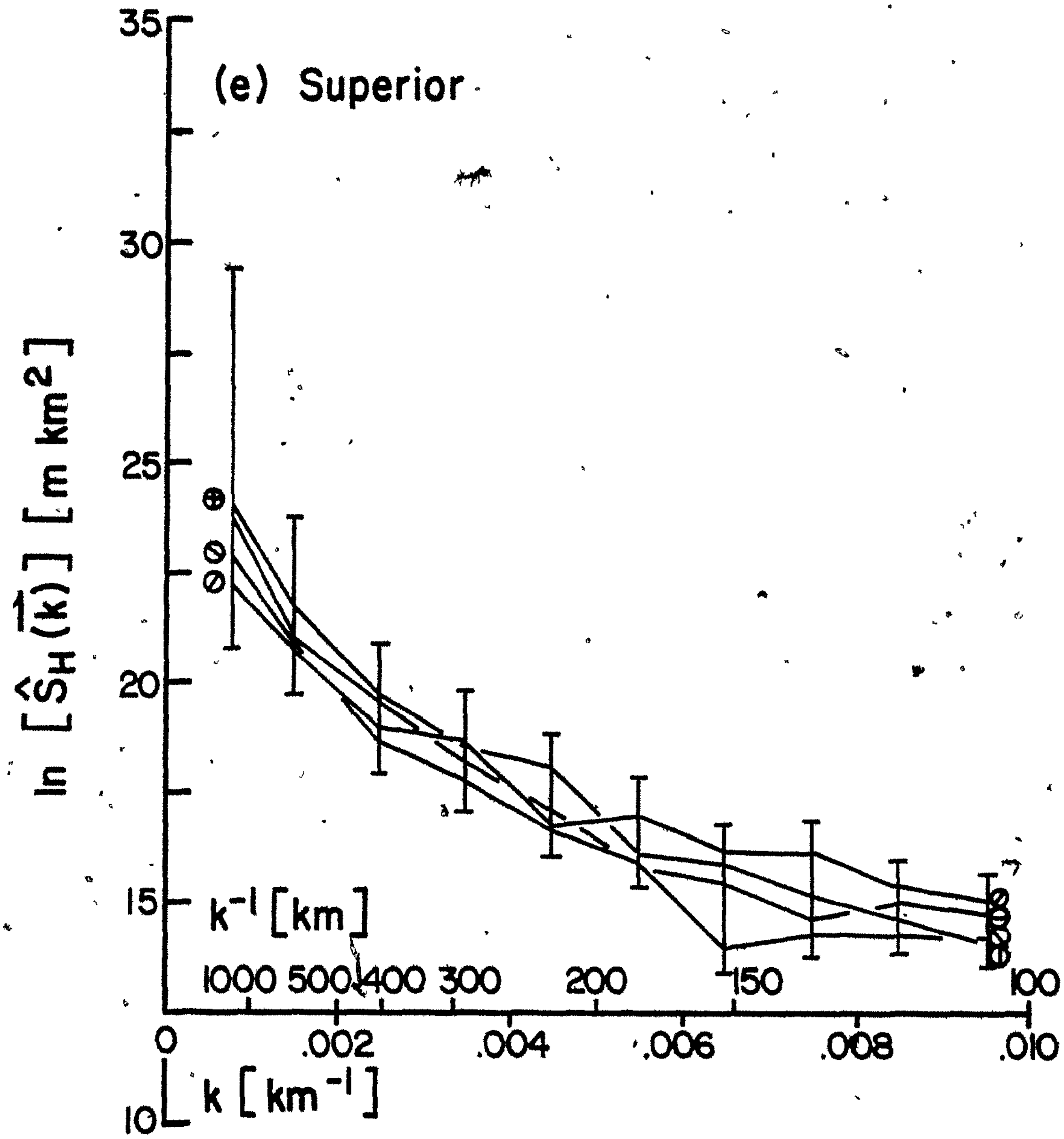
(e) Superior
35
30
25
20
15
10
ln [$\hat{S}_H(\vec{k})$] [m km^2]
k^{-1} [km]
1000 500 400 300 200 150 100
0 .002 .004 .006 .008 .010
k [km^{-1}]

strike direction at some of the intermediate wavenumbers [Figure 5-5(a)], a result comparable to the space domain distribution of Cordilleran topography illustrated in Figure 2-2(a). The structurally complex Churchill and Superior provinces are seen to be essentially isotropic in their topographic character [Figures 5-5(d,e)].

The general degree of topographic isotropy of the five study areas was considered sufficient to permit ensemble averaging of the raw spectral data of each through all directions of $\vec{k}$ with the resulting averaged spectra being considered to be reliable indicators of each region's inherent topographic character. These five annularly averaged spectra are presented in Figure 5-6; 95% confidence bounds have been omitted from the Grenville and Churchill spectra for the sake of clarity but are approximately the same size as the others. Examination of Figure 5-6 shows that, as would be expected, the power of topography of various wavenumbers k is generally smaller for regions of relatively greater tectonic age. The observed data for each k are to be separately considered as functions of time. Thus, the age of the topography of each sampled geological province needs to be determined. In order to compare the topography of the various provinces in this way, it is necessarily assumed that the spectral configuration of the topography of each was initially approximately the same, the implication of this being that mountain-building processes have not significantly changed since the Archean. Because the anisotropy of topography, as discussed above, is not being considered no geographic orientation of the data sets is required.

Figure 5-6. The observed topography power spectra $\hat{S}_H$ as functions of $|\vec{k}|$. For clarity the 95% confidence intervals of the Grenville [G] and Churchill [C] spectra are omitted but are approximately the same size as the others.

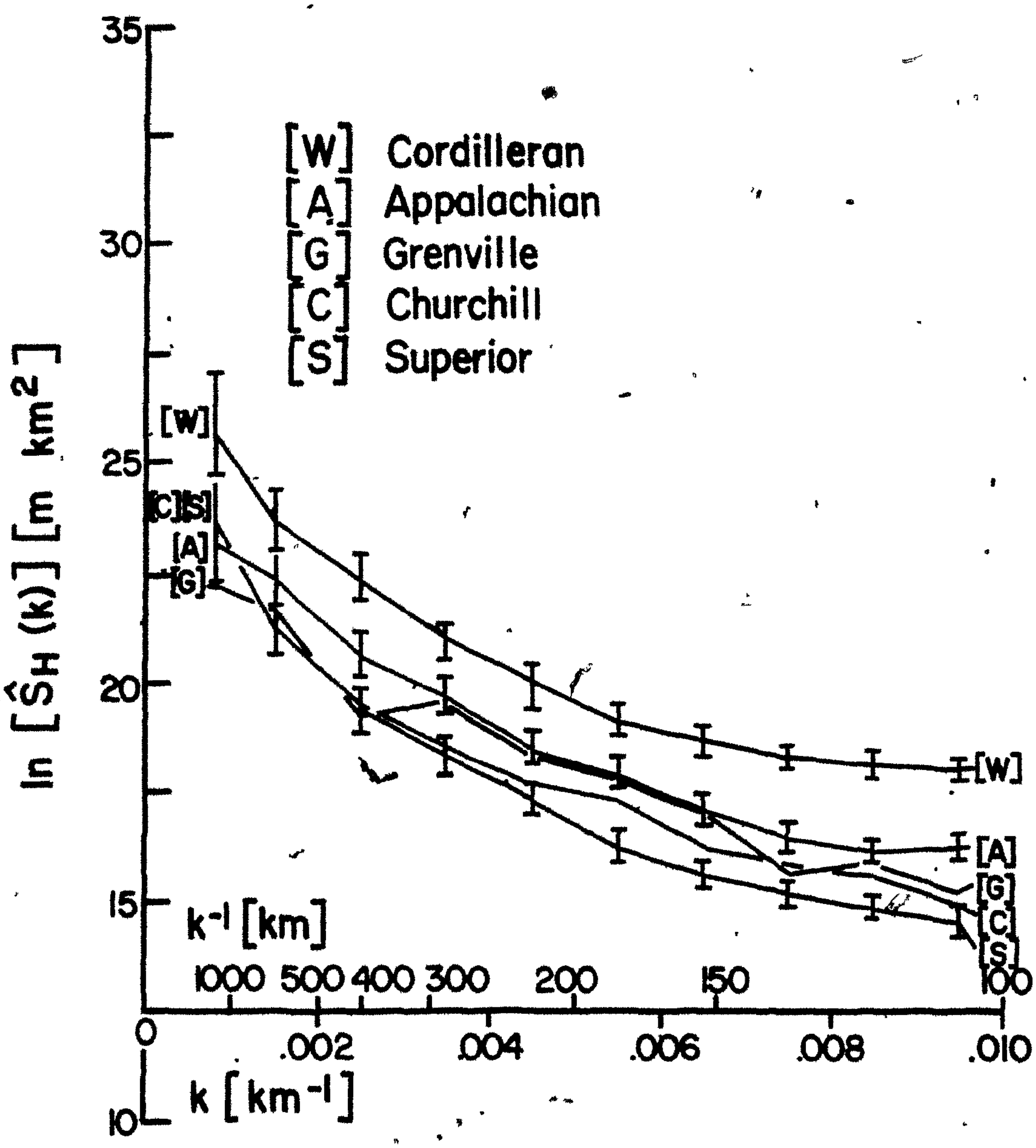
[W] Cordilleran
[A] Appalachian
[G] Grenville
[C] Churchill
[S] Superior
$\ln [\hat{S}_H(k)]$ [m km^2]
35
30
25
20
15
10
[W]
[C][S]
[A]
[G]
k^{-1} [km]
1000 500 400 300 200 150 100
0 .002 .004 .006 .008 .010
k [km^{-1}]
[W]
[A]
[G]
[C]
[S]

5.3.3 Age of North American topography. The production of continental crust, or at least the determination of its structure and topography, occurs during successive periods of orogeny taking place over hundreds of millions of years. In terms of the simple models of post-orogenic topographic evolution being considered at present, the rheology and isostatic character of the continental lithosphere during the orogenic phase of its development, no doubt very complex, is intractable. In Model 1, it is implicitly assumed that by the end of the orogenic phase a competent lithosphere exists which underlies the topography produced by the orogeny and that, up until this time, this topography was supported by the tectonic forces inherent in its construction. Thus, the age of the topography would be the age of the last orogenic pulse, after which it is assumed the tectonic forces rapidly dissipate. In Model 2, on the other hand, the lithosphere is assumed to be thermally weakened at this time such that as tectonic forces vanish the remnant topography exists in a state of local isostatic compensation. Then, after some length of time during which cooling, as well as erosion, has taken place, the lithosphere acquires rheological properties assumed to persist until the time of observation. Thus, the characteristic age of the topography used in the Model 2 analysis should be less than in Model 1 by an amount related to the cooling efficiency of the lithosphere. In the present case, however, in which the topography being considered, with the exception of that of the Cordilleran region, is geologically very old and the timing of respective termination of orogenesis only approximate, the same ages of topography will be assumed for both models.

(i) Cordilleran region. The most recent deformational event affecting the crust of the Cordilleran study area was the Laramide orogeny which began near the beginning of the Cenozoic era, ~65 Ma ago. In the Canadian portion of the study area it had, for the most part, ended early in the Oligocene, ~35 Ma ago [Douglas et al. 1970], although uplift of the Coast Mountains, based on mapping of deformed erosion surfaces, persisted until the Pliocene, ~2-7 Ma ago [Wheeler and Gabrielse 1972]. The United States portion of the study area is dominated by the Basin and Range province, the present mountain ranges of which having formed since the early Miocene, ~20-25 Ma ago [Hamilton and Myers 1966]. The relief of the Rocky Mountains, east of the Basin and Range province, was primarily developed during an uplift phase in the late Pliocene [Stearn et al. 1979]. Volcanic construction of topography persists until the present.

Essentially, the Cordilleran region of North America is one which is currently tectonically active [e.g. Atwater 1970, Hamilton and Myers 1966] and, for the purposes of the present analysis, in which its topographic character is compared with that of regions very much older, it shall be considered to have not yet entered a period of post-tectonic erosional and isostatic evolution. Thus, in terms of Model 1 or 2, the observed topography power spectrum of the Cordilleran study area is assumed to be equivalent to $[1-\psi(k)\rho_o/\rho_m]^2\ |L_o(\vec{k})|^2$ or $|H_\ell(\vec{k})|^2$ respectively.

(ii) Appalachian region. The most recent orogenic episodes affecting the Appalachian structural province were the Acadian in the north during the Devonian period, 350-400 Ma ago, and the Alleghanian in the south during the late Paleozoic, 250-300 Ma ago [Stearn et al. 1979]. The differential timing of Appalachian deformation was a result of the progressive closure of the Iapetus [Protoatlantic] Ocean from north to south with consequent continental collision. There is some question whether the long wavelength features of Appalachian topography derive mainly from these Paleozoic orogenies or whether they were strongly influenced by events associated with the rifting of Pangea and the early formation of the Atlantic Ocean during the Mesozoic [e.g. King 1972]. The former shall be assumed here and a median age of 300-350 Ma assigned to the topography of the Appalachian study area. Considerable erosion of the Appalachians had already occurred by the time of Mesozoic continental rifting [Stearn et al. 1979] and it is assumed that the uplift associated with the thermal origin of the rifting was broad and uniform enough so as not to greatly affect the spectral configuration of the pre-existing topography.

(iii) Canadian Shield. The topographic character of the Grenville, Churchill, and Superior structural provinces of the Canadian Shield may be assumed to derive from the Grenvillian, Hudsonian, and Kenoran orogenies dating respectively from ~900-1100 Ma, ~1600-1800 Ma, and ~2400-2600 Ma [Stockwell 1964].

Ambrose [1964] discusses at length evidence that the present erosional topography of the Canadian Shield was developed in pre-Paleozoic time and that the basic drainage pattern of the Shield, which may be presumed to exert significant control on the long wavelength features of the topography, such as those of interest here, is at least as old. His study is based for the most part on the nature of the topography adjacent to and beneath flat-lying early Paleozoic outliers which are widely distributed throughout the Shield. Ambrose also states, based on the same kinds of observations, that "erosion of bedrock during Pleistocene glaciation was minor or negligible" [p. 851], a position supported by many other authors [e.g. Gravenor 1975, Sugden 1976, Andrews and Miller 1979] although detractors do exist [e.g. White 1972].

Although the large scale topography of the Canadian Shield structural provinces can with reasonable confidence be assumed to be tectonic in origin and vary in age according to the most recent effective orogenic event, the existence of early Paleozoic, mainly Ordovician, outliers throughout the Shield, and preservation of large tracts of early Paleozoic strata beneath Hudson Bay and adjacent areas, indicates that a widespread erosional hiatus occurred during a period of 100-200 Ma ending at the latest in the Middle Devonian, approximately 375 Ma ago [Ambrose 1964]. In consideration of the models of very long term topographic evolution being examined here, the length of the inferred non-erosional period is relatively short: the erosional hiatus affects no more than 20% of the life span of the Grenville topography and perhaps as little as 4% of that of the Superior. Geological observations indicate that ~~most~~ of the erosion of the Canadian Shield structural provinces, as they exist at present, occurred prior to the Paleozoic erosional hiatus [Ambrose 1964]. It is expected that the results of the models will be compatible with this observation because it has been assumed in the models that erosion rate at any time is proportional to the height of the topography remaining at that time.

The overall effect of the hiatus on the ability of the models to reproduce the erosional and topographic evolution of the study areas is therefore assumed to be negligibly small. A related problem is that parts of the Churchill and Superior study areas are still overlain by Paleozoic sediments [cf. Figure 2-1]. However, in each case the extent of the cover is less than ~20% and it can be assumed that the observed topographic power spectrum of each is dominated by the cratonic portion of the topography. That the topographic power of the younger Churchill study area is generally greater than that of the Superior [cf. Figure 5-6] is evidence of the validity of this assumption.

5.3.4 Observed topography decay functions. The observed topography power spectrum of the Cordilleran region of North America has been assumed to characterize, in terms of either Model 1 or 2, the spectral configuration of initial topography $[1-\psi(k)\rho_o/\rho_m]^2|L_o(\vec{k})|^2$ or $|H_\ell(\vec{k})|^2$ existing at t=0 or t=t_c respectively. In order to avoid further explicit consideration of $L_o(\vec{k})$ or $H_\ell(\vec{k})$ the power spectral estimates $\hat{S}_H(k)$ of the five study areas graphed in Figure 5-6 have been normalized by the Cordilleran observations. The normalized estimates, referred to as $\hat{S}_H'(k)$ are replotted in Figures 5-7(a-j) as functions of the assumed age of the topography [cf. subsection 5.3.3] for each of the observed spectral wavelengths k_r^{-1}.

Examination of Figures 5-7(a-j) shows that, in general, (1) topographic power at a given wavenumber decreases with age and that most of the reduction occurs during the first few hundred million years

Figure 5-7. Normalized topography decay data $\hat{S}'_H$ [cf. text], with 95% confidence intervals, observed at spectral wavelengths (a) 1300 km, (b) 600 km, (c) 400 km, (d) 286 km, (e) 222 km, (f) 182 km, (g) 154 km, (h) 133 km, (i) 118 km, and (j) 105 km. Choice of time axis confidence intervals is qualitative. Also shown [except for (a)] are best-fitting linear regression lines passing through the origin [solid lines], sample overall best-fitting Model 1 decay curves [$D=10^{21}$ Nm, $\tau=1$ Ma, $\sigma=350$ Ma; plotted with dashed lines], sample overall best-fitting Model 2 decay curves [$D=10^{24}$ Nm, $\tau=1$ Ma, $\sigma=250$ Ma; plotted with open dots], and Model 2 decay curves adjusted according to the σ-criterion [$\sigma=300$ Ma; cf. text, Figure 5-14; plotted with filled dots in (b-f)].

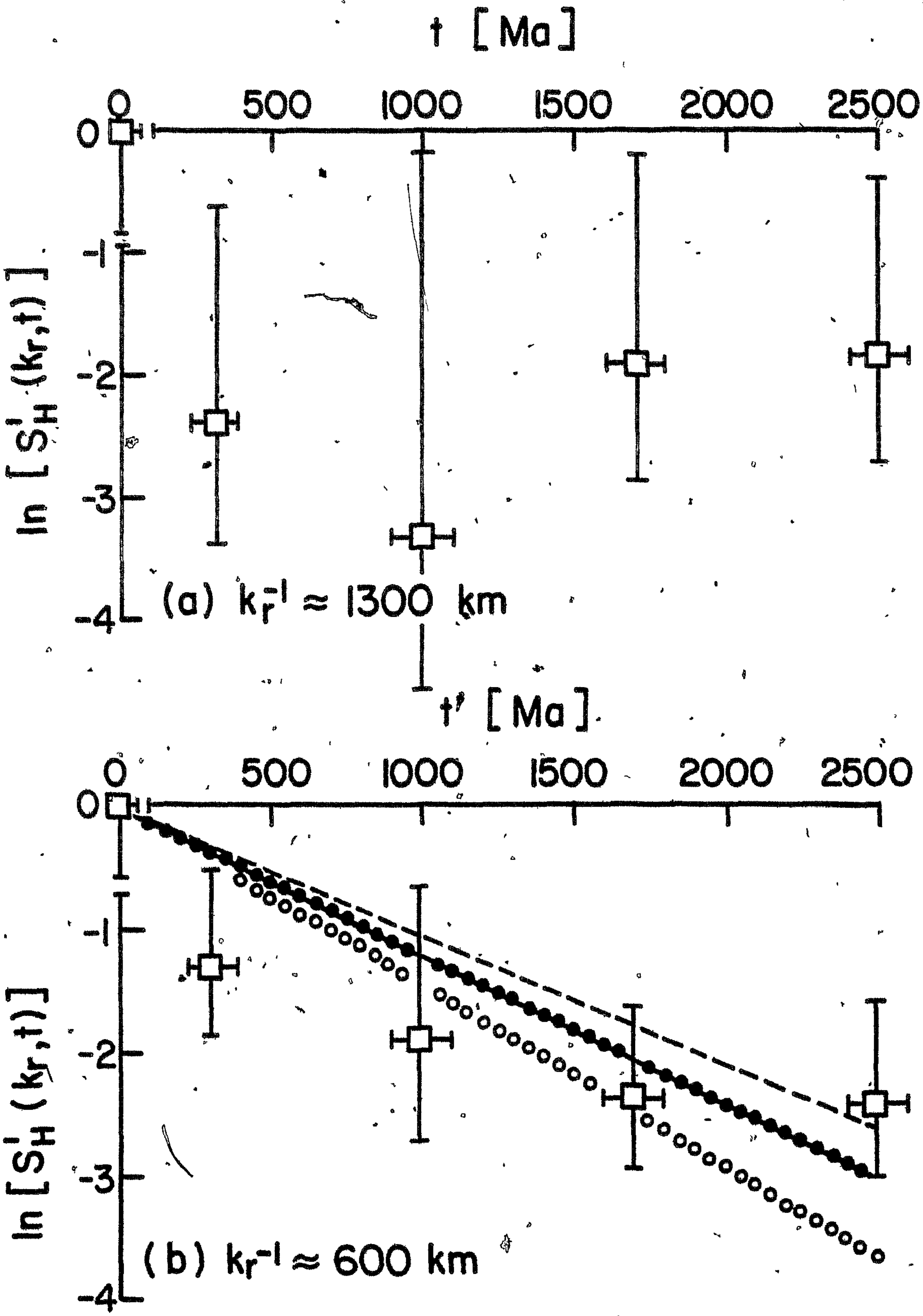
t [Ma]
0
500
1000
1500
2000
2500
0
-1
-2
-3
-4
ln [$S_H^I(k_r,t)$]
(a) $k_r^{-1} \approx 1300$ km
t' [Ma]
0
500
1000
1500
2000
2500
0
-1
-2
-3
-4
ln [$S_H^I(k_r,t)$]
(b) $k_r^{-1} \approx 600$ km

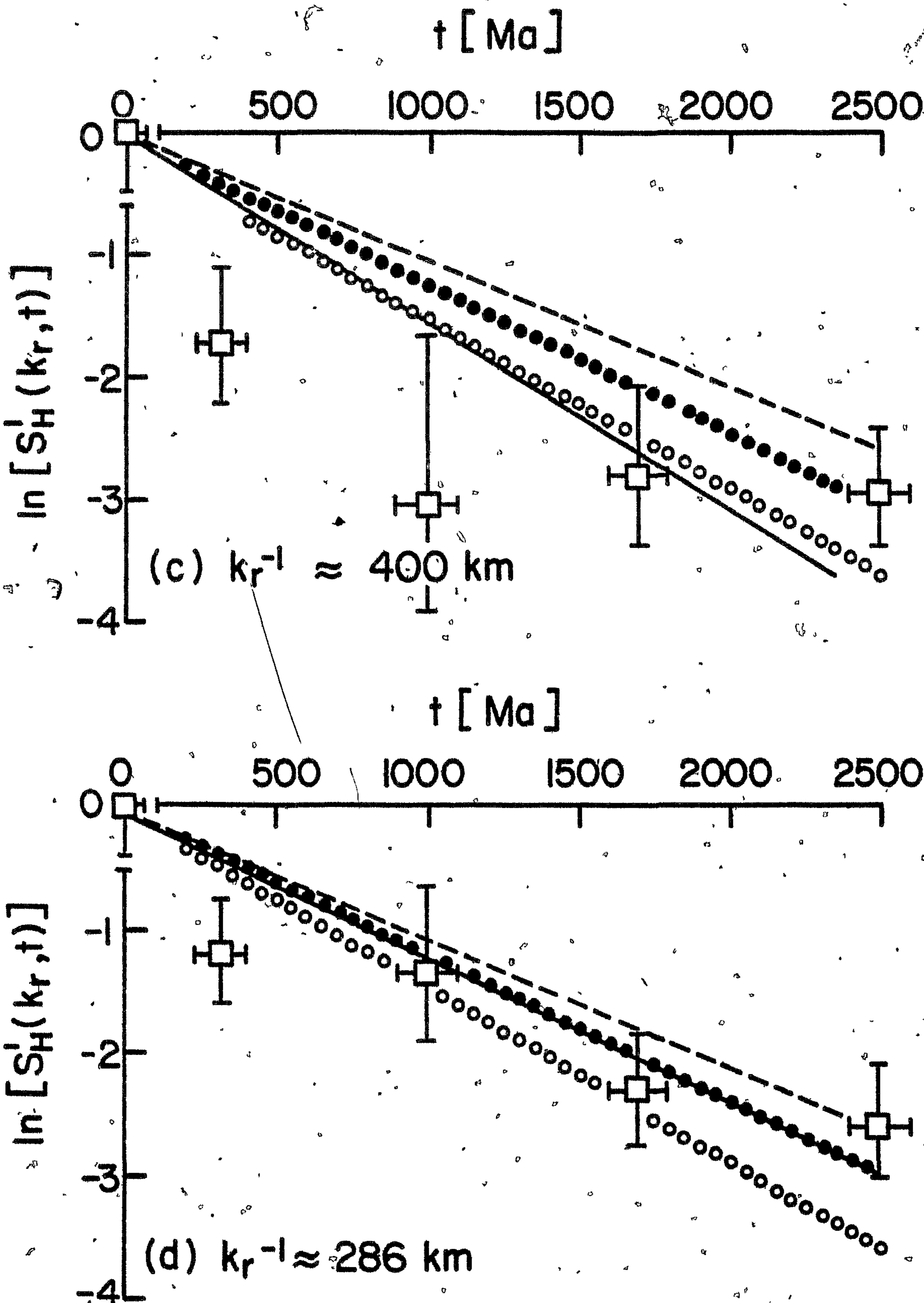

t [Ma]
0
500
1000
1500
2000
2500
0
-1
-2
-3
-4
ln [$S_H^1(k_r, t)$]
(c) $k_r^{-1} \approx 400$ km
t [Ma]
0
500
1000
1500
2000
2500
0
-1
-2
-3
-4
ln [$S_H^1(k_r, t)$]
(d) $k_r^{-1} \approx 286$ km

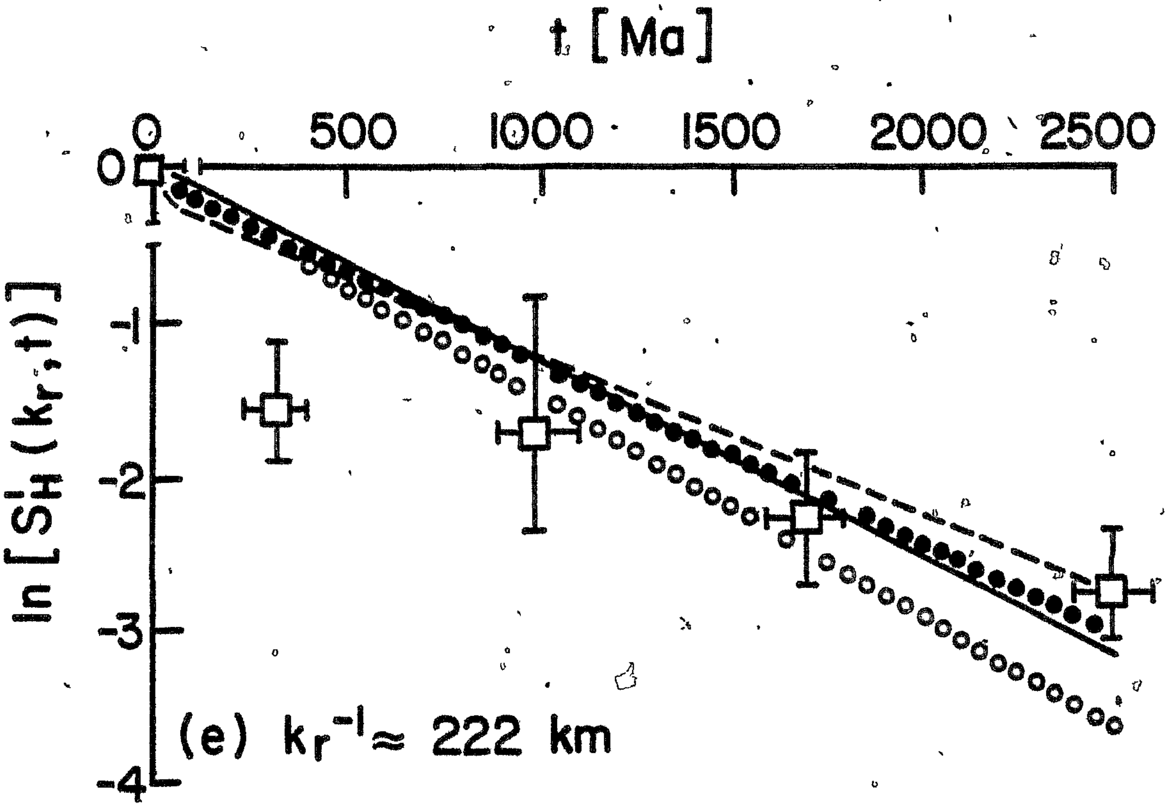
t [Ma]
0
500
1000
1500
2000
2500
0
-1
-2
-3
-4
ln [$S_H^1(k_r,t)$]
(e) $k_r^{-1} \approx 222$ km

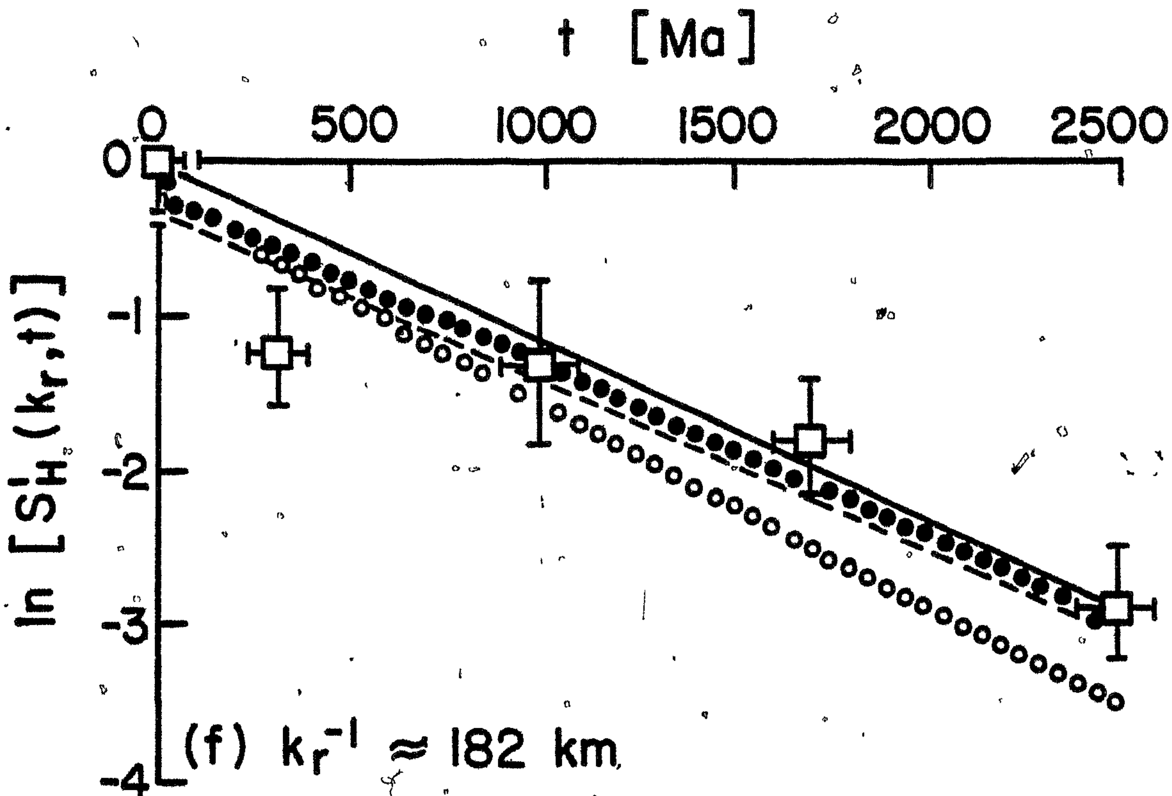
t [Ma]
0
500
1000
1500
2000
2500
0
-1
-2
-3
-4
ln [$S_H^1(k_r,t)$]
(f) $k_r^{-1} \approx 182$ km

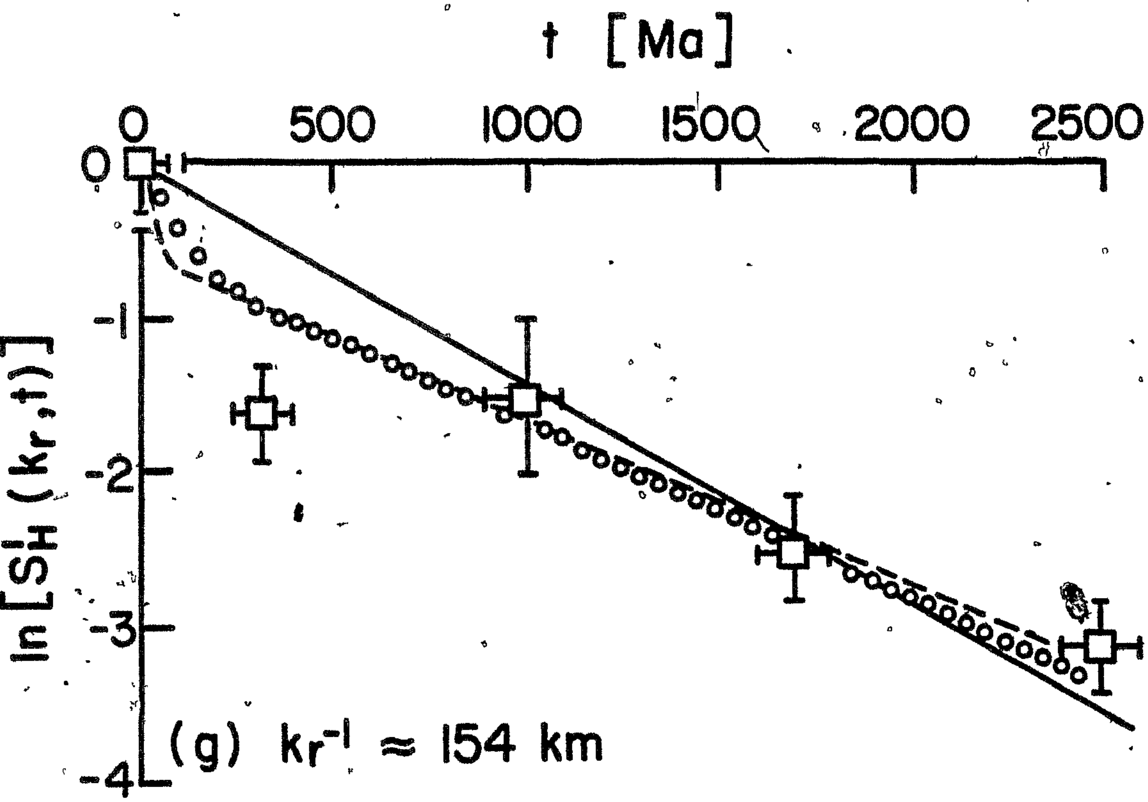
t [Ma]
0
500
1000
1500
2000
2500
ln[S¹H(kr,t)]
0
-1
-2
-3
-4
(g) kr⁻¹ ≈ 154 km

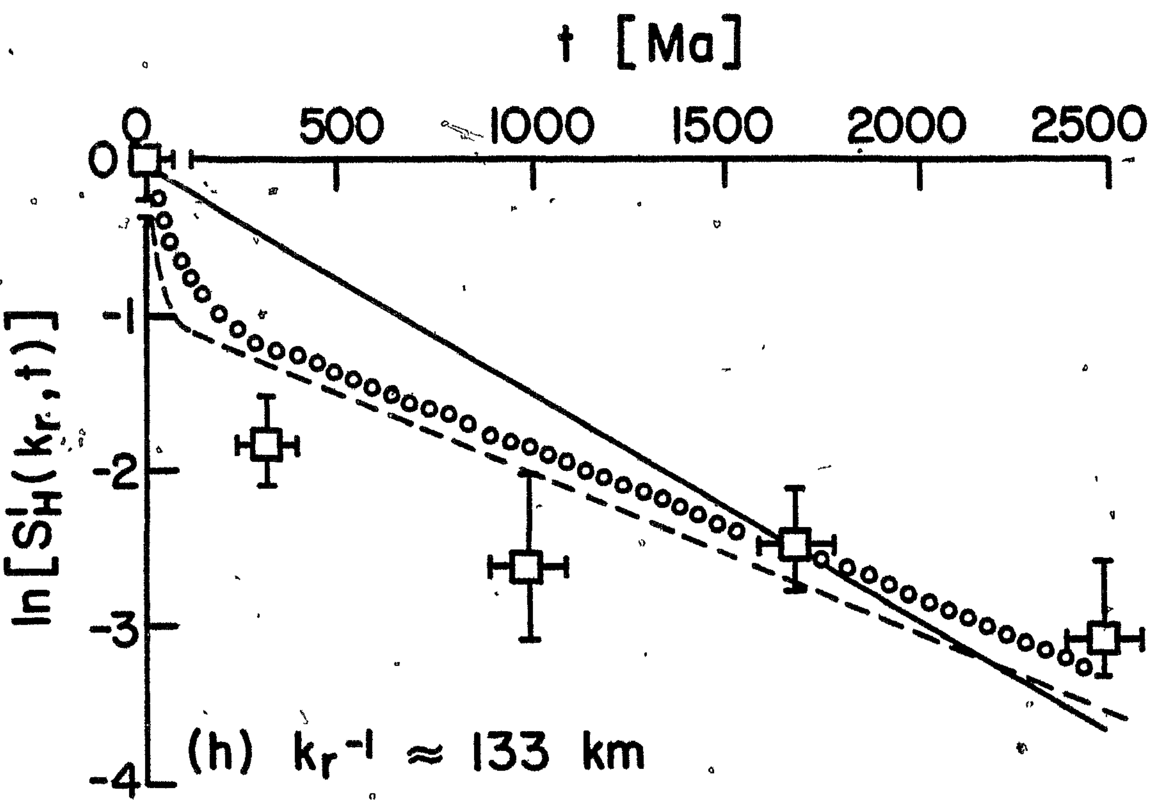
t [Ma]
0
500
1000
1500
2000
2500
ln[S¹H(kr,t)]
0
-1
-2
-3
-4
(h) kr⁻¹ ≈ 133 km

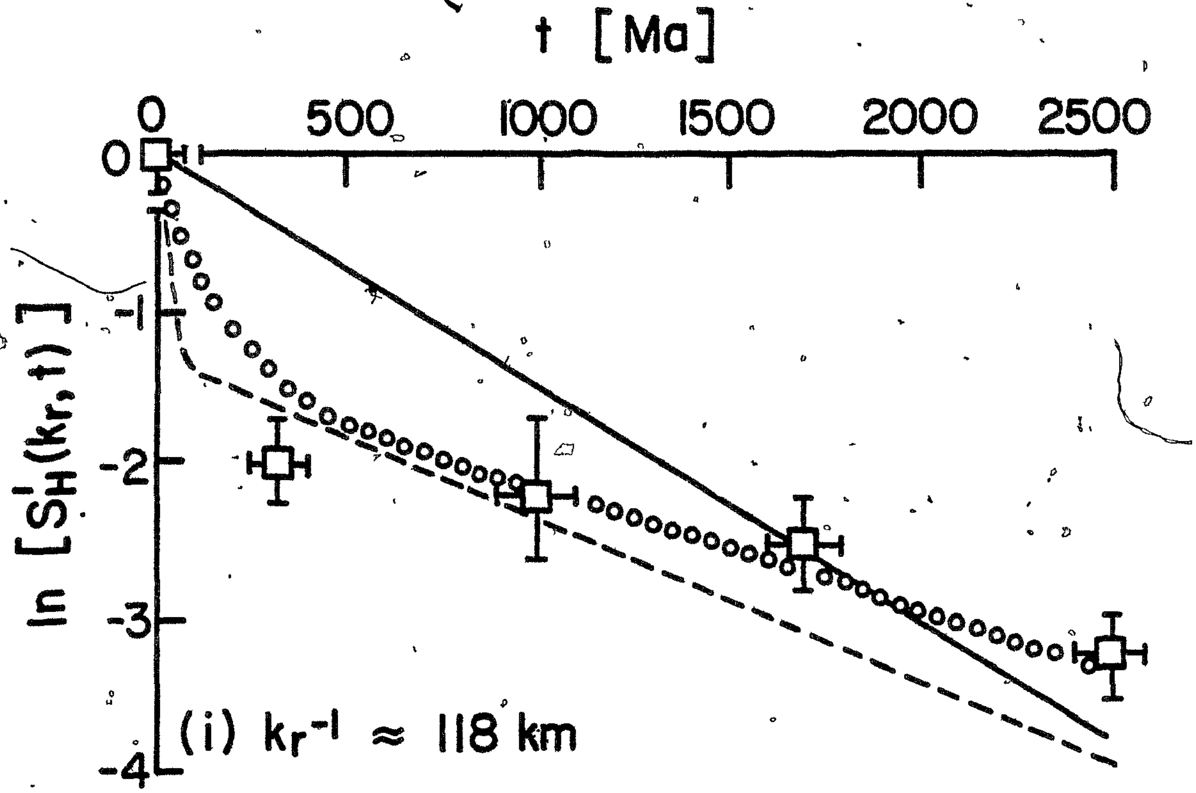
t [Ma]
0
500
1000
1500
2000
2500
0
-1
-2
-3
-4
ln [$S_H^1(k_r,t)$]
(i) $k_r^{-1} \approx 118$ km

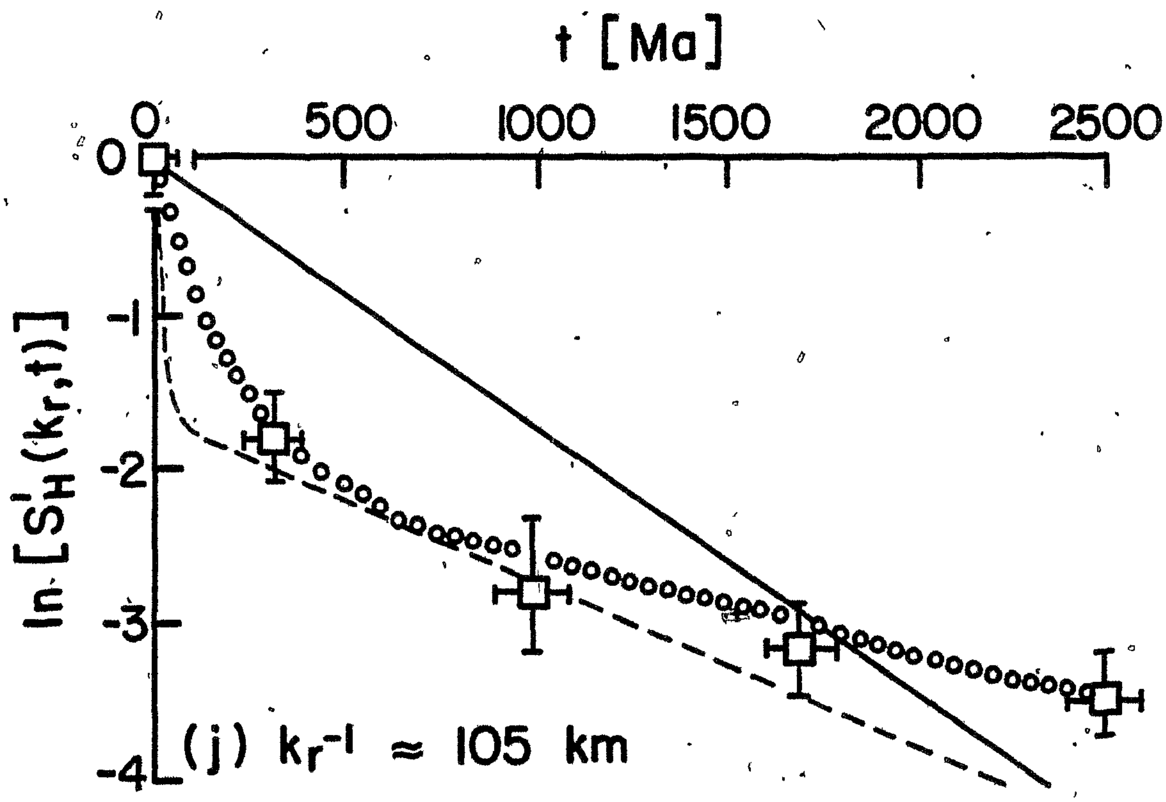
t [Ma]
0
500
1000
1500
2000
2500
0
-1
-2
-3
-4
ln [$S_H^1(k_r,t)$]
(j) $k_r^{-1} \approx 105$ km

after orogenesis and (2) the shorter the topographic wavelength, the greater the net power reduction at a given time, attesting to a decreasing erosion time constant $\sigma(k)$ as k increases.

The 900-1100 Ma spectral estimates, from the Grenville province, are based on a data set which is less than half the size of the other data sets used in the analysis [cf. Table 2-1]. Their generally larger confidence intervals and greater scatter, especially at longer wavelengths where raw spectral data are particularly sparse, can probably be attributed to this fact. In the same way, the generally more consistent overall patterns of topographic decay evident at the shorter wavelengths is likely related to the availability of more raw spectral data at these wavelengths. Post-tectonic events affecting topography, such as transient thermal uplift of the lithosphere and/or super-lithospheric ice and water loading, because they are expected to be regional in scale, are also less likely to affect the higher frequency spectral components. Because of the poor confidence associated with the 1300 km wavelength decay function it is not included in the subsequent analysis of the topography power observations.

5.3.5 General characteristics of model predictions. Equations (5-25, 43) govern the change of topographic amplitude $H(\vec{k},t)$ as determined by Models 1 and 2 respectively. The model parameters common to each are the topography and plate substratum densities ρ_o and ρ_m, flexural rigidity D, viscous relaxation and erosion time constants τ and $\sigma(k)$. Additionally, Models 1 and 2 are dependent on initial topography $L_o(\vec{k})$ and $H_\ell(\vec{k})$. The model predictions, as for the case of the elastic plate analysis in Chapter 3, are not expected to be very sensitive, within reasonable bounds, to the choice of ρ_o and ρ_m and, therefore, to reduce the number of unknowns, they are assumed, as before, to be 2700 and 3300 kg m^{-3} respectively. For purposes of making a general assessment of the behaviour of modelled $H(\vec{k},t)$ as parameters are varied, changes in k and D can be combined in the single parameter

$$\psi(k) = \left[1 + \frac{[2\pi k]^4 D}{\rho_m g}\right]^{-1} \qquad (3\text{-}5ii)$$

which varies in the range [0,1]: $\psi(k)\approx 0$ is the case in which there is no isostatic response to topography, at short wavelengths or high D; and $\psi(k)=1$ corresponds to the case of local isostatic compensation [cf. subsection 3.2.3]. Examination of the structure of the model equations (5-25,43) reveals that scaling of t in terms of one or other of the time constants σ and τ or that scaling of σ and τ to one another is not profitable.

Figures 5-8,9,10 show examples of the natural logarithm of topographic power predicted by Models 1 and 2 for various model parameters. The topographic power is simply the square of the predicted amplitudes as provided by Equations (5-25,43). These results are presented as functions of time normalized so that they are zero when $t=0$ [or $t=t_c$ for Model 2] and so that they are comparable to the observations presented in Figures 5-7(a-j). This means they have been normalized by the square of the initial instantaneous elastic deformation, $H^2(k,0) = [1-\psi(k)\rho_o/\rho_m]^2|L_o(\vec{k})|^2$, or by the square of the initially locally compensated topography $|H_\ell(\vec{k})|^2$ for Model 1 or 2 respectively.

Figure 5-8. Normalized topography decay curves S_H' [cf. text] for elastic plate Model 1 or 2; ψ varies as shown; slopes are determined by Equation (5-45).

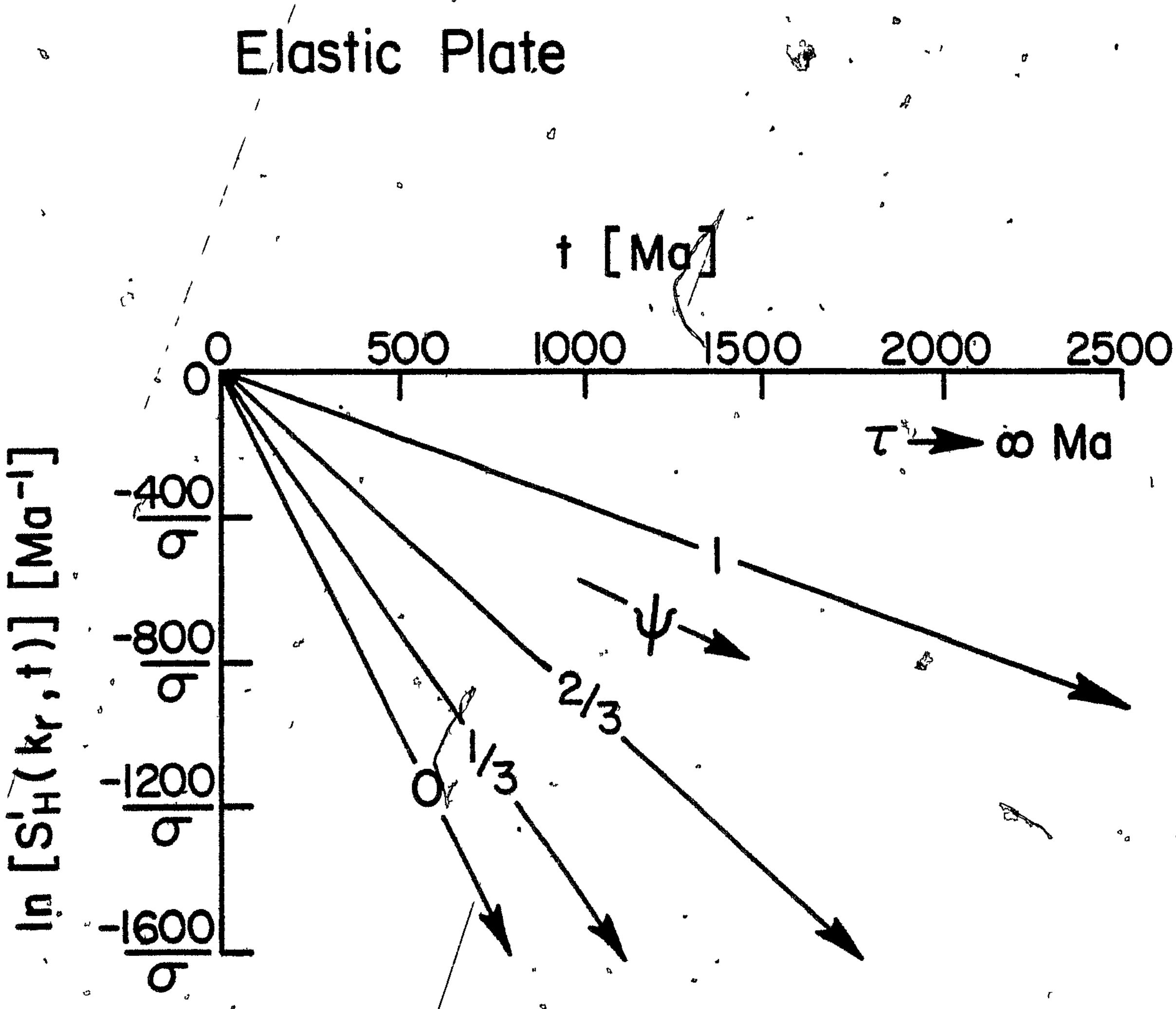
Elastic Plate
t [Ma]
0
500
1000
1500
2000
2500
0
$\tau \rightarrow \infty$ Ma
$\ln[S_H^1(k_r, t)]$ [Ma^{-1}]
-400/σ
-800/σ
-1200/σ
-1600/σ
1
ψ
2/3
1/3
0

These normalized model topography power spectral predictions are written as $S_H'(k,t)$.

The natural logarithm of normalized topographic power $\ln[S_H'(k_r,t)]$, for a given wavenumber k_r, in the case of elastic plate rheology [i.e., $\tau\to\infty$], described by Equations (5-23) and (5-40) for Models 1 and 2 respectively, plots as a straight line with slope [cf. Equation (5-21ii)]

$$-2\alpha_e = -2\left[\frac{1 - \psi(k)\rho_o/\rho_m}{\sigma(k)}\right] \tag{5-45}$$

within the bounds $0\leq\psi(k)\leq1$. This result is illustrated in Figure 5-8. Theoretical decay curves are the same for both Models 1 and 2 because of the normalization procedure. Note that changes in σ effects only a scaling change in the curves. In the context of Model 1, the reason topographic decay slows as ψ increases is because for greater ψ, as isostatic compensation becomes increasingly local, more of the initial load $L_o(\vec{k})$ is "buried" in the lithosphere's flexural downwarp. With less exposed topography the erosion rate is reduced and the life span of the topography is enhanced. In the case of Model 2, as ψ increases, there is more topographic rebound as erosion occurs resulting in a reduction of the rate of decay of the topography.

Theoretical topography decay curves characteristic of a viscoelastic plate are more complex and results for Models 1 and 2 are discussed separately.

(i) Model 1. The general features of the Model 1 results, considering first Figure 5-9(a) for which σ=100 Ma are as follows.

Figure 5-9. Normalized Model 1 topography decay curves S'_{H_0} for (a) σ=100 Ma and (b) σ=500 Ma; parameters ψ and τ vary as shown. Decay curves of locally compensated eroding topography are plotted with dashed lines for reference.

(a) Model I

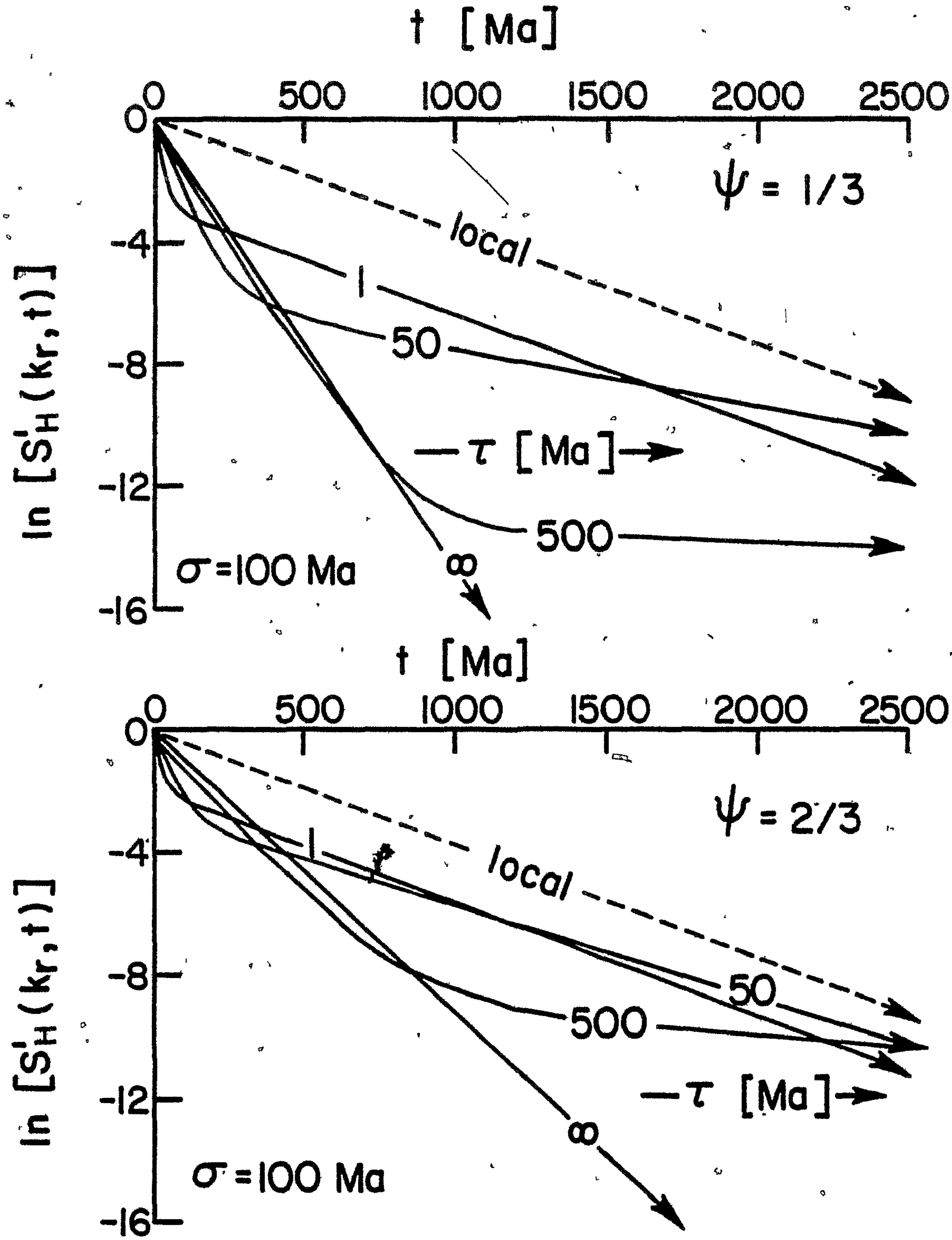
t [Ma]
0
500
1000
1500
2000
2500
0
-4
-8
-12
-16
ln [S'H (kr, t)]
ψ = 1/3
local
1
50
— τ [Ma] →
500
∞
σ = 100 Ma
t [Ma]
0
500
1000
1500
2000
2500
0
-4
-8
-12
-16
ln [S'H (kr, t)]
ψ = 2/3
local
1
50
500
— τ [Ma] →
∞
σ = 100 Ma

(b) Model I

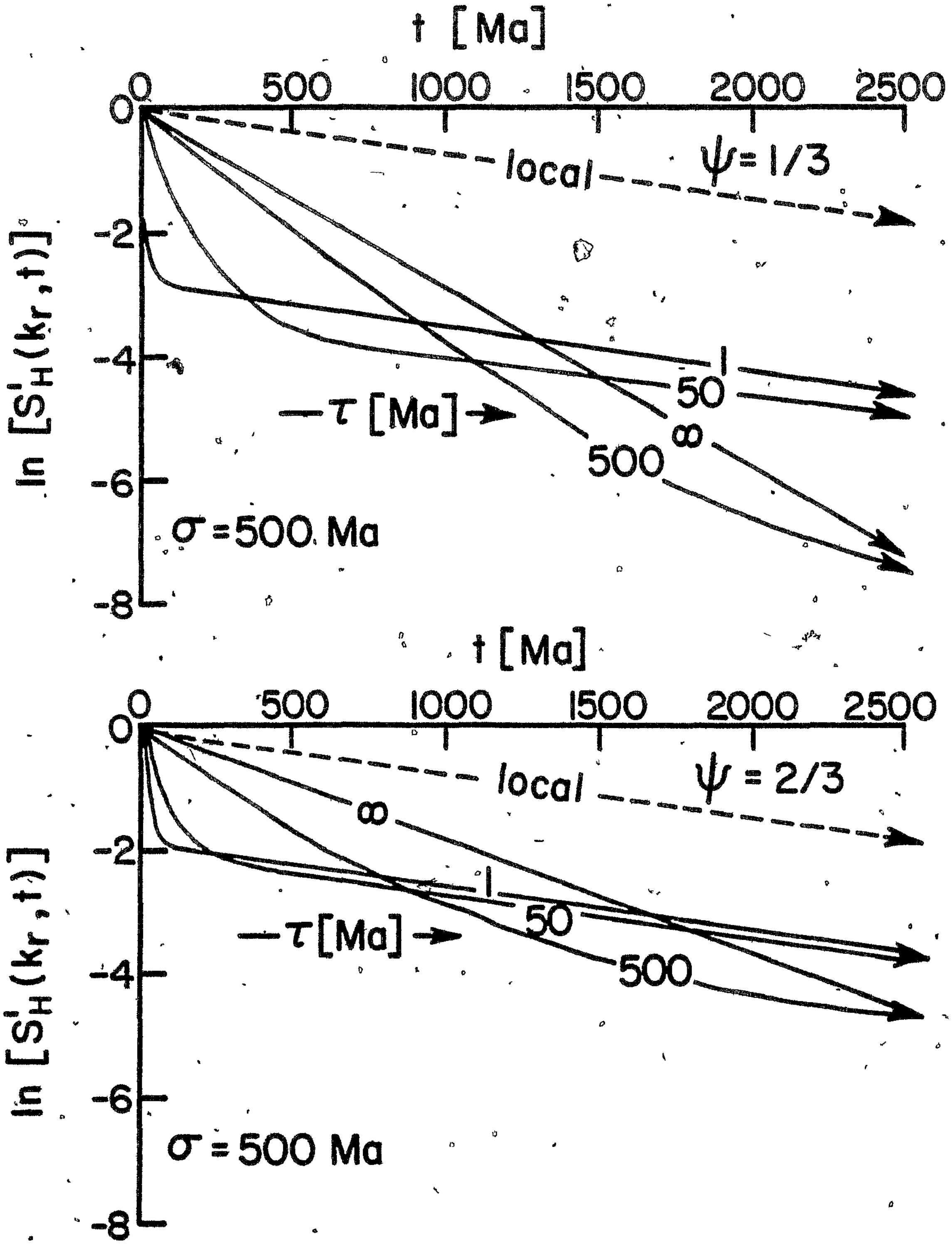
t [Ma]
0
500
1000
1500
2000
2500
0
-2
-4
-6
-8
ln [S'_H(k_r, t)]
local
ψ = 1/3
1
50
∞
500
— τ [Ma] →
σ = 500 Ma
t [Ma]
0
500
1000
1500
2000
2500
0
-2
-4
-6
-8
ln [S'_H(k_r, t)]
local
ψ = 2/3
∞
1
50
500
— τ [Ma] →
σ = 500 Ma

(1) For small viscous relaxation time constant, $\tau \ll \sigma$, e.g. $\tau=1$ Ma, there is an early phase of rapid topography reduction, associated more with the relaxation of the stresses incurred by the initial elastic deformation rather than with erosion, after which time the topography is locally compensated and decays in a like manner [parallel to the $\psi=1$ or local compensation curve which is dashed onto Figures 5-9(a,b) for reference]. As ψ is smaller [cf. the upper and lower diagrams of Figure 5-9(a)] this early reduction phase is enhanced because the initial elastic flexure was lessened. The timing of this phase, however, is not significantly affected by changes in ψ. (2) As τ increases, the plate response becoming "more" elastic and "less" viscous, the early viscous relaxation phase is suppressed and, rather, the decay curve at first mimics the elastic plate decay curve and then begins to flatten such that a condition of steady-state topography is almost attained. (3) Figure 5-9(b) illustrates Model 1 results for the same $[\psi,\tau]$ pairs as Figure 5-9(a) but with σ increased to 500 Ma meaning that the rate of erosion has been considerably reduced. Note the change of vertical scale between (a) and (b). Examination of Figures 5-9(a,b) reveals that changes in σ approximate the effect of a σ-scaling factor along the time axis: as σ increases, the onset of flattening occurs after a greater length of time and is favoured by larger values of τ. As a result, the period during which the curves resemble their respective elastic decay curves is much longer.

(ii) Model 2. Model 2 topography power decay curves for the same parameters as those of the Model 1 analysis are illustrated in Figures 5-10(a,b). The major difference between Model 1 and Model 2

Figure 5-10. Normalized Model 2 topography decay curves S_H' for (a) σ=100 Ma and (b) σ=500 Ma; parameters ψ and τ vary as shown.

(a) Model 2

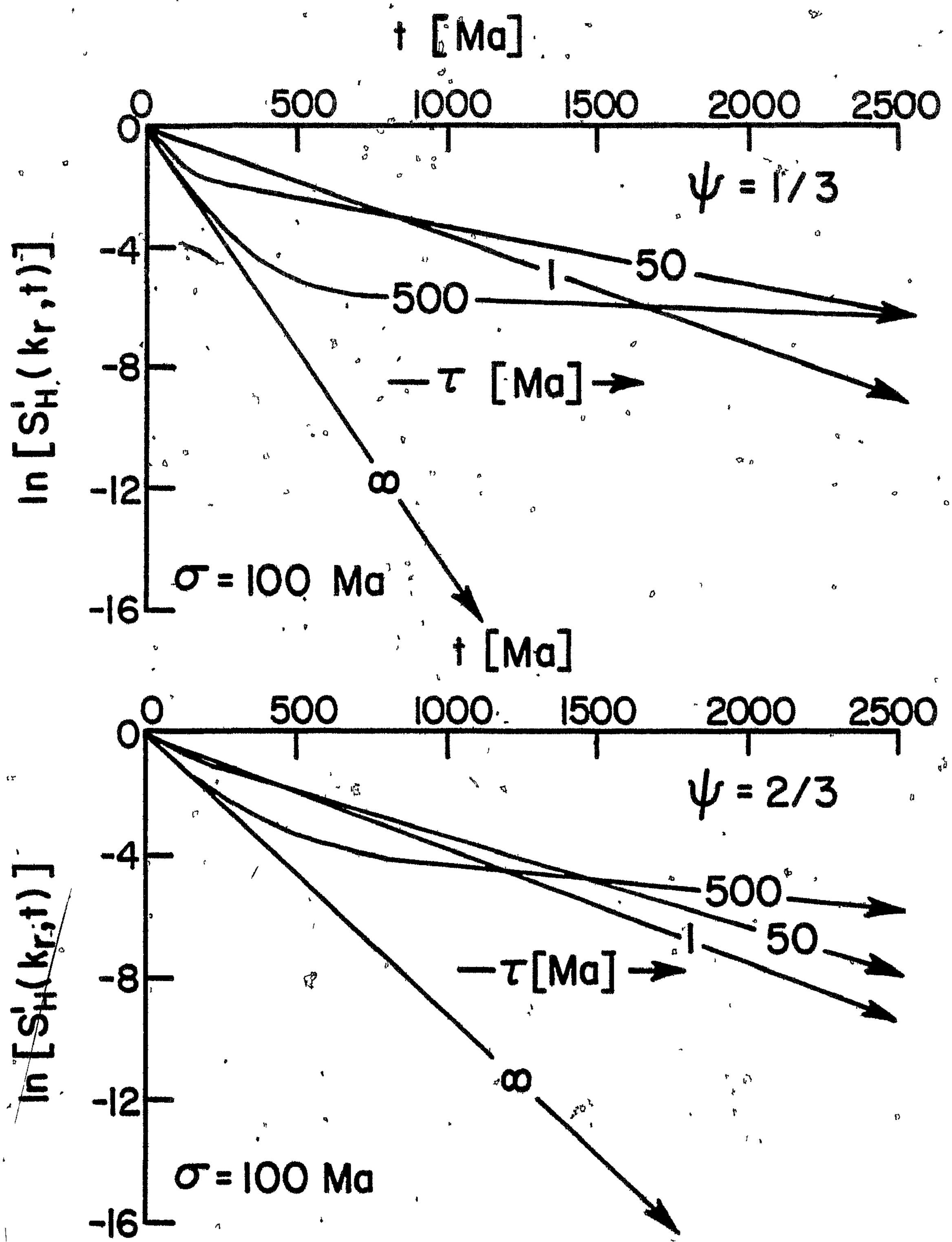
t [Ma]
0
500
1000
1500
2000
2500
0
-4
-8
-12
-16
ψ = 1/3
50
1
500
— τ [Ma] →
∞
σ = 100 Ma
ln [S'_H (k_r, t)]
t [Ma]
0
500
1000
1500
2000
2500
0
-4
-8
-12
-16
ψ = 2/3
500
50
1
— τ [Ma] →
∞
σ = 100 Ma
ln [S'_H (k_r, t)]

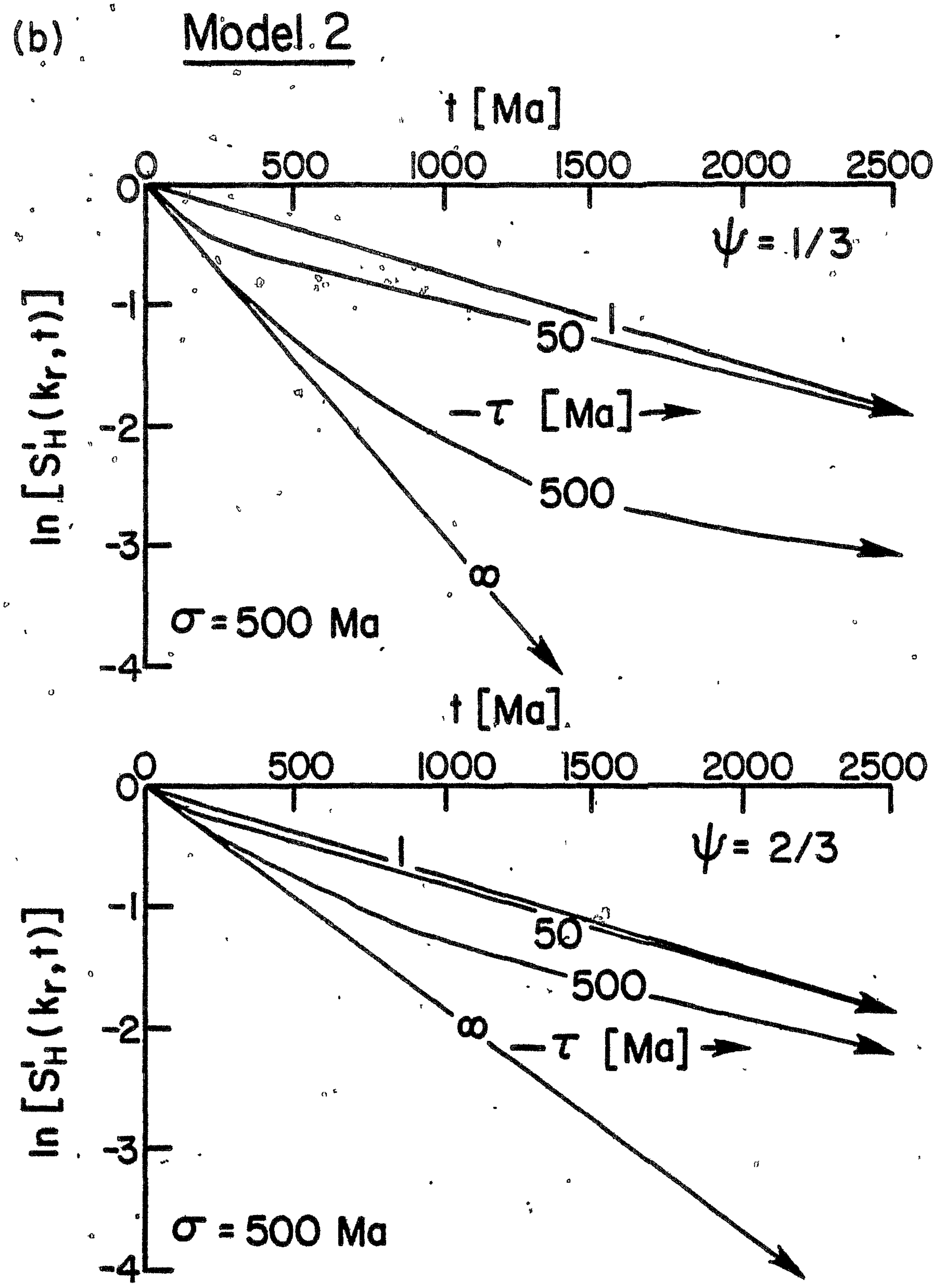
(b)
Model 2
t [Ma]
0
500
1000
1500
2000
2500
ψ = 1/3
1
50
500
∞
−τ [Ma]→
ln [S'H(kr, t)]
0
-1
-2
-3
-4
σ = 500 Ma
t [Ma]
0
500
1000
1500
2000
2500
ψ = 2/3
1
50
500
∞
−τ [Ma]→
ln [S'H(kr, t)]
0
-1
-2
-3
-4
σ = 500 Ma

decay curves is that the latter set does not display the early viscous relaxation phase of topographic decay, characteristic of Model 1, because the topography is in an a priori state of local isostatic compensation. Otherwise, the essential pattern of the respective sets of curves is similar, particularly with respect to the onset and degree of flattening as it relates to the choice of values of the model time constants σ and τ. This was to be expected, of course, since the exponential decay of each model [cf. Equations (5-25,43)] is controlled by equivalent parameters: the roots $-r_1$ and $-r_2$ of $s^2+\alpha s+\beta=0$.

The important feature of the model predictions is that $\ln[S_H'(k_r,t)]$ for a given wavenumber k_r decays linearly if the lithosphere behaves elastically [or if there is local compensation] throughout the term of the evolution of the topography but that topographic decay may be significantly suppressed if viscous relaxation is allowed, potentially to the point at which the topography acquires a steady-state characteristic.

5.3.6 Results. A first-order fit to the topography power spectra decay observations can be found by simple linear regression for each k_r. The regression lines are assumed to pass through the origin. This set of best-fitting straight lines, plotted onto Figures 5-7(b-j) with solid lines, can be interpreted directly in terms of the $\psi(k)=0$ or 1 [one or the other for all k_r] extrema of an elastic plate model corresponding to conditions of no isostatic compensation or complete local compensation. This result is independent of choice of Model 1 or 2 [subsection 5.3.5]. In such a case, $\psi(k)=0$ or 1, the slopes of the regression lines provide values of the erosion time constants $\sigma(k)$ by Equation (5-45); these are plotted in Figure 5-11. Bounds on $\sigma(k)$ estimates in Figure 5-11 were derived from the linear regression of the upper and lower 95% confidence limits of the topography decay observations in Figures 5-7(b-j). There is some suggestion that σ is proportional to $k^{-1/3}$, assuming it vanishes as $k\to\infty$, an indication that the erosion model [Equations (4-1)] used to calculate the theoretical decay curves of Models 1 and 2, to which these observations shall be compared, is realistic. Moreover, these results imply that $\sigma(k)$ does not greatly vary in the range of k for which observations exist.

It warrants re-emphasizing that these best-fitting regression lines comprise a consistent set of model predictions only if $\psi(k)$ is either zero or unity for all observed wavenumbers k. This requirement can be restated in terms of the flexural rigidity D in light of the smallest and largest of the observed wavelengths being considered, 105 and 600 km respectively. Recall that

$$\psi(k) = \left[1 + \frac{[2\pi k]^4 D}{\rho_m g}\right]^{-1} \qquad (3\text{-}5ii).$$

Therefore, for $\psi(k) \leq 0.01$ when k^{-1}=600 km, $D \geq 2.9 \times 10^{26}$ Nm; conversely, for $\psi(k) \geq 0.99$ when k^{-1}=105 km, $D \leq 1.3 \times 10^{19}$ Nm. While the flexural rigidity of continental lithosphere, modelled in terms of a thin elastic plate, cannot with certainty be expected to lie within these bounds, such a result appears to be probable in the light of previous research [e.g. Walcott 1971a, Banks <u>et</u> <u>al</u>. 1977, McNutt and Parker 1978, Beaumont 1978, 1981]. Therefore it is unlikely that the model with $\psi(k)$ either zero or unity for all observed wavenumbers is correct.

Figure 5-11. Values of the erosion time constant σ [filled circles] based on linear regression of observed topography decay data; error bars are based on 95% confidence limits of the observations [cf. text, Figures 5-7(b-j)]. Also shown [dashed line] is a sample function fitted to the data.

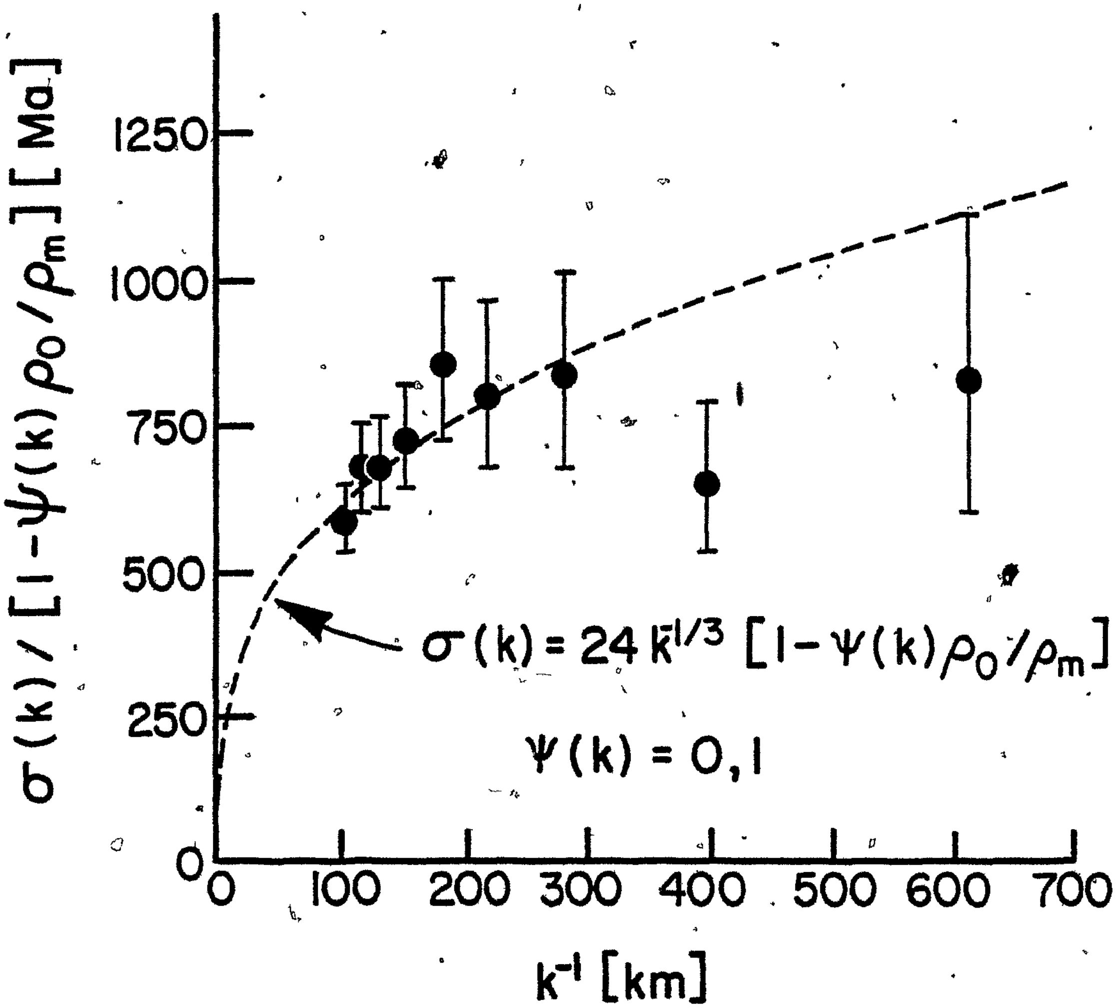

$\sigma(k) / [1-\psi(k)\rho_0/\rho_m]$ [Ma]
1250
1000
750
500
250
0
0
100
200
300
400
500
600
700
k^{-1} [km]
$\sigma(k) = 24\,k^{-1/3}\,[1-\psi(k)\rho_0/\rho_m]$
$\psi(k) = 0,1$

Of course, straight lines fitted to the observed data can also be interpreted in terms of any elastic plate model [cf. subsection 5.3.5] with ψ varying as a function of k depending on the flexural rigidity D of the plate if D lies within the range 10^{19}–10^{26} Nm. However, because of the internal constraint of k dependence of ψ imposed on any set of predicted results [consisting of topography decay curves for the entire range of observed wavenumbers], it is unlikely that any such elastic plate model, in the absence of <u>ad hoc</u> readjustments of $\sigma(k)$ to alter the slopes of the modelled straight line decay curves, could maintain the best overall fit provided by the linear regression lines. Note that as k increases, from Equation (3-5ii), $\psi(k)$ decreases, and that the slope of the decay curve, from Equation (5-45) would increase. Similarly, as k increases, $\sigma(k)$ is intuitively expected to decrease, also resulting in an increase in the hypothetical slope of the topographic decay curve. In other words, the two effects are not compensatory.

The overall misfit between model predictions and the observations is simply defined as

$$M_H = \sum_{r=1}^{N_k} \sum_{s=1}^{N_t} \left| \ln[S'_H(k_r,t_s)/\hat{S}'_H(k_r,t_s)] \right| \qquad (5\text{-}46)$$

where N_k and N_t are the number of observed wavenumbers and times for which normalized power spectral estimates $\hat{S}'_H(k,t)$ exist. If model parameters are arbitrarily chosen such that the predicted normalized power spectral estimates $S'_H(k,t)$ reproduce those provided by the linear regression lines shown in Figures 5-7(b-j), then the total overall misfit calculated using (5-46) is 22.5 and is referred to as the linear regression misfit M_H^R.

Visual inspection of the observed decay curves and their fitted regression lines shows, without need of statistically rigorous hypothesis testing, that there is a systematic lack of fit between the two. It is known from the analysis of the general characteristics of model predictions in subsection 5.3.5, however, that it may be possible to better fit the observations, in the context of either Model 1 or 2, if the lithosphere has the facility of viscous relaxation.

Overall misfits M_H, as defined in Equation (5-46), were calculated, for both Models 1 and 2, for model parameter triplets $[\sigma,\tau,D]$ letting (1) σ vary in the range 50-1500 Ma with increment 50 Ma, (2) τ assume values of $[0.5,1,10,25,50,100,250,500,\infty]$ Ma, and (3) D vary in the range 10^{18}-10^{27} Nm incrementing in powers of 10. Surface and substratum densities ρ_o and ρ_m were assumed to be, as noted earlier, 2700 kg m^{-3} and 3300 kg m^{-3} respectively. For purposes of preliminary analysis, σ was taken to be constant as a function of k during each misfit calculation.

Figures 5-12(a) and 5-13(a), for Models 1 and 2 respectively, show minimum calculated M_H', defined

$$M_H' = M_H - M_H^R \qquad (5\text{-}47),$$

where M_H^R=22.5, the linear regression misfit; thus, the zero contours on Figures 5-12(a) and 5-13(a) enclose regions of τ-D space for which the viscoelastic models provide better reproduction of the data than does the simple linear regression. Figures 5-12(b) and 5-13(b) indicate which values of σ were used to compute the respective minimum misfits M'_H. In each, the region $M'_H<0$ has been shaded for easier reference. Examination of M'_H calculated thus, for both Models 1 and 2, reveal that the best overall fit of the observations is strongly affected by the choice of σ and is best attained when σ falls in the range 200-400 Ma.

(i) Model 1: Figures 5-12. In general the Model 1 M'_H are not very sensitive to choice of τ. At the smallest values of D the predicted decay curves are those produced essentially by local isostatic compensation [$\psi=1$], as discussed above, with slopes determined by σ which is, in all [τ,D] pairs, 250 Ma for all k. The internal consistency forced by constant σ means, of course, that these predicted $\psi=1$ sets of decay curves cannot quite reproduce the misfit provided by arbitrary linear regression and thus $M'_H>0$ in this region.

$M'_H\leq 0$ when $D=10^{20}-10^{21}$Nm. The mechanism which effects the improved misfit in this region of τ-D space is the same throughout and relates to the initial phase of rapid topographic decay resulting from viscous relaxation rather than from erosion as discussed in subsection 5.3.5. The best reproduction of the observations is provided by models with $D=10^{21}$Nm and small values of τ where $M'_H\leq -5$; in this region the predicted decay curves are insensitive to choice of τ. A sample set, using τ=1 Ma and σ=350 Ma, is plotted with dashed lines in Figures 5-7 (b-j) where they can be compared to the observations. Note that the initial viscous relaxation phase is ineffective when $k_r^{-1}\geq 286$ km, corresponding to $\psi(k)\geq 0.99$ for $D=10^{21}$ Nm. The goodness-of-fit of the

Figure 5-12. (a) Model I normalized minimum misfit M_H' [Equations (5-46,47)] and (b) value of σ providing M_H' as functions of model parameters D and τ; shaded region in (b) corresponds to $M_H'<0$ in (a).

(a)

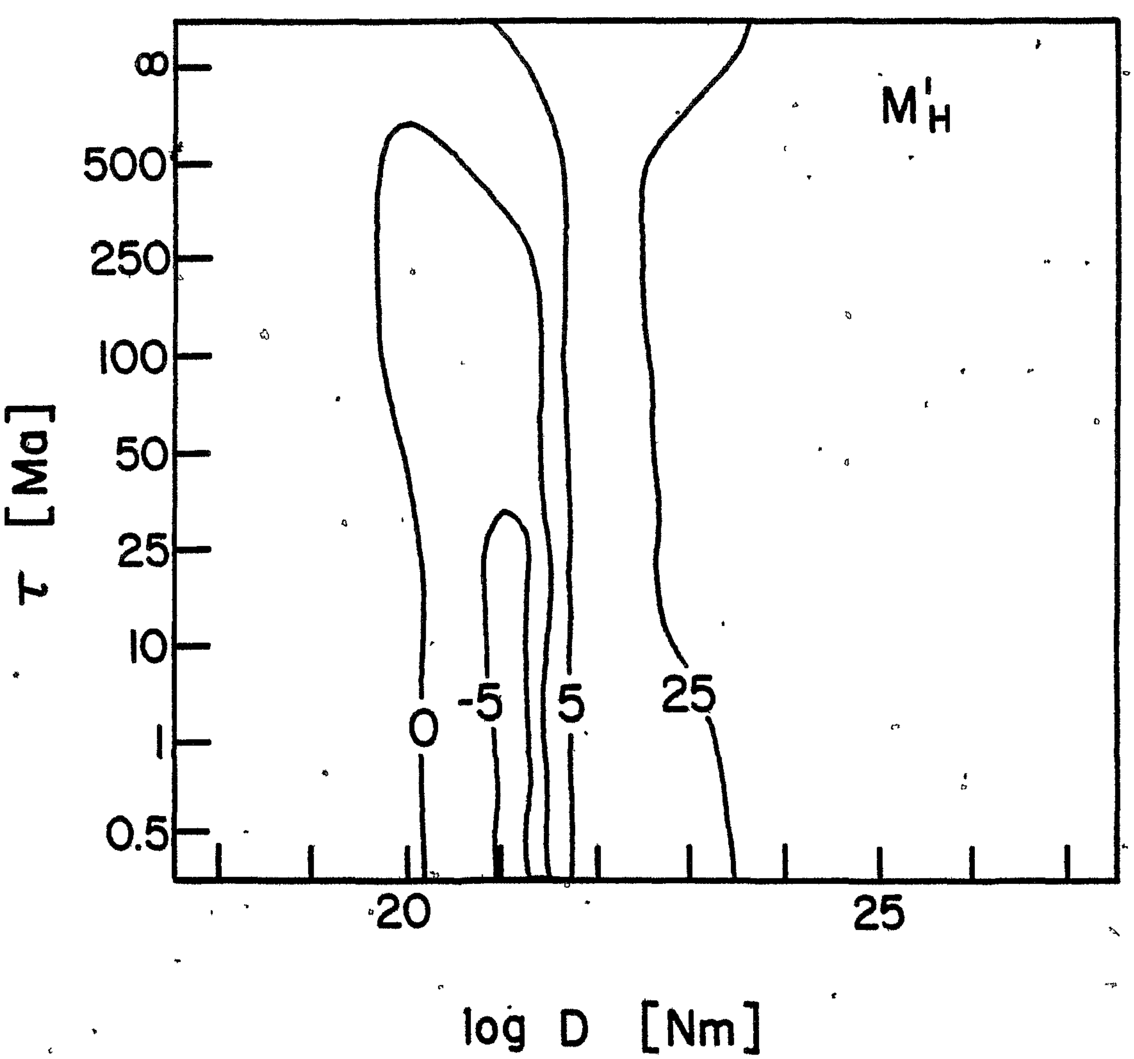

(b)

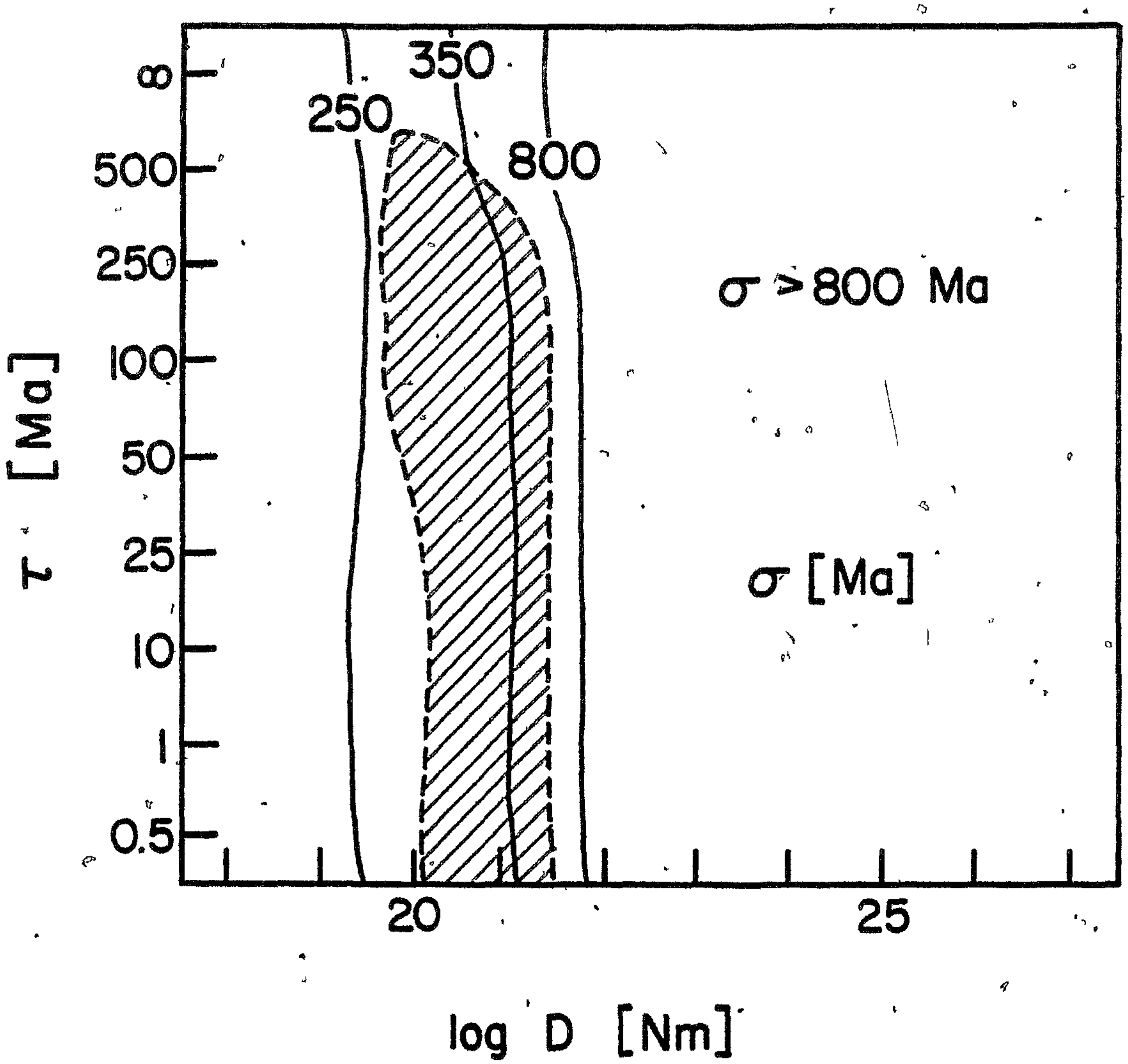

sample curves at these low wavenumbers is not as good as that provided by linear regression.

One way to judge the acceptability of the results, which are based on best-fitting rheological model parameters τ and D for constant $\sigma(k)$, is to test what kinds of adjustments to σ for various k_r improves the overall fit. Intuitively, and from the $\psi(k)$ extrema results, illustrated in Figure 5-11, it is expected that σ decreases as k increases. Internally consistent adjustments of this kind [such that no $\sigma(k_1)<\sigma(k_2)$ if $k_1<k_2$] serving to maintain or improve M_H for a given [τ,D]-set of decay curves can be considered a satisfactory result. A reverse effect can be taken as unsatisfactory and argues for refutation of the model. This feature of the model predictions, for any given [τ,D] pair, shall be referred to as the σ-criterion. In the case of Model 1, everywhere within the best-fitting, $M_H'\leq 0$, τ-D space shown in Figure 5-12(a) the σ-criterion is not satisfied.

(ii) Model 2: Figures 5-13. Note the equivalence, as is expected [cf. subsection 5.3.5], between Model 2 M_H' and those of Model 1 [Figure 5-12(a)] for (1) an elastic plate [$\tau\to\infty$], (2) small D where isostatic response is effected by local compensation, and (3) large τ and D where little or no isostatic compensation occurs. Otherwise, there are regions in Model 2 τ-D space which provide better overall fit than for Model 1. In general, within the $M_H'\leq 0$ region of Figure 5-13(a) the misfit is not strongly sensitive to choice of τ for any given D; throughout this region, in which there are three separate zones with $M_H'\leq -5$, the character of the predicted topography decay curves, for each [τ,D] pair, is somewhat uniform. Note that the

Figure 5-13. (a) Model 2 normalized minimum misfit M_H'. [Equations (5-46,47)] and (b) value of σ providing M_H' as functions of model parameters D and τ; shaded region in (b) corresponds to $M_H'<0$ in (a).

(a)

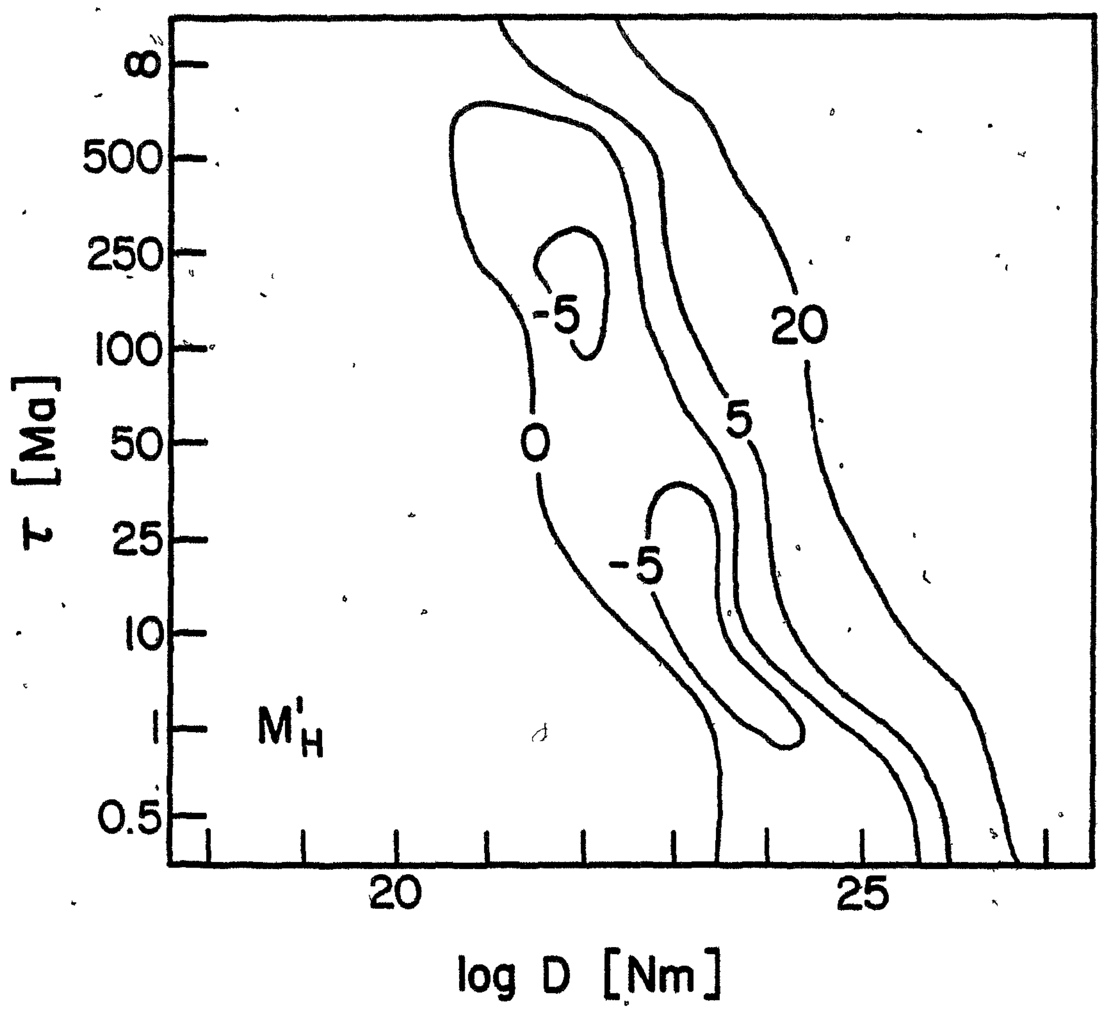

(b)

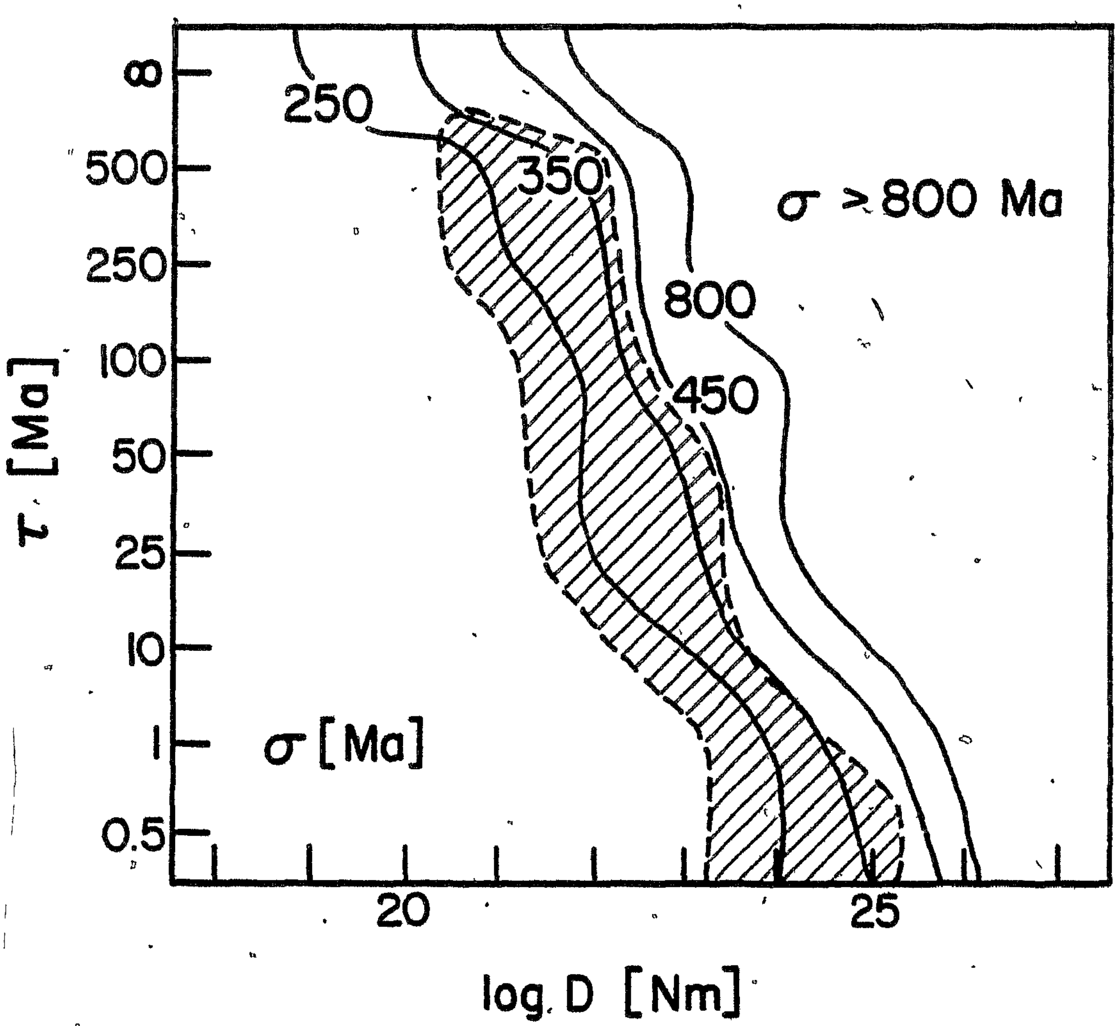

∞
500
250
100
50
25
10
1
0.5
τ [Ma]
250
350
450
800
σ > 800 Ma
σ [Ma]
20
25
log D [Nm]

diagonal trend of the $M_H' \leq 0$ zone of the Model 2 τ-D map reflects the controlling effect of the ratio $\psi(k)/\tau$ in Equation (5-43ii), which gives $H(\vec{k},t)$, and in α and β [Equations (5-19ii,iii)], which determine the arguments of the exponential functions in (5-43ii). As D gets larger, for the range of k under consideration, ψ tends to vary according to D^{-1} so that the predicted topography decay curves are virtually unchanged as long as the product of τ and D is a constant.

While it is necessarily stressed that no single set of curves within this best-fitting region of τ-D space is significantly better than any of the others, particularly noting the approximate form of the observations, topography decay curves predicted for $D=10^{24}$ Nm and $\tau=1$ Ma, for purposes of illustration, are plotted with open dots on Figures 5-7(b-j). The erosion time constant σ providing the best misfit for this [τ,D] pair is 250 Ma [Figure 5-13(b)]. Also plotted, using filled dots, are Model 2 predictions, for $D=10^{24}$ Nm and $\tau=1$ Ma, adjusted according to the σ-criterion, which yielded satisfactory results. These adjusted decay curves, with the exception of that for 400 km wavelength topography, are seen to be more closely aligned with the best-fitting regression lines. Values of σ used in the adjusted calculations are plotted as a function of k^{-1} in Figure 5-14. Their distribution suggests that σ may be proportional to $k^{-1/4}$ if it vanishes as $k \to \infty$.

The plotted set of predicted topography decay curves is characterized by a moderately good fit to observations at the small wavelengths $k_r^{-1} \leq 182$ km. At larger k^{-1} decay curves are essentially linear [in terms of the logarithm of $S_H'(k,t)$], as was the case for

Figure 5-14. Values of the erosion time constant σ [filled circles] based on best-fitting Model 2 results adjusted according to the σ-criterion [cf. text]; also shown [dashed line] is a sample function fitted to the adjusted σ values.

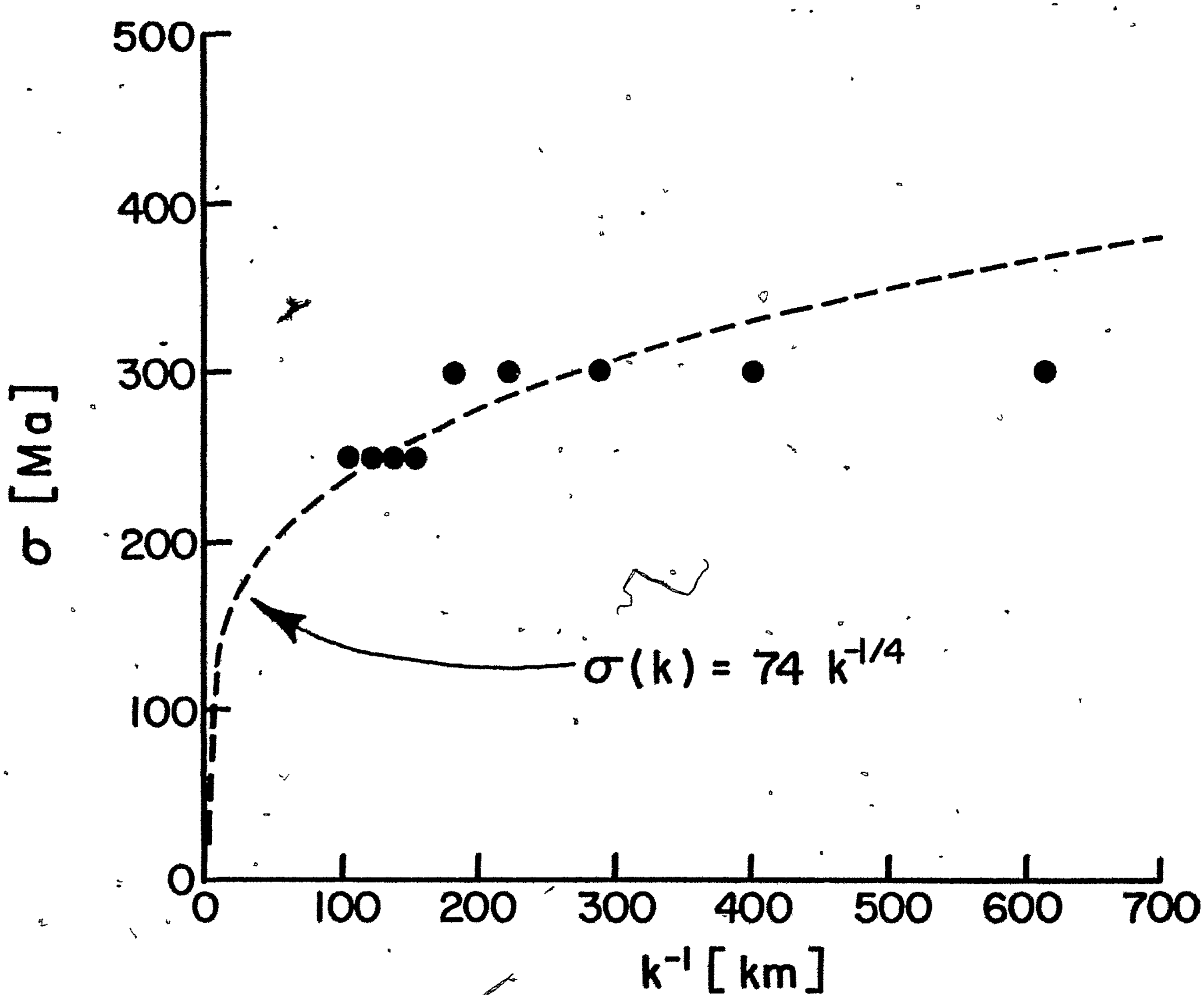

500
400
300
200
100
0
σ [Ma]
0
100
200
300
400
500
600
700
k⁻¹ [km]
$\sigma(k) = 74\ k^{-1/4}$

Model 1, although, unlike Model 1, the linearity is not a consequence of local isostatic compensation [$\psi \simeq 1$]. Rather, when $D=10^{24}$ Nm, as in the present case, for $k_r^{-1} \geq 222$ km, $\psi(k)$ can be as small as 0.05. The decay curves in this range do not really provide an adequate fit to the observations in the sense that topographic power is consistently overestimated at t=325 Ma compared to observed Appalachian topographic power. On the other hand, it should be noted that these linear decay curves, calculated for $[\tau,D]$ pairs which provide best misfit M_H over all observed values of k, virtually coincide, except for $k_r^{-1}=400$ km, with the best-fitting straight line found by linear regression. In other words there is some internal consistency in the $[\tau,D]$ models: at smaller k^{-1} there is good fit and at larger k^{-1}, although the physics of Model 2 can provide only a linear decay curve when the observations suggest otherwise, at least the models predict the best possible linear decay curve available.

5.3.7 <u>Confidence in results</u>. In the preceding subsection, theoretical model predictions were compared to statistical estimates of continental topography power spectra without the benefit of formal statistical constraints. This approach was considered suitable in the present case because of the many assumptions inherent to the construction of the theoretical models and to the reduction of the observations. In turn, any geophysical conclusions arising from the analysis are necessarily non-specific, emphasizing more the refutation of classes of models of lithosphere behaviour rather than the acceptance of particular geophysical properties thereof. That the observations provide only limited constraint within the rheological parameter space of the

Figure 5-15. Model 2 normalized minimum misfit M_H', as a function of parameters D and τ, based on observed topography decay data normalized by the upper 95% confidence limit of the Cordilleran topography power spectral estimates.

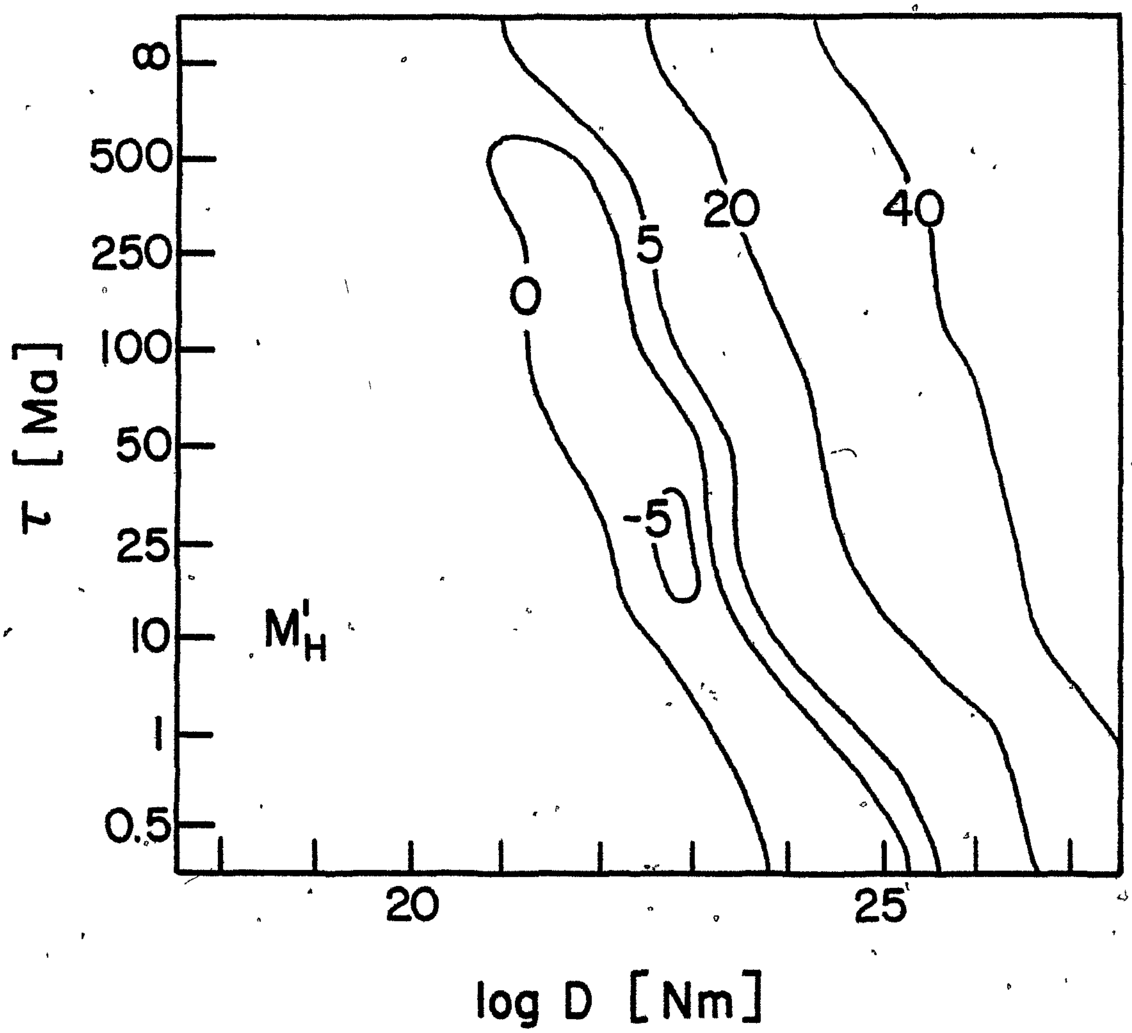

∞
500
250
100
50
25
10
1
0.5
τ [Ma]
M'_H
0
5
20
40
-5
20
25
log D [Nm]

Figure 5-16. Model 2 normalized minimum misfit $M_H^{\prime\circ}$, as a function of parameters D and τ, based on observed topography decay data normalized by the lower 95% confidence limit of the Cordilleran topography power spectral estimates.

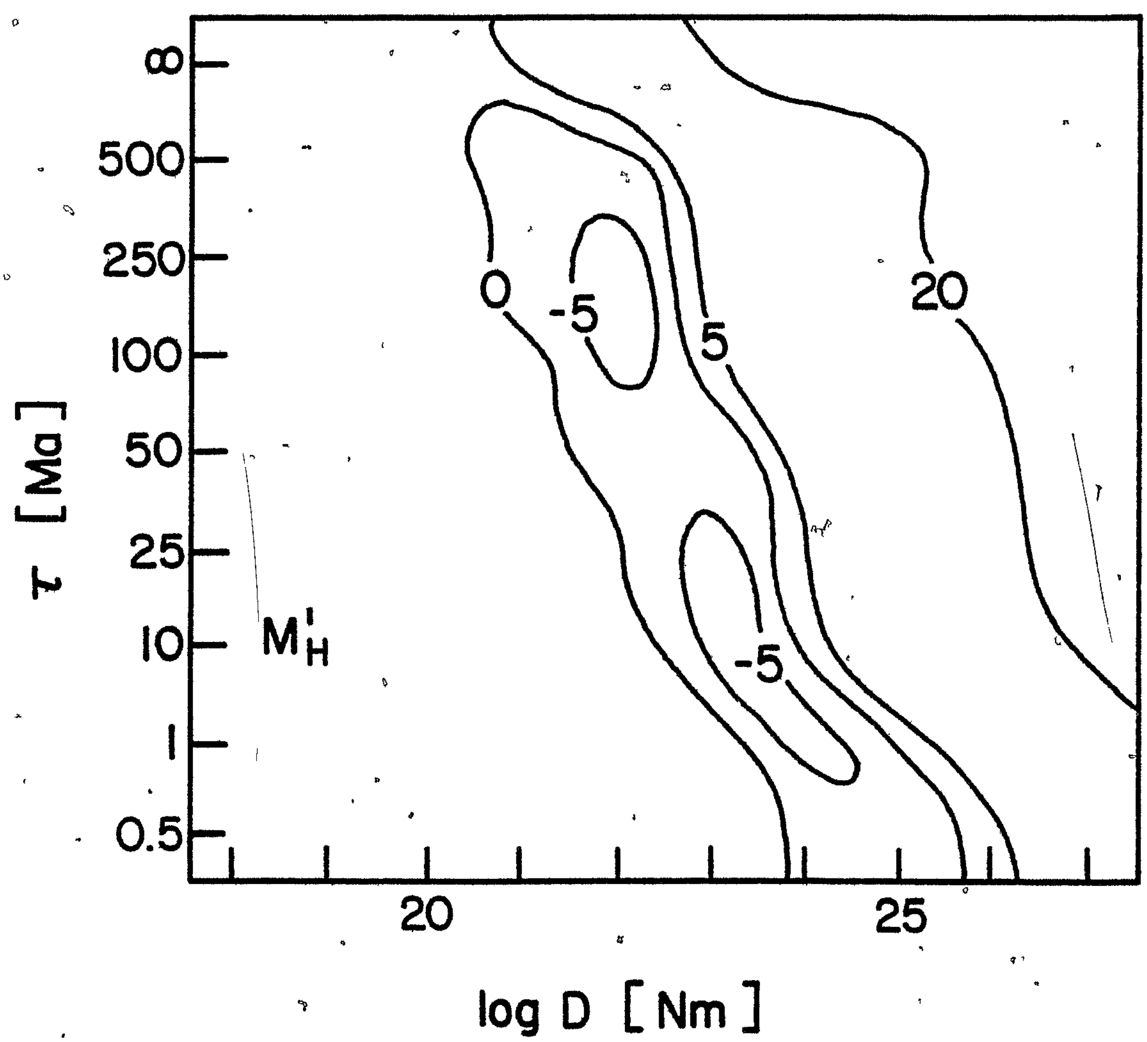
∞
500
250
100
50
25
10
1
0.5
τ [Ma]
M'_H
0
-5
5
20
-5
20
25
log D [Nm]

models contributes a posteriori justification for the informal approach taken.

The observed data were presented with their respective 95% confidence limits and perhaps the most serious statistical short-cut that was taken was the lack of consideration of the variance of the data within these bounds. In particular, the main source of uncertainty in this respect are the 95% confidence intervals associated with the Cordilleran estimates which were used to scale the other spectral data. It is intuitive, at least retrospectively, from the general nature of the results that such considerations will not greatly affect their outcome. To illustrate this, τ-D misfit maps for Model 2 are presented in Figures 5-15 and 5-16 respectively based on spectral estimates normalized by the upper and lower 95% confidence limits of the Cordilleran data. In each case, the misfits have been calculated relative to their appropriate best-fitting set of linear regression lines. As would be expected, the optimal erosion time constant σ is reduced somewhat in the first case [to 200-250 Ma from 250-300 Ma], corresponding to the need for more rapid erosion, and increased in the second case [to 350-400 Ma]. Otherwise, the best-fitting rheological parameter space of Model 2 is unchanged. Similar results occur for Model 1.

5.4 Isostatic Response Functions

5.4.1 Introduction. The isostatic response functions Q(k) of the major geological provinces of North America considered in this study were analyzed in terms of a time-invariant thin elastic plate model of continental lithosphere in Chapter 3. The observed response functions [Figures 3-3(a,b)] are characterized, very generally, by increasingly rapid fall-off to zero with increasing k as the tectonic age of their source regions increases. This feature of the observations was not clearly reflected in the results of the analysis because of uncertainties in data and variability in model parameters, particularly the density structure of the upper lithosphere.

In this section the temporal variation of the response function observations are considered in terms of time-dependent isostatic models developed in section 5.2. They are Model 1, in which a uniform viscoelastic thin plate lithosphere is loaded suddenly by topography which subsequently erodes, and Model 2, in which topograpy, formed above a thermally weakened orogenically active lithosphere and therefore in a highly compensated isostatic state, erodes subsequent to the lithosphere having cooled and achieved greater flexural compentency. The theoretical isostatic response functions Q(k,t) characteristic of these models can be derived from the theoretical topography $H(\vec{k},t)$ and deformation $W(\vec{k},t)$ functions, defined by Equations (5-25,26) and Equations (5-43, 44) for Models 1 and 2 respectively, in the manner described in subsection 5.2.6.

In particular, the theoretical Q(k,t) functions can be judged in the light of the results of section 5.3, in which the evolution of continental topography, as determined by the topography power spectra of the studied geological provinces, was compared to that predicted by the models. The results of section 5.3 indicated that the continental lithosphere, in response to topographic loads, may have the facility of viscous relaxation but did not strongly constrain the choice of rheological model parameters τ and D, particularly τ.

As noted above, isostatic response functions are difficult to interpret, chiefly because gravity anomalies cannot be uniquely determined by a particular density structure. The interpretation of the topography power spectra was not affected in this way. Therefore, the theoretical isostatic response functions are considered mainly in terms of their ability to further constrain the range of acceptable model parameters indicated by the topography analysis although their general attributes will also be discussed.

5.4.2 Model 1 results. Model 1, in the elastic [$\tau \to \infty$] plate case, is equivalent to the time-invariant model discussed in Chapter 3, in which the lithosphere at any time responds only to the remnant topographic load at that time, even as it erodes. The isostatic response function characterizing such a model is therefore not time-dependent, a feature which can be verified by inspecting Equations (5-23) and (5-24) which respectively define the topography and lithospheric deformation as functions of time of the elastic Model 1. Since this model was discussed at length in Chapter 3 it is not considered here.

The viscoelastic models for which the best fit to the topographic data was attained [subsection 5.3.6] are characterized by a flexural rigidity $D=10^{21}$ Nm and various viscous relaxation constants $\tau \leq 25$ Ma. Q(k,t) for these models, evaluated for times equal to the tectonic ages assumed for the studied geological provinces [subsection 5.3.3], are presented in Figure 5-17. Other parameters were chosen

Figure 5-17. Theoretical isostatic response functions Q(k,t) of a sample best-fitting [i.e. topography decay analysis, subsection 5.3.6] viscoelastic Model 1; parameters and topographic ages as shown. Local isostatic compensation exists for t≥325 Ma.

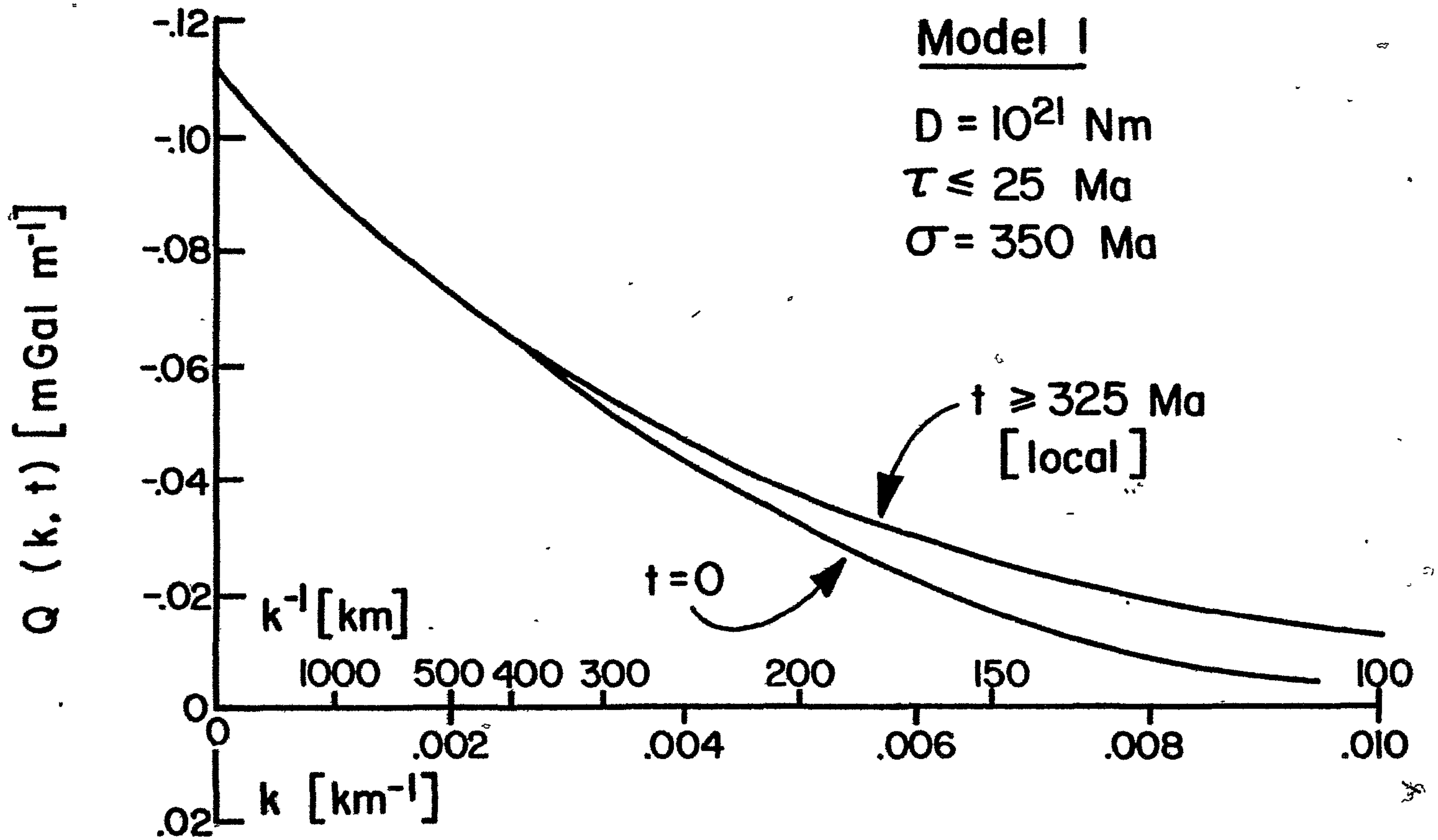
Model I
D = 10^21 Nm
τ ≤ 25 Ma
σ = 350 Ma
t ≥ 325 Ma
[local]
t = 0
Q (k, t) [mGal m^-1]
-.12
-.10
-.08
-.06
-.04
-.02
0
.02
k^-1 [km]
1000
500
400
300
200
150
100
0
.002
.004
.006
.008
.010
k [km^-1]

as follows: (1) load and mantle densities ρ_o and ρ_m were assumed to be 2700 and 3300 kg m^{-3} as always; (2) a single compensation depth z_m of 35 km, a depth compatible with commonly observed crustal thicknesses [e.g. Goodacre 1972], was chosen; and (3) the erosion time constant $\sigma(k)$ was taken to be a constant 350 Ma as a function of k, the $\sigma(k)$ function which characterized the best-fitting topography results.

Like their analogous topography decay curves, the calculated Model 1 isostatic response functions are not sensitive to choice of τ. This result is not surprising since both the topography $H(\vec{k},t)$ and deformation $W(\vec{k},t)$ functions, with gravity anomalies derived from the latter [Equation (3-11)], are controlled by exponential functions with equivalent arguments [Equations (5-25,26)]. In addition, Figure 5-17 shows that there is no temporal variation in the calculated $Q(k,t)$ for $t \geq 325$ Ma. This result was also signified by the topography decay analysis: the best-fitting model predictions [Figures 5-7(b-j)] are characterized by viscous effects only prior to the Appalachian data point at 325 Ma and these effects are due to the relaxation of the initial elastic flexure of the lithosphere which occurs instantaneously as the topographic load is applied. Subsequent to this initial relaxation, the topography, and its isostatic response evolves as in a state of local compensation because the time constant of erosion, σ, is much larger than that of the viscous relaxation, τ.

It follows that significant time-dependence of Model 1 isostatic response function $Q(k,t)$ will occur only when the ratio t/τ is small and will be favoured by small values of σ. Temporal effects in $Q(k,t)$ are also enhanced as D increases because less elastic flexure, resulting from the negative load associated with erosion, will occur as the plate increases in strength and therefore "requires" more viscous relaxation of the instantaneous flexure. For illustrative purposes, Q is plotted in Figure 5-18 as it varies in time for a plate with $D=10^{22}$ Nm, τ=500 Ma, and $\sigma(k)$=350 Ma. Values of τ of this order are required to detect changes in Q(k,t) throughout the very long time range considered here. It can be seen, for suitable parameters, that Model 1 predicts that the rebound effects of erosion progressively lag behind the erosion itself resulting in overcompensation of the remnant topography and therefore greater negative values of Q(k,t) as k and t increase. It is observed that this can result in the reversal of the k gradient of Q(k,t).

5.4.3 Model 2 results. In Model 2, low density crustal roots, resulting in local compensation of initial topography, are assumed to form during the early stages of continental evolution when the lithosphere is thermally activated and flexurally weak because of tectonism. Because these isostatically compensating structures are presumed to be subsequently "frozen" into the cooled and strengthened lithosphere, it is expected that the theoretical isostatic response functions of Model 2 will be more widely characterized by large negative values indicative of overcompensation of remnant eroded topography than were those of Model 1. Clearly, the overcompensation of topography in Model 2 is favoured by the same factors as in Model 1, small t/τ and σ and large D, but will be more pronounced than in Model 1.

Figure 5-18. Theoretical isostatic response functions Q(k,t) of a sample viscoelastic Model 1; parameters and topographic ages as shown.

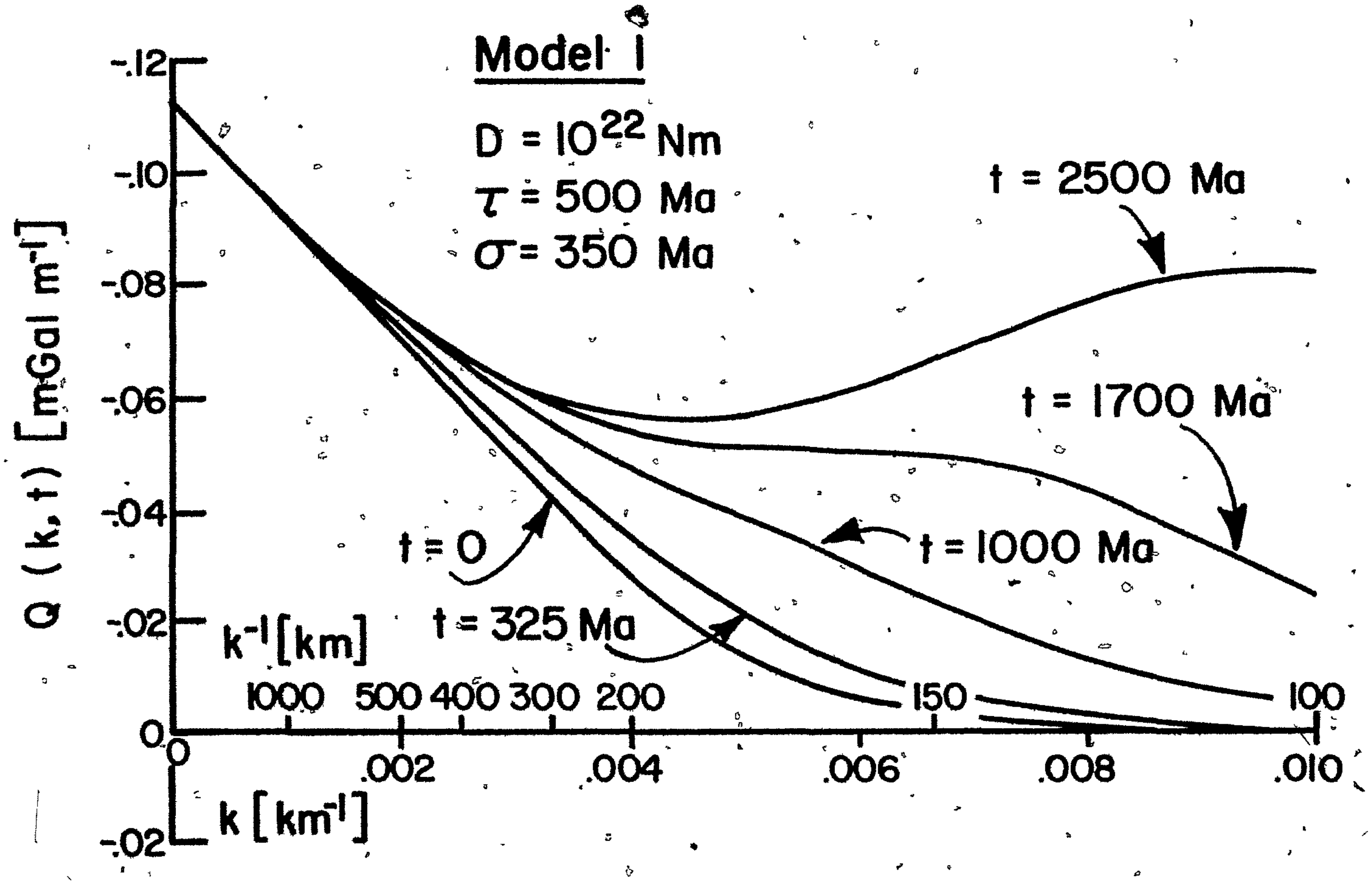

Model I
D = 10^22 Nm
τ = 500 Ma
σ = 350 Ma
t = 2500 Ma
t = 1700 Ma
t = 1000 Ma
t = 0
t = 325 Ma
Q (k, t) [mGal m^-1]
k^-1 [km]
1000 500 400 300 200 150 100
k [km^-1]
-.12
-.10
-.08
-.06
-.04
-.02
0
-.02
0
.002
.004
.006
.008
.010

The most important difference between the two models occurs in the case of an elastic [$\tau \to \infty$] lithosphere: the isostatic response function of the Model 2 lithosphere, unlike Model 1, will be time-dependent. This result can be verified by inspection of Equations (5-40) and (5-41) which respectively define the theoretical topography and deformation functions of Model 2 in the elastic case. In the limit as $t \to \infty$, topography vanishes but deformation, and therefore the gravity anomaly, associated with the initial locally compensated topography does not entirely do so. Therefore, in such circumstances, the isostatic response, which is the gravity normalized by topography, approaches infinity. It should be noted, although Model 2 specifically supposes that a lithosphere with no flexural strength instantaneously becomes flexurally competent and then maintains its strength uniformly through time, that the overcompensating effects of topographic erosion is a general result for any lithosphere which cools, thickens, and becomes more rigid progressively through time, whether or not the initial state was one of local isostasy.

An example of the temporal evolution of $Q(k,t)$ for Model 2 is shown in Figure 5-19; the response functions have been calculated for an elastic plate with flexural rigidity $D=10^{21}$ Nm, a value chosen to be compatible with results of the observed response function analysis of Chapter 3, but one which is less than those interpreted from other kinds of continental loads [Cochran 1980; cf. subsection 3.1.2]. Densities and compensation depth are as for Model 1 [subsection 5.4.2]; σ is taken to be a constant 400 Ma, the best choice of σ for a [$D=10^{21}$ Nm, $\tau \to \infty$] model on the basis of the observed topographic decay [cf. Figure 5-13(b)]. Old eroded topography is seen to be markedly

Figure 5-19. Theoretical isostatic response functions Q(k,t) of a sample low rigidity [D=10^{21} Nm] elastic Model 2; parameters and topographic ages as shown. Note that at t=0 topography is compensated locally.

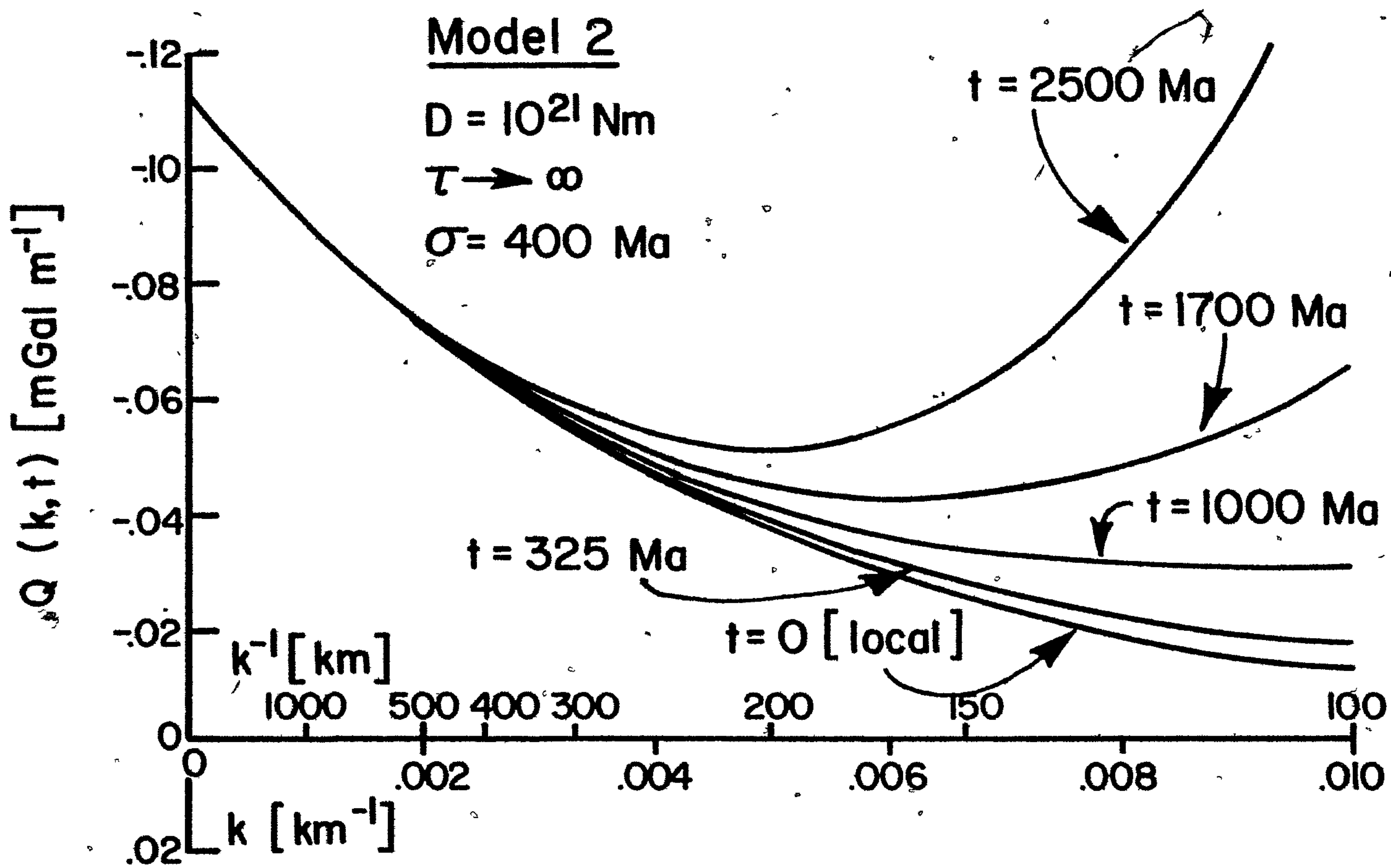

Model 2
D = 10²¹ Nm
τ → ∞
σ = 400 Ma
t = 2500 Ma
t = 1700 Ma
t = 1000 Ma
t = 325 Ma
t = 0 [local]
Q (k,t) [mGal m⁻¹]
-.12
-.10
-.08
-.06
-.04
-.02
0
.02
k⁻¹ [km]
1000
500
400
300
200
150
100
0
.002
.004
.006
.008
.010
k [km⁻¹]

overcompensated; higher choice of D would serve to greatly exaggerate the observed overcompensation.

The overcompensating effects of Model 2 evolution can be substantially reduced if the lithosphere is allowed viscous relaxation. Of particular interest are models within the best-fitting [τ,D] parameter space defined by the topographic decay analysis [Figure 5-13(a)]. As before, theoretical results for different parameter pairs in this range are not greatly distinctive. Q(k,t) functions characterizing models for [τ,D]=[1 Ma, 10^{24} Nm], [10 Ma, 10^{23} Nm], and [100 Ma, 10^{22} Nm] parameter pairs are very similar and those for the first pair are plotted as they vary in time in Figure 5-20. The assumed erosion time constant σ is, as always, that indicated by the best-fitting topography decay curve and is, in this case, 250 Ma. Densities and compensation depth are as before. The interactions of the time constants σ and τ are such that no temporal changes in the theoretical response functions occur when $t \geq 1000$ Ma. The effects of isostatic overcompensation are observed but are not severe. Viscous relaxation significantly attenuates the overcompensation; in contrast, consider the D=10^{24} Nm elastic Model 2 Q(k,t) functions for the various observations times, also plotted, using dashed lines, in Figure 5-20. The erosion time constant σ used for these curves was 400 Ma, the largest value of σ which seems likely from the topography analysis. Smaller values, of course, will serve to further accentuate the exaggerated state of topographic overcompensation indicated by the isostatic response functions; very large values of σ greater than 1000 Ma are required in order that the t=2500 Ma Q(k,t) function has a consistently positive gradient [downwards in Figure 5-20] in the indicated range of $k \leq 0.01$ km^{-1}. The double

Figure 5-20. Theoretical isostatic response functions Q(k,t) of a sample best-fitting [i.e. topography decay analysis, subsection 5.3.6] viscoelastic Model 2 [solid lines] and a medium rigidity [$D=10^{24}$ Nm] elastic Model 2 [dashed lines]; parameters and topographic ages as shown. Note that at t=0 topography is compensated locally.

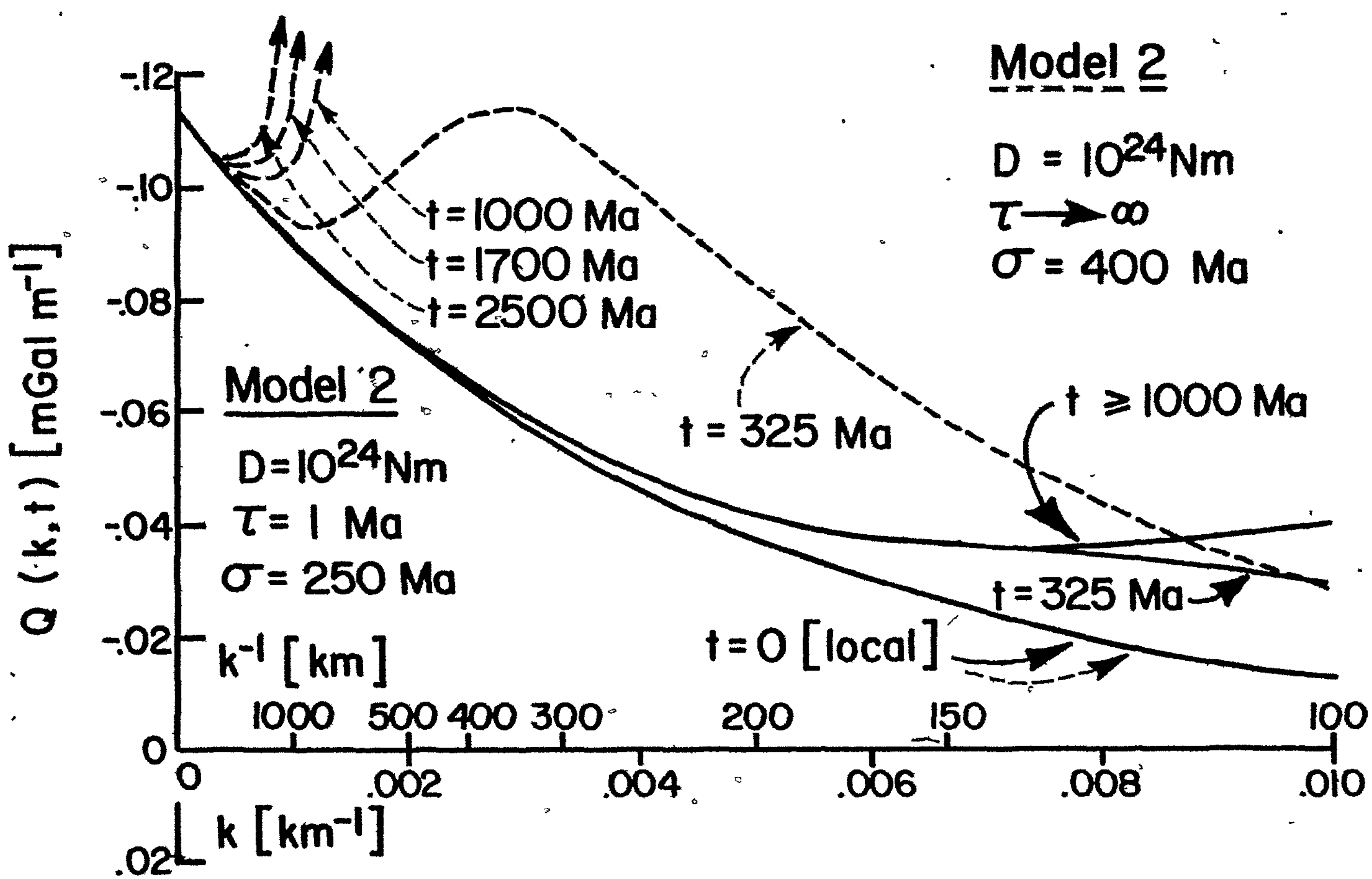

Model 2
D = 10^24 Nm
τ → ∞
σ = 400 Ma
Model 2
D = 10^24 Nm
τ = 1 Ma
σ = 250 Ma
t = 1000 Ma
t = 1700 Ma
t = 2500 Ma
t = 325 Ma
t ≥ 1000 Ma
t = 325 Ma
t = 0 [local]
Q (k,t) [mGal m^-1]
k^-1 [km]
k [km^-1]
-.12
-.10
-.08
-.06
-.04
-.02
0
.02
1000
500
400
300
200
150
100
0
.002
.004
.006
.008
.010

reversal of the gradient of the t=325 Ma curve is an interesting feature characteristic of some pairs of Model 2 parameters; it should be noted, however, that it is enhanced in the present case by the use of constant σ as a function of wavenumber k. Greater topographic overcompensation, indicated by larger negative values of Q(k,t) at the higher wavenumbers, would be favoured if σ decreases with increasing k, which is physically intuitive and is supported by the observed topography decay curves [e.g. Figures 5-11,14].

5.5 Discussion

5.5.1 Continental isostatic response functions. The analysis of the theoretical isostatic response functions of Models 1 and 2 presented in section 5.4 has shown that (1), in the case of both models, even if isostatic response functions were perfectly observable, because the theoretical response functions are no more sensitive to model parameters than were the theoretical topography decay curves, they could not help distinguish among the preferred model parameters indicated by the topography decay results; (2) given the quantitative uncertainties associated with real estimates of continental isostatic response functions, no dependence of response functions on the tectonic ages of source regions would likely be evident if the lithosphere is characterized by the preferred parameter sets of either Model 1 or Model 2; and (3), given suitable model parameters and enough time, the tendency of erosion is to produce large negative values of Q(k,t), indicative of overcompensation of the eroded remnant topography, especially as the wavenumber of the topography increases.

With respect to the latter observation, it is tempting but probably not justifiable to point to the k=0.009 km^{-1} $\hat{Q}(k,t)$ estimate from the Superior province as evidence of overcompensation [Figure 3-3 (b)]; however, the fact remains that no continental isostatic response function, among those presented here [Chapter 3] or elsewhere [Lewis and Dorman 1970, Banks and Swain 1978, McNutt and Parker 1978, McNutt 1980] is clearly characterized by elevated values as k increases to and becomes larger than 0.01 km^{-1}. In fact, in the case of the observed response functions of the present study, there is a tendency toward more rapid fall-off as k increases. Of course, variations in compensation depths between regions cannot be discounted in this respect [subsection 3.4.2]; nor can the effects of increasing geological noise as a percentage of the gravity signal, as the topography erodes and the implied isostatic gravity signal decreases with advancing tectonic age, be ignored.

If, for this reason, the reliability of continental isostatic response function estimates at the higher wavenumbers, say those greater than 0.0075 km^{-1}, is sufficiently doubtful that they may be ignored, then the erosion of topography, accommodated in terms of either Model 1 or 2, easily explains why low values of lithospheric rigidity D are returned from response functions interpreted by means of the simple elastic plate model [Chapter 3]. The crucial feature of an observed response function which determines D, as discussed by Cochran [1980] and McNutt [1980], is its curvature in the $0.001<k<0.005$ km^{-1} region. More rapid fall-off of Q here is indicative of higher D [cf. Figure 3-4].

However, Figures 5-17 through 5-20 illustrate that the effect of erosion, for suitable model parameters, is to elevate rather than suppress the response function at the crucial wavenumbers. In the case of Model 2, the <u>maximum</u> flexural rigidity which could be returned by interpreting an observed isostatic response function in terms of the simple non-erosional elastic plate model would be the flexural rigidity of the lithosphere in effect at the time of formation of the topography. An extreme case of Model 2 has been assumed here: that D was initially zero, resulting in local isostatic compensation, but Model 2 could be formulated according to any "frozen in" initial isostatic state as long as the lithosphere subsequently becomes thicker and stronger.

The potential unreliability of observed $\hat{Q}(k,t)$ at high k notwithstanding, the isostatic behaviour of a Model 2-type lithosphere, as reflected by the calculated theoretical response functions, appears to preclude pure elasticity as a viable rheology. Figure 5-20 shows, for an elastic lithosphere with $D=10^{24}$ Nm, that topography of even the very smallest observable wavenumbers is exceptionally overcompensated after, at most, 1000 Ma, the age of the Grenville province. As noted earlier, Model 2 has been formulated in such a way to provide extreme results: particularly, the lithosphere, after orogenesis, will not become suddenly thick and flexurally competent but will do so gradually depending on its efficiency of cooling. Erosion which occurs during this time will be more easily compensated than the model assumes; however, the time constant of erosion, in the context of the assumed erosion model, is of the order of a few hundred million years, several times greater than that characterizing continental lithospheric cooling [Sclater <u>et al</u>. 1980] and it is therefore expected that overcompensation effects will be strongly maintained. Thus, viscous relaxation in the continental lithosphere, perhaps with a time constant τ as small as 1 Ma, is indicated by considerations of observed and theoretical isostatic response functions if a Model 2-type evolution of continental lithosphere is assumed. The classical argument that the maintenance of medium scale [of the order of hundreds of kilometres wavelength] gravity anomalies in old continental regions such as the Canadian Shield requires a strong, non-relaxing crust [e.g. Jeffreys 1976] appears to be overstated; rather, the gravity anomalies which do persist in such regions are perhaps explicable in terms of geodynamic processes rather than static ones.

5.5.2 Early topographic evolution. A feature of the theoretical normalized topography decay curves [subsection 5.3.6, Figures 5-7 (b-j)] common to both Models 1 and 2 is their [logarithmic] linearity for the smallest of the observed wavenumbers k_r. Although Model 2 at least predicts linear decay curves which are equivalent [except for k_r^{-1}=400 km] to the best-fitting linear regression lines, both models essentially fail in this respect because the observed data are systematically non-linear [Figures 5-7(b-j)]. In particular, normalized power spectral data derived from the Appalachian region [t=325 Ma] are consistently smaller than the models predict. This feature of the results is discussed below in terms of the potential effects of some of the inherent model and observational assumptions.

(i) Appalachian data. The Appalachian data may be less reliable than data from the other study areas because its source area is smaller [except for that of the Grenville data]; narrow [and therefore particularly susceptible to affectations due to smoothing during the data reduction process]; and because of its history of involvement with the opening of the present Atlantic Ocean and with sedimentary basin development on the continental margin. Figure 2-1 shows that a considerable portion of the Appalachian study area consists of the Grenville province or is covered by sediments [including those of the Atlantic continental shelf]. The topographic signal from these areas could certainly contribute to a lower level of power measured for the entire study area. The reason the Appalachian study area was made as large as it is, at the expense of geological and topographic homogeneity, was to provide more data for more and statistically better estimates of its isostatic response function and topography power spectrum.

(ii) Model parameters. The implications of the Appalachian misfits can be judged on the attributes of the models themselves. Best-fitting model parameters were determined on the basis of constant parameters σ, τ, and D. Wavenumber dependence of σ was investigated [the σ-criterion] in subsection 5.3.6; although better low k results for Model 2 were thus provided, no more satisfactory fit of the Appalachian data was returned. Parameters τ and D were assumed constant in time and space, a requisite feature of the models in terms of their physical linearity and mathematical development [section 5.2]. However, if, in reality, the rheology of the lithosphere is such that it implies that τ and D do possess time and space dependencies, these dependencies may be reflected in the observations. What kinds of t and k dependencies of τ and D tend to improve the misfit of the Appalachian data, or the early evolution of the models in general, and are the physical implications of the dependencies reasonable?

First, consider the effects of k dependencies in terms of the general model characteristics presented in Figures 5-8,9 and 10. (1) The mechanism by which Model 1 effects early topographic decay [subsection 5.3.5, Figures 5-9(a,b)] is viscous relaxation of the initial elastic flexure associated with the application of the topographic load; this fails to occur at small wavenumbers because the plate is insufficiently strong to maintain flexure. As a result the long wavelength topography is immediately in a state of local isostatic equilibrium for the indicated best-fitting choices of τ and D. In such a case $\tau(k)$ dependence will be inconsequential; rather, curvature in the low k decay curves can only be achieved by means of greater D such that initial elastic flexure is sustainable. Such a D(k) dependence is presumably opposite in effect to that expected from a rheologically non-linear lithosphere in which strain rate would depend on some power of the applied stress. (2) Figures 5-10 show that early topographic reduction effected by Model 2 is favoured either by smaller values of ψ, leading to larger values of D, or by larger values of τ. Thus, allowing D to vary with k in order to successfully model the low k observations implies a D(k) dependency similar to that of Model 1: D larger for smaller wavenumbers. (3) A similar result applies for $\tau(k)$ in Model 2; again, this is opposed to what might qualitatively be expected, that longer wavelength topography "sees" more deeply into the lithosphere where temperatures are higher and viscosity, and therefore τ, is smaller.

Secondly, consider possible forms of functions D(t) and $\tau(t)$ which would improve the early evolution of the modelled topography. (1) In either Model 1 or 2, as pointed out many times, it is general that the rate of topographic reduction is favoured by small values of ψ, hence large values of D [Figures 5-8,9,10]. Thus, to control the slope of the decay curve by letting D vary as a function of t, such that the slope would decrease through time and therefore reproduce the general form of the observations, would require $dD(t)/dt<0$. This result is incompatible with the probable characteristic of continental lithosphere that it cools and thickens with age [e.g. Sclater et al. 1980]. (2) As noted above, in Model 1, as long as τ is small enough to allow for the early viscous relaxation phase to occur in the requisite amount of time, it cannot be modified to improve the model's ability to reproduce the Appalachian data; thus no obvious $\tau(t)$ function is implied by the misfit. (3) In the case of Model 2, it is difficult to judge the effects of temporal variations in τ throughout the entire 2500 Ma range of observed t; however, it remains that larger τ results in more rapid decay [Figures 5-10(a,b)] and therefore it may be presumed that $\tau(t)$ would have to decrease through time in order to better reproduce the observed early evolution of topography. This result, like the D(t) result, is not compatible with a cooling lithosphere.

Thus, it seems the lack of success of the present simple linear viscoelastic uniform plate models to describe the early [~t<500 Ma] evolution of continental topography, as evidenced by the Cordilleran and Appalachian observed topography power spectra, cannot be explained in terms of qualitative effects expected of more rheologically and structurally complex models of which the present models are only approximations.

However, it is also necessary to consider the effects of a time-dependent σ function; the result of such a consideration is less equivocal. It seems reasonable that the observed topography decay data may be better reproduced if σ is smaller than the indicated 200-400 Ma in the early phase of evolution. This may be equivalent to an erosional process in which erosion rate is proportional to some power greater than one of the topographic amplitude rather than being linearly proportional as assumed in this study in order to allow the analytical formulation of the models to be tractable [Equations (4-1)]. Such a possibility cannot be ruled out; in particular, $\sigma(k,t)$ which increases as a function of time in combination with elastic plate isostatic behaviour could presumably match the observations. In this context, however, overcompensation of eroded topography, in terms of a Model 2-type scheme, as discussed in subsection 5.5.1, would remain a problem and, because early topography would erode more rapidly, such overcompensation may become even more significant. It should also be noted, since the visco-elastic, linear erosion models, particularly Model 2, are reasonably successful at high wavenumbers k, that if σ time-dependencies, or equivalently erosion rates which are non-linearly proportional to topographic amplitude, do occur, they are themselves k-dependent.

(iii) Initial topography. There are other factors, not related to the assumed erosion model or to implied variations in the rheological model parameters, which may be contributing to the apparent depressed level of the Appalachian topography power spectrum. The most important of these is the assumption that the present-day topography of the Cordilleran study area represents the initial state of either of Models 1 and 2. There are two aspects to consider. The first is that the spectral amplitudes found in the Cordilleran region are assumed to be comparable to those which initially existed in the Appalachian region. In this context, it is noteworthy that the Cordilleran and Appalachian mountain-belts consist of similar gross tectonic elements [Dewey and Bird 1970]. Accordingly, there is no reason to believe that the initial topographic power of each orogen would be greatly different.

Secondly, the choice of the present as the initialization time t=0 or t_c [for Model 1 or 2] may be premature. With respect to the very long term topographic evolution being considered, an error of ±100-200 Ma is unlikely to be significant in terms of the implications of the models [cf. Figures 5-7]. The potential effects of larger errors are as follows.

For Model 1, the initialization time t=0 can be no later than the present. The Cordilleran topography exists and it is isostatically compensated in a fashion not greatly dissimilar to that of older regions [cf. Chapter 3]. If t=0 is assumed to be sometime in the past then the Appalachian misfit is only worsened.

On the other hand, in terms of Model 2, the consistent overestimation of Appalachian topographic power could be reduced if the initialization time t_c is sometime in the future rather than at the present. Evidence that this may be so, at least over part of the Cordilleran study area, is provided by anomalously high heat flow observations [e.g. Sclater et al. 1980]. Figure 5-21 illustrates the

Figure 5-21. Normalized topography decay data $\hat{S}_H$, with 95% confidence intervals, observed at spectral wavelength 286 km [cf. subsection 5.3.4, Figure 5-7(c)], showing best-fitting linear regression line <u>not</u> forced through the origin. Potential future normalized origins fall within the stippled region [cf. text].

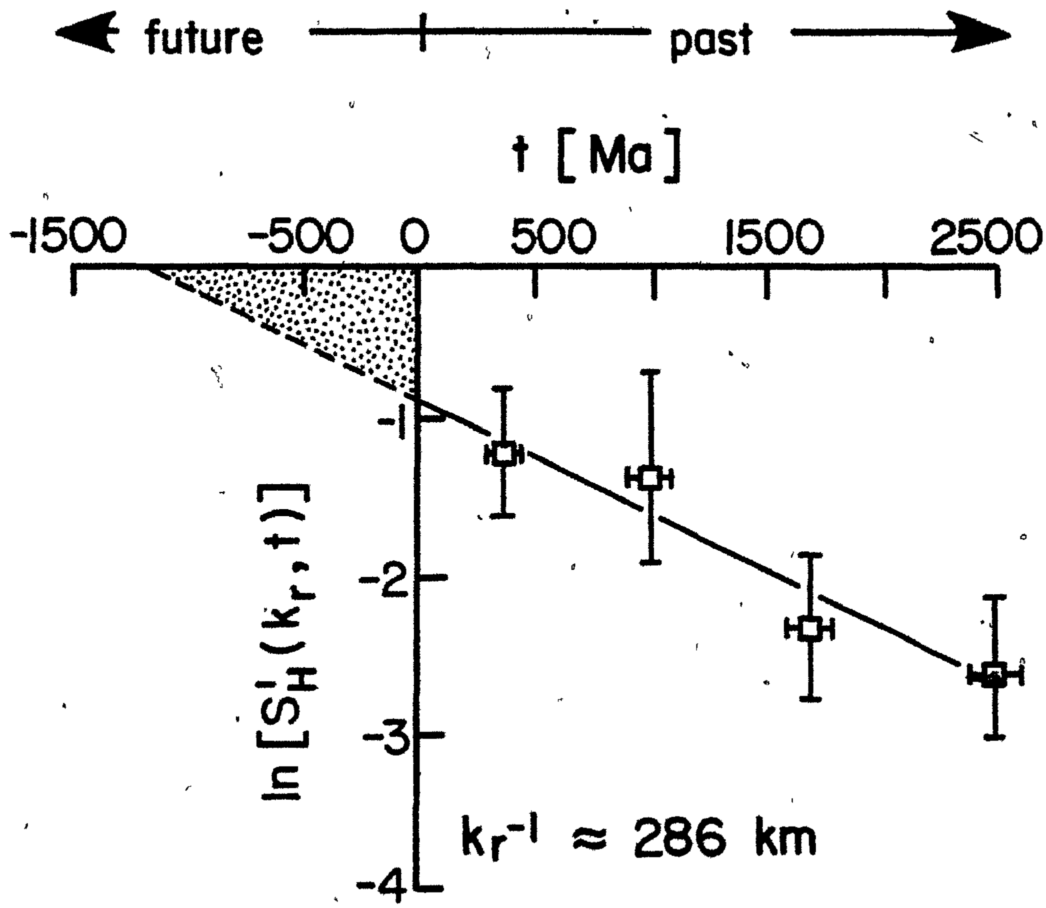

future
past
t [Ma]
-1500
-500
0
500
1500
2500
-1
-2
-3
-4
ln [S'_H (k_r , t)]
k_r^-1 ≈ 286 km

possible consequences of a premature choice of t_c. As an example, the 286 km wavelength topography decay data have been redraughted showing their best-fitting regression line not forced to pass through the origin. If it is assumed that the power of the Cordilleran topography will not actually increase in the future, then the "initial" topographic power $|H_\ell(\vec{k})|^2$ existing when the lithosphere becomes flexurally competent at some future time t_c will plot within the stippled region of Figure 5-21. If the degree of power in the present topography is maintained until that time, because of continual tectonic rejuvenation of eroded terranes, then the origin of the normalized topography power measured at t_c would plot along the future time axis as drawn. Alternatively, if erosion of Cordilleran topography prior to a future t_c is not offset by tectonic uplift, then the future normalized origin would plot below the time axis. Any such future initial topography $|H_\ell(\vec{k})|^2$ falling along the extrapolated portion of the regression line would allow the resulting topography decay curve to be modelled successfully by an elastic lithosphere.

In the present case, data at the larger observed wavenumbers are more successfully reproduced by Model 2, in terms of the Appalachian observations, than those at small wavenumbers. This feature of the results may be a consequence of the assumption that the lithosphere attains flexural competence suddenly. If the lithosphere actually cools and thickens gradually, its acquisition of effective flexural strength may appear to occur earlier at short wavelengths than it does at long wavelengths. Thus, long wavelength Cordilleran topography may at present be evolving in a pre-Model 2 fashion [that is, its erosion is isostatically compensated locally], whereas short wavelength topography may already be in a state of Model 2-type evolution.

(iv) Models. Models 1 and 2 can be considered to be end-members of a spectrum of models of the evolution of continental topography with the model most closely approximating the real developmental process falling between them. For example, a contributory mechanism by which Model 2-type topography may initially achieve local isostatic compensation may be the early Model 1-type viscous relaxation [of a thin, flexurally weak uniform viscoelastic lithosphere] accompanied by topographic "sinking" [cf. subsection 5.3.5]. This kind of mechanism can easily account for greater decay of small wavenumber topography, as apparently required by the observations, during the first one or two hundred million post-orogenic years depending on the flexural rigidity D of the lithosphere during this time. [It is necessarily large enough that local isostatic compensation is not essentially effected by the initial elastic flexure only.] The acquisition of local compensation by the existing topography would be rapid, in terms of the concurrent cooling and progressive strengthening of the lithosphere, if the viscous relaxation time constant τ was relatively small [say, $\tau \leq 25$ Ma]. Subsequently, as even greater cooling and strengthening of the lithosphere takes place, secondary topographic evolution of Model 2-type would occur. It is probable, in such a scheme, that the primary Model 1-type topographic development would have been initiated not by the sudden application of the topography onto the lithosphere but rather by the removal from the system of extrinsic tectonic forces which had been supporting previously established topography.

5.5.3 Erosion model parameters. The topography decay curve misfit analysis presented in subsection 5.3.6 indicated that it is probable that the erosion time constant function $\sigma(k)$, of the form postulated in subsection 4.2.1,

$$\sigma(k) = \omega k^{-\varepsilon}; \quad \omega,\varepsilon>0 \qquad (4\text{-}2),$$

where ω and ε are constants, is not strongly dependent upon wavenumber k. Wavenumber dependence of σ was investigated by means of the σ-criterion in which an a priori assumed constant σ spectrum was adjusted according to its ability to produce improved overall misfits. Only for the best-fitting Model 2 parameters were such adjustments profitable provided they were consistent with the form of $\sigma(k)$ described by Equation (4-2). The results, plotted in Figure 5-14, did not greatly constrain parameters ω and ε. Nevertheless, it follows from the observation of weak wavenumber dependence of σ that $\varepsilon<1$ and from the observed best-fitting σ values of 200-400 Ma, in the wavelength range 600 km$\leq k^{-1}\leq$100 km, that $\omega>1$ Ma km^{-1}. One sample function visually fitted to the data in Figure 5-14 indicates $\omega\simeq74$ Ma km^{-1} and $\varepsilon\simeq0.25$.

These results are not inconsistent with those of the South Island, New Zealand tectonic uplift-topography analysis presented in Chapter 4. Figure 4-5 shows that ω and ε values such as those implied by North American topographic decay, noted above, are out of the range of those which would be discernible on the basis of the New Zealand data. Recall that for this to be so the erosion model must be reliable and/or the uplift rate-topography transfer function must be observable up to wavenumbers as great as $[4.5\omega/t]^{1/\varepsilon}$ [Equation (4-20)] where t is the length of time during which tectonic uplift has occurred. Thus, if the postulated erosion model, Equation (4-2), is assumed to be valid for k^{-1}>50 km, and the model parameters ω and ε are assumed, as above, to be 74 Ma km^{-1} and 0.25 respectively, then to be able to extract such parameters from observed data using the technique applied to South Island, requires that the length of time of continuous tectonic uplift of the test region, maintained by a single tectonic regime, be 885 Ma, a tectonically unreasonable length of time. Although the New Zealand uplift rate-topography transfer function results are not inconsistent with those expected on the basis of the theory and therefore do not reject the fundamental erosion model, it may be concluded that such a technique, applied to other regions, will not provide any further test of the model or constraint on its parameters.

5.5.4 Viscoelastic continental lithosphere. The two theoretical models of the evolution of continental topography developed in this chapter and in terms of which the topography and isostatic response functions of several major geological provinces of North America have been discussed are simple approximations of much more complex geodynamic processes which account for the formation and subsequent modification of continental topography. The ability of the models to reproduce the topography and isostatic response data allows neither to be characterized by a particular pair of rheological parameters τ and D. It is likely that the true post-orogenic development of continental topography comprises elements of both of the simple theoretical Models 1 and 2. Nevertheless, the results of the analyses are such that it is possible to make general conclusions.

Model 2-type topographic evolution of continents is probably more important than that of Model 1 for the following reasons. (1) In the first case, Model 2 is intuitively more geodynamically reasonable. It is fairly well-established, on the basis of heat flow [Sclater et al. 1980] and seismological [Kono and Amano 1978, Panza 1980] observations that the continental lithosphere does cool and thicken with age. The isostatic evolution of topographic loads on continents may therefore be analogous with that of oceanic loads with the important exception that significant subsequent erosion of the former takes place. (2) The isostatic response function of the Cordilleran geological province [Figure 3-3(a)] supports Model 2. It is characterized by distinct curvature and rapid fall-off at wavenumbers larger than the other observed response functions, features which can either be interpreted as due to a very low lithospheric flexural rigidity [McNutt 1980] or to a lack of erosional effects [subsection 5.5.1]. (3) The flexural rigidity of the lithosphere based on the best fit of Model 1 to the observed topography decay data is 10^{21} Nm, a value which is substantially smaller than that suggested by the analysis of individual continental loads in terms of an elastic lithosphere [10^{24}-10^{25} Nm; Cochran 1980] and smaller than that suggested by the analysis of the formation of foreland basins in terms of a viscoelastic lithosphere [10^{25} Nm; Beaumont 1981]. (4) The best-fitting Model 1 decay curves predict very little topographic erosion by t=100-200 Ma, the majority of the effective topographic decay during this time being accomplished by viscous relaxation and concurrent "sinking" of topography into a position of local isostatic equilibrium; similarly, the isostatic response functions of continental regions would reflect this condition of local isostasy after this short period of time, apparently in contrast with the observations [Figures 3-3, 3-7]. (5) The Model 2 topography decay results provide a range of best-fitting pairs of rheological parameters τ and D [Figure 5-13(a)] among which are included $D=10^{23}$ Nm, τ=25 Ma; $D=10^{24}$ Nm, τ=1 Ma; and $D=10^{25}$ Nm, τ=0.5 Ma; parameters which do not compare unfavourably with those suggested by the foreland basin analysis [$D=10^{25}$ Nm, τ=27.5 Ma; Beaumont 1981]. (6) The Model 2 best-fitting topography decay results, unlike those of Model 1, are satisfactorily adjusted according to the σ-criterion [Figures 5-7 (b-f), 5-14].

If it can be concluded thus that Model 2-type evolution dominates the post-orogenic topographic development of continents, then the major implication of the results is that the occurrence of viscous relaxation of elastic stresses, with a characteristic time constant τ which is potentially very small [~1 Ma], cannot be ruled out in the continental lithosphere. This contrasts with the classical view that topographic relief of continents, should viscous deformation occur, would flow away during the observed life spans of cratonic regions. Rather, it has been shown that the interaction of the viscous relaxation of elastic deformation associated with topographic and with erosionally-induced loads is such that a condition of dynamic equilibrium resulting in steady-state topography can almost be achieved [subsection 5.3.5, Figures 5-10]. The crucial assumptions inherent to this conclusion relate to the requirements (1) that the continental lithosphere cools and strengthens with time after the last tectonic event, that the topography is initially compensated by a weak lithosphere, and that this initial compensation is subsequently "frozen into" a thicker, stronger lithosphere and (2) that large scale erosion of continental topography can be approximated by the model described by Equations (4-1) in which the rate of erosion of spectral topography is linearly proportional to the amplitude of the topography which remains at any given time.

With respect to the second of these assumptions, it has been noted [subsection 5.5.2] that the effects of non-linearly proportional erosion to topographic amplitude combined with elastic plate rheology may suitably reproduce the character of the observed topography decay curves. Similarly, the consequences of an incorrect choice of the initial topography power spectrum may be such that the observations are compatible with an elastic model [subsection 5.5.2(iii)]. The elastic plate option cannot therefore be dismissed. However, the presumed form of the isostatic response functions characterizing such a model, as discussed in subsection 5.5.1, also seems to preclude purely elastic behaviour during the process of isostatic compensation of erosion. In this respect, elastic-plastic behaviour of continental lithosphere cannot be dismissed by the present results. In such a case, the stresses induced by erosion, whenever they exceeded the lithosphere's yield strength, would be relaxed episodically by cataclastic or ductile plastic flow.

5.6 Summary

Geodynamic models have been developed which quantitatively describe the long term erosional decay of continental topography and its associated lithospheric flexure. In the models it is assumed that (1) continental lithosphere is characterized by linear [Maxwell] viscoelastic rheology and (2) the rate of erosion of topography is linearly proportional to its height as discussed in Chapter 4. Two general loading models have been considered: Model 1, in which a uniform viscoelastic thin plate lithosphere is loaded suddenly by topography which subsequently erodes, and Model 2, in which topography, formed above a thermally weakened orogenically active lithosphere and therefore in a state of local isostatic compensation, erodes subsequent to the lithosphere having cooled and achieved greater flexural competency.

The models have allowed, for the first time, the investigation of the rheology of the continental lithosphere in terms of the long term erosional decay of continental topography. The form of the topographic decay has been established by comparing the observed topography power spectra of several North American geological provinces of vastly different tectonic ages.

The results of a misfit analysis of model predictions and observations show that, for both Models 1 and 2, the best overall reproduction of the observed decay curves is provided by a viscoelastic as opposed to purely elastic lithosphere. However, in neither case do the misfit results strongly constrain the values of the rheological model parameters, flexural rigidity D and viscous relaxation time constant τ. On the other hand, the erosion time constant σ characteristic of the wavelengths of topography being considered is relatively well-established by the misfit results. They suggest that it falls in the range 200-400 Ma and, in the case of Model 2 results, that it increases slightly with increasing topographic wavelength.

The important theoretical result of viscoelastic Models 1 and 2 is that viscous relaxation of elastic stresses arising from past topography and/or from past and present erosion can progressively reduce the rate at which topography decays. The reduction is such that eventually a condition of steady-state topography can almost be achieved. This feature of the models is in general agreement with the form of the observed decay curves. However, both models fail to predict sufficient early topographic decay as evidenced by the Appalachian data. This may be partly due to the geological heterogeneity of the Appalachian study area. Otherwise, the Appalachian misfits do not seem to be explicable in terms of the implied effects of depth- and time-dependent rheological model parameters D and τ. However, the potential consequences of incorrect assumptions regarding (1) the linear erosion model and/or (2) the representation of the present-day Cordilleran topography power spectrum as the initial topography power spectrum may be compatible with the Appalachian data. In each case for Model 2 and in the former case for Model 1 the implications are such that a purely elastic rheological model cannot be ruled out.

Models 1 and 2 are considered to be simple end-members of a spectrum of more complex models of the post-orogenic evolution of continental topography with the best model likely comprising elements of each. Model 2-type topographic evolution is probably dominant because heat flow and seismological observations show that the continental lithosphere apparently does cool and thicken with age. In the present case, the topographic misfit results of Model 2 are better than those of Model 1 and the possible values of rheological parameters returned by Model 2 are more consistent with those based on other kinds of analyses than are those returned by Model 1.

The theoretical response functions Q(k,t) of Models 1 and 2 have also been formulated and represent the first attempt to quantitatively determine the effects of erosion on response functions observed in old continental regions. The purely elastic Model 1 isostatic response function is equivalent to the model discussed in Chapter 3. Otherwise, both Models 1 and 2 predict isostatic overcompensation of old topography to a degree depending on the chosen model parameters.

The theoretical isostatic response functions of Models 1 and 2 have been calculated for their best-fitting parameters determined from the topography decay analysis. In the case of Model 1 the results indicate that the topography of the Appalachian and older North American geological provinces should be in a state of local isostatic compensation. This contradicts the one-norm misfit results of Chapter 3 but cannot be ruled out because the standard errors associated with observed $\hat{Q}$ are so large. In the case of Model 2 the theoretical response functions indicate that topography in the upper range of observed wavenumbers of the Appalachian and older regions should be overcompensated. The degree of overcompensation is not great enough that it would necessarily be expected to be recognized in the observed data given their large standard errors. However, it was noted that the tendency of any detectable erosional effects in $\hat{Q}(k)$ would be to return artificially low lithospheric flexural rigidities if interpreted in terms of the non-erosional elastic model [Chapter 3]. Such results could be comparable with those of previous studies [Banks <u>et al</u>. 1977, Banks and Swain 1978, McNutt and Parker 1978, Stephenson 1978, Cochran 1980, McNutt 1980.]

The theoretical isostatic response function of even a weak [$D=10^{21}$ Nm] elastic Model 2 lithosphere appears to preclude pure elasticity as a viable lithosphere rheology. In such a case, erosion results in extreme isostatic overcompensation of remnant topography. The resulting stresses can either be continuously relaxed by viscous flow as explicitly modelled in the present study or by periodic plastic failure of the lithosphere.

Chapter 6. The Effects of Small Scale Convection in the Upper Mantle on Isostatic Response Functions

6.1 Introduction

6.1.1 Surface topography and gravity and small scale mantle convection. The consensus of most Earth scientists is that the motion of lithospheric plates is driven by some form of thermal convection which derives its energy from primordial heat and/or heat produced by radioactive elements distributed in the mantle. There are, however, few observations to provide independent evidence of the existence and nature of the hypothesized mantle circulation. In this respect some attention has been given to long wavelength gravity anomalies and topography of the Earth's surface on the grounds that the topography may be a result of plate flexural uplift dynamically supported by forces associated with the mantle convection [e.g. McKenzie 1967]. Anderson et al. [1973], for example, showed that differences in bathymetric depth and gravity anomalies at active mid-ocean ridges are correlated in a way similar to that predicted by numerical models of convection in a Newtonian fluid [McKenzie et al. 1974]. More recent investigations in the North Atlantic [Sclater et al. 1975] and in the Central Pacific [Watts 1976] have tended to support the conclusions of Anderson et al. [1973]. Both Sclater et al. and Watts considered two-dimensional data comprising residual bathymetric depth anomalies, those corrected for the effects of lithospheric age, and surface derived gravity observations. Later, Cochran and Talwani [1977] disputed the existence of a consistent direct correlation between long wavelength gravity anomalies and bathymetry throughout the world's oceans. They argued that the lithosphere must be strongly decoupled from the main body of the asthenosphere if the gravity anomalies are to have their source beneath the lithosphere. McKenzie et al. [1980] suggest that Cochran and Talwani's [1977] failure to detect a global relationship between long wavelength gravity and residual depth was due to inadequate sampling of gravity data.

An alternative approach to the problem of the relationship between gravity anomalies and topography which may clarify the uncertainties in its interpretation is one in which the relationship is determined systematically in the wavenumber ($\vec{k}$) domain in terms of a linear transfer function [or admittance], $Q(\vec{k})$, referred to previously as the isostatic response function. McKenzie [1977] calculated the behaviour of $Q(\vec{k})$ for simple models as it depends on the Rayleigh number, the degree of internal heating, viscosity variations, and the depth of the convecting layer. He did not take into account the effect on Q of the deflection of an abrupt density interface within the lithosphere, such as the Mohorovicic discontinuity, during its flexure by the forces derived from convection. The comparison of observed to McKenzie's theoretical values of Q is further complicated by the possible presence of topography on the surface of the lithosphere not associated with deformation caused by underlying convection. McKenzie and Bowin [1976], for example, attempted to detect the effects of convection in observations of gravity and bathymetry made along two profiles in the Atlantic Ocean but found that the observed $Q(\vec{k})$ could best be explained by isostatic compensation within the lithosphere to simple surface loading by topography. No deformation of the plate by convection was detected.

Convective flow in the Earth may occur with two distinct horizontal length scales: (1) large scale mass circulation of the lithosphere plates themselves in combination with some form of return flow at an as yet undetermined depth in the mantle and (2) small scale Rayleigh-Benard convection in the upper mantle which provides the mechanism of heat transport to the base of the lithosphere evident under the older parts of oceans and under continents. It was the effect of the smaller scale of convection which McKenzie and Bowin [1976] attempted to detect; its hypothetical existence is based on theoretical analyses of the efficiency of heat transport in convective systems [Richter 1973, McKenzie and Weiss 1975] and on experimental results [Richter and Parsons 1975]. For oceanic regions younger than approximately 70 Ma mean depth varies as the square root of age, an observation which can be satisfactorily explained in terms of the oceanic lithosphere behaving as a simple cooling boundary layer in the large scale convective flow regime. In older regions the mean oceanic depth is less than predicted by square root relation suggesting the presence of an efficient heat transfer to the base of the lithosphere by small scale convection. Parsons and McKenzie [1978] have modelled the onset of small scale convection in terms of the development of a thermal instability beneath the oceanic lithosphere, assumed to be a mechanically rigid boundary layer, as it thickens with age.

Depending on the Rayleigh number [Ra] of the convecting layer and the velocity of the upper boundary [the lithospheric plate], theory

[Richter 1973] and experiments [Richter and Parsons 1975] demonstrate that the small scale circulation may eventually take the form of longitudinal rolls aligned with axes parallel to the direction of shear between the plate and the underlying layer, shown schematically in Figure 6-1(a). For Ra = 10^6, an estimate based on the results of numerical models compared to observations of heat flux [McKenzie et al. 1974], Richter and Parsons [1975] suggest, from scaled experimental results, that the formation of longitudinal rolls would take from 20-50 Ma to several hundred million years for absolute plate velocities in the range 10-2 cm yr^{-1}. More complex patterns of small scale convection cells, such as a bimodal configuration [Figure 6-1(b)], may be possible if the age versus plate velocity constraint is not met or if Ra is larger. Similarly, if the horizontal movement of the lithospheric plate is decoupled from that of the mantle below by the presence of a low viscosity zone beneath the plate [e.g. Richter and McKenzie 1978] such that the shearing between them is minimized, then longitudinal convection rolls are unlikely to be stable beneath even the fastest moving plates [Skilbeck and McKenzie 1979] and any small scale convective flow would probably be multi-modal. Such is the case of the planform of small scale convection, based on the GEOS 3 determination of the geoid and extensive bathymetric data, beneath the Pacific Ocean presented recently by McKenzie et al. [1980]. The observed geoidal and bathymetric undulations are, however, elliptical in shape with the elongated direction believed by the authors [McKenzie et al. 1980] to reflect the direction of motion of the Pacific plate relative to a hot spot frame of reference.

Figure 6-1. (a) Schematic drawing of sub-lithospheric convection cells in the form of longitudinal rolls aligned with axes parallel to the shear between the lithospheric plate and the underlying asthenosphere. (b) Schematic drawing of sub-lithospheric convection cells having a bimodal configuration. The directions of absolute plate motion and mantle return flow are indicated by the large open arrows but note that these directions are not necessarily antiparallel; flow in a vertical section of one cell is shown by the smallest arrows; the volcanoes serve to illustrate the direction of absolute plate motion and that the lithosphere is loaded at its surface as well as its base. Note that these schematic drawings are not drawn to any realistic scale [from Stephenson and Beaumont 1980].

(a)

(b)

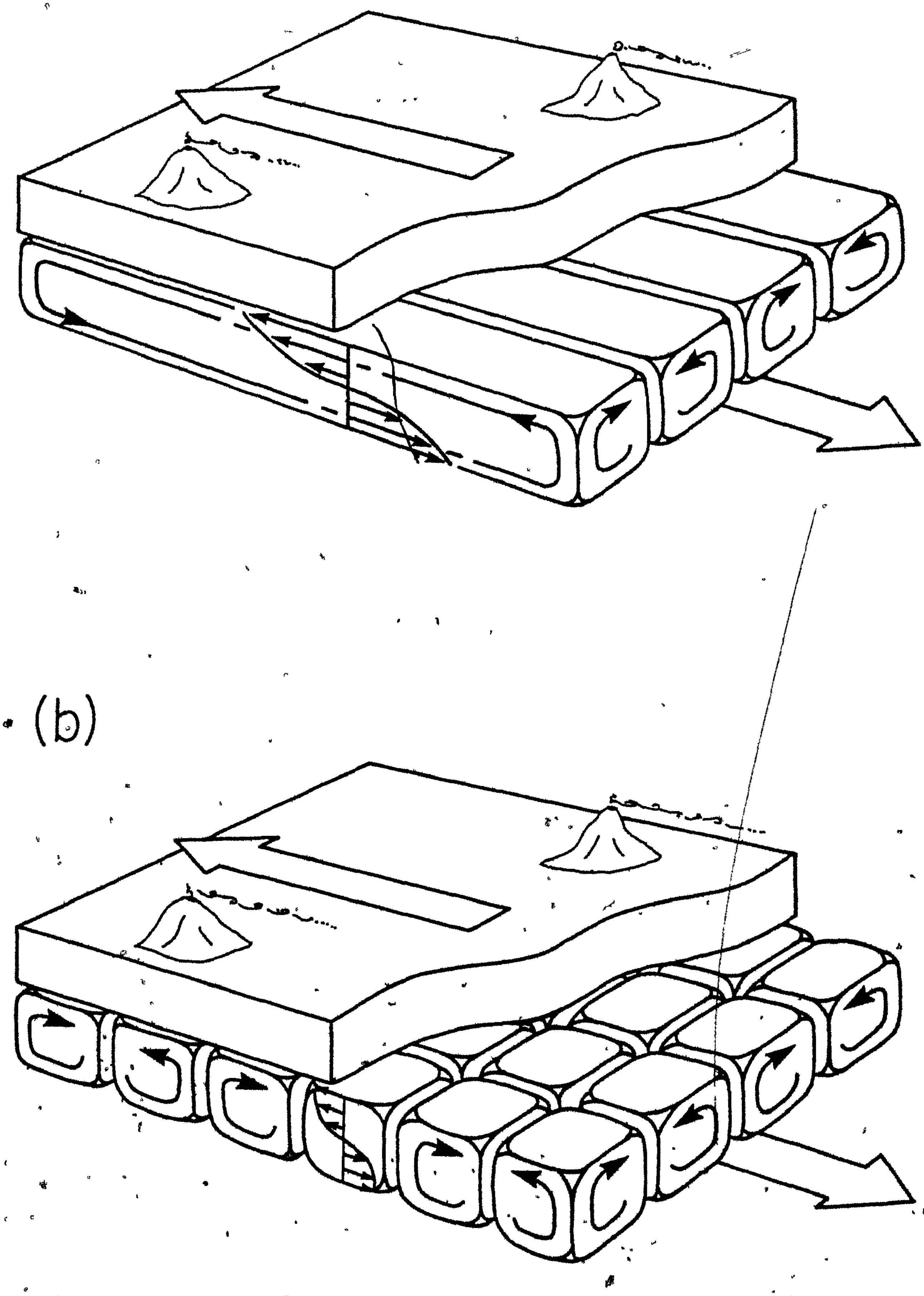

6.1.2 A test for the presence of small scale convection. In a plate model of the lithosphere, isostatic compensation to surface loads is effected by flexure of the plate as discussed in previous chapters. The form of the compensation is revealed by the wavenumber domain relationship between the load and deflection, measurable as the topography $H_T(\vec{k})$, and its associated gravity signature $G_T(\vec{k})$, and can be approximated by the linear transfer function $Q_T(\vec{k})$ [Figure 6-2(a)] such that

$$Q_T(\vec{k}) = \frac{G_T(\vec{k}) - N(\vec{k})}{H_T(\vec{k})} \qquad (6\text{-}1).$$

Here, $Q_T(\vec{k})$ is equivalent to what has been in previous chapters referred to as the isostatic response function $Q(\vec{k})$. It is a special case of the admittance, mentioned in subsection 6.1.1, between topograpy and gravity, in which it is assumed the only load causing flexure of the lithosphere is that of tectonically uplifted surface topography.

Recall that in order to estimate $Q_T(\vec{k})$ [or $Q(\vec{k})$] it has been normally assumed that the topography can be measured perfectly, whereas $G_T(\vec{k})$ is subject to geological noise $N(\vec{k})$ that is mainly caused by lateral density variations in the upper crust. Assuming the noise is uncorrelated with topography, isostatic response functions have been estimated by a process of ensemble averaging [Equation (2-8)]. The ensembles of data which have been averaged comprised all of those which fell within a given wavenumber band or annulus [Figure 2-9], symmetric about the origin, on the assumption that the lithosphere was directionally isostropic in its response to a point load; estimates of isostatic response $\hat{Q}$ and coherence $\hat{\gamma}^2$ were therefore found as functions of wavenumber modulus $|\vec{k}|$. For the same reason, $\hat{Q}(|\vec{k}|)$ has been taken to be a

Figure 6-2. Linear models employed in the interpretation of observed topographic and gravity data; symbols are explained in the text. (a) A model in which the lithosphere is loaded only by tectonically induced topography on its surface; (b) a model in which the lithosphere is also loaded at its base by forces associated with convection [from Stephenson and Beaumont 1980].

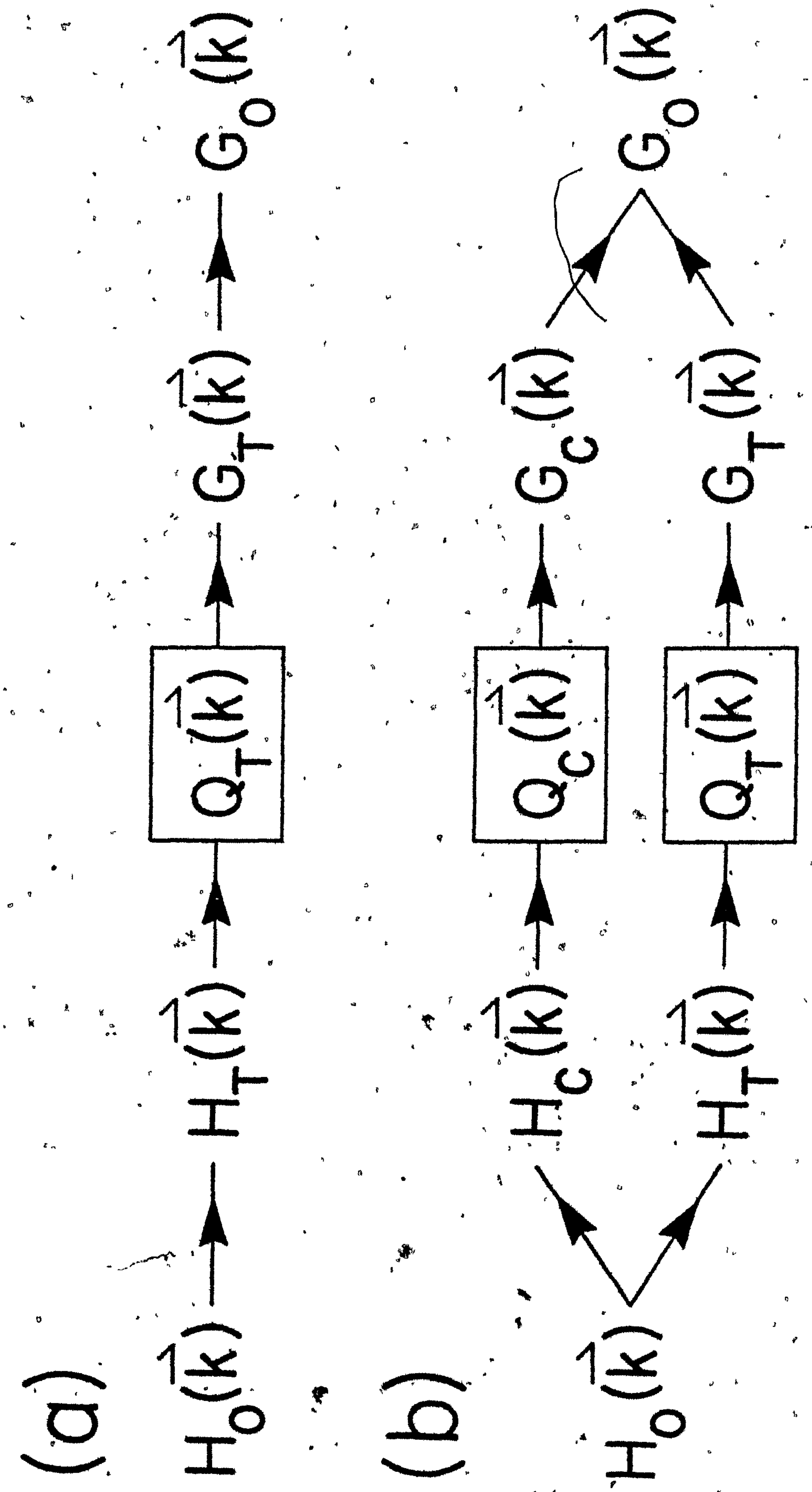
(a)
(b)
H_o(k)
H_T(k)
Q_T(k)
G_T(k)
G_o(k)
H_C(k)
Q_C(k)
G_C(k)

real function, though no a priori assumption to this effect was required using Equation (2-8).

However, consider a model in which the lithosphere is loaded at its base by forces associated with small scale upper mantle convection in addition to surficial topography. This class of model has two independent transfer functions [Figure 6-2(b)], which are assumed to be linear, such that the observed admittance is

$$Q(\vec{k}) = \frac{G_T(\vec{k}) + G_C(\vec{k}) - N(\vec{k})}{H_T(\vec{k}) + H_C(\vec{k})} = \frac{Q_T(\vec{k})H_T(\vec{k}) + Q_C(\vec{k})H_C(\vec{k}) - N(\vec{k})}{H_O(\vec{k})} \tag{6-2}$$

$G_C(\vec{k})$ and $H_C(\vec{k})$ are the components of the observed gravity and topography signals caused by convective forces and $Q_C(\vec{k})$ is their transfer function. Similarly, $Q_T(\vec{k})$ relates tectonic topography $H_T(\vec{k})$ to its induced gravity signal $G_T(\vec{k})$. $H_O(\vec{k})$, the observed topography, is obviously the sum of $H_C(\vec{k})$ and $H_T(\vec{k})$. Note that $H_T(\vec{k})$, as in Equation (6-1), comprises the topographic load itself as well as a deflection of the lithosphere in response to that load. The estimate of the admittance, $Q(\vec{k})$, can be derived as before by Equation (2-8) and shall continue to be referred to as the isostatic response function even though there may be dynamic forces supporting the lithosphere. If the lithosphere responds isotropically to point loads applied both from above and below both $Q_T(\vec{k})$ and $Q_C(\vec{k})$ are real functions but $Q(\vec{k})$ is complex since $H_C(\vec{k})$ and $H_T(\vec{k})$ are unlikely to have the same spatial phase and $Q_T(\vec{k})$ is unlikely to be equal to $Q_C(\vec{k})$. In general, $H_C(\vec{k})$ will only be non-zero for those wavenumbers, $\vec{k}$, for which convection cells exist. Elsewhere, $H_C(\vec{k})=0$ and $Q(\vec{k})$ will be a true estimate of $Q_T(k)$ [Equation (6-4)]. Furthermore, if convection is in the form of rolls aligned with axes parallel to the shear between the lithospheric plate and the underlying asthenosphere [Figure 6-1(a)] or has a bimodal configuration with similar orientation [Figure 6-1(b)], apparently anomalous values of $Q_T(\vec{k})$ will be observed only in those directions which are normal to the modal directions of convective flow.

The presence of small scale convection in the upper mantle can therefore be tested by examining whether the isostatic response function of a continental or oceanic region is real and isotropic. Its detectability will depend on the relative magnitudes of the H_T-H_C and G_T-G_C pairs. Continental regions are of primary interest in the present study and the Canadian Shield has been chosen as a test area because it is tectonically very old and therefore has a small $H_T(\vec{k})$.

6.2 Canadian Shield Observations

6.2.1 Isostatic response functions and coherence. Two overlapping but relatively rotated portions of the Canadian Shield have been analyzed: one with dimensions 3200 km by 1600 km [area I, Figure 6-3; the same region studied in Chapter 3] and the other 3000 km by 1500 km [area II, Figure 6-3], each containing approximately the same number of evenly distributed data which were prepared for analysis in the usual manner [subsection 2.2.1]. However, the observed isostatic response functions have been computed using free-air gravity anomalies, rather than Bouguer anomalies as in previous applications in this thesis, and are designated as $Q'(\vec{k})$. The free-air gravity field of area I of the

Figure 6-3. Location of the regions for which $\hat{Q}'(\vec{k})$ and $\hat{\gamma}^2(\vec{k})$ were computed; the "A" direction of anomalous isostatic response [see text] is shown by the arrows labelled 40^{o} and 60^{o}. The parallel diagonal lines are explained in the text [from Stephenson and Beaumont 1980].

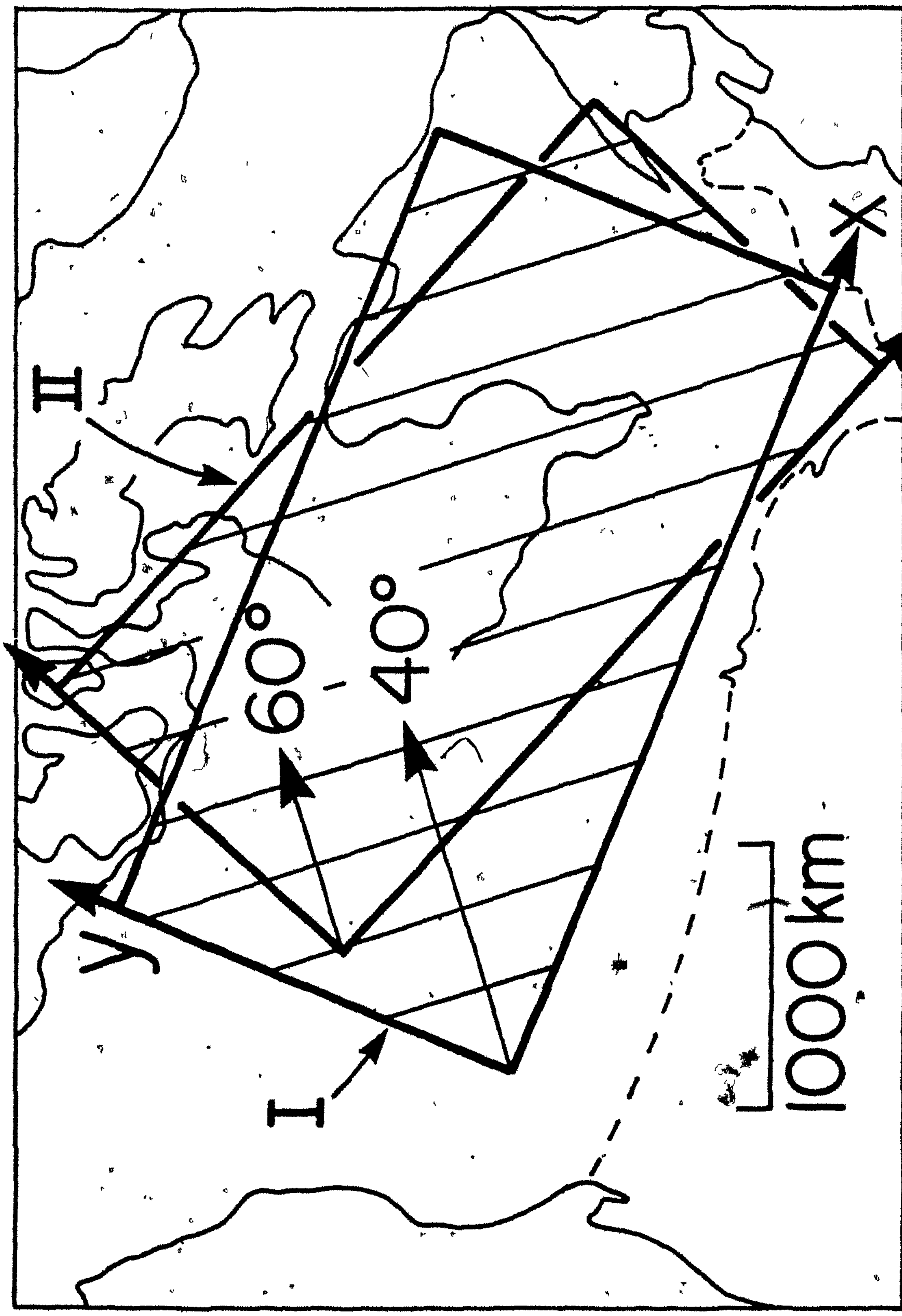

II
60°
40°
X
V
I
1000 km

Canadian Shield is shown in Figure 6-4.

The relationship in the space domain between free-air and Bouguer gravity anomalies, $g_f(\vec{r})$ and $g_b(\vec{r})$ respectively, is

$$g_f(\vec{r}) = g_b(\vec{r}) + 2\pi\Gamma\,\rho_o\,h(\vec{r}) \quad , \qquad (6\text{-}3)$$

where $-2\pi\Gamma\,\rho_o\,h(\vec{r})$, known as the Bouguer correction, represents the gravitational attraction of an infinite slab of density ρ_o and height $h(\vec{r})$ above the datum surface; Γ is the gravitational constant. The Fourier transform of (6-3) is

$$G_f(\vec{k}) = G_b(\vec{k}) + 2\pi\Gamma\,\rho_o\,H(\vec{k})$$

and therefore

$$\frac{G_f(\vec{k})}{H(\vec{k})} = \frac{G_b(\vec{k})}{H(\vec{k})} + 2\pi\Gamma\,\rho_o \qquad (6\text{-}4).$$

The effects of geological [non-isostatic] noise on the free-air and Bouguer gravity fields are essentially equivalent; thus, Equation (6-4) indicates that the relationship between isostatic response functions for each, $Q'(\vec{k})$ and $Q(\vec{k})$ respectively, is very simple:

$$Q'(\vec{k}) = Q(\vec{k}) + 2\pi\Gamma\,\rho_o \qquad (6\text{-}5);$$

$2\pi\Gamma\rho_o$=0.11 mGal m^{-1} for ρ_o=2700 kg m^{-3}.

Figure 6-4. The free-air gravity field of area I of the Canadian Shield [cf. Figure 6-3] detrended of the GEM8 [16 x 16] field. Positive values are indicated by stippling; contour interval is 20 mGal. Dimensions are 3200 km by 1600 km. Tectonic legend: Cd - Cordilleran orogen, Ch - Churchill province, Gr - Grenville province, Sp - Superior province, Sv - Slave province; cv - regions of Phanerozoic sedimentary cover.

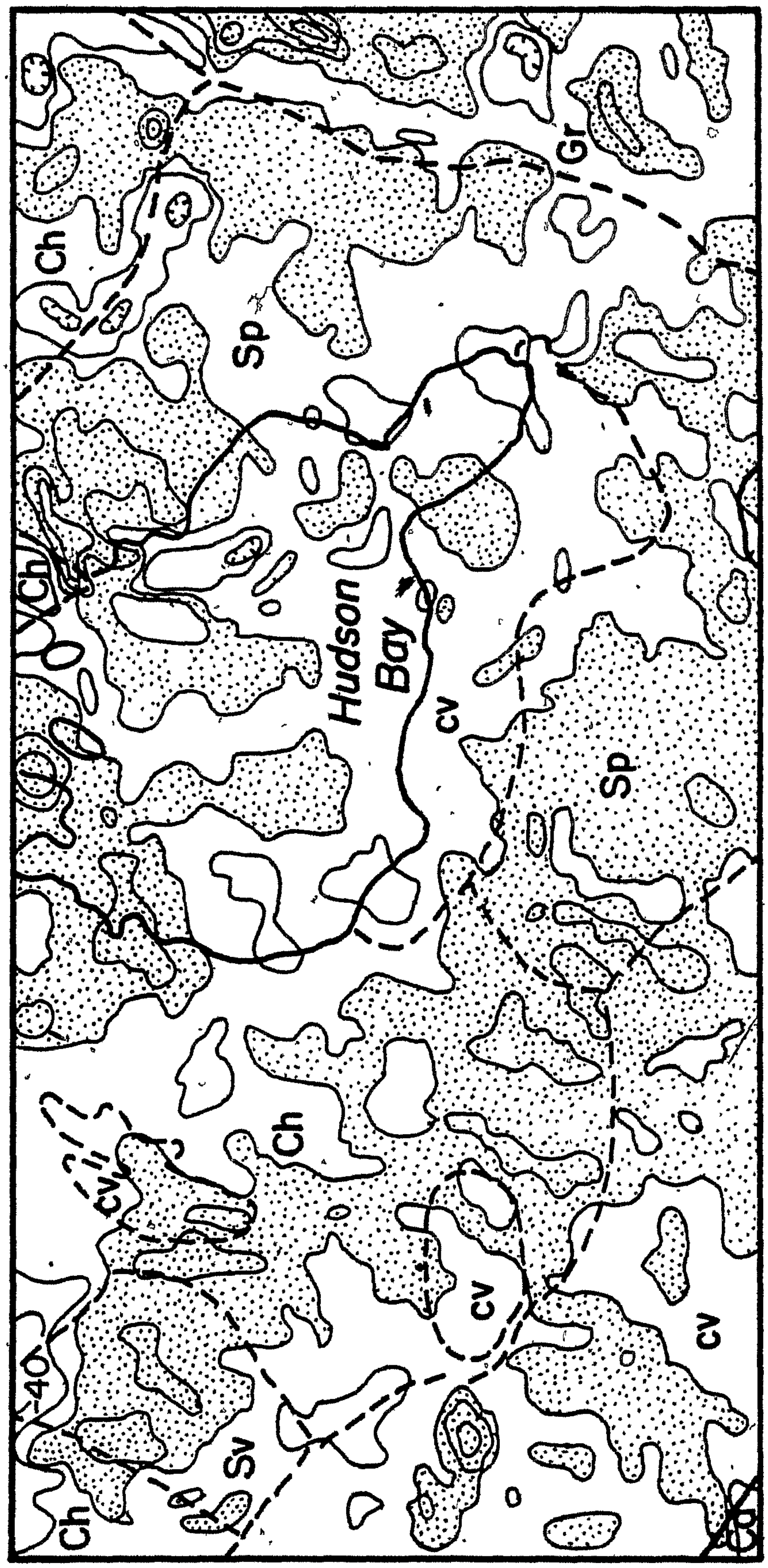
Hudson Bay
Sp
Sp
Ch
Ch
Ch
Ch
cv
cv
cv
cv
Gr
Sv
40

The reason for observing $Q'(\vec{k})$ in the present analysis is that free-air gravity anomalies and surface topography are expected to be incoherent at their observable intermediate to long wavelengths where any effects of small scale convection might be most discernible.

$\hat{Q}'$ and $\hat{\gamma}^2$ as functions of $|\vec{k}|$ for area I of the Canadian Shield [Figure 6-3] are shown in Figure 6-5. Note that for the very long wavelengths, as $|\vec{k}|$ approaches zero, so also does $\hat{Q}'$ indicating that the gravity effect of long wavelength topography is isostatically compensated by densities at some depth in the lithosphere. Coherence $\hat{\gamma}^2(|\vec{k}|)$ at long wavelengths is essentially nil also implying efficient isostatic compensation. Conversely, the computed values of $\hat{Q}'(|\vec{k}|)$ at short wavelengths, as $|\vec{k}|$ increases, approach 0.11 mGal m^{-1}, the Bouguer correction, the gravity effect of the topography itself, indicating that there is no effective isostatic compensation of short wavelength topographic features. Such features are supported by the strength of the lithosphere. Coherence between topography and gravity at short wavelengths should increase somewhat, either because features are not compensated or because the compensation lies too deeply in the crust to be detected. In fact $\hat{\gamma}^2$ remains very small as $|\vec{k}|$ increases, an indication of the large amount of the gravity signal not related to the topography of the region. Q as a function of wavenumber modulus $|\vec{k}|$ for area II [Figure 6-3], though not illustrated here, is similar to that for area I.

As was recalled in subsection [illegible].1.2, observed isostatic response functions have previously been taken to be the real part of the admittance between observed topography and gravity on the grounds that they measure an isotropic response to the impulse of surface loads

Figure 6-5. The real component [circles], with error bars corresponding in length to two standard errors, and the amplitude [squares] of the isostatic response function $\hat{Q}'$, and the coherence squared $\hat{\gamma}^2$ [triangles] as functions of wavenumber modulus $|\vec{k}|$ for area I of the Canadian Shield.

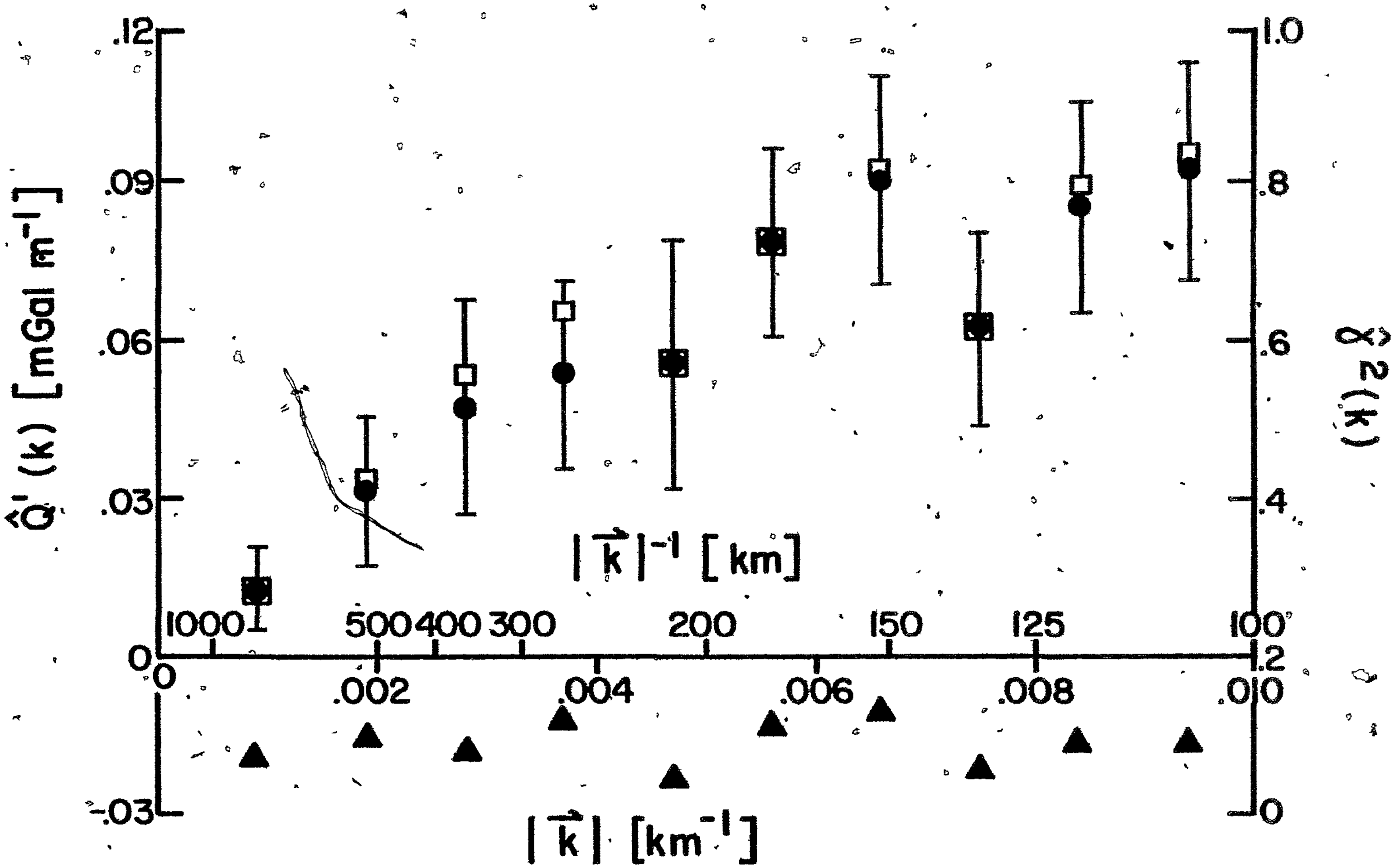

$\hat{Q}'(k)$ [mGal m^{-1}]
.12
.09
.06
.03
0
-.03
$|\vec{k}|^{-1}$ [km]
1000
500
400
300
200
150
125
100
0
.002
.004
.006
.008
.010
$|\vec{k}|$ [km^{-1}]
1.0
.8
.6
.4
.2
0
$\hat{\gamma}^2(k)$

only. In the present application, in which the effects of a second source of lithospheric loading are sought, it is not correct to make the a priori physical assumption that Q' is solely a real function. Therefore, the amplitudes of the response function estimates are also plotted in Figure 6-5. Note that they are for the most part similar to Real[Q'] testifying to small values of the imaginary component of the admittance estimates.

Q' for both areas I and II of the Canadian Shield has also been computed as a function of $\vec{k}$ by averaging within wavenumber annuli through an azimuthal arc length of 30° [Figures 6-6(a), 6-7(a)]. These results are comparable to those for $Q(|\vec{k}|)$, Figure 6-5, insofar as the values increase from zero to more than 0.10 mGal m^{-1} from the longest to shortest wavelengths. Associated standard errors are relatively large as shown by the extensive zones [diagonally hatched] in which the values are not greater than zero by more than one standard error. However, anomalous values in the area labelled A and B contrast substantially to those at equivalent wavelengths in Figure 6-5. Relatively large imaginary components in the estimates of the amplitude of $Q'(k)$ contribute to the anomalously high values in areas A and B. To judge better the significance of these anomalies, which suggest a directionally anisotropic $Q'(\vec{k})$, the hypothesis $H_o: Q''_r = Q'_{rs}$ was tested using an F-distributed statistic formulated through the principle of extra sums of squares [Draper and Smith 1967]. The Q'_{rs}, for annulus r, were computed from data in the 30° arc centred on azimuth s; Q''_r were computed from the ensemble of remaining data in the annulus. For areas A and B of data set I and area B of data set II [Figures 6-6(b), 6-7(b)] the probability that the process which induces the isostatic response is

Figure 6-6. (a) The amplitude of $\hat{Q}'$ in mGal m^{-1}; (b) the probability that the hypothesis Ho [see text] is true, equivalent to the level of significance at which Ho can be rejected; and (c) $\hat{\gamma}^2$ as functions of $\vec{k}$ for data in area I. Note that data along the $-\vec{k}_x$ and $\vec{k}_x$ axes are symmetric about the origin; the $\vec{k}_x$ and $\vec{k}_y$ directions are analogous to the spatial x and y coordinates [Figure 6-3]; the amplitude of $\hat{Q}'$ minus its associated standard error is zero or less in the diagonally lined region; features labelled A and B are discussed in the text [from Stephenson and Beaumont 1980].

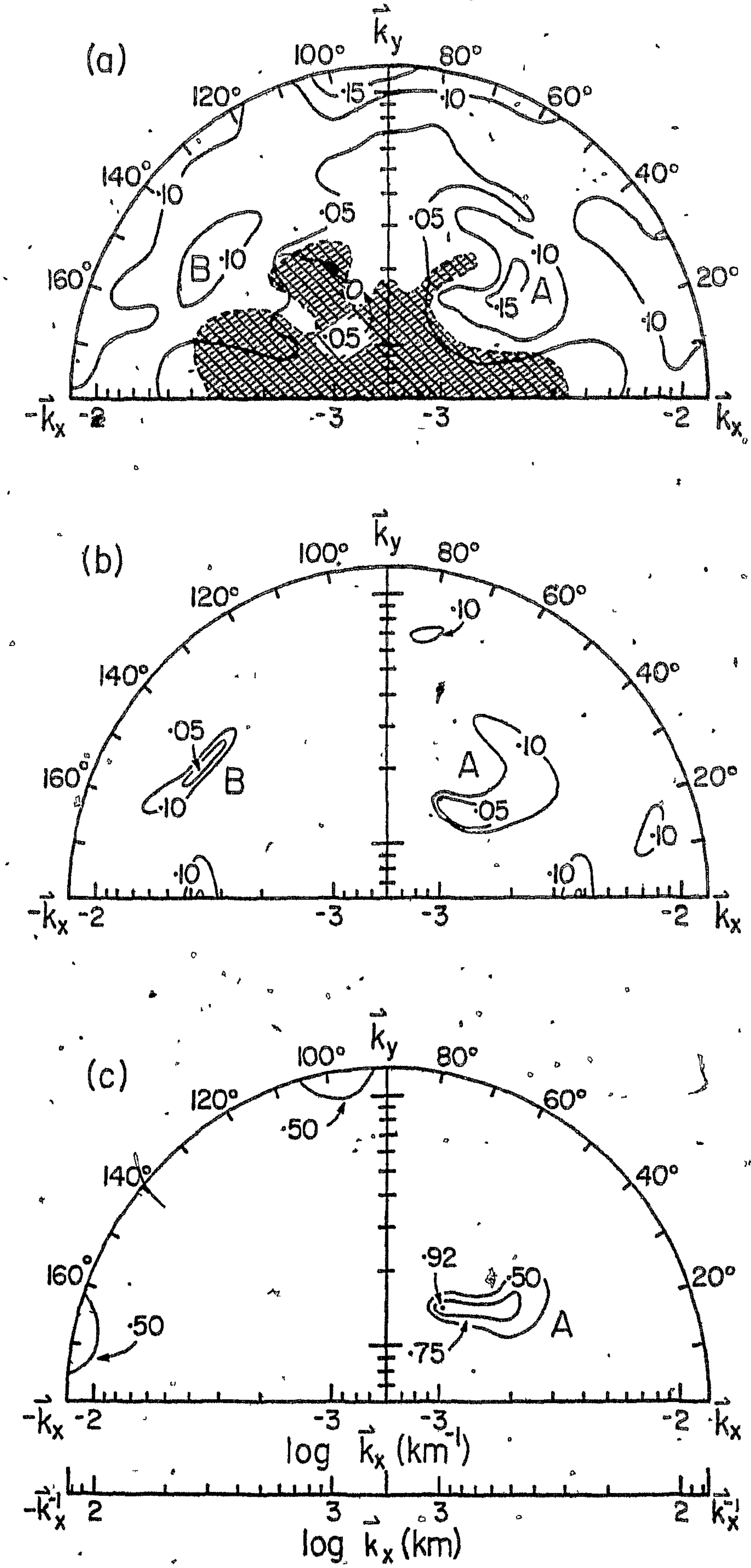
(a)
(b)
(c)
$\vec{k}_y$
$-\vec{k}_x$
$\vec{k}_x$
A
B
log $\vec{k}_x$ (km^{-1})
$-\vec{k}_x^{-1}$
$\vec{k}_x^{-1}$
log $\vec{k}_x$ (km)

Figure 6-7. (a), (b), and (c) Same as Figure 6-6 but for data in area II [from Stephenson and Beaumont 1980].

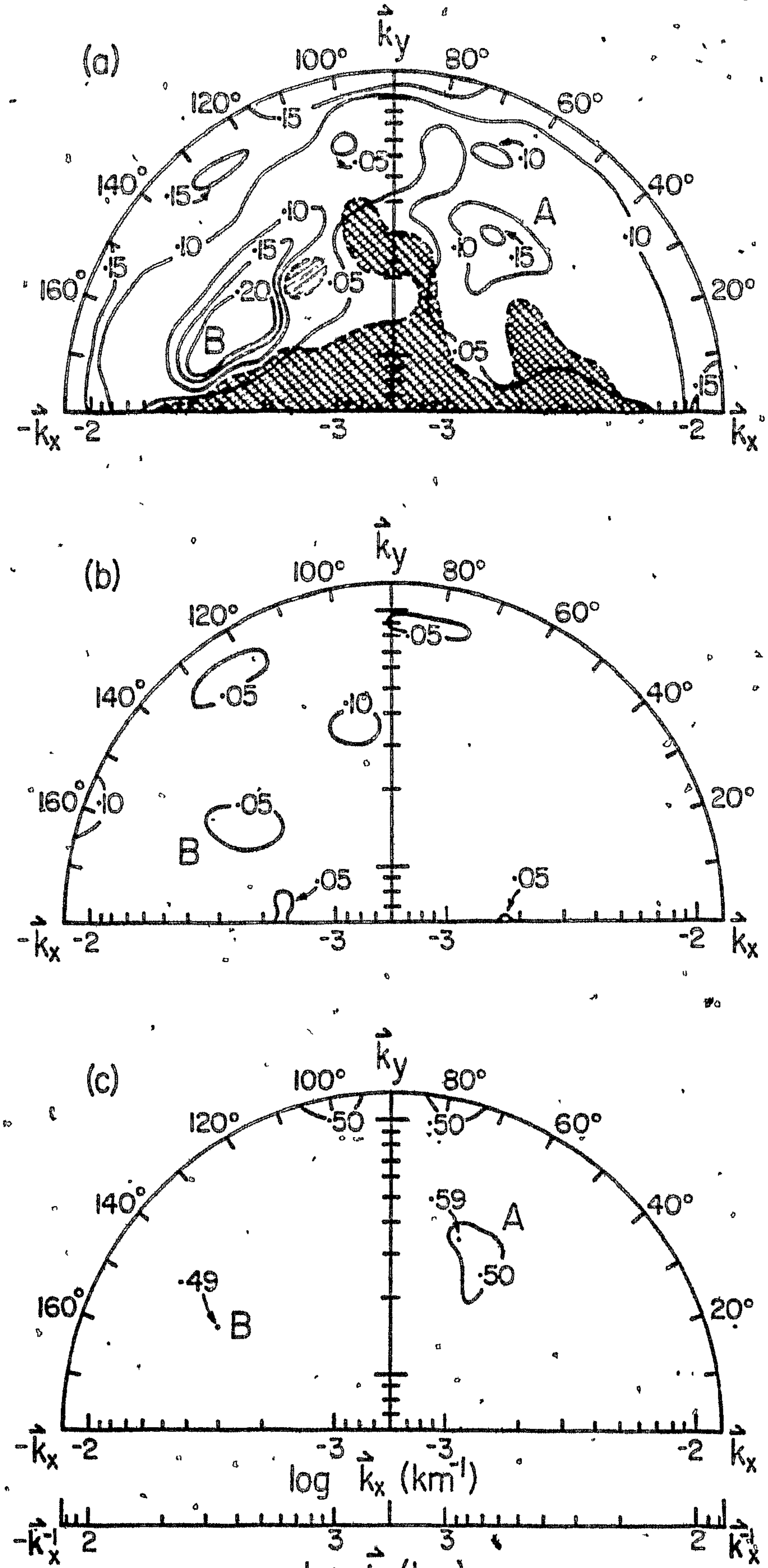

(a)
(b)
(c)
$\vec{k}_y$
100°
80°
120°
60°
140°
40°
160°
20°
A
B
·05
·10
·15
·20
·50
·59
·49
$-\vec{k}_x$ -2 -3 -3 -2 $\vec{k}_x$
log $\vec{k}_x$ (km^{-1})
$-\vec{k}_x^{-1}$ 2 3 3 2 $\vec{k}_x^{-1}$
log $\vec{k}_x$ (km)

the same as in other directions at the appropriate wavelength is less than 5%. The effects of coherent geological noise of course cannot totally be discounted. Furthermore, although there is no significant [arbitrarily defined as greater than 0.5] anomaly in γ^2 at B in either of the data sets [Figures 6-6(c), 6-7(c)], the free-air gravity and topography signals at A are exceptionally coherent, particularly in data set I. At similar wavelengths, 200-600 km, coherence predicted by reasonable rheological models of the lithosphere in response to surface loading as well as shown by results shown in Figure 6-5 and observations discussed in Chapter 3 is very much smaller or is non-existent. The probability that this increased correlation is caused by highly correlated random geological noise is <5%, as demonstrated by the F-test, if the noise is directionally isotropic.

6.2.2 Power spectra. Quantitative interpretation of the individual gravity and topography power spectra is difficult because the spectra are not expected to be directionally isotropic even in the absence of convection and because there is a strong trend to increasing power at long wavelengths. The spectra have been detrended by normalizing each directional spectral estimate by its corresponding annularly averaged estimate; that is,

$$\hat{S}'_H(\vec{k}) = \hat{S}_H(\vec{k})/\hat{S}_H(|\vec{k}|)$$

and

$$\hat{S}'_G(\vec{k}) = \hat{S}_G(\vec{k})/\hat{S}_G(|\vec{k}|)$$

Figure 6-8. (a) The normalized [see text] topography power spectrum $\hat{S}'_H$ and (b) the normalized free-air gravity power spectrum $\hat{S}'_G$ as functions of $\vec{k}$ for area I of the Canadian Shield. $\hat{Q}'(\vec{k}) > 0.10$ mGal m^{-1} within the cross-hatched regions [cf. Figure 6-6(a)].

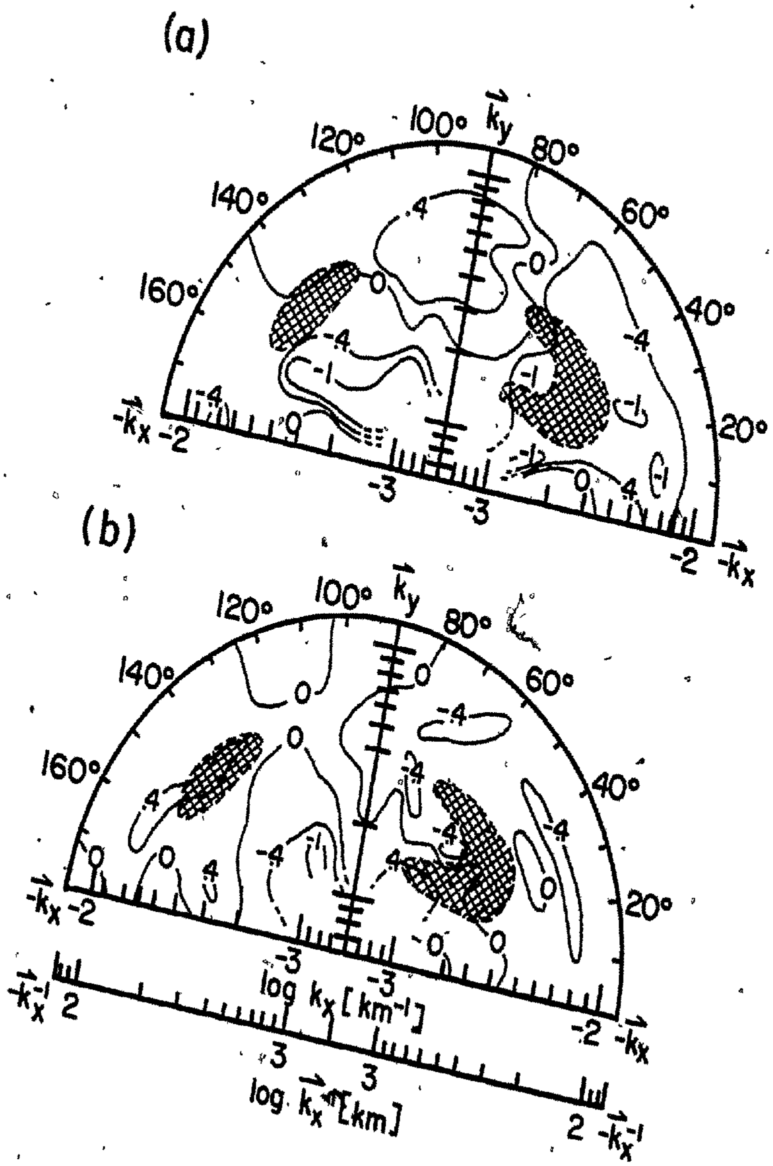
(a)
(b)
120°
100°
80°
140°
60°
160°
40°
20°
-2
-3
-3
-2
log k_x [km^-1]
3
3
2
2
log k_x^-1 [km]

where $\hat{S}_H'(\vec{k})$ and $\hat{S}_G'(\vec{k})$ are the normalized topography and gravity power spectra respectively. The natural logarithms of $\hat{S}_H'(\vec{k})$ and $\hat{S}_G'(\vec{k})$ are plotted in Figures 6-8(a,b). Thus, positive values indicate regions where the spectral power is greater than the average of the power in all directions at the corresponding wavenumber. The cross-hatched areas refer to isostatic response anomalies A and B, defined by the $\hat{Q}'(\vec{k}) =$ 0.10 mGal m^{-1} contour in Figure 6-6(a). It should be noted, in terms of the 95% confidence intervals associated with the directional spectral estimates, that the variations in $\hat{S}_H'(\vec{k})$ and $\hat{S}_G'(\vec{k})$ shown in Figures 6-8 (a,b) have little significance.

For wavenumbers other than those of small magnitude in the second quadrant there is, in general, little evidence in Figures 6-8(a,b) of correlation between topography and free-air gravity. This result is compatible with the small coherence squared estimates for the Canadian Shield [Figure 6-6(c)] and indicates that little of the free-air gravity field in the region is due to isostatic compensation of surface topography. There is, however, some suggestion that the anomalous isostatic response at A and B is related to an increase in the power of the gravity signal [Figure 6-8(b)].

6.2.3 Residual gravity anomalies. The observed gravity field can be separated into its isostatic and residual components, the former being that part of the signal due to the observed topography and its isostatic compensation, by assuming a particular mode of compensation mechanism. The results presented in Chapter 3, in which observed $\hat{Q}(|\vec{k}|)$ were compared to the theoretical isostatic response of a thin elastic plate, showed that local isostatic compensation, with a compensation depth of 35 km, provided a suitable model for the observed response of area I of the Canadian Shield [Figure 3-5(c)]. The residual gravity map presented in Figure 6-9 has been produced by subtracting the gravity signal predicted by filtering the observed topography of area I with the indicated local response function model $Q'(|\vec{k}|)$ from the observed free-air gravity field. Filtered results in the border regions of the study area are not meaningful because of the tapering function applied to the data prior to Fourier transformations. For this reason they have not been included in Figure 6-9.

Because of the small coherence between the free-air gravity and the topography of area I of the Canadian Shield, it is not surprising that the residual gravity field is very similar to the total field [cf. Figure 6-4]. A northwest-southeast trending fabric, parallel to the direction of the perturbation indicated by anomaly A in the isostatic response data [cf. Figure 6-3] is discernible in both the gravity maps. It is not clear whether this fabric is uncorrelatable with the gross geological and physiological structures of the study area. A similar trend is quite evident in the latter, their main elements being, from southwest to northeast, the contact between Phanerozoic cover rocks and exposed Precambrian Shield, Hudson Bay, and the Superior-Churchill structural boundary. There also are some gross geological elements, primarily the Grenville-Superior, Superior-Churchill, and Churchill-Slave structural boundaries, which are oriented approximately parallel to the direction of the anomaly B perturbation in the isostatic response results. The internal structural fabric of

Figure 6-9. The residual free-air gravity field [total field less that part attributable to local isostatic response of the surface topography] of area I of the Canadian Shield. Positive values are indicated by stippling; contour interval is 20 mGal. Tectonic legend is the same as Figure 6-4.

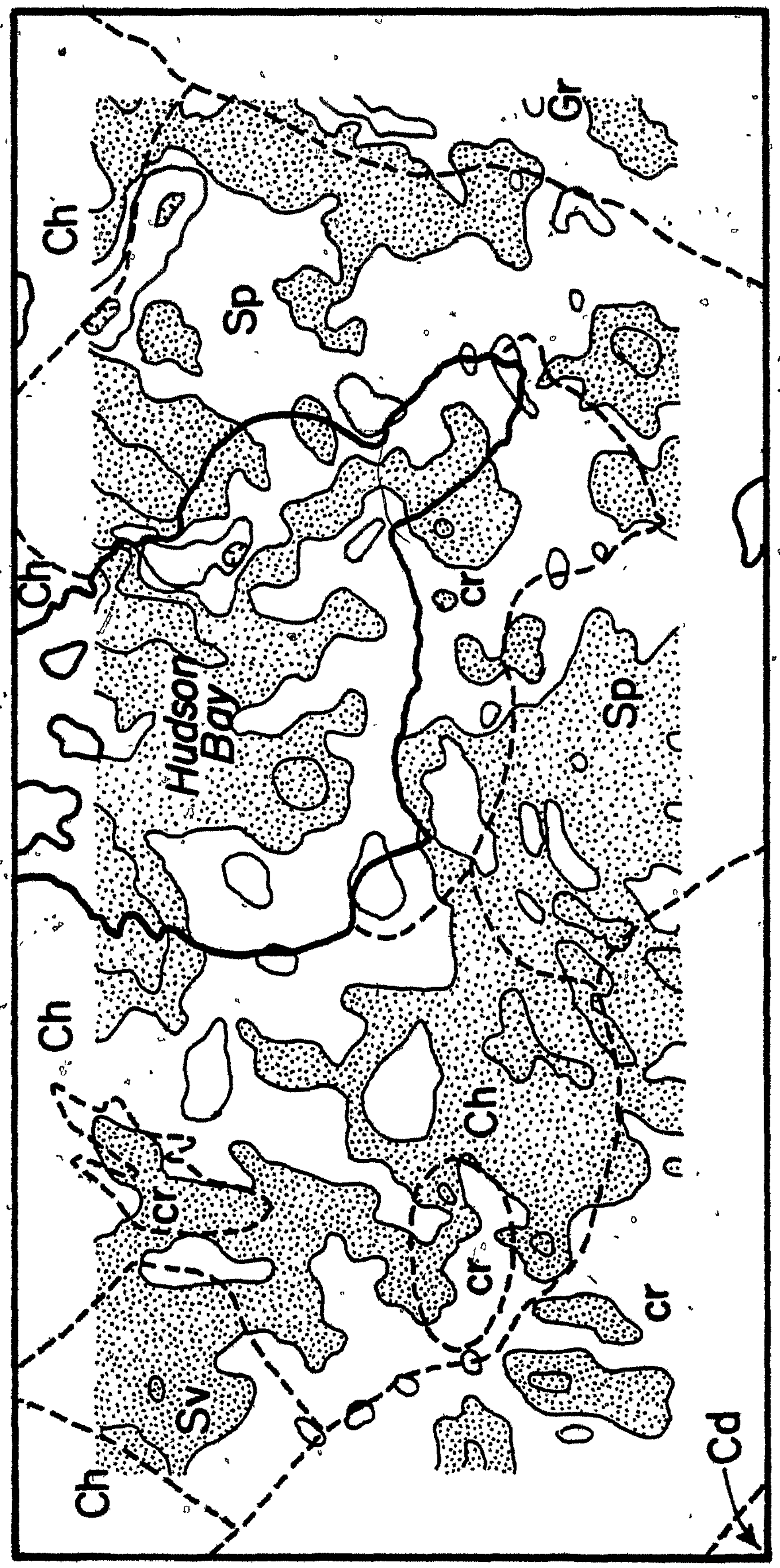
Hudson Bay
Ch
Sp
Gr
cr
Sv
Cd

Figure 6-10. The normalized residual free-air gravity power spectrum as a function of $\vec{k}$ for area I of the Canadian Shield. $\hat{Q}'(\vec{k})>0.10$ mGal m^{-1} within the cross-hatched regions [cf. Figure 6-6(a)].

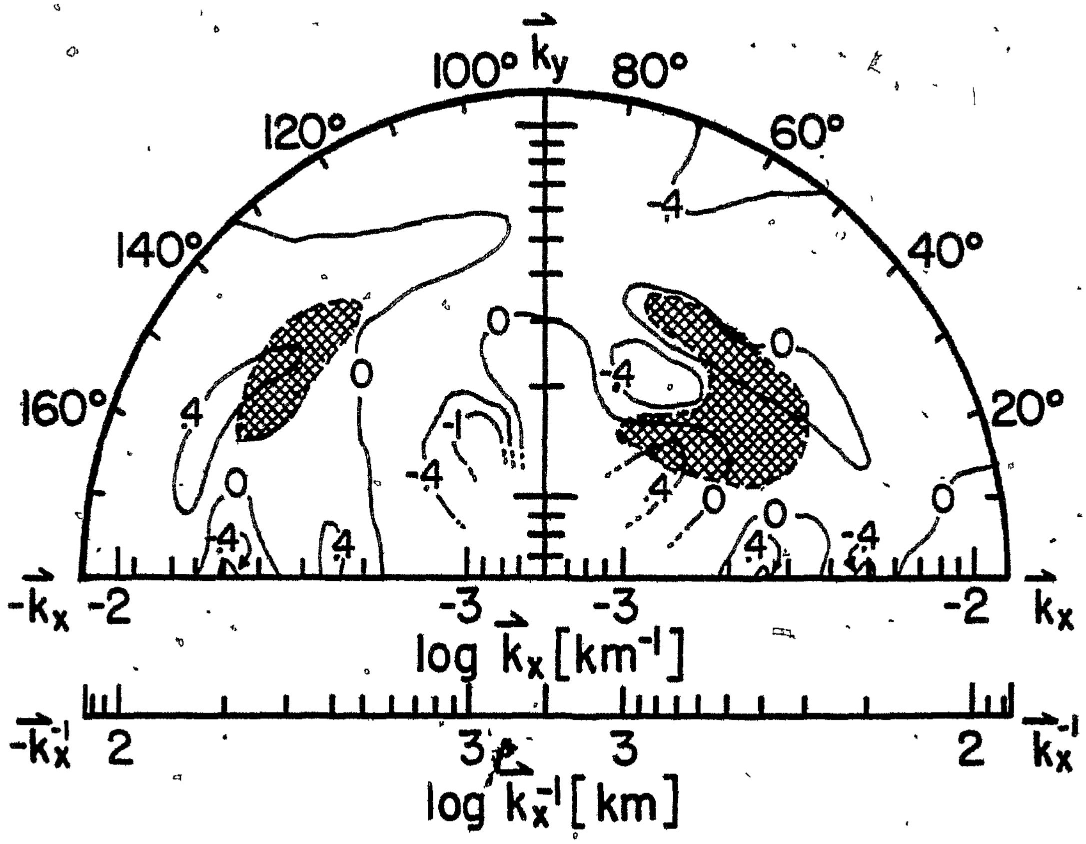

$\vec{k}_y$
100°
80°
120°
60°
140°
40°
160°
20°
0
-4
4
-1
$-\vec{k}_x$ -2
-3
-3
-2 $\vec{k}_x$
log $\vec{k}_x$ [km^{-1}]
$-\vec{k}_x^{-1}$ 2
3
3
2 $\vec{k}_x^{-1}$
log $\vec{k}_x^{-1}$ [km]

the Superior and Churchill provinces is, in general, similarly oriented [Price and Douglas, eds. 1972].

The natural logarithm of the power spectrum of the residual gravity field, normalized in the same fashion as the topography and total gravity field were in subsection 6.2.2, is plotted as a function of $\vec{k}$ in Figure 6-10. The results indicate more strongly than the total field results did [cf. Figure 6-8(b)] that there is a correlation between anomalous isostatic response of the Canadian Shield and increased gravity spectral power.

6.3 Discussion

6.3.1 Rotation of data. The reason for analyzing two overlapping data sets was simply to check for internal consistency of the results and to avoid accepting those which were artifacts of the method of analysis related to the choice of geometry. Because each data set contains a large subset of the other the results for each were expected to be similar, except rotated with respect to the coordinate axes. This is partly the case: anomaly A in $\hat{Q}'(\vec{k})$ for set I, for example, is centred approximately on the 40^{o} azimuth whereas for set II [Figure 6-7 (a)] it centres on 60^{o}. The 20^{o} rotation is appropriate to the orientation of the two data sets since the anomaly reflects a spatial perturbation normal to its wavenumber domain azimuth [cf. the parallel diagonal lines in Figure 6-3]. Anomalies A and B, elsewhere in the results of $\hat{Q}'(\vec{k})$ and $\hat{\gamma}^{2}(\vec{k})$ in the two data sets, are also located accordingly. The

F-test, as it was formulated, however, appears not to have been a totally appropriate statistical judge of the significance of features A and B in data set II since feature B is so pervasive at the anomalous wavelengths. In this respect it should be noted that the estimates of the amplitude of $\hat{Q}'(\vec{k})$ in anomaly B for both data sets are, in fact, equivalent within bounds established by their respective standard errors. More importantly, the wavelength of anomaly B in set I is centred at approximately 200 km whereas in set II it ranges from 200 to nearly 400 km. This frequency shift may be partly because the raw spectra are digitized on a cartesian grid; since the spatial dimensions of the two data sets are not the same neither are the frequencies for which spectral estimates exist. Furthermore, the cartesian gridded spectral estimates for one data set compared to the other may be thought of as having been rotated in some cases through the polar annular boundaries which during a rotation remain stationary. The wavenumbers of the annuli were chosen to be the same for each data set. Mostly, however, the differences in the results for the two data sets are attributable to having too few data in each spectral estimate to sufficiently reduce the high level of noise which is derived both from the finite nature of the data sets and from variations in the geology of continental crust.

6.3.2 <u>Anisotropy of the observed isostatic response and small scale convection</u>. On the basis of the seemingly correct rotations of the salient features of $\hat{Q}'(\vec{k})$ and $\hat{\gamma}^2(k)$ between the two data sets, it is concluded that the anomalous anisotropies in the observations are not methodological in origin. Whether the results reflect pronounced effects in the gravity field of directionally non-random geological structures [cf. subsection 6.2.3] or whether they indicate that the isostatic response of the Canadian Shield is truly significantly isotropic is equivocal.

With respect to the former supposition, however, it remains that not only is the spectral power of the residual gravity field apparently greater in the anomalous directions [Figure 6-10] but that this "excess" gravity signal also has significantly greater coherence with the topography than elsewhere. Yet, the residual gravity is completely independent of the gravity effect of the surface topography itself. Additionally, if the anomalous results are geological in origin and are therefore related to the overall structural fabric of the Canadian Shield study area, their restriction to a particular spectral range may be problematic. This is because large scale geological structures usually mimic those occurring at a continuum of smaller scales, including those at the microscopic level [S. Hanmer 1980, pers. comm.].

On the other hand, a truly anisotropic isostatic response function could be the result of a mechanically anisotropic lithosphere, an interpretation for which there is little or no supporting evidence, either observational or theoretical; alternatively, it may be indicative of small scale sub-lithospheric convective flow as explained earlier [subsection 6.1.2].

If the convection cell model is adopted as a working hypothesis, the presence of two anomalous directions [features A and B in the estimates of $\hat{Q}'(\vec{k})$] which are approximately perpendicular to one another suggests that the form of the convection is bimodal [Figure 6-1(b)].

The approximate orientation of one of the characteristic directions [corresponding to anomaly A in the data] is shown by the parallel diagonal lines in Figure 6-3; the wavelength of both modes of convection cell is in the range of 600-200 km suggesting that penetration to the 650 km mantle phase transition probably does not occur even if the cells have a unitary aspect ratio.

Further interpretation of the results in terms of the properties of the convecting layer is not possible because $Q_C(\vec{k})$ cannot be accurately estimated unless $H_T(\vec{k}) << H_C(\vec{k})$ [Equation (6-2)], a condition that requires a billiard ball Earth in the absence of convection. Even a knowledge of $Q_T(\vec{k})$ is not useful because the observed topography cannot be partitioned into its convective and tectonic components. Furthermore, convectively induced anomalies in $Q(\vec{k})$ will almost always be obscured in data from areas of significant tectonic topography [Equation (6-2)]. This may explain why the anomaly was less distinct in a data set which encompassed a region twice as large as the Canadian Shield set I and included a considerable portion of the United States; this data set had a relatively large $H_T(\vec{k})$.

Alternatively, the shear flow between lithosphere and asthenosphere is not necessarily uniformly parallel under any single plate. Preliminary numerical models of net flow based on the relative motions and geometry of plates [Chase 1979] suggest that this may be the case for the North American plate. Under the Canadian Shield, however, the mean net flow vectors calculated by Chase are aligned in a direction approximately parallel [taking into account differences in map projections] to that indicated by the isostatic response data [Figure 6-3].

Shear stress vectors at the base of the lithosphere in the region of the Canadian Shield computed from kinematic models of large scale mantle flow by Hager and O'Connell [1979] are similarly oriented. It should be noted, however, that in both these models the directions of the assumed plate motion and the computed return asthenospheric flow are not antiparallel beneath the Canadian Shield and that the consequences of this type of flow regime on small scale convection are unknown. The correspondence of one of the characteristic directions in a bimodal configuration of convection with the direction of shear between the lithosphere and asthenosphere is, of course, consistent with the theory of small scale convection discussed previously. The planform of convection will depend on the properties of the convecting layer as well as the velocity of the overlying plate and the duration of the applied shear [Richter and Parsons 1975]. The age of sea-floor spreading in the North Atlantic does not necessarily provide any insight regarding the persistence of the direction of the shear flow beneath the Canadian Shield; therefore the likelihood of a bimodal configuration of convection under the Canadian Shield cannot with certainty be tested against the theoretical predictions. Recently, Yuen <u>et al</u>. [1981] have argued that the stability of multimodel small scale convective flow in the upper mantle is strongly dependent upon a pronounced sub-lithospheric low viscosity zone, the existence of which beneath the Canadian Shield cannot be resolved on the basis of glacio-isostatic observations [Quinlan 1981]. Seismological observations [e.g. Forsyth 1975] suggest, however, that the mantle low velocity zone, which may be analogous to the low viscosity zone, is less evident beneath old lithosphere than it is beneath young.

6.4 Summary

A new methodology has been advanced to detect the effects of small scale Rayleigh-Benard convection in the upper mantle and has been applied to a portion of the Canadian Shield. It represents the first attempt [cf. Stephenson and Beaumont 1980] to identify small scale convection beneath continental lithosphere. The theoretical framework of small scale convection is not well-constrained and this is particularly true of convection beneath continents where it is capped by a thicker, more structurally complex lithosphere than beneath oceans. The mechanical behaviour of continental lithosphere itself, and therefore how it would respond to forces derived from convection, is not a subject about which there is geophysical consensus. Consequently, the results of the present analysis, in which the effects of a bimodal scheme of small scale convection may have been recognized, are speculative. This is especially true because the indicated modal directions are conformable with the gross structural and physiological trends of the study area. It is noteworthy in this respect, however, that one of these directions, corresponding to anomaly A in the results, is also conformable with the orientation of shear stress vectors at the base of the lithosphere in the study area based on numerical models of large scale mantle flow.

Chapter 7. Summary and Prospectus

7.1 Continental Isostatic Response Functions

It was originally intended that the present study would place greater emphasis than it ultimately does on what isostatic response functions reveal about the rheology and structure of the continental lithosphere. When the study was begun the work of Banks et al. [1977] and McNutt and Parker [1978] had been recently published. Particularly interesting was McNutt and Parker's result that the apparent flexural rigidity of the Australian lithosphere was less than that of the tectonically younger United States. They interpreted this to be due to a viscoelastic continental lithosphere but acknowledged that the results were subject to problems arising from the geological heterogeneity of the study areas and the potential effects of topographic erosion. It was hoped in the present study to address these problems and, having done so, to find evidence to either support or refute the viscoelastic model. The idea was to calculate isostatic response functions for each of the large, essentially homogeneous geological provinces of North America, to determine whether their differences, if any, were correlatable with their inferred tectonic ages, and then to interpret the changes in terms of a rheological model of the lithosphere. At the time, no published continental isostatic response function had been calculated from data derived from a single geologically homogeneous study area.

In Chapter 2 the data used in subsequent analyses were introduced and the methods of data reduction described. Standard techniques were employed although the method chosen to minimize the effects of using finite data sets differs from those of Lewis and Dorman [1970] and McNutt [1978]. Synthetic data were analyzed to prove the method's suitability.

The calculated isostatic response functions were presented in Chapter 3 and were initially interpreted in terms of the simplest model available, the time-invariant elastic thin plate model of Banks et al. [1977]. Because of the errors associated with the response function estimates and because of the inherent non-uniqueness of calculated gravity anomalies, it was difficult to place a great deal of confidence in the results of the interpretation. In general, as the geological age of the study area increases the observed isostatic response function falls off to zero [implying the existence of either very deep or no isostatic compensation] at smaller wavenumbers. The results of a one-norm misfit analysis suggested that the qualitative differences in the observed response functions are controlled more by changes in the depth of the compensating density discontinuity [i.e., in general becoming deeper with increasing tectonic age] than by changes in lithospheric flexural rigidity. Even so, the best-fitting elastic plate models required that the flexural rigidity varies by at least two orders of magnitude between the different sampled geological provinces. It was concluded on this basis that a <u>single</u> elastic plate model with time-invariant physical properties would not suitably characterize all of the observed isostatic response functions. Because there is no geodynamic reason to believe that the rheological properties of an elastic lithosphere should vary arbitrarily in some way not related to the tectonic age of the lithosphere, the time-invariant elastic model in general was tentatively rejected. Any conclusions based on the observed isostatic response functions were considered to be only tentative because of large errors associated with the individual response function estimates.

In Chapter 5 expressions for the theoretical isostatic response functions of a thin plate viscoelastic [Maxwell] lithosphere loaded by eroding topography were developed. The viscoelastic model of McNutt and Parker [1978] was not considered because it does account for the erosion of tectonically old topography and, in fact, requires topography to grow through time. Rather, two simple erosion-dependent loading models were investigated: Model 1, in which the uniform viscoelastic lithosphere is loaded suddenly by topography which subsequently erodes, and Model 2, in which topography, formed above a thermally weakened orogenically active lithosphere and therefore in a state of local isostatic equilibrium, erodes after the lithosphere has cooled and achieved some greater degree of flexural strength. Models 1 and 2 represent the first attempts to quantitatively describe the long term isostatic evolution of long wavelength eroding continental topography.

The parameters of even the simple time-invariant elastic isostatic response model, flexural rigidity D and compensation depth(s) z_m, were too insensitive to be confidently constrained by a careful analysis of model and observation misfits. Additional parameters in the erosional isostatic models are the erosion time constant α, which is probably a function of wavenumber, and the viscous relaxation time constant τ. Because of the additional complexity of the erosional models it was concluded that a rigorous approach to their interpretation, such as a misfit analysis, would not be profitable. Rather, only general observations were made.

In both Models 1 and 2, the general effects of erosion through time are those of progressively more pronounced overcompensation of topography as wavenumber increases. This feature of the models contrasts with the observed isostatic response functions which tend to fall off to zero values at smaller wavenumbers as the geological age of the study area increases. In the absence of systematic changes in compensation depths between geological provinces, as discussed in Chapter 3, there is no way the erosional isostatic models can reproduce this apparent time dependency in observed response functions. In this respect, the best the models can do is to predict essentially unchanging isostatic response functions through time.

In the case of Model 1 this would require either (1) an elastic plate rheology, resulting in a model equivalent to that of Banks et al. [1977] discussed and tentatively rejected in Chapter 3; or (2) viscoelastic rheology with a viscous relaxation constant τ relatively small compared to the erosion constant σ, resulting in local isostatic compensation of Appalachian and older topography [Figure 5-17], a feature of the observations also not wholly in agreement with the misfit analyses of Chapter 3. Isostatic evolution of continental lithosphere solely in terms of Model 1-type development is therefore considered unlikely.

In the case of Model 2, the terms of which require the lithosphere to cool and thicken through time, a time-invariant theoretical isostatic response is not strictly possible. Reduction of erosional effects [i.e., isostatic overcompensation] through time is favoured by very slow erosion rates [large σ] and/or small viscous relaxation time constants τ. Models with parameters $D=10^{22}-10^{25}$ Nm, τ=100-0.5 Ma, σ=250-300 Ma, and z_m'=35 km result in isostatic response functions which do not vary greatly for times greater than the age of the Appalachian region [e.g. Figure 5-20]. This result is not inconsistent with the observations given their large standard errors and the possibility that compensation depth varies from region to region.

The general implication of the Model 2 results was that the continental lithosphere is unlikely to have a purely elastic rheology. In such a case, part of the crustal root providing local isostatic compensation to initial topography remains in the lithosphere after some or all of the topography has been eroded. This results in marked overcompensation of remnant topography. Since marked overcompensation is not indicated by the isostatic response functions observed in tectonically old regions of North America, it was concluded that the flexural stresses induced by erosion are relaxed within geological lengths of time. In this respect, the viability of a viscoelastic model of continental lithosphere with parameters such as those listed above, has been explicitly illustrated. It was noted, however, that a possible alternative mode of relaxation of the inferred erosional stresses, not considered in the present thesis, is plastic failure. In this context, plastic failure may include large scale faulting of the upper part of the lithosphere.

In Chapter 6, it was shown how observed isostatic response functions could be analyzed in order to detect the effects of small scale Rayleigh-Benard convection in the upper mantle. The postulated technique does not require a knowledge of the mechanics of the isostatic compensation of surface topography and therefore is not subject to the interpretive difficulties associated with gravity anomalies discussed in Chapters 3 and 5. Rather, it depends on the interaction of the isostatic response function characterizing surface topography and its compensation and the potentially existing analogous transfer function characterizing the lithospheric topography and gravity signal produced by sub-lithospheric convection. A result of any such interaction is that the observed isostatic response function may not be real and directionally isotropic as it is normally assumed. The method was applied to the Canadian Shield data set where the erosionally attenuated topographic signal was an advantage rather than a source of uncertainty as in the lithosphere rheology and structure investigation. The results of the Canadian Shield analysis, in which the effects of a bimodel scheme of small scale convection may have been recognized, are speculative because one of the indicated modal directions is conformable with the gross structural and physiological trends of the study area.

The postulated detection technique may be used in oceanic as well as continental regions provided sufficient data exist. However, its future application is limited by (1) the need for minimal tectonic [surface] topographic signal and (2) theoretical considerations which suggest that small scale convection may be stable within a narrow range of physical conditions. With respect to the second category, the theoretical framework of small scale convection in the upper mantle is not well-constrained and its physical viability continues to be a subject of debate [e.g. Yuen et al. 1981].

7.2 Evolution of Continental Topography

Two modes of the evolution of continental topography have been considered in the present study. The first, presented in Chapter 4, pertains to regions undergoing tectonic uplift and is independent of extrinsic isostatic effects. The theoretical linear transfer function relating topography and tectonic uplift rate was formulated on the premise that the observed form of the topography is produced solely by the interaction of the uplift and erosion. The technique was applied to South Island, New Zealand, for which a map of uplift rate data was available [Wellman 1979].

The reason for the South Island uplift-topography analysis was to indirectly test a suggested linear erosion model which postulates that the erosion rate of harmonic topography is proportional to the amplitude of the topography remaining at any time and that the proportionality factor depends on the topographic wavenumber. It was concluded on the basis of the South Island analysis that the postulated harmonic erosion relation could not be rejected at wavenumbers less than or equal to 0.01 km^{-1}. Thus, the non-linear effects on erosion of local changes in lithology, climate, and vegetation are implicitly assumed to be significant only at greater wavenumbers and the erosion relation could therefore be suitably applied to longer wavelength isostatic response problems such as those summarized in section 7.1.

However, it was pointed out in Chapter 4 that the form of the theoretical uplift rate-transfer function was such that it could not be expected to constrain the parameters of the erosion model by considering the South Island data. This result was confirmed in Chapter 5 in terms of the probable parameter values implied by the isostatically controlled erosion of topography characteristic of North American geological provinces. In the context of the postulated harmonic erosion model, the erosion constant of topography having a wavelength in the range ~100-1000 km is evidently in the range 200-400 Ma.

In Chapter 5, the post-tectonic evolution of North American topography was modelled in terms of the thin plate viscoelastic [Maxwell] lithosphere isostatic Models 1 and 2 [cf. section 7.1]. The analysis represents the first attempt to characterize the rheology of the continental lithosphere by investigating the long term erosional decay of continental topography. The form of the topographic decay was established by comparing the observed topography power spectra of the studied North American geological provinces. Accordingly, it was assumed that the spectral configuration of the topography of each was initially approximately the same thus implying the existence of a stable continental lithosphere and similar modes of mountain-building in the Archean as at the present [e.g. Davies 1979]. The topography power spectrum of the tectonically young Cordilleran region of western North America was assumed to be representative of initial continental topography. Erosion was quantified in terms of the relation postulated and discussed in Chapter 4 and was incorporated into the viscoelastic lithosphere isostatic deformation models as feedback in a linear filter network.

The results of a misfit analysis of model predictions and observations showed, for both Models 1 and 2, that the best overall reproduction of the observed decay curves is provided by a viscoelastic as opposed to purely elastic lithosphere. Model 2 provided smaller minimum misfit than Model 1 but neither set of results strongly constrained the values of the rheological model parameters, flexural rigidity D and viscous relaxation time constant τ. Possible Model 2 parameters are not inconsistent with those determined by Beaumont [1981] from a model of the stratigraphic evolution of the Alberta Foreland Basin on a stable viscoelastic lithosphere [$D=10^{25}$ Nm; $\tau=27.5$ Ma].

For the most part both models fail to adequately reproduce the early phase of post-tectonic topographic decay evidenced by the Appalachian spectral data, a feature of the observations apparently not explicable in terms of the implied effects of depth- and time-dependent rheological model parameters D and τ. It was shown, however, that the implications of the Appalachian data in combination with an incorrect assumption regarding either the linear erosion relation and/or the representation of the present-day Cordilleran topography spectrum as the initial topography spectrum are such that a purely elastic lithosphere model could not be ruled out. Nevertheless, the isostatic response analysis summarized in section 7.1 does seem to preclude pure elasticity as a viable lithosphere rheology. In this respect, the important result of the topography decay analysis is that the present-day remnant topography of very old continental regions such as the Canadian Shield could have been supported during its entire evolution by a viscoelastic lithosphere with a relaxation time constant as small as 1-10 Ma. The theoretical models have shown that the combined effects of erosion and viscous relaxation of elastic stresses induced by past and present topographic and erosional loading are favourable to a reduction in the decay rate of topography compared to that of eroding topography loading an elastic lithosphere.

7.3 Prospectus: Geodynamic Modelling of Old Continental Regions

Further observation of the relationship between distributed continental topography and gravity, as it is formalized by the isostatic response function, is unlikely to be profitable in terms of the geodynamic modelling of continental lithosphere. This is primarily a reflection of the complexity and interaction of the many orogenic processes and diverse tectonic elements inherent to the formation and accretion of new continental crust. The result is that too much of the gravity signal observed on continents is not related to topographic variation and its isostatic compensation. Therefore, further application of the kinds of flexural models developed in this thesis, in which the important role of erosion in the isostatic process has been quantitatively considered, will necessarily be toward the construction of geodynamic models of particular structural elements of continental regions.

Of course, given that old continental regions have undergone large amounts of erosion, the recognition of structural analogues between young and geologically old terranes may be problematic. In this respect, large scale gravity anomalies continue to serve as indicators of the gross internal structure of continental lithosphere. Consider, for example, the large amplitude, paired, linear gravity anomalies associated with the structurally and/or radiometrically recognized boundaries between the various geological provinces of the Canadian Shield. These gravity anomalies have been interpreted, in general, as signatures of vestigal sutures between collided continental blocks of different thickness, age, and internal structure [Gibb and Thomas 1976; cf. Thomas 1975, Thomas and Tanner 1975, Kearey 1976, Gibb and Thomas 1977, Thomas and Gibb 1977, Thomas et al. 1978, Thomas and Kearey 1980]. Typically, such gravity models indicate that the younger of the adjacent crustal blocks is thicker and denser than the older and that the base of the crust of the latter dips toward the inferred contact between them over a distance of 100-200 km [Gibb and Thomas 1976].

Beaumont [1978, pers. comm.; 1981] has suggested that the wavelengths of the Precambrian "suture zone" gravity anomalies may vary according to the age of the inferred continental collision and that the suture zones themselves may be highly eroded direct descendents of the marginal fold-thrust mountain/foreland basin tectonic element of Phanerozoic mountain belts [e.g. Coney 1973]. In North America these include the Rocky Mountains and Alberta Foreland Basin of the eastern margin of the Canadian Cordillera and the Valley and Ridge province of the Southern Appalachians and westward adjacent Paleozoic foreland basins [Figure 7-1].

Fold-thrust mountains and adjacent foreland basins are mechanically coupled in their evolution in that it is the regional isostatic subsidence generated by the former which supplies the foredeep in which the sediments of the latter accumulate [Price 1973]. In terms of the geotectonic cycle envisaged by Dewey and Bird [1970], foreland basins form on stable continental lithosphere either in a back-arc environment during the island arc/subduction/thermal doming ["cordilleran"] orogenic phase [Figure 7-2(a)] and/or suprajacent to suturing and subduction during a continent-continent collision orogenic phase [Figure 7-2(b)]. Beaumont [1981], from whom Figure 7-2 is taken, refers to these two kinds of foreland basin as retroarc and peripheral basins respectively [cf. Dickinson 1974]. In either case, the foreland basin sedimentary sequence is underlain by "miogeosynclinal" sediments formed on a pre-existing subsiding Atlantic-type continental shelf.

Among the postulated Canadian Shield analogues of Phanerozoic fold-thrust mountain/foreland basin terranes, the most easily recognizable is the "suture" peripheral to Superior province [cf. Figure 7-1] which is characterized by the lower Proterozoic sedimentary and volcanic rocks of the Labrador Trough and Cape Smith Fold-Belt [e.g. Gibb and Walcott 1971, Davidson 1972]. Miogeosynclinal, shelf-type, sediments found in the western part of the Labrador Trough [Davidson 1972] may be equivalent to the basal miogeosynclinal sequence of the conceptual model of Phanerozoic foreland basins [Figure 7-2]. To the north in the Labrador Trough and along the southern margin of the Cape

Figure 7-1. Generalized tectonic map of North America [after King and Edmonston 1972] showing the main geological provinces and locations of the cross-sections shown in Figure 7-2: A-A', Cordilleran; B-B', Appalachian; C-C', Grenville; D-D', Churchill-Cape Smith; E-E', Churchill-Labrador Trough. Legend: (1) Phanerozoic orogens: Ap - Appalachian, Cd - Cordilleran; (2) Canadian Shield structural provinces: Ch - Churchill, Gr - Grenville, Nn - Nain, Sp - Superior, Sv - Slave; (3) cr - regions of Phanerozoic or Proterozoic sedimentary cover. Diagonally lined regions are fold-thrust zones; FB signifies foreland basin.

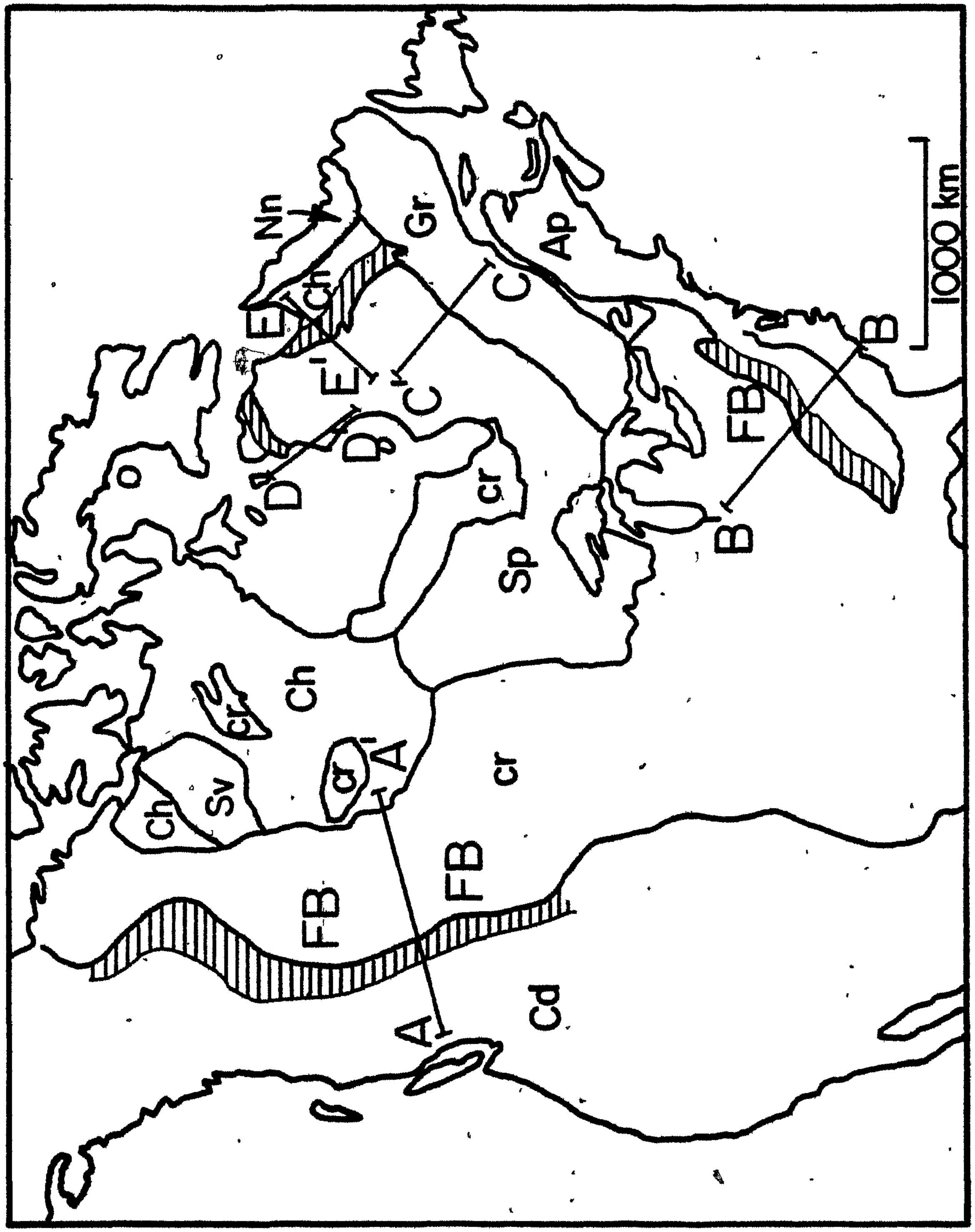
Nn
Gr
Ap
C
C'
E
E'
Ch
D
D'
cr
Sp
FB
B
B'
1000 km
Ch
cr
Sv
Ch
cr
A'
A
FB
FB
cr
Cd

Figure 7-2. Schematic illustration of the formation of (a) retroarc and (b) peripheral foreland basins by the flexural bending of cratonic lithosphere. In each case the foreland basin is deposited unconformably on an underlying Atlantic-type margin. (a) Retroarc basins are formed next to "cordilleran" orogens whereas (b) peripheral foreland basins occur as a result of continent-continent collision [from Beaumont 1981].

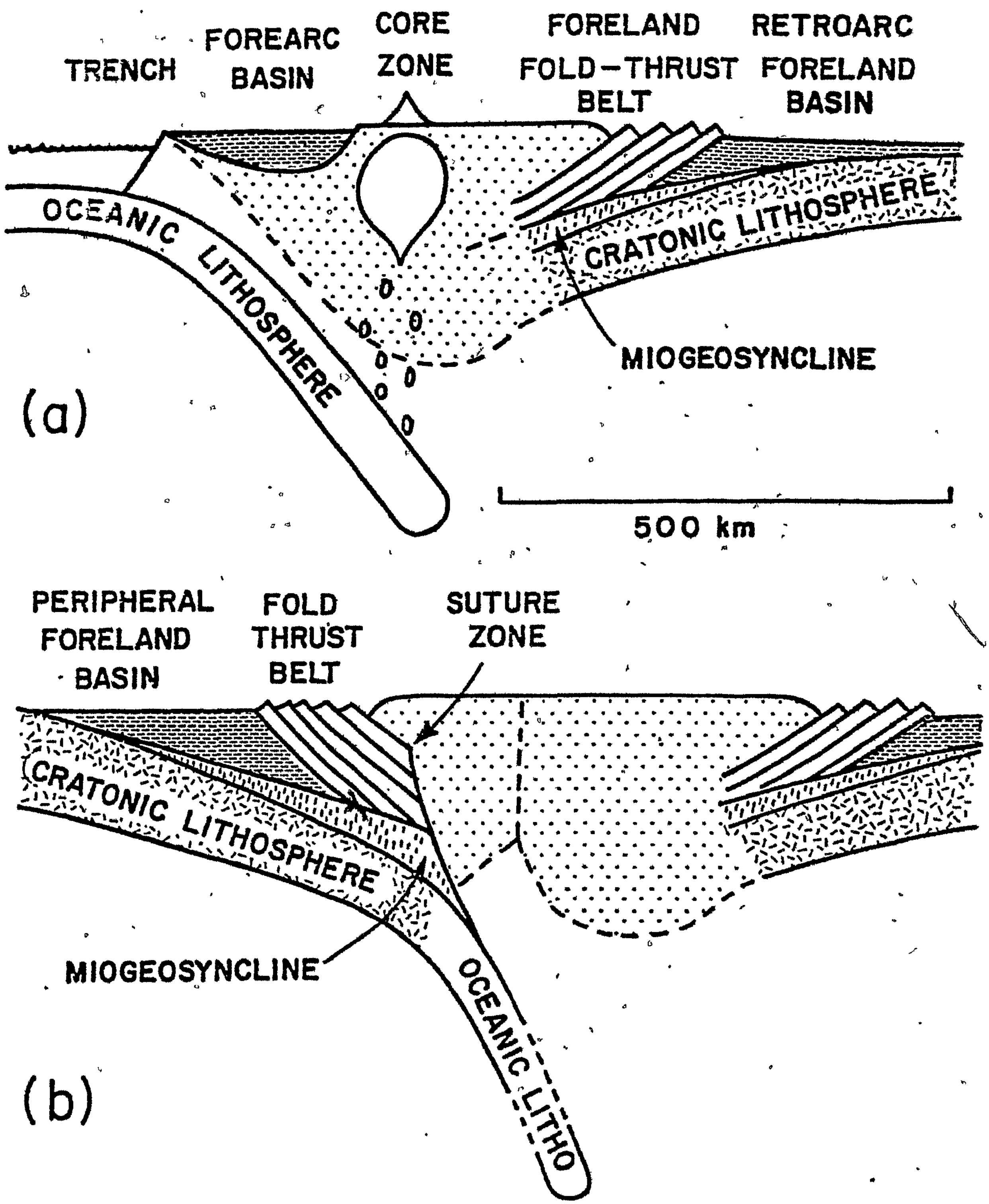
TRENCH
FOREARC BASIN
CORE ZONE
FORELAND FOLD-THRUST BELT
RETROARC FORELAND BASIN
OCEANIC LITHOSPHERE
CRATONIC LITHOSPHERE
MIOGEOSYNCLINE
(a)
500 km
PERIPHERAL FORELAND BASIN
FOLD THRUST BELT
SUTURE ZONE
CRATONIC LITHOSPHERE
MIOGEOSYNCLINE
OCEANIC LITHO
(b)

Smith Fold-Belt it is probable that miogeosynclinal facies rocks have been removed by erosion [Dimroth 1970]. Thrusting of the eastern part of the Labrador Trough is westerly, or cratonward, in orientation [Dimroth 1970, Kearey 1976], similar to the sense of thrusting and décollement in younger fold-thrust regions such as the Rocky Mountains and Appalachian Valley and Ridge [Coney 1973, Price 1973, Bird and Dewey 1970].

The pre-existing passive continental margin, at which the basal miogeosynclinal sedimentary sequence of foreland basins has developed [e.g. Beaumont 1981], is assumed to have formed by previous continental rifting and sea-floor spreading. Provided it is sufficiently old that it has cooled to thermal equilibrium [~200 Ma; Beaumont 1981], the subsequent development of the superimposed foreland basin can be assumed to be relatively unaffected by thermally controlled subsidence. Beaumont [1981] quantified such a scheme and showed that the stratigraphic form of the Alberta Foreland Basin can be successfully modelled in terms of a thin viscoelastic plate lithosphere with flexural rigidity $D=10^{25}$ Nm and relaxation time constant $\tau=27.5$ Ma.

Figure 7-3 illustrates that the Bouguer gravity anomalies associated with the Albertan and Appalachian Foreland Basins as well as those associated with the Precambrian Grenville Front [Grenville-Superior "suture"; cf. Thomas and Tanner 1975], the Cape Smith Fold Belt, and the Labrador Trough [Churchill-Superior "suture"; cf. Kearey 1976, Thomas and Gibb 1977, Thomas et al. 1978, Thomas and Kearey 1980] can be generated in a first-order fashion by a single elastic flexure-type deformational model of the lithosphere. The locations of the

Figure 7-3. Bouguer gravity profiles [solid lines] from the cross-sections located in Figure 7-1 compared to the theoretical gravity profiles [dashed lines] of the single layer broken elastic plate flexure model illustrated in Figure 7-4; chosen flexural parameters λ as shown. Slashes refer to fold-thrust zones [or to the location of the Grenville Front in the case of profile C-C']; FB refers to foreland basin.

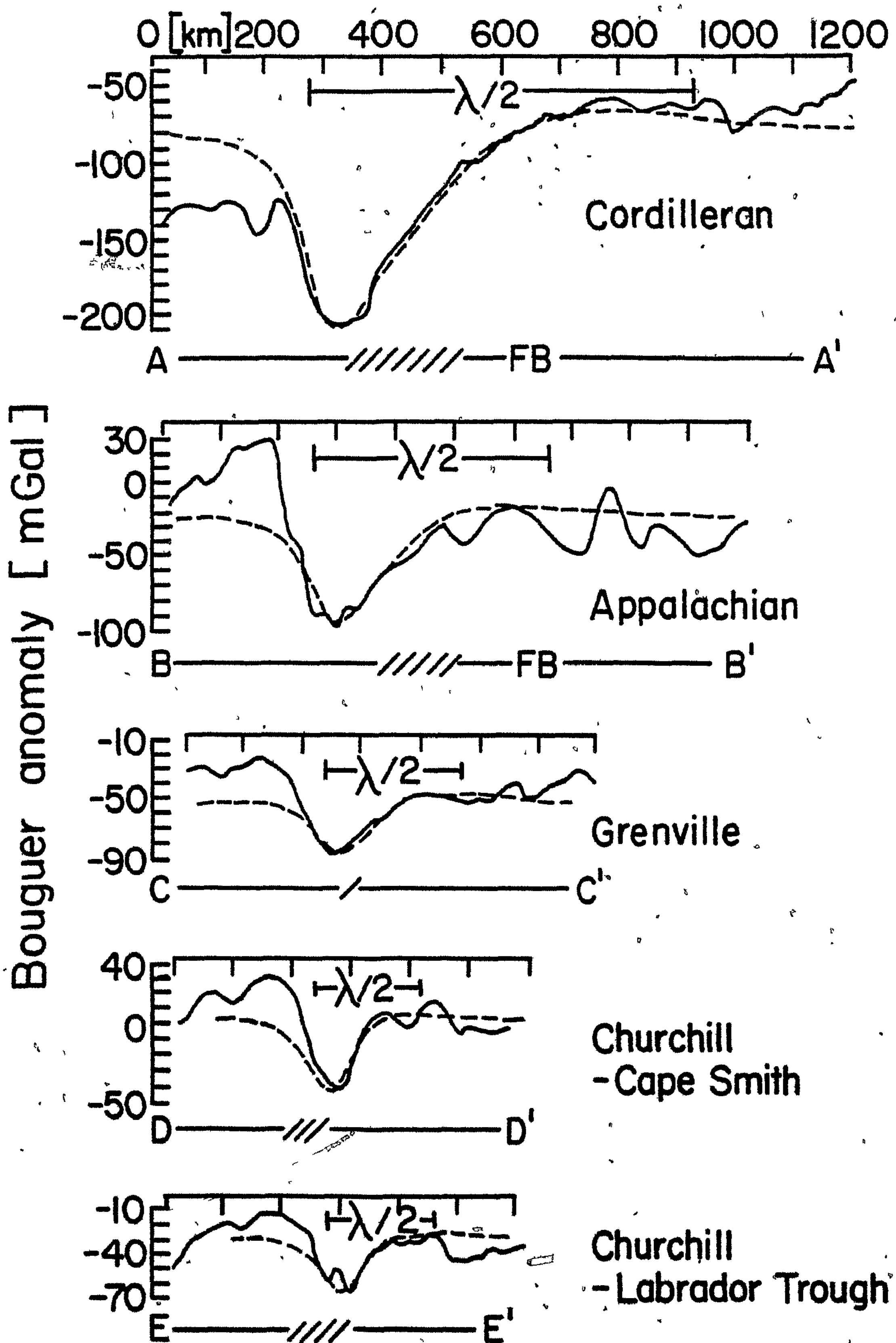
0 [km] 200 400 600 800 1000 1200
-50
-100
-150
-200
λ/2
Cordilleran
A FB A'
30
0
-50
-100
λ/2
Appalachian
B FB B'
-10
-50
-90
λ/2
Grenville
C C'
40
0
-50
λ/2
Churchill
-Cape Smith
D D'
-10
-40
-70
λ/2
Churchill
-Labrador Trough
E E'
Bouguer anomaly [mGal]

gravity profiles, plotted with solid lines Figure 7-3, are shown in Figure 7-1; they were derived from the raw gravity data provided by the Canadian and American governments' Earth Physics Branch and National Oceanic and Atmospheric Administration respectively and have been detrended of the Goddard Earth Model 8 [Wagner et al., 1977] spherical harmonic representation of the Earth's gravity field [cf. subsection 2.2.1].

The theoretical gravity anomalies, plotted with dashed lines in Figure 7-3, refer to the model illustrated in Figure 7-4 comprising a broken thin elastic plate overlying a fluid substratum flexed downward by a point load applied at the free edge. In reality the load would be distributed and would be due to the fold-thrust mountains and sediment accumulation within the foreland basin. The deformation of a broken thin elastic plate loaded at its free edge such as shown in Figure 7-4 can be found by solving the thin elastic plate equation [Equations (3-1)] under appropriate boundary conditions and is [e.g. Walcott 1970b, Hanks 1971, Parsons and Molnar 1976]

$$w(x) = P_o' \exp\,[-2\pi x/\lambda]\ \cos\,[2\pi x/\lambda] \qquad (7\text{-}1i)$$

where

$$P_o' = \frac{2P_o}{\Delta\rho g\lambda} \qquad (7\text{-}1ii);$$

P_o is the magnitude of the point load at the free edge [dimensionally a force per unit width in two dimensions], $\Delta\rho$ is the density difference of the underlying substratum and surficial infilling materials, g is the gravitational acceleration, and λ, called the flexural parameter, is defined as

$$\lambda = \left[\frac{4D}{\Delta\rho g}\right]^{1/4} \tag{7-2}$$

where D is the elastic flexural as defined in Equation (3-1ii). The gravity anomaly generated by deformation w(x) has been calculated by taking its Fourier transform,

$$W(k) = \frac{P_o'}{2\pi} \frac{\lambda^{-1} + ik}{[2\lambda^{-2}-k^2]+i[2k\lambda^{-1}]} \tag{7-3}$$

the origin having been assumed to be coincident with the free edge of the plate, and substituting into Equation (3-10),

$$G(k) = 2\pi\Gamma\ W(k) \int_0^\infty \frac{\partial\rho}{\partial z} \exp[-2\pi kz]\ dz \tag{3-10}$$

where Γ is the gravitational constant. The form of (3-10) is such that a solution for the vertical density gradient of the lithospheric plate could be found by inverting the observed gravity spectrum. In the present case, however, the simple one-layer forward model [Figure 7-4] has been considered such that Equation (3-10) reduces to [cf. subsection 3.3.2; Equations (3-18,19,20)]

$$G(k) = 2\pi\Gamma\ W(k)\ \Delta\rho\ \exp[-2\pi kz_m] \tag{7-4}$$

Figure 7-4. The single layer broken elastic plate flexure model. P_o' is the displacement of the free edge of the plate caused by a point load P_o; P_o approximates the effect of the fold-thrust mountain/foreland basin load [stippled region]. Bouguer gravity anomalies are generated in the areas marked $\pm\Delta\rho$.

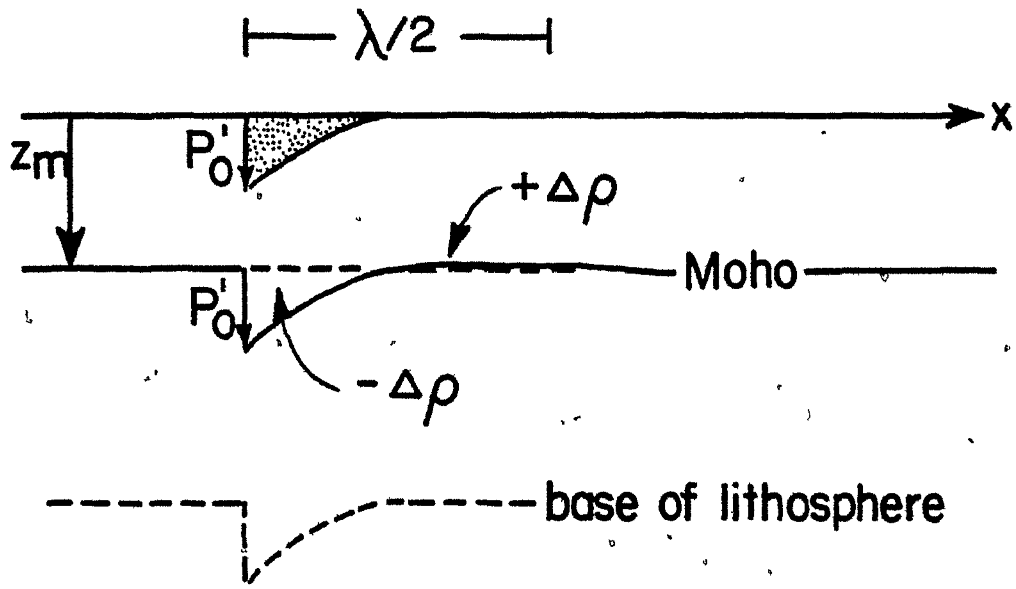
λ/2
x
z_m
P_0'
$+\Delta\rho$
Moho
P_0'
$-\Delta\rho$
base of lithosphere

where z_m is the normal [undeformed] depth to the single lithospheric density interface, assumed to be the Mohorovicic discontinuity at the base of the crust. The theoretical gravity spectrum calculated thus [Equation (7-4)] was then inverse Fourier transformed into the space domain to provide the modelled profiles shown in Figure 7-3.

The profiles in Figure 7-3 are arranged in order to increase in tectonic age from top to bottom and are presented such that the flexured cratonward lithospheric block lies consistently to the right-hand side of the diagram.

These preliminary calculations show that the gravity anomaly generated by a single flexure-type model does provide a reasonably good first-order reproduction of all the observed gravity profiles regardless of their tectonic age. The unexplained left-hand side positive gravity anomaly characterizing all but the Cordilleran may indicate upward flexure of the orogenic lithospheric block related to post-tectonic erosion of topography. The results imply that all of the cross-sections may have a common origin as fold-thrust mountain/foreland basin regions as postulated by Beaumont [1981]. In each calculation z_m and $\Delta\rho$ were assumed to be 35 km and 600 kg m^{-3} respectively. The other parameters of the flexure model, P_o and λ, appear to vary in a manner which is consistent with the relative variations of the tectonic ages of the observed cross-sections [Figure 7-5(a)]. Figure 7-5(b) shows the variation in the flexural parameter recast in terms of the flexural rigidity D [Equation (7-12)].

The apparent decrease through time of the elastic flexural rigidity may imply viscous relaxation of elastic flexural stresses

Figure 7-5. (a) Model parameters λ and P_o and (b) λ recast in terms of flexural rigidity D [Equation (7-2)] as schematic functions of the tectonic age of the cross-sections.

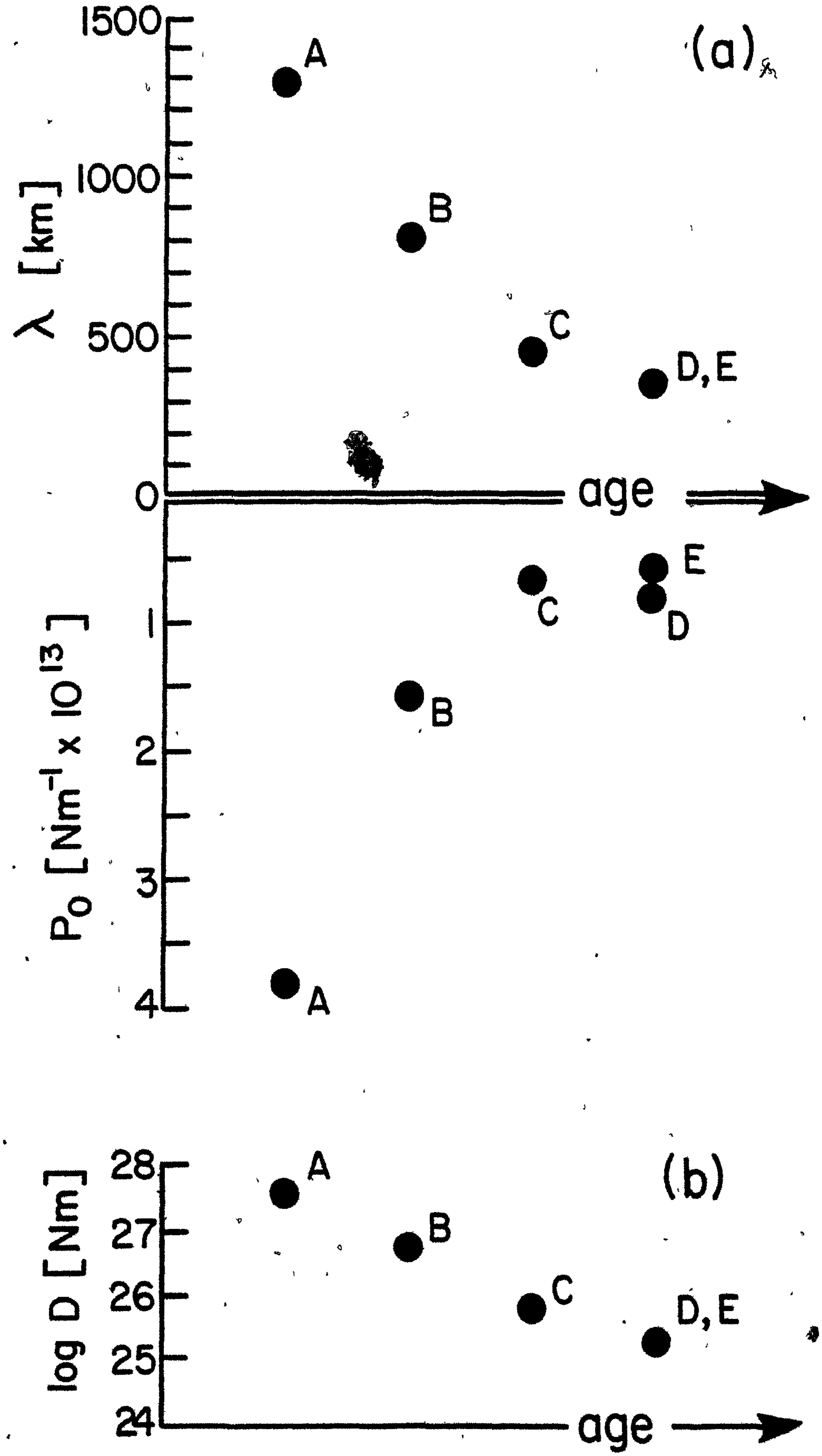

(a)
λ [km]
1500
1000
500
0
age
P_o [$Nm^{-1} \times 10^{13}$]
1
2
3
4
A
B
C
D, E
E
D
(b)
log D [Nm]
28
27
26
25
24
age

[e.g. Walcott 1970a, McNutt and Parker 1978, Cochran 1980] but such a conclusion is equivocal because of the certain importance of the erosional history of the applied load in the viscoelastic model. The decrease in the effective load P_o in the elastic models is indicative of erosional reduction.

Erosion may play an important role even in the earliest stages of foreland basin development. In Beaumont's [1981] model of the Alberta Foreland Basin, although basin subsidence is initiated by the regional lithospheric flexure induced by the load of the adjacent fold-thrust mountain belt, a controlling factor in its ensuing development is the large scale erosion of the fold-thrust belt. Subsequent evolution of the fold-thrust mountain/foreland basin region, in the absence of renewed orogenic activity and/or further cratonward thrusting, may be presumed to be driven entirely by the erosion and removal of the mountain and basin materials.

The preliminary elastic flexure model results presented here suggest that more complete modelling of Precambrian "suture" zone gravity anomalies may readily be accommodated in terms of lithospheric flexure controlled by the erosional evolution of Phanerozoic fold-thrust mountain/foreland basin regions. It is proposed that the techniques developed in this thesis, in which the isostatic effects of an eroding load on a linear viscoelastic lithosphere have been quantified, might be profitably applied to the construction of a single geodynamic model of continental "suture" zones. It is expected that the results of such a study could further characterize the rheology of stable continental lithosphere, especially in respect to the question of the existence or non-existence of viscous relaxation of elastic stresses in the lithosphere within the geological time frame.

References

Adams, C.J.D., (1979). Age and origin of the Southern Alps, in R.I. Walcott and M.M. Cresswell, eds., The Origin of the Southern Alps. R. Soc. N.Z. Bull. 18: 73-78.

Adams, John, (1980). Contemporary uplift and erosion of the Southern Alps, New Zealand: Summary. Geol. Soc. Am. Bull. (I) 91: 2-4.

Airy, G.B., (1855). On the computations of the effect of the attraction of the mountain masses as disturbing the apparent astronomical latitude of stations in geodetic surveys. Phil. Trans. R. Soc. Lond. (B) 145: 101-104.

Ambrose, J.W., (1964). Exhumed paleoplains of the Precambrian Shield of North America. Am. J. Sci. 262: 817-857.

Anderson, R.N., D. McKenzie, and J.G. Sclater, (1973). Gravity, bathymetry and convection in the Earth. E. Planet. Sci. Lett. 18: 391-407.

Andrews, J.T. and G.H. Miller, (1979). Glacial erosion and ice sheet divides, northeastern Laurentide Ice Sheet, on the basis of the distribution of limestone erratics. Geology 7: 592-596.

Atwater, T., (1970). Implications of plate tectonics for the Cenozoic tectonic evolution of Western North America. Geol. Soc. Am. Bull. 81: 3513-3536.

Banks, R.J., R.L. Parker, and S.P. Huestis, (1977). Isostatic compensation on a continental scale: local versus regional mechanisms. Geophys. J. R. astr. Soc. 51: 431-452.

Banks, R.J. and C.J. Swain, (1978). The isostatic compensation of East Africa. Proc. R. Soc. Lond., A, 364: 331-352.

Beaumont, C., (1978). The evolution of sedimentary basins on a viscoelastic lithosphere: theory and examples. Geophys. J. R. astr. Soc. 55: 471-497.

__________, (1979). On rheological zonation of the lithosphere during flexure. Tectonophysics 59: 347-365.

__________, (1981). Foreland basins. Geophys. J. R. astr. Soc. 65: 291-329.

Bird, J.M. and J.F. Dewey, (1970). Lithosphere plate-continental margin tectonics and the evolution of the Appalachian orogen. Geol. Soc. Am. Bull. 81: 1031-1060.

Brenner, N., (1968). Cooley-Tukey Fast Fourier Transform. Mass. Inst. Tech. Lincoln Laboratory.

Caldwell, J.G., W.F. Haxby, D.E. Karig, and D.L. Turcotte, (1976). On the applicability of a universal elastic trench profile. Earth Pl. Sci. Lett. 31: 239-246.

Chase, C.G., (1979). Asthenospheric counterflow: a kinematic model. Geophys. J. R. astr. Soc. 56: 1-18.

Cochran, J.R., (1973). Gravity and magnetic investigations in the Guiana basin, Western Equatorial Atlantic. Geol. Soc. Am. Bull. 84: 3249-3268.

__________, (1979). An analysis of isostasy in the world's oceans 2. Midocean ridge crests. J. Geophys. Res. 84: 4713-4729.

__________, (1980). Some remarks on isostasy and the long-term behaviour of the continental lithosphere. Earth Pl. Sci. Lett. 46: 266-274.

__________ and M. Talwani, (1977). Free-air gravity anomalies in the world's oceans and their relationship to residual elevation. Geophys. J. R. astr. Soc. 50: 495-552.

Coney, P.J., (1973). Plate tectonics of marginal foreland thrust-fold belts. Geology 1: 131-134.

Dallmeyer, R.D., (1975). Incremental $^{40}Ar/^{39}Ar$ Ages of biotite and hornblende from retrograded basement gneisses of the southern Blue Ridge: their bearing on the age of Paleozoic metamorphism. Am. J. Sci. 275: 444-460.

Davidson, A., (1972). The Churchill province, in R.A. Price and R.J.W. Douglas, eds., Variations in Tectonic Styles in Canada. Geol. Ass. Can. Spec. Pap. 11: 381-433.

Davies, G.F., (1979). Thickness and thermal history of continental crust and root zones. E. Pl. Sci. Lett. 44: 231-238.

Davies, P.A. and S.K. Runcorn, eds., (1980). Mechanisms of Continental Drift and Plate Tectonics. Academic Press, London, 362 pp.

Detrick, R.S. and A.B. Watts, (1979). An analysis of isostasy in the world's oceans 3. Aseismic ridges. J. Geophys. Res. 84: 3637-3653.

Dewey, J.F. and J.M. Bird, (1970). Mountain belts and the new global tectonics. J. Geophys. Res. 75: 2625-2647.

Dickinson, W.R., (1974). Plate tectonics and sedimentation, in W.R. Dickinson, ed., Tectonics and Sedimentation. Soc. Econ. Geol. Paleont. Spec. Publ. 22: 1-27.

Dimroth, E., (1970). Evolution of the Labrador geosyncline. Geol. Soc. Am. Bull. 81: 2717-2741.

Doetsch, Gustav, (1974). Introduction to the Theory and Application of the Laplace Transformation. Springer-Verlag, New York, 326 pp.

Doherty, J.T. and J.B. Lyons, (1980). Mesozoic erosion rates in northern New England. Geol. Soc. Am. Bull. (I) 91: 16-20.

Dorman, L.M. and B.T.R. Lewis, (1970). Experimental isostasy. 1. Theory of the determination of the Earth's isostatic response to a concentrated load. J. Geophys. Res. 75: 3357-3365.

______________________________, (1972). Experimental isostasy. 3. Inversion of the isostatic Green function and lateral density changes. J. Geophys. Res. 77: 3068-3077.

Douglas, R.J.W., H. Gabrielse, J.O. Wheeler, D.F. Stott, and H.R. Belyea, (1970). Geology of Western Canada in R.J.W. Douglas, ed., Geology and Economic Minerals of Canada. Geol. Surv. Can., Ottawa: 365-488.

Draper, N.R. and H. Smith, (1967). Applied Regression Analysis. Wiley, New York, 407 pp.

England, P.C. and S.W. Richardson, (1980). Erosion and the age dependence of continental heat flow. Geophys. J. R. astr. Soc. 62: 421-437.

Forsyth, D.W., (1975). The early structural evolution and anisotropy of the oceanic upper mantle. Geophys. J. R. astr. Soc. 43: 103-162.

_____________, (1979). Lithospheric flexure. Rev. Geophys. Space Phys. 17: 1109-1114.

Fralick, P.W., (1981). Tectonic and Sedimentological Development of a late Paleozoic Wrench Basin: the Eastern Cumberland Basin, Maritime Canada. M.Sc. thesis, Dalhousie University, Halifax, 178 pp.

Gibb, R.A. and M.D. Thomas, (1976). Gravity signature of fossil plate boundaries in the Canadian Shield. Nature 262: 199-200.

_________________________, (1977). The Thelon Front: a cryptic suture in the Canadian Shield? Tectonophysics 38: 211-222.

__________ and R.I. Walcott, (1971). A precambrian suture in the Canadian Shield. Earth Pl. Sci. Lett. 10: 417-422.

Goodacre, A.K., (1972). Generalized structure and composition of the deep crust and upper mantle in Canada. J. Geophys. Res. 77: 3146-3161.

Gordon, R.B., (1979). Denudation rate of central New England determined from estuarine sedimentation. Am. J. Sci. 279: 632-642.

Gravenor, C.P., (1975). Erosion by continental ice sheets. Am. J. Sci. 275: 594-604.

Green, A.G., N.L. Anderson and O.G. Stephenson, (1979). An expanding spread seismic reflection survey across the Snake Bay – Kakagi Lake greenstone belt, northwestern Ontario. Can. J. Earth Sci. 16: 1599-1612.

Gunn, R., (1943a). A quantitative evaluation of the influence of the lithosphere on the anomalies of gravity. J. Franklin Inst. 236: 47-65.

_______, (1943b). A quantitative study of isobaric equilibrium and gravity anomalies in the Hawaiian Islands. J. Franklin Inst. 236: 373-390.

_______, (1944). A quantitative study of the lithosphere and gravity anomalies along the Atlantic coast. J. Franklin Inst. 237: 139-154.

Hager, B.H. and R.J. O'Connell, (1979). Kinematic models of large-scale flow in the Earth's mantle. J. Geophys. Res. 84: 1031-1048.

Hamilton, W. and W.B. Myers, (1966). Cenozoic tectonics of the western United States. Rev. Geophys. 4: 509-549.

Hanks, T.C., (1971). The Kuril Trench-Hokkaido Rise System: large shallow earthquakes and simple models of deformation. Geophys. J. R. astr. Soc. 23: 173-189.

Haxby, W.F., D.L. Turcotte and J.M. Bird, (1976). Thermal and mechanical evolution of the Michigan Basin. Tectonophysics 36: 57-75.

Heiskanen, W.A. and F.A. Vening Meinesz, (1958). The Earth and its Gravity Field. McGraw-Hill, New York, 470 pp.

Hurley, P.M., H. Hughes, W.H. Pinson, Jr. and H.W. Fairbairn, (1962). Radiogenic argon and strontium diffusion parameters in biotite at low temperatures obtained from Alpine Fault uplift in New Zealand. Geochim. et Cosmochim. Acta 26: 67-80.

Jeffreys, H., (1976). The Earth, 6th ed. Cambridge U. Press, Cambridge, 574 pp.

Jenkins, G.M. and D.G. Watts, (1968). Spectral Analysis and its Applications. Holden-Day, San Francisco, 525 pp.

Kearey, P., (1976). A regional structural model of the Labrador Trough, northern Quebec, from gravity studies, and its relevance to continent collision in the Precambrian. Earth Pl. Sci. Lett. 28: 371-378.

King, L.H., (1972). Relation of plate tectonics to the geomorphic evolution of the Canadian Atlantic Provinces. Geol. Soc. Am. Bull. 83: 3083-3090.

King, P.B., (1977). The Evolution of North America. Princeton Univ. Press, Princeton, N.J., 197 pp.

________ and G.J. Edmonston, (1972). Generalized tectonic map of North America. U.S. Geol. Surv., Washington.

Kono, Y. and M. Amano, (1978). Thickening model of the continental lithosphere. Geophys. J. R. astr. Soc. 54: 405-416.

Louden, K.E., (1981). A comparison of the isostatic response of bathymetric features in the north Pacific Ocean and Phillipine Sea. Geophys. J. R. astr. Soc. 64: 393-424.

________ and D.W. Forsyth, (in press). Crustal thickness and mantle compensation near the Kane Fracture Zone from topography and gravity measurements: I. Spectral analysis approach. Geophys. J. R. astr. Soc.

McKenzie, D.P., (1967). Some remarks on heat flow and gravity anomalies. J. Geophys. Res. 72: 6261-6273.

________, (1977). Surface deformation, gravity anomalies and convection. Geophys. J. R. astr. Soc. 48: 211-238.

________ and C. Bowin, (1976). The relationship between bathymetry and gravity in the Atlantic Ocean. J. Geophys. Res. 81: 1903-1915.

__________, J.M. Roberts and N.O. Weiss, (1974). Convection in the Earth's mantle: towards a numerical solution. J. Fluid Mech. 62: 465-538.

__________, A. Watts, B. Parsons and M. Roufosse, (1980). Planform of mantle convection beneath the Pacific Ocean. Nature 288: 442-446.

__________ and N. Weiss, (1975). Speculations on the thermal and tectonic history of the Earth. Geophys. J. R. astr. Soc. 42: 131-174.

McNutt, M.K., (1978). Continental and Oceanic Isostasy. Ph.D. thesis, University of California, San Diego, 192 pp.

__________, (1979). Compensation of oceanic topography: an application of the response function technique to the Surveyor area. J. Geophys. Res. 84: 7589-7598.

__________, (1980). Implications of regional gravity for state of stress in the Earth's crust and upper mantle. J. Geophys. Res. 85: 6377-6396.

__________ and R.L. Parker, (1978). Isostasy in Australia and the evolution of the compensation mechanism. Science 199: 773-775.

Menard, H.W., (1961). Some rates of regional erosion. J. Geol. 69: 154-161.

Munk, W.H. and D.E. Cartwright, (1966). Tidal spectroscopy and prediction. Phil. Trans. R. Soc. Lond. 259: 533-581.

Nadai, A., (1963). Theory of Flow and Fracture of Solids, vol. 2. McGraw-Hill, New York.

Neidell, N., (1963). A statistical study of isostasy. Geophys. Prospecting, 11: 164-175.

New Zealand, (1976). New Zealand topographical maps. Department of Lands and Surveys, Wellington, 4 sheets.

Owens, L.B. and J.P. Watson, (1979). Landscape reduction by weathering in small Rhodesian watersheds. Geology 7: 281-284.

Panza, G.F., (1980). Evolution of the Earth's lithosphere, in P.A. Davies and S.K. Runcorn, eds., Mechanisms of Continental Drift and Plate Tectonics. Academic Press, London: 75-87.

Parker, R.L., (1973). The rapid calculation of potential anomalies. Geophys. J. R. astr. Soc. 31: 447-455.

Parsons, B. and D. McKenzie, (1978). Mantle convection and the thermal structure of the plates. J. Geophys. Res. 83: 4485-4496.

Parsons, B. and P. Molnar, (1976). The origin of outer topographic rises associated with trenches. Geophys. J. R. astr. Soc. 45: 707-712.

Pollack, H.N. and D.S. Chapman, (1977). On the regional variation of heat flow, geotherms, and lithospheric thickness. Tectonophysics 38: 279-296.

Pratt, J., (1855). On the attraction of the Himalaya Mountains and of the elevated regions beyond upon the plumb-line in India. Phil. Trans. R. Soc. Lond. (B) 145: 53-100.

Price, R.A., (1973). Large-scale gravitational flow of supracrustal rocks, southern Canadian Rockies, in K.A. DeJong and R.A. Scholten, eds., Gravity and Tectonics. Wiley, New York: 491-502.

_________ and R.J.W. Douglas, eds., Variations in Tectonic Styles in Canada. Geol. Ass. Can. Spec. Pap. 11, 688 pp.

Pugh, J.C., (1955). Isostatic readjustment in the theory of pediplanation. Geol. Soc. Lond. Quart. J. 111: 361-369.

Quinlan, G.M., (1981). Numerical Models of Postglacial Relative Sea Level Change in Atlantic Canada and the Eastern Canadian Arctic. Ph.D. thesis, Dalhousie University, Halifax, 499 pp.

Rayner, J.N., (1971). An Introduction to Spectral Analysis. Pion Ltd., London, 174 pp.

Richardus, P. and R.K. Adler, (1972). Map Projections for Geodesists, Cartographers and Geographers. North-Holland Publishing Co., Amsterdam, 174 pp.

Richter, F.M., (1973). Convection and the large-scale circulation of the mantle. J. Geophys. Res. 78: 8735-8745.

____________ and D. McKenzie, (1978). Simple plate models of mantle convection. J. Geophys. 44: 441-471.

____________ and B. Parsons, (1975). On the interaction of two scales of convection in the mantle. J. Geophys. Res. 80: 2529-2541.

Roberts, G.E. and H. Kaufman, (1966). Table of Laplace Transforms. W.B. Saunders Co., Philadelphia, 367 pp.

Sandwell, D.T. and K.A. Poehls, (1980). A compensation mechanism for the Central Pacific. J. Geophys. Res. 85: 3751-3758.

Sclater, J.G., C. Jaupart and D. Galson, (1980). The heat flow through oceanic and continental crust and the heat loss of the Earth. Rev. Geophys. Space Phys. 18: 269-311.

____________, L.A. Lawver and B. Parsons, (1975). Comparison of long wavelength residual elevation and free air gravity anomalies in the North Atlantic and possible implications for the thickness of the lithospheric plate. J. Geophys. Res. 80: 1031-1052.

Sinha, M.C., K.E. Londen and B. Parsons, (in press). The crustal structure of the Madagascar Ridge. Geophys. J. R. astr. Soc.

Skilbeck, J.N. and D.P. McKenzie, (1979). An approximate method for determining the stability of two-scale flow in the mantle. Pure and Applied Geophys. 117: 958-987.

Sneddon, I.N., (1951). Fourier Transforms. McGraw-Hill, New York, 542 pp.

Stearn, C.W., R.L. Carroll and T.H. Clark, (1979). Geological Evolution of North America, 3rd. ed. John Wiley and Sons, New York, 566 pp.

Stephenson, R., (1978). Isostatic response of lithosphere in Canada. Geol. Ass. Can./Min. Ass. Can. Abs. with Program 3: 498.

______________ and C. Beaumont, (1980). Small-scale convection in the upper mantle and the isostatic response of the Canadian Shield, in P.A. Davies and S.K. Runcorn, eds. Mechanisms of Continental Drift and Plate Tectonics. Academic Press, London: 111-122.

Stockwell, C.H., (1964). Fourth report on structural provinces, orogenies, and time-classification of rocks of the Canadian precambrian shield. Geol. Surv. Can. Paper 64-17 (II): 1-21.

Swain, C.J., (1976). A FORTRAN IV program for interpolating irregularly spaced data using the difference equations for minimum curvature. Computers and Geosciences 1: 231-240.

Thomas, M.D., (1975). The correlation of gravity and geology in Southeastern Quebec and Southern Labrador. Gravity Map Series, Earth Physics Branch, Maps 64-67, 96-98, Ottawa, 49 pp.

__________ and R.A. Gibb, (1977). Gravity anomalies and deep structure of the Cape Smith foldbelt, northern Ungava, Quebec. Geology 5: 169-172.

__________, D.W. Halliday and R. Stephenson, (1978). Gravity anomalies and geological structure in northern Labrador and northeastern Quebec. Gravity Map Series, Earth Physics Branch, Maps 157-161, Ottawa, 38 pp.

__________ and P. Kearey, (1980). Gravity anomalies, block-faulting and Andean-type tectonism in the Eastern Churchill Province. Nature 283: 61-63.

__________ and J.G. Tanner, (1975). Cryptic suture in the eastern Grenville Province. Nature 256: 392-394.

Tukey, J.W., (1967). Spectrum calculations in the new world of the Fast Fourier Transform, in B. Harris, ed., Advanced Seminar on Spectral Analysis of Time Series. Wiley, New York: 25-46.

Turcotte, D.L. and K. Burke, (1978). Global sea-level changes and the thermal structure of the Earth. E. Pl. Sci. Lett. 41: 341-346.

____________, D.C. McAdoo and J.G. Caldwell, (1978). An elastic-perfectly plastic analysis of the bending of the lithosphere at a trench. Tectonophysics 47: 193-205.

____________ and E.R. Oxburgh, (1967). Finite amplitude convective cells and continental drift. J. Fluid Dynamics 28: 29-42.

Vening Meinesz, F.A., (1931). Une nouvelle méthode pour la réduction isostatique régionale de l'intensité de la pesanteur. Bull. Géod. 29.

Wagner, C.A., F.J. Lerch, J.E. Brownd and J.A. Richardson, (1977). Improvement in the geopotential derived from satellite and surface data (GEM 7 and 8). J. Geophys. Res. 82: 901-914.

Walcott, R.I., (1970a). Flexural rigidity, thickness, and viscosity of the lithosphere. J. Geophys. Res. 75: 3941-3954.

____________, (1970b). Flexure of the lithosphere at Hawaii. Tectonophysics 9: 435-446.

____________, (1972). Gravity, flexure, and the growth of sedimentary basins at a continental edge. Geol. Soc. Am. Bull. 83: 1875-1878.

____________, (1976). Lithosphere flexure, analysis of gravity anomalies, and the propagation of seamount chains, in G.H. Sutton, M.H. Manghnani, and R. Moberly, eds. The Geophysics of the Pacific Ocean Basin and its Margin. Am. Geophys. U., Geophys. Monogr. 19: 431-438.

__________, (1979). Plate motion and shear strain rates in the vicinity of the Southern Alps, <u>in</u> R.I. Walcott and M.M. Cresswell, eds., <u>The Origin of the Southern Alps</u>. R. Soc. N.Z. Bull. <u>18</u>: 5-12.

Watts, A.B., (1976). Gravity and bathymetry in the Central Pacific Ocean. J. Geophys. Res. <u>81</u>: 1533-1553.

__________, (1978). An analysis of isostasy in the world's oceans 1. Hawaiian-Emperor Seamount Chain. J. Geophys. Res. <u>83</u>: 5989-6004.

__________ and J.R. Cochran, (1974). Gravity anomalies and flexure of the lithosphere along the Hawaiian-Emperor seamount chain. Geophys. J. R. astr. Soc. <u>38</u>: 119-141.

__________, J.R. Cochran and G. Selzer, (1975). Gravity anomalies and flexure of the lithosphere: a three-dimensional study of the Great Meteor Seamount, Northeast Atlantic. J. Geophys. Res. <u>80</u>: 1391-1398.

__________ and M. Talwani, (1974). Gravity anomalies seaward of deep-sea trenches and their tectonic implications. Geophys. J. R. astr. Soc. <u>36</u>: 57-90.

Wellman, H.W., (1979). An uplift map for the South Island of New Zealand, and a model for uplift of the Southern Alps, <u>in</u> R.I. Walcott and M.M. Cresswell, eds., <u>The Origin of the Southern Alps</u>. R. Soc. N.Z. Bull. <u>18</u>: 13-20.

Wheeler, J.O. and H. Gabrielse, (1972). The Cordilleran Structural province, in R.A. Price and R.J.W. Douglas, eds., Variations in Tectonic Styles in Canada. Geol. Ass. Can. Spec. Paper 11: 1-81.

White, W.A., (1972). Deep erosion by continental ice sheets. Geol. Soc. Am. Bull. 83: 1037-1056.

Yuen, D.A., W.R. Peltier and G. Schubert, (1981). On the existence of a second scale of convection in the upper mantle. Geophys. J. R. astr. Soc. 65: 171-190.